Infrared spectroscopy of volcanic gases at Masaya, Nicaragua

Thesis

INFRARED SPECTROSCOPY OF VOLCANIC GASES AT MASAYA, NICARAGUA

A thesis submitted for the degree of Ph.D.

by

Lisa Anne Horrocks

B.A., M.A. *(Cantab)*

Department of Earth Sciences

The Open University

2 March 2001

ABSTRACT

Volcanic gases carry valuable information about processes occurring at active volcanoes, and so their accurate measurement and analysis are highly desirable. Masaya is a low-lying persistently active basaltic volcano, which is renowned for strong passive gas emission unaccompanied by lava extrusion, although it has also undergone plinian eruptions in the past. Its consistent behaviour sustains a reliable tropospheric plume, making it an ideal location at which to study volcanic degassing.

During February–March 1998 and March 1999, Masaya's gas plume composition was investigated using the new ground-based remote sensing technique of open-path Fourier transform infrared spectroscopy. This technique meets criteria for safe and accurate quantitative characterisation of volcanic gases and on a temporal resolution previously impracticable. Flexibility of operation is the chief merit of OP-FTIR, since a range of infrared sources are available (e.g. an active lamp, the sun or hot volcanic vents). Laboratory calibration experiments using primary gas standards confirmed that the instrument and subsequent spectral analysis provide highly accurate concentration measurements for volcanic species, with errors typically around 5 %.

Results showed that Masaya's plume composition was little changed between the field seasons. Average molar ratios for SO_2/HCl, HCl/HF, CO_2/SO_2 and H_2O/SO_2 were 1.6, 4.9, 2.2 and 72, respectively, in 1998, and 1.6, 5.1, 2.3 and 66 in 1999. These ratios, coupled with simultaneous COSPEC-derived SO_2 data, indicated that emission rates, especially of HCl and HF, were high compared with other passively-degassing volcanoes. Measurements using the spectrometer with different infrared sources and at different locations downwind demonstrated that tropospheric scavenging processes had little discernible effect on plume composition.

In the light of these new OP-FTIR gas data, possible physical mechanisms for the degassing behaviour at Masaya Volcano have been discussed. In order to account for all the observations, an integrated model, in which gas emission rates are primarily controlled by degassing-driven convection in the conduit, is proposed.

DEDICATION AND ACKNOWLEDGEMENTS

This thesis is dedicated to the memory of Professor Peter Francis. He was witty, mischievous and intelligent: an inspiring supervisor, and a friend. He often opened his talks on volcanic gases with the question, "Telegrams from within, or Chinese whispers?" This thesis sets out to answer him.

I hope that he would have been pleased with it.

Acknowledgements

In three and a half years spent working on this project, I have, inevitably, been guided, instructed, encouraged and accompanied along the way by many people, to whom I owe a great deal of thanks. My acknowledgments fall into five categories.

Clearly the content of this thesis relied heavily on fieldwork carried out in the springs of 1998 and 1999. Many people were instrumental, either in facilitating the work in Nicaragua, or in providing discussion and company whilst there. Mike Burton, Peter Francis, Clive Oppenheimer and Matthew Watson were industrious and diligent co-investigators; it was great fun to work with them too. I benefited from collaborating with Glyn Williams-Jones, Alex Beaulieu, Katie St-Amand, Pierre Delmelle and John Stix while in the field and on return. The logistics of the operation were smoothed over as a result of efforts by INETER, Parque Nacional de Masaya and the British Embassy in Managua: particular thanks are due to Marie-Louise Archer for her enthusiasm, and an invitation to an enjoyable reception with the Ambassador in 1998.

Some aspects of the thesis were the product of laboratory studies. At the OU, I thank Andy Tindle, John Watson and Kay Chambers, who all contributed towards successful work with the electron microprobe. Mike Carroll at Bristol University taught me about melt inclusions in his lab. Calibration and validation work with the FTIR would have been impossible without the facilities of the National Physical Laboratory in Teddington. I thank Bill Bell, Nick Davies and Nick Martin from NPL, and Clive Oppenheimer and Hayley Duffell from Cambridge for their generous assistance and thought-provoking discussion afterwards.

The conception and development of the ideas and arguments presented here are almost impossible to trace, but many people were involved in guiding discussion. My colleagues in the Cambridge/OU FTIR group were the major support: thanks are due to Peter Francis, Mike Burton, Clive Oppenheimer, Hayley Duffell, Marie Edmonds and Adam Maciejewski. A number of individuals at the OU contributed to my thinking: Steve Blake, Chris Hawkesworth, Nick Rogers, Hazel Rymer, David Rothery. I am grateful to many others for questions, answers, information and suggestions: Jeremy Phillips, Jenni Barclay, David Pyle, Pierre Delmelle, Jim Walker, Bob Symonds—to name a few. There will have been others too.

On the administrative side, I must thank NERC for funding me; Janet Dryden, for organising all the PhD students and their supervisors; and John Taylor and Andy Lloyd for teaching me how to make posters and slides. I am extremely grateful for Steve Blake and Clive Oppenheimer stepping into the breach after Peter's death to supervise my final year.

Finally, I owe the biggest thanks to the crowd of supporters on the sideline. Getting to know my office mates and contemporaries at the OU was an unexpected bonus. As ever, my family extended unconditional support and confidence through all the ups and downs. Most of all, I thank David, who coped with having a volcanologist for a wife (and consequently all the stolen limelight) absolutely magnificently.

"May the glory of the Lord endure forever;
may the Lord rejoice in his works—
he who looks at the earth, and it trembles,
who touches the mountains, and they smoke."

Psalm 104, verses 31–3

CONTENTS

List of Figures

CHAPTER 1
GENERAL INTRODUCTION TO VOLCANIC GAS MEASUREMENT AND MASAYA VOLCANO, NICARAGUA

"Telegrams from within" – volcanologists have been considering the potential of exhaled gases to relay valuable information about a volcano's behaviour since well before Matsuo first coined this phrase in 1975 (Matsuo, 1975, cited in Notsu *et al.* 1993). In order to tap this information, two challenges exist, first, to make accurate and useful gas measurements, and second, to correctly interpret measured compositions and emission rates. In this thesis, I aim to address both of these challenges. A relatively new gas measurement technique, that of open-path Fourier transform infrared spectroscopy (OP-FTIR), will be presented, examined and developed, and gas data collected at Masaya Volcano will be analysed, and used to explain the current volcanic activity.

Following this introductory chapter, the thesis starts with an overview of infrared spectroscopy including a description of the instrument used for fieldwork and a calibration for SO_2 measurement, based on the results of controlled tests. In Chapter 3, I present technical detail concerning the retrieval of gas concentrations from spectra collected in different modes at Masaya, and discuss uncertainty bounds. Chapters 4 to 6 contain the discussion of the retrieved data. First, the measured gas compositions are assessed in terms of potential interactions between plume gases and the atmosphere (Chapter 4), before being interpreted for their volcanological implications (Chapter 5). Finally, in Chapter 6, I discuss potential physical models for degassing at Masaya, given the constraints of gas composition and emission rates provided by the field observations. The concluding chapter contains some thoughts about the future use of OP-FTIR for volcanic gas monitoring, as well as some suggestions for further research at Masaya Volcano.

In this introduction, I will deal with some fundamental questions about volcanic gas monitoring and the choice of Masaya Volcano as the test location for this thesis:

(a) What are the motivations behind studies of volcanic gases, and what information can they provide?

(b) Why is open-path Fourier transform spectroscopy a promising new tool for gas measurements, compared to the other available techniques?

(c) What makes Masaya Volcano an appropriate location at which to use OP-FTIR?

(d) How can gas data contribute to an improved understanding of volcanic activity at Masaya?

1.1 Motivation for Volcanic-Gas Studies

Gases from volcanoes have been studied since the earliest days of volcanology when Davy first collected gases in wine bottles on Graham Island in 1831. The motivations for modern volcanic-gas studies fall into four broad categories, loosely connected with different stages in the volcano-magmatic system (figure 1-1). Gas measurements enable investigations into both the chemistry of magmas and processes of magma degassing, volcano monitoring for risk mitigation, and research into the environmental impact of gases from volcanoes.

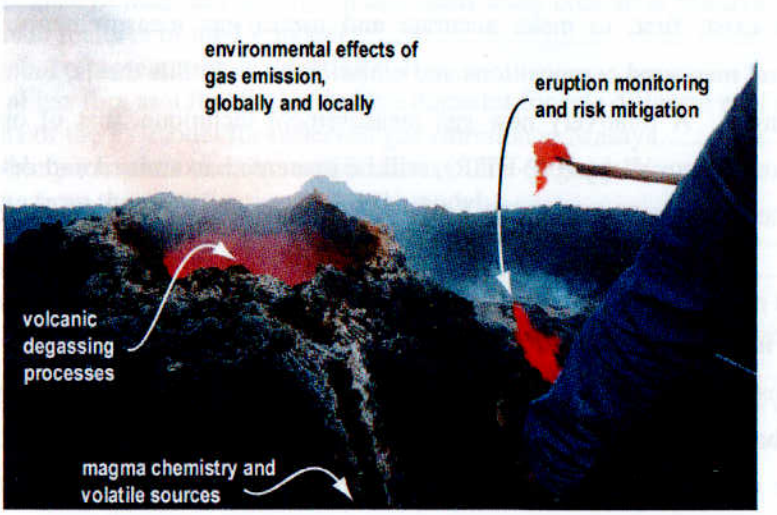

Figure 1-1: Lava pool on the flanks of Etna's South-East Crater. Volcanic gas studies contribute to an increased understanding of magma chemistry and the sources of volatiles emitted at the surface, to models of volcanic degassing processes, to better monitoring of eruptions and to further insight into atmospheric effects of volcanogenic "pollutant" gases.

1.1.1 Magma chemistry

Volcanic gas studies provide insight into the composition, amounts and origins of dissolved magmatic volatiles. Systematic compilation of gas data from a range of volcanoes indicates a broad correlation between gas composition and tectonic setting, related to the different volatile sources available at different settings (Symonds *et al.* 1994), shown schematically in figure 1-2. I discuss these different sources in more detail in Section 1.2. It is, however, becoming apparent that despite these broad correlations, individual volcanoes have characteristic gas signatures owing to unique combinations of magma source, processing, storage, and eruptive regime. Recent eruptions and gas monitoring at the Cook Inlet volcanoes Augustine (Kodosky *et al.* 1991, Rose *et al.* 1988, Symonds *et al.* 1992, Symonds *et al.* 1990), Redoubt (Gerlach *et al.* 1994, Hobbs *et al.* 1991) and Spurr (Doukas & Gerlach 1995), provided evidence that gas compositions and emission rates from adjacent volcanoes along an arc can be very different. Despite the expected similarities in their magma sources, there were significant differences in magmas, volcanic activity and gas composition at these volcanoes. At arc volcanoes, it is also possible to

use information from volcanic-gas studies to address longstanding issues such as the balance between contributions from mantle, subducted slab and sediments to the source of arc magmas (e.g. Fischer *et al.* 1998).

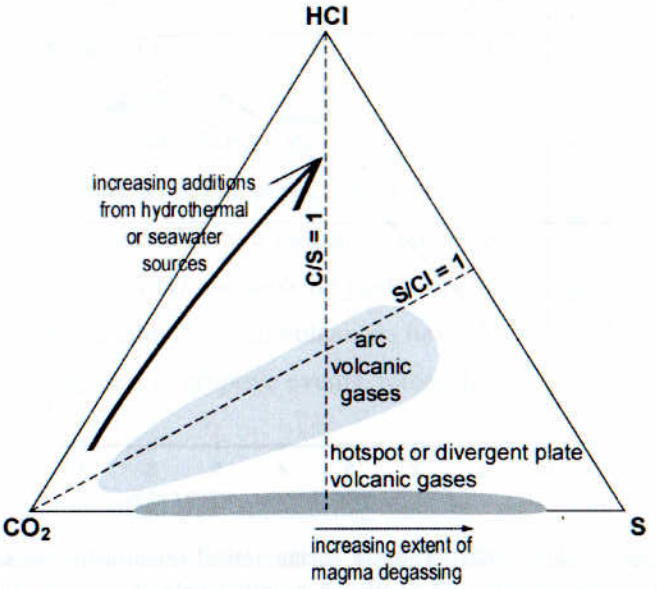

Figure 1-2: A schematic illustration of relative CO_2, S and Cl contents in gases emitted from different volcanoes (from data cited in Giggenbach 1996, Martini 1996, Symonds *et al.* 1994). Gases from hotspot or divergent plate volcanoes are noticeably different from arc volcanic gases in their negligible proportions of Cl, which is ultimately sourced from subduction processes. Increased amounts of Cl are present if gases are the product of strong hydrothermal interaction or a particularly Cl-rich source. The proportion of S to C in gases, especially from rift-related volcanoes, is related to the extent of degassing of a batch of magma.

1.1.2 Magma degassing processes

The compositions of volcanic gases should reflect the environment of the final vapour-melt equilibrium, prior to gas segregation, controlled fundamentally by the solubility laws affecting individual gas components, along with pressure, temperature and redox conditions. Measured compositions may also have been modified by secondary processes as gases percolated out through the volcanic pile. Detailed analysis of gas geochemical data can therefore provide an insight into shallow-level magmatic and degassing processes. At Mount Etna, time-series data on the S, Cl and F content of gases from the summit craters, coupled with their emission rates, enabled a model of magma storage and degassing regimes relating to eruptive and non-eruptive situations to be proposed (Pennisi & Le Cloarec 1998). Section 1.2 will cover gas solubilities in magmas and pressure-temperature constraints.

Eruptive style and strength are controlled, at least in part, by the dissolved volatile content in a magma, the ability of a magma to pond and degas passively, and the extent to which vapours have accumulated at depth. Figure 1-3 shows one suggestion of the link between eruptive velocity and initial dissolved gas content (Wilson 1980). A number of theoretical models have

been put forward to describe volcanic eruptions in terms of, among other parameters, dissolved and released gas amounts (e.g. Jaupart & Allegre 1991, Parfitt & Wilson 1995). Gas studies at active volcanoes are needed to test such models.

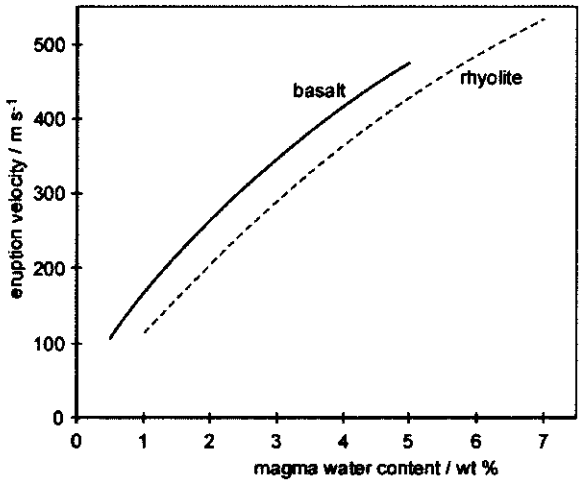

Figure 1-3: after Wilson (1980), Table 1. A theoretical relationship between dissolved water content of the magma and explosive eruption velocity, for basalt and rhyolite magma types.

Amounts and emission rates of gases exhaled from passive volcanoes provide mass constraints on the degassing magma bodies involved (Allard *et al.* 1994, Francis *et al.* 1993). The consistently high rates of degassing from Mount Etna between 1975 and 1995 with comparatively low rates of magma extrusion required significant volumes of magma stored and replenished within or beneath the edifice (Allard 1997).

Much current work concerning the volatile content of magmas and magma degassing comes from petrological studies, specifically the analysis of glass inclusions in phenocrysts (e.g. Barclay *et al.* 1996, Stix *et al.* 1993, Wallace & Gerlach 1994). Villemant and Boudon (1998, 1999) modelled the composition of fluids released during open- and closed-system degassing at Mt Pelée, based on measurements of the halogen and water contents of melt inclusions in phenocrysts from the 650 yr B.P. eruption. These authors found that samples following the closed-system path were linked to Plinian activity, whereas effusive activity was the response to open-system degassing. Degassing models, like this one, derived from petrology, would be greatly strengthened if allied to gas studies.

1.1.3 Volcano monitoring and risk mitigation

The utility of gas monitoring in terms of hazard prediction is founded upon an assumption that changes in gases (compositions and emission rates) will be precursors to eruptive changes: this assumption is reasonable, considering observed syn- and post-eruptive changes, linked with magma movements, and spatial differences, linked with degree of degassing of a magma body.

Secondary processes such as mixing of gases with meteoric/hydrothermal components, or thermal re-equilibration can be recognised in data to indicate volcanological changes such as cooling and system sealing. Compositional trends during the post-eruptive period of Showa-Shinzan (Japan) indicated prolonged magma degassing coupled with increasing meteoric contributions as the dome cooled (Symonds *et al.* 1996). At Galeras, short-term sharp variations in gas compositions and emission rates, related to sealing of the hydrothermal system, were identified prior to explosive events during the 1990s (Fischer *et al.* 1996, Stix *et al.* 1993). Unfortunately, while published work on post-eruptive gas changes is widely available, robust studies that follow changes in gases from a volcano's pre-eruptive state, through an eruption (or at least an increased state of activity) and into the post-eruptive phase, are scarce. The reason for this is obvious enough: gas measurements at volcanoes have usually been made in a sporadic and *ad hoc* manner, often in response to eruptive events, rather than as part of the routine monitoring effort.

Recent events have shown that gas monitoring can be extremely useful in confirming assessments of hazard potential as volcanic crises develop. Since 1972, the mainstay instrument for remote monitoring of gas emissions has been the Correlation Spectrometer (COSPEC), although this is limited to detection of SO_2 only. Changes in SO_2 emission rate prior to eruptive activity have been documented for several volcanoes (e.g. Malinconico 1987). Major decisions about alert level changes and evacuations prior to the climactic eruption of Mt Pinatubo in 1991 hinged, at least partly, on the measurement of a tenfold increase in sulfur dioxide emissions over two weeks (Daag *et al.* 1996, Punongbayan *et al.* 1996). At the time of writing, high levels of gas emission from the Soufrière Hills Volcano in Montserrat, continuing after 5 years, (MVO report by Norton & Young 2000) confirmed that the eruption was far from over. At Mt Etna, premonitory increases of SO_2 emission, significantly above background levels were detected days or even hours before eruptive events in 1977 (Malinconico 1979) and linked to magma rising in the conduit. In contrast, more recent routine monitoring of SO_2 at Etna (Bruno *et al.* 1999, Caltabiano *et al.* 1994) has shown that 4 to 6 weeks prior to the onset of eruptive crises, there have been drastic drops in flux, followed by progressive rises, culminating in paroxysmal emission rates at 2 to 5 times mean flux values. The development of new remote gas monitoring techniques, such as OP-FTIR, should allow more widespread use of a range of gas data, including gas concentration ratios, in volcanic risk mitigation. The techniques currently available for volcanic gas measurements are summarised in Section 1.3.

Motivations 2 and 3 are closely linked: progress towards the more pragmatic goal of risk mitigation also requires progress towards the more abstract goal of increased understanding of gases in volcanic systems. But *vice versa*, gas data collected through routine monitoring campaigns are essential to test models and refine understanding. Even at a single volcano, chemical signals vary as the system develops from open to closed with respect to surrounding

hydrothermal or meteoric input. It follows that there is no simple general model for volcano degassing: each volcano, and each eruption, presents separate problems. It can be difficult to apply the lessons learned at one volcano to an adjacent one. To understand the role of degassing at a given volcano, either for hazard mitigation or for purely scientific motives, consistent observations sustained over the duration of the activity are essential.

1.1.4 Environmental effects

The final motivation for studying volcanic gases is connected with their wider impact on the environment, both locally and globally. The major component of gas emissions from volcanoes is generally H_2O, followed by CO_2, but the next most abundant species are acid components like SO_2 and HCl. These gases are responsible for local damage as they are deposited from plumes, but if injected into the stratosphere, they can have global climatic effects due to the radiative properties of their aerosols.

Passively degassing volcanoes, such as Masaya, sustain gas plumes that remain in the troposphere. Sulfur dioxide and hydrogen chloride emitted from these volcanoes may be rapidly converted via heterogeneous processes to acidic aerosols, which then deposit from the plume. In terms of developing remote gas-monitoring methodologies, better understanding of the processes of aerosol formation and acid deposition occurring in tropospheric plumes is needed. Deposition of acids from plumes can have considerable impact on vegetation and human health (figure 1-4). Downwind from Masaya, a swath of land under the plume is devoid of any vegetation except resilient grasses, compared with lush coffee plantations in the same area but away from the plume. According to Johnson and Parnell (1986), the only plants surviving in the plume-affected region are shrubs capable of neutralising acid rain at their leaf surfaces. Baxter (1982) noted that populations living downwind were regularly exposed to levels of SO_2 and sulfate aerosol above W. H. O. recommended maxima, and that eye and skin irritation linked with the volcanic acid rain had been reported.

Figure 1-4: The detrimental effects of Masaya gases on vegetation downwind are clearly seen.

Large volcanic eruptions loft great quantities of volcanic gases into the stratosphere where their effects are more widespread. The atmospheric impact of the June 1991 eruption of Mt Pinatubo is reviewed by Self *et al.* (1996) and McCormick *et al.* (1995). Pinatubo released a total of 20×10^9 kg of SO_2 into the middle–lower stratosphere, which oxidised to 30×10^9 kg of sulfate aerosol, the largest perturbation to the stratospheric aerosol layer in the 20th Century. The aerosol cloud spread rapidly around the Earth over 3 weeks and attained global coverage a year after the eruption. The net climate effect of this eruption was an observed surface cooling in the Northern Hemisphere of about 0.5 °C in 1992–93 (see also Stenchikov *et al.* 1998). In addition, as a result of the increase in stratospheric aerosol particles, the Southern Hemisphere ozone hole increased to an unprecedented size in 1992. Although the atmospheric effects of Pinatubo were profound, large volcanic eruptions in the past are estimated to have produced aerosol loadings of 4 times (Tambora in 1815) or even 40 times (Toba, 74 ka BP) that of Pinatubo, with associated greater scales of impact (McCormick *et al.* 1995).

Several estimates of the global volcanic emission of CO_2, SO_2 and halogen gases have been made. While these budgets are currently fairly poorly constrained (owing to a paucity of gas data, an incomplete understanding of gas composition variability from volcano to volcano, and disagreement about the best method for scaling to the total number of volcanoes active at any one time across the world), they do allow for some comparison between natural and anthropogenic emissions of these components into the atmosphere. Gerlach (1991) considers that sub-aerial volcanoes release 7.9×10^{13} kg yr^{-1} of CO_2, only 0.4 % of anthropogenic CO_2 emissions. Bluth *et al.* (1993) estimate that the total volcanic emission of SO_2 to the Earth's atmosphere is of the order of 13×10^9 kg yr^{-1}, which is 5–10 % of the anthropogenic flux. For HCl, Symonds *et al.* (1988) calculated the annual volcanic emission of HCl to be $0.4–11 \times 10^9$ kg, values similar to their estimate for anthropogenically produced Cl. Well constrained estimates of volcanic gas release are important for considerations of past Earth-atmosphere evolution and the environmental effects of supervolcanoes or flood-basalt episodes, as well as in models for future climate change.

1.2 Volatiles in magmas and magma degassing

The sources and solubilities of volatile components in magmas are complex subjects requiring extensive ongoing geochemical research. However, a consideration of these topics is necessary in order to understand and interpret gas compositions measured at volcanoes. This section provides a brief introduction to the sources and solubilities of the major volatiles in magmas, and the physical processes by which degassing can occur. Throughout, the focus is on basaltic arc volcanoes, appropriate to studies at Masaya Volcano, the subject of this thesis.

1.2.1 Sources of volatiles and influence of tectonic setting on volcanic gas composition

The composition of gases released from volcanoes is fundamentally controlled by the volatiles available in magma source regions. Symonds *et al.* (1994) and Giggenbach (1996) presented gas data collected from a number of different volcanoes: gases from arc volcanoes have relatively more HCl and less CO_2 than gases from intraplate (or hotspot) volcanoes (see figure 1-2). These differences can be easily linked to differences in source: whereas intraplate volcanoes tap purely a mantle source region, the source for arc volcanoes includes both a mantle component and subducted slab components. Altered oceanic crust traps large amounts of water, CO_2, halogens and sulfur, which can be recycled through arc magmatism (Alt *et al.* 1993, Ito *et al.* 1983, Michael & Schilling 1989).

In addition to primary magmatic sources, the gases released from volcanoes may be influenced by secondary sources, such as a shallow level seawater component, meteoric fluids or a hydrothermal system input. Symonds *et al.* (1990) proposed that interactions between seawater and magma at shallow levels (<3 km) might account for some of the chlorine enrichment in gases released from Augustine. In a detailed long time-series study of fumarolic gases from Showa-Shinzan, Symonds *et al.* (1996) were able to show how changing gas compositions through the post-eruptive phase reflected increasing contributions from a secondary, meteoric, source. Significant long-term trends included gases becoming increasingly H_2O-rich, due to progressive influx of meteoric water, and both C/S and S/Cl ratios decreasing dramatically, as the more soluble components were progressively outgassed from the magma reservoir.

There is growing evidence that high pre-eruptive volatile contents are common in basaltic magmas from subduction zone settings (Alt *et al.* 1993, Metrich *et al.* 1999, Sisson & Layne 1993), connected with efficient cycling of subducted components (seawater or sediments). Central American volcanoes, in particular, have been noted for their especially water-rich products (Roggensack *et al.* 1997, Sisson & Layne 1993). Estimates of parent magma volatile contents at a basaltic arc volcano like Masaya are available from a survey of published data for other locations (e.g. Holloway & Blank 1994, Metrich *et al.* 1999, Papale & Polacci 1999,

Roggensack *et al.* 1997, Sisson & Layne 1993). Melt concentrations of 1200 ppm (mass) S, 0.4 wt % CO_2 and 4–5 wt % H_2O are typical, with Cl and F less well constrained.

1.2.2 Solubilities of major volatiles in basaltic magma

The second control on the composition of volcanic gases is the solubility behaviour of individual species in the magma. In addition to pressure and temperature, the composition of the melt affects the solubility of volatile components within it. This section reviews current understanding of the solubility of the major volatile species of interest (H_2O, CO_2, S, Cl and F) in basaltic magmas. A seminal paper was the work by Anderson (1975), who summarised progress in the area of gas solubilities and gas compositions to that date. Since then, improvements in measurement techniques have resulted in a wealth of experimental studies on matrix glasses and glass inclusions in phenocrysts, enhancing available data and models.

1.2.2.1 H_2O

Holloway and Blank (1994) review two models for water solubility in magma, the Burnham model (Burnham & Jahns 1962) and the Stolper model (Stolper 1982). These models allow theoretical solubilities to be calculated, for specified pressure, temperature, and magma composition, and model predictions have been shown to compare well with measurements on natural samples (e.g. figure 5 in Holloway & Blank 1994). Figure 1-5 shows the regular solution curve for H_2O in tholeiitic basaltic magma determined by the Stolper model.

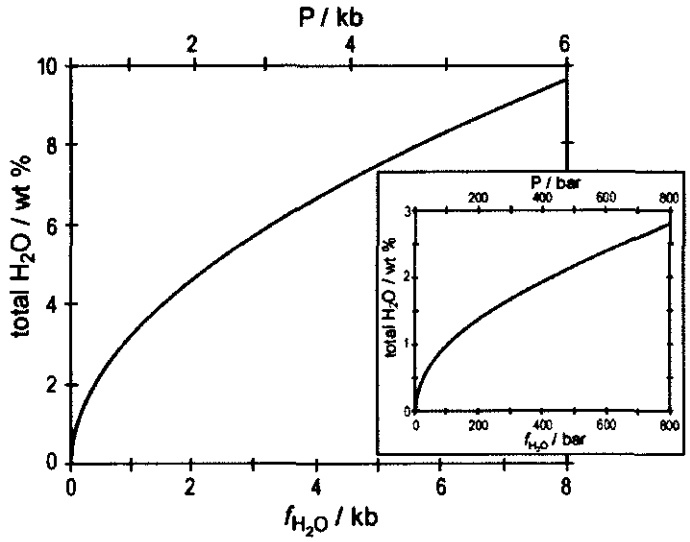

Figure 1-5: redrawn from Dixon *et al.* (1995). Variation of dissolved water content with pressure for tholeiitic basalt, according to the Stolper model. The inset is an enlargement of the shaded area (H_2O < 3 wt %).

The effect of temperature on water solubility at low pressures is poorly known. The Burnham model predicts a moderate decrease in solubility with increasing temperature, broadly in agreement with measurements on albitic and haplogranitic melts (Holloway & Blank 1994). For

basaltic melts at pressures below 200 MPa, H_2O solubility as a function of temperature has been little studied, despite the fact that this is the important range for processes of volcanic degassing.

An alternative approach is a purely empirical one, where water concentrations in basaltic glasses quenched at different pressures and temperatures are measured, and a fit to the data is determined. A commonly cited empirical expression (e.g. in Jaupart & Tait 1990) for the solubility of water in basaltic magma as a function of pressure is:

$$x(P) = 6.8 \times 10^{-8} P^{0.7} \qquad (1\text{-}1)$$

with $x(P)$ denoting solubility in mass fraction, and P pressure in Pa.

Pursuing the empirical approach, Dixon *et al.* (1995) conducted experiments to determine H_2O and CO_2 solubilities in tholeiitic basaltic (MORB) glasses and found their results to be in good agreement with the Stolper model (figure 1-5). Extrapolation of their model results to a pressure of 1 atm yielded a H_2O solubility of 0.11 wt%, comparable to an experimentally determined value of 0.10–0.11 wt % for a tholeiitic melt.

1.2.2.2 CO_2

Although carbon dioxide is the second-most abundant gas emitted from volcanoes, its relatively low concentrations in erupted lavas points to its relatively low solubility in melts, compared with the other major volatile species. Experimental results show increasing amounts of dissolved CO_2 with increasing pressure, and a negative temperature dependence (Blank & Brooker 1994). The relationship between CO_2 solubility and melt composition is poorly constrained.

A theoretical (thermodynamic) approach to calculating CO_2 solubility in basaltic melt, using a modified Redlich-Kwong equation of state, is outlined by Holloway and Blank (1994). In their experiments on MORB glasses, Dixon *et al.* (1995) determined CO_2 solubilities at relatively low pressures that were in agreement with this theoretical approach, and their model is shown in figure 1-6. The 1 atm solubility of carbon dioxide in basalt at 1200 °C, extrapolated from their results, is 0.5 ppm.

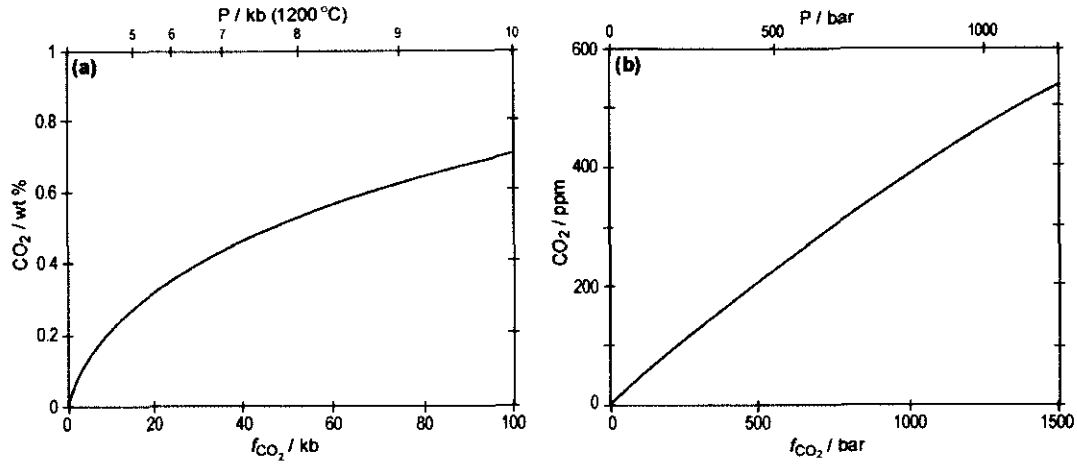

Figure 1-6: redrawn from Dixon *et al.* (1995). Solubility of CO_2 in tholeiitic basalt, as a function of pressure. (a) Over high pressures. (b) At low pressures relevant to degassing.

A simplified, yet commonly used, expression (and e.g. cited in Jaupart & Tait 1990, from Stolper & Holloway 1988) for the pressure dependence of CO_2 solubility in basalt is:

$$x(P) = 4.4\times10^{-12} P \qquad (1\text{-}2)$$

with $x(P)$ denoting solubility in mass fraction, and P pressure in Pa.

1.2.2.3 H_2O-CO_2 mixtures

The relative proportions of H_2O and CO_2 dissolved in a magma influence their solubilities. The experiments conducted on MORB glasses by Dixon *et al.* (1995) confirmed that both H_2O and CO_2 solution in basaltic melts follow Henry's law behaviour, for pressures lower than about 200 MPa. Figure 1-7 (modified from Dixon & Stolper 1995) shows the variation in total solubility for a CO_2-H_2O mixture in basaltic melt based on a Henrian model for these two components.

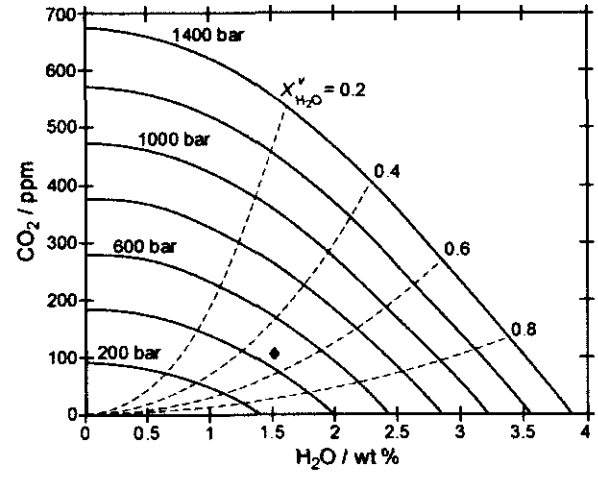

Figure 1-7: Redrawn from Dixon *et al.* (1995). Solubility for a CO_2–H_2O mixture in basaltic melt over pressures relevant to degassing. Continuous curves are isobars; dashed curves are for constant vapour composition. For example, melts containing 1.5 wt% H_2O and 110 ppm CO_2 (at ♦) are saturated at 480 bar with a vapour of $X^v_{H_2O} = 0.5$.

This simple behaviour of H_2O-CO_2 solubilities allows for straightforward calculation of the degassing of basaltic melts (w.r.t. these species) as they ascend and erupt. A path for closed-system degassing from different initial volatile contents can easily be defined, but the exact path that a degassing magma will follow will depend on the extent to which fluid is lost from the system (i.e. how open the system is w.r.t. gases). This relationship was cited as a potential gas geobarometer by Sabroux (1983): measurement of the proportions of CO_2:H_2O in the gas phase should provide information on the depth of melt-vapour equilibrium.

1.2.2.4 Sulfur

Experimental investigations have demonstrated that sulfur solubility in silicate liquids is dependent on temperature, pressure, melt composition and redox state: much of this work is reviewed by Carroll and Webster (1994). In contrast to the simple behaviour of volatiles such as H_2O and CO_2, which partition between a silicate melt and a vapour phase (or fluid), sulfur behaviour is complicated because basaltic liquids frequently coexist with immiscible sulfur-rich phases. The sulfur rich phase can be either a sulfide liquid (under reduced conditions) or anhydrite (under oxidised conditions), both of which have been identified in erupted products (e.g. Fournelle *et al.* 1996, Metrich *et al.* 1999). S partitions between the silicate melt and the secondary sulfur-rich phase, rather than behaving as a true incompatible element.

Because S has several different oxidation states, its solubility is strongly affected by the oxidation state of the magma itself, a property inherited from a magma's source region (Carmichael 1991). So processes controlling S concentration in basalts are different in ridge and subduction settings because of differences in redox conditions (i.e. oxygen fugacity). Figure 1-8 shows that under relatively reduced conditions, such as for MORB (ΔNNO of approximately -1), sulfur dissolves into the melt as S^{2-} (equation 1-3), whereas under relatively oxidizing conditions, such as at arcs (ΔNNO between 0 and +1), sulfur dissolves as S^{6+} (equation 1-4) (Metrich & Clocchiatti 1996).

$$FeO_{melt} + \tfrac{1}{2}S_2 = FeS_{melt} + \tfrac{1}{2}O_2 \qquad (1\text{-}3)$$

$$S^{2-}_{melt} + 2O_{2\,melt} = SO^{2-}_{4\,melt} \qquad (1\text{-}4)$$

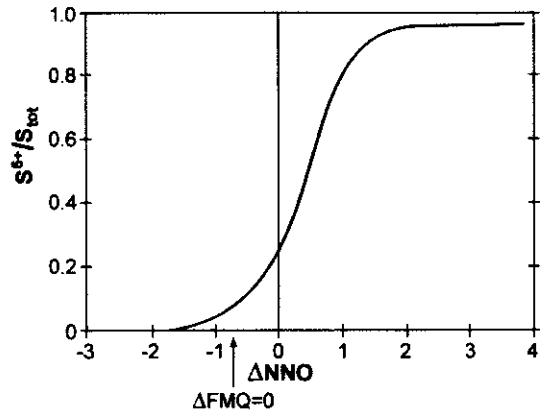

Figure 1-8: Redrawn from Metrich and Clocchiatti (1996). The diagram illustrates the dependence of sulfur speciation dissolved in silicate melts upon oxygen fugacity. ΔNNO is equal to log f_{O2} (sample) – log f_{O2} (Ni-NiO buffer) at same pressure and temperature. ΔFMQ is equal to log f_{O2} (sample) – log f_{O2} (quartz-fayalite-magnetite buffer) at same pressure and temperature.

Melt composition is an extremely important factor in this behaviour, with Fe content (and other trace metals) controlling partitioning between silicate melt and sulfide, and Ca content controlling partitioning between silicate and anhydrite through equations 1-5 and 1-6. Figure 1-9 illustrates this control.

$$FeO_{silicate} + \tfrac{1}{2}S_2 = FeS_{sulfide} + \tfrac{1}{2}O_2 \qquad (1\text{-}5)$$

$$CaO_{silicate} + \tfrac{1}{2}S_2 + \tfrac{3}{2}O_2 = CaSO_{4\,anhydrite} \qquad (1\text{-}6)$$

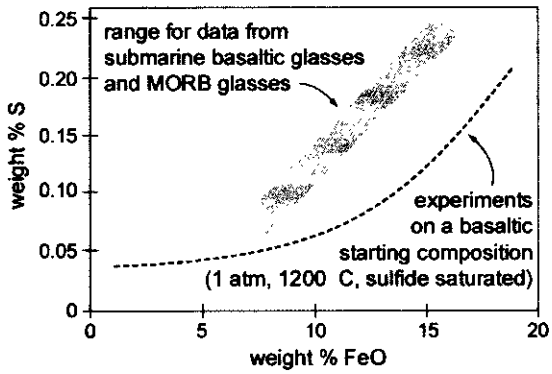

Figure 1-9: Redrawn from Carroll and Webster (1994). Dissolved S in basalts is a strong function of melt composition, and especially Fe content, for both natural (shaded region) and experimental (dashed curve) melts.

Experiments in silicate liquids with no secondary S phase present ("sulfur undersaturated") indicate that S solubility passes through a well-defined minimum at ΔNNO~0 (e.g. Carroll & Webster 1994, Kress 1997), but the results of Scaillet *et al.* (1998) on anhydrite or sulfide saturated systems (which appear to be the norm in nature) are slightly different (figure 1-10). Distribution of S between melt and fluid is still highly dependent on redox state: if anhydrite is the second phase, S is more readily partitioned into the fluid and an increase in pressure of nearly 200 MPa made no detectable difference on this behaviour. For situations in which an immiscible

sulfide phase is present, S partitions from the melt into this secondary phase rather than any coexisting vapour.

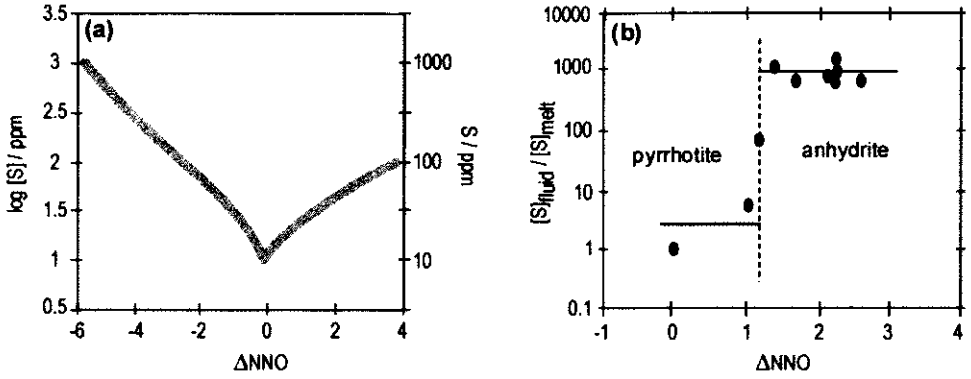

Figure 1-10: S solubility as a function of oxygen fugacity. (a) Redrawn from Carroll and Webster (1994, figure 5). Sulfur solubility from experiments on S-undersaturated tholeiitic melt at 1200–1300°C. (b) Redrawn from Scaillet *et al.* (1998, figure 1). The effect of oxygen fugacity on the fluid/melt partition coefficient of sulfur calculated from experiments on a dacitic sample equilibrated at varying oxygen fugacities with an H-S-O fluid phase. Oxygen fugacity controlled the nature of the excess S phase (pyrrhotite or anhydrite).

Work investigating the dependence of S solubility on pressure is equivocal: Carroll and Webster (1994) review two sets of high-pressure experiments on sulfide-saturated materials which gave opposing results. For anhydrite-saturated experiments, S solubility increased with increasing pressure. Wallace and Carmichael (1992) used a theoretical thermodynamic approach to estimate the effect of pressure on sulfur solubility in a basic magma saturated with sulfide. They conclude that as pressure is increased a higher S fugacity is required to maintain saturation with an immiscible Fe-S-O liquid phase. However, because the relationship between sulfur fugacity and dissolved sulfur content has the same pressure dependence as the sulfide liquid immiscibility, the dissolved S content in a basic magma is not expected to change as a function of pressure.

At shallower levels, it has often been generally accepted that S does not partition from basaltic magmas into a vapour phase except at pressures lower than about 100 bars (e.g. Dixon *et al.* 1991, Gerlach 1986). This idea comes from observations that S does not appear to be lost to a vapour phase during submarine eruptions of basalt, although extensive loss of S by degassing does occur in subaerial or shallow submarine eruptions. This has yet to be substantiated by experiment, but it certainly reflects the higher solubility of S in basalts as compared to more silicic magmas. Evidence from several more evolved arc volcanoes points to the probability of accumulations of S-rich vapour phases at some depth, prior to eruptions such as Pinatubo, Redoubt and Mt St Helens (Gerlach & McGee 1994, Gerlach *et al.* 1994, Wallace & Gerlach 1994). Giggenbach (1996) suggests an empirical Henry's Law constant for S solubility in White Island andesite of 480 mg/kg bar: this can hardly be taken as a figure appropriate in all situations.

S solubility in melts is strongly temperature dependent in so far as temperature changes affect f_{O2}: however for a given ΔNNO or ΔFMQ, and no secondary S phases present, S solubility is approximately independent of temperature. For sulfide or anhydrite saturated conditions, S solubility increases with increasing temperature, for given pressure and ΔFMQ (Carroll & Webster 1994).

The bulk volatile content of a magma is likely to affect solubility relations for any individual species, as was seen for H_2O-CO_2 mixtures. As noted by Dixon and Stolper (1995), the solubility of one component in a magma is expected to reduce as the proportions of other volatiles in the mixture increase, and so, regardless of their oxidation state, water-rich magmas will degas more sulfur at a given pressure than water-poor magmas.

1.2.2.5 Chlorine

Chlorine solubilities can be determined experimentally as the concentration of Cl in a silicate glass that was equilibrated with a Cl-bearing aqueous fluid or an immiscible chloride melt. At high pressures, Cl partitions into an alkali chloride phase, while at lower pressures relevant to volcanic degassing it partitions into an aqueous fluid or vapour (HCl): the solubility behaviour of Cl in melts is expected to vary considerably depending on which partitioning phase is stable, and hence with pressure. In a study of Cl behaviour associated with the 79 A.D. Vesuvius eruption, Signorelli and Capaccioni (1999) find different solubilities at different stages in the magma evolution associated with pressure changes leading up to, and during, the eruption.

There is a strong influence of composition on Cl solubility in silicate melts (Iwasaki & Katsura 1967). Carroll and Webster (1994) noted that Cl solubilities in mafic melts are not well known, and suggested that the solubility of HCl is generally similar to that of CO_2, significantly less than that of H_2O for equivalent pressure, temperature and melt composition. However, unlike for CO_2, erupted products from volcanoes are rarely fully degassed of chlorine, attesting to a relatively high solubility for HCl, even at low pressures.

More recently, Webster *et al.* (1999) determined chloride solubilities in basalt and andesite melts and found that they vary directly with pressure and melt composition: solubility in basalt melt is an order of magnitude greater than that in silicic melts. At 2 kb, the average Cl content of an anhydrous basalt was ~2.6 wt%, substantially greater than the solubility of CO_2 (e.g. <0.1 wt%) but less than that of H_2O (e.g. 5–6 wt%). At 1 bar, Cl content was only slightly less (~2 wt%). These authors find that their data indicate a relationship between Cl solubility and pressure of the form:

$$x(P) = 0.303P + 2 \qquad (1\text{-}7)$$

where x(P) is wt% Cl and P is in kbar. Conversely, in experiments on much more silicic melts, Metrich and Rutherford (1992) found that Cl contents decreased with increasing pressure, reflecting the importance of magma composition as a control on chlorine behaviour.

There is a complex relationship between Cl and H_2O solubilities in melts, with Cl solubility sensitive to H_2O content at low H_2O abundances, but insensitive at high H_2O contents (Webster *et al.* 1999). Chloride and water concentrations in basaltic glasses from Fuego, Guatemala, showed a negative correlation (Sisson & Layne 1993). This relationship was confirmed by Webster *et al.* (1999), who found that chloride is highly soluble in water-poor melts.

1.2.2.6 Fluorine

Compared to other volatiles, fluorine is highly soluble in silicate melts, with many melts able to dissolve up to 10 wt% (Webster 1990). In their review, Carroll and Webster (1994) noted (citing Holloway 1981) that HF solubilities in silicate melts should be similar to those of H_2O, because of molecular similarities, and that, in natural silicate melts at pressures of 1–4 kbar, the solubility of F is greater than that of H_2O and significantly greater than those of Cl, S or CO_2 for similar conditions. Few published studies have investigated F solubilities, and even fewer address, specifically, the degassing of F from magmas during ascent and decompression towards the surface. Anhydrous melts at 1 bar may retain significant quantities of F during and after eruption (Carroll & Webster 1994), and, compared with the other volatile species considered, F can be most easily retained in crystallising magmas, by incorporation into apatite.

Pennisi and Le Cloarec (1998) estimate that, at Etna, between 10 and 30 % of the initial magmatic F is degassed from present day hawaiitic melts: this supports the general idea of poor (although not negligible) degassing of F from magmas. The fact that relatively large quantities of HF are measured in plumes from actively degassing volcanoes (e.g. Francis *et al.* 1998, Symonds *et al.* 1994, Symonds *et al.* 1988, Thordarson *et al.* 1996) indicates that the solubility behaviour of F is complex at low pressures, with F able to partition strongly from melt in the presence of mixed volatile fluids. In general, significant volcanic HF emission seems to involve very shallow magma degassing. Future work investigating F solubility in magmas will be greatly enhanced by new measurement techniques, such as nuclear microprobe (Mosbah *et al.* 1995).

1.2.3 Physical mechanisms of gas release

While the composition of gases from volcanoes is largely controlled by volatile source compositions and volatile solubilities, the rates of gas emission are also influenced by physical mechanisms of degassing. Physical processes are important on two scales: firstly, at the macroscale, in transport of sufficient quantities of gas or gas-rich magma to the surface to account for observed rates of degassing. Secondly, at the microscale, some physical mechanism is needed to separate gas from a bubbly magma layer into the free atmosphere.

While there are numerous published models dealing with macroscale issues for volcanic degassing (e.g. Cardoso & Woods 1999, Cashman & Blundy 2000, Jaupart & Vergniolle 1989, Kazahaya *et al.* 1994, Phillips & Woods 2000, Proussevitch & Sahagian 1998, Proussevitch *et al.* 1993, Stevenson & Blake 1998, Voight *et al.* 1999, Woods & Cardoso 1997), the issue of gas transfer across a magma-air interface to the atmosphere has been less widely addressed. Although the phenomenon of bubble bursting is poorly understood, gas escape as bubbles reach the surface of low viscosity basaltic melts is generally considered a rapid process, since overpressure is likely to be sufficient to cause bubbles to burst on reaching the surface (J. Phillips, pers. com.).

Many studies of explosive volcanic degassing exist in the literature, especially given recent large-scale explosive eruptions such as at Pinatubo, Philippines, and Soufriere Hills Volcano, Montserrat. However, published research relevant to the case of non-explosive, or passive, volcanic degassing is much more limited. One important characteristic of Masaya volcano is its sustained excessive passive degassing, with almost negligible eruption of lava. Laboratory experiments have frequently been used to develop physical models for degassing at basaltic volcanoes (e.g. Jaupart & Vergniolle 1989, Stevenson & Blake 1998), and in Chapter 6 I discuss the application of two published models to Masaya's behaviour.

1.3 Techniques for measuring volcanic gases

There are two related approaches to studying volcanic gases: quantification of the rates and amounts of gases emitted, and characterisation of their composition. The former is generally a more difficult practical challenge than the latter. There are currently no available techniques that allow for complete one-stage measurement of total gas composition *and* emission rate. The techniques that do exist are generally able either to characterise the composition of a sample of gas, or to quantify the emission rate of one component. While direct sampling techniques provide the most detailed compositional information, they are restricted to accessible vents, and are unsuitable for syn-eruption monitoring. Correlation spectroscopy (COSPEC) is a simple and robust method for measuring emission rates of sulfur dioxide, but is subject to large errors. OP-FTIR spectroscopy provides a remote method for determining plume gas compositions, but requires careful atmospheric radiative transfer modelling. Satellite-based sensors deliver emission rate information safely and rapidly, but currently only for larger plumes extending well into the atmosphere: monitoring of a tropospheric plume like that at Masaya volcano is impossible by today's satellite technologies. Great advances in technology for tropospheric monitoring are occurring (a summary and prognosis is presented by Roscoe and Clemitshaw (1997)), and some new techniques will be transferable to a volcanic application, as OP-FTIR has been.

1.3.1 Direct sampling

Direct sampling refers to any technique involving the collection of a portion of gas from a volcanic plume or fumarole. Ground-based methods include the use of filter packs, Giggenbach bottles and condensing systems. Samples are subsequently analysed in a laboratory using a wide range of standard gravimetric, chromatographic, spectroscopic and isotopic techniques. These approaches have been usefully reviewed by Le Guern (1983) and Symonds *et al.* (1994). A seminal example of the use of direct sampling to monitor a post-eruptive phase is the work by Symonds *et al.* (1996) over 31 years following the extrusion of the Showa-Shinzan dome. While direct techniques are capable of delivering precise data and provide the foundation for all volcanic gas studies, they are subject to a number of limitations:

(a) Only vents that can be safely approached can be sampled, usually restricting gas sources to subordinate relatively low temperature vents.

(b) On sampling, the identity of original gas species and their oxidation states may be obscured due to reactions with solvents or containers. For example, H_2S, SO_2 and sulfur may be reported altogether as SO_2 or sulfate. Complex thermochemical restorations can be performed to infer the original gas compositions, redox conditions and temperatures (e.g. Gerlach 1993).

(c) Practical considerations dictate that routine monitoring of volcanic gases by these methods throughout eruptions is impossible. Most published data are based on either a single sampling campaign, or on samples widely spaced in time.

Airborne sampling methods provide a useful extension and somewhat greater flexibility in approach than those which are ground-based. Aircraft have been used to carry on-board filter packs, spectroscopic techniques such as the MIRAN and LI-COR analysers for CO_2 (e.g. Casadevall *et al.* 1983, Gerlach *et al.* 1997), and closed-path FTIR spectrometers for SO_2 and other gases (e.g. Gerlach *et al.* 1998, McGee & Gerlach 1998). Aircraft are notoriously expensive to operate, however, limiting the frequency of operations. They are also impractical for sampling major, ash-laden eruption plumes.

An alternative to conventional direct sampling is the use of automated continuous recording electrochemical sensors. McGee and Sutton (1994) reported use of this technique at Mt St Helens, where they used a sensor that detected undifferentiated reducing gases. Similar sensors have also been used successfully at Vulcano, Italy, for continuous ground level monitoring of CO_2, SO_2 and H_2S in the atmosphere (Valenza 1998). Although susceptible to destruction during the course of a major eruption, such sensors are currently the only means of collecting continuous gas data.

1.3.2 Ground-based remote sensing techniques

Methods that do not require the collection and analysis of a gas sample are termed "remote". Their major advantage over direct sampling techniques is the fundamental issue of safety, since measurements can be made at distances away from the volcanic vent. They have many other benefits, however: first, they are non-intrusive, eliminating the possibility of secondary reactions, contamination or condensation of gases during sampling. Second, since data are transferred directly from sensor to a computer, plume gas concentrations may be available in near-real time. This is an important issue for monitoring, given that conventional sampling techniques involving 'wet chemistry' may take days or weeks to complete. Finally, remote sensing permits observations of even the most intense phases of activity, not accessible to other means.

All remote-sensing techniques, whether ground-based or on satellite platforms, rely on principles of optical spectroscopy: molecules or particles in the atmosphere transmit energy at characteristic frequencies in the electromagnetic spectrum. By detecting characteristic absorptions or emissions, these techniques can retrieve amounts of the species of interest within the optical path. Some instruments (e.g. COSPEC) measure energy in a single spectral band, whereas others (e.g. OP-FTIR) can detect across broad regions.

1.3.2.1 COSPEC (Correlation Spectroscopy)

The COSPEC, initially designed for monitoring environmental SO_2, has been a standard tool for volcano monitoring since it was first used in 1971 at Mt. Mihara, Japan (Stoiber *et al.* 1983). It contributed significantly, for example, to the successful forecasting of the massive June 1991 eruption of Mt. Pinatubo. With the onset of seismic unrest, SO_2 emissions, which increased by tenfold over two weeks, identified that magma was involved, and rising, and that eruption could be imminent (Daag *et al.* 1996, Punongbayan *et al.* 1996). Additionally, COSPEC-derived SO_2 emission rates have provided the reference against which global volcanic contributions of CO_2, and other gases, to the atmosphere have been estimated (e.g. Williams *et al.* 1992).

Under its usual operation, the COSPEC is mounted in a car (or plane or boat) and driven under the plume (figure 1-11). Essentially, the instrument measures the absorption of scattered solar UV radiation, in a wavelength band of 300-316 nm, by SO_2 molecules in the optical path. The result is a transect of signal against distance, which is calibrated against internal standard SO_2 reference cells. Volcanic SO_2 flux estimates are made by multiplying this plume SO_2 cross-section with appropriate wind speed measurements. The COSPEC can also be operated from a static position mounted onto a tripod.

Figure 1-11: The COSPEC mounted in a truck for SO_2 emission measurements at Masaya. The telescope points vertically to collect sky UV passing through the plume. Inside, it is connected to a chart recorder and/or a laptop compute for digital datalogging.

COSPEC has several advantages for routine volcano monitoring: it delivers gas emission rates; it is portable; utilises a natural source of UV radiation; does not require precise pointing; can operate even through overcast skies; has modest power requirements and does not require specialist technicians for operation. As a robust method to make quantitative estimates of the SO_2 emissions, it can provide a useful measure of the overall level of activity of a volcano.

The main disadvantage of the COSPEC is that it is a rather blunt tool: cumulative errors range between 15 and 40% (Stoiber *et al.* 1983). COSPEC data sets are thus typically noisy, and large quantities of data are required to identify significant trends. The largest source of error lies in obtaining good plume-speed data. Aircraft traverses provide the best results, since the aircraft navigational equipment can be used to derive wind speeds directly, but their expense is higher than ground-based surveys. Additionally, dust or aerosol in the plume attenuates UV radiation

and results in a reduction of the measured SO_2 flux from the actual value. COSPEC faces a more fundamental limitation, however, which is that new instruments are no longer manufactured, and spare parts are rarely available.

1.3.2.2 OP-FTIR (Open-path Fourier Transform Infrared Spectroscopy)

Since this thesis is devoted to volcanic gas measurements by OP-FTIR, the technique is introduced only briefly here. Chapter 2 develops the technical basis and specifics of its application at volcanoes in much greater detail. Initially developed for laboratory and industrial applications, OP-FTIR spectrometers are now commercially available as small, field portable instruments (figure 1-12), suitable for a wide range of applications. Unlike the COSPEC, it is a broad band instrument (spectral range of 4200 to 400 cm^{-1}, i.e. 2.4–25 μm, depending on the IR detector in use); so a number of gas species can be analysed simultaneously. Unlike laboratory instruments, which place a sample in a closed cell in the path of the infrared beam, in field application the infrared radiation passes through an open atmospheric (plus volcanic) path before reaching the detector. Closed-path FTIRs have been used at volcanoes, but these are direct sampling instruments and their capability is limited by the need to fly them directly through gas plumes.

Figure 1-12: (a) The Midac OP-FTIR spectrometer. (b) Spectrometer in use for sun-source gas plume measurements on Mt Etna.

Naughton *et al.* (1969) were the first to use an infrared spectral technique to investigate volcanic gases, when they measured the composition of the main gaseous components in a fountain at Kilauea. Gases injected into the stratosphere from the large eruptions of El Chichon (Mankin & Coffey 1984) and Pinatubo (Mankin *et al.* 1992) were detected by open-path infrared spectroscopy using fixed and airborne spectrometers. Keys *et al.* (1998) were able to detect tropospheric volcanic HCl from Mount Erebus due to a favourable set of circumstances, with a static high resolution solar-tracking FTIR spectrometer.

A field portable open-path infrared spectrometer was first used by Notsu *et al.* (1993) at Asama Volcano to detect absorptions due to SO_2, and Mori *et al.* (1993) detected both HCl and SO_2 from

Unzen with the same instrument. Francis *et al.* (1998, 1995) measured SO_2 and HCl using a field portable spectrometer at Mt Etna and Vulcano, and were also able to detect SiF_4 (Francis *et al.* 1996a). Oppenheimer *et al.* (1998b) used the same spectrometer but from a helicopter to constrain HCl:SO_2 ratios in the volcanic plume from Montserrat. Love *et al.* (1998) applied open path FTIR to the plume from Popocatepetl and measured SO_2, HCl and HF in absorption and SO_2 and SiF_4 in emission. The first OP-FTIR measurements of carbon species in volcanic gases were reported by Mori and Notsu (1997) in data from Aso Volcano; both CO_2 and volcanic H_2O have been constrained in spectra from Masaya Volcano by Burton *et al.* (2000), and in this thesis.

Perhaps the chief merit of OP-FTIR spectroscopy is its flexibility. Because several sources of infrared radiation can be employed, such as artificial lamps, hot rocks on the volcano itself, the sun, and exceptionally the moon, it is almost always possible to find a field configuration from which to make measurements. Near-real time analyses with high temporal resolution are possible. Most of the volcanically important gases have been detected: H_2O, SO_2, CO_2, CO, COS, HCl, HF (Burton *et al.* 2000, Mori & Notsu 1997). H_2S has not been detected to date because detection limits are rather high for this gas. Francis *et al.* (1996a) detected the trace gas SiF_4 in measurements at Mt Etna and Vulcano: this gas had not previously been reported in volcanic gases because it cannot be distinguished from HF in conventional analyses. While most OP-FTIR studies have measured absorption by gases of infrared radiation from warm sources, Love *et al.* (1998) showed that it is also possible to measure gases in emission, against a cold sky background.

Although OP-FTIR spectroscopy is clearly a powerful and appropriate new tool for volcanology, there remain several challenges:

(a) At its current stage in development, field equipment is still quite cumbersome and less easily portable than the COSPEC. This is mainly because the spectrometer is optically joined to a bulky telescope which collects and focuses the incoming radiation. Trials are underway to investigate the feasibility of making high quality measurements with the spectrometer unit alone: this would significantly improve the instrument's portability.

(b) Measurements with the sun as the IR source hold the greatest potential for gas plume observations at safe distances from the active vent. However, it can be difficult to contrive a suitable geometry such that one views the sun through the plume.

(c) Data retrieval can be complex (Chapters 2 and 3). Working over short path lengths (100-200 m) using artificial lamp sources provides the simplest data to analyse, but is often not practical. Since solar measurements involve an optical path through the whole atmosphere, careful radiative transfer modelling is needed.

(d) Data are retrieved as column amounts of individual gas species in the path (i.e. a concentration-pathlength product), and these can be combined to give concentration ratios: absolute gas concentrations in the plume depend on the path length, which is not always accurately known. Comparisons with data from conventional analytical techniques are not straightforward. For example, column amounts of SO_2 but not sulfur are retrieved by FTIR, whereas conventional analyses variously report some or all of SO_2, H_2S, sulfate, and sulfur.

(e) Given their high ambient concentrations, CO_2 and H_2O present particularly difficult measurement challenges. Absorption by atmospheric CO_2 and H_2O across a number of spectral regions may also prevent analysis of other gas species within these regions.

(f) Measurements by OP-FTIR spectroscopy are subject to the same challenges of interpretation as other remote-sensing techniques, which sample volcanic gases after they have entered and interacted with the surrounding atmosphere. These techniques provide access to major eruption plumes inaccessible to conventional sampling, but measurement variability arising from atmospheric mixing processes may disguise true at-vent "volcanic" variations. For example, soluble gases such as HCl and SO_2 may be scavenged from the plume into condensing water vapour at widely different rates: measured changes in plume SO_2/HCl ratios might not directly reflect volcanic causes. This is a newly opening area of research. OP-FTIR studies promise to contribute not only to understanding of volcanic systems, but also to broader questions of tropospheric chemistry.

1.3.2.3 Other ground-based techniques

There are many more techniques which have been used at volcanoes, either on an experimental basis, or as an overflow from fence-line atmospheric monitoring applications. I mention just three of them here.

GASPEC: CO_2 is potentially the most useful gas for volcano monitoring, due to its low solubility in magmas and unreactive nature, but its measurement presents enormous challenges because of the high ambient concentration (~ 365 ppm) of CO_2. Within a few hundred metres of the source vent, CO_2 concentrations have typically declined to only a few ppm above background, a particularly difficult problem for instruments using solar radiation subject to absorptions across the whole thickness of the atmosphere. The CO_2 GASPEC is a thermal radiometer which measures incident IR radiation in the narrow band at 10.2-11.2 μm (~ 940 cm^{-1}). It has been developed specifically for the purpose of measuring CO_2 emissions in a very similar way to that in which the COSPEC monitors SO_2 (Williams & Dick 1995). It is mounted in a car and driven under the plume: variations in the detected radiance correspond to variations in the total vertical

burden of CO_2 plus other radiating species. Plume CO_2 amounts are isolated by comparisons of the in-plume radiance with the radiance observed in ambient air away from the plume, and with that of light filtered through an internal CO_2 calibration cell. A transect of signal against distance is obtained and combined with wind-speed measurements to provide a CO_2 emission rate.

Tests at power plants and Central American volcanoes (Dowrick 1999) indicate that the GASPEC can successfully detect a plume signal, but the calculated CO_2 emission rates are frequently 3 orders of magnitude too high. It seems that the instrument is unable to distinguish the pure CO_2 signal from that of other ambient components such as water vapour and possibly aerosols in the plume. It may be that the use of this single spectral window is inherently flawed, as energy transmitted from species other than CO_2 is not only significant, but also variable over the course of a single plume traverse in an unquantifiable manner.

Differential absorption LIDAR (DIAL): Widely used in atmospheric pollution monitoring, DIAL has only rarely been applied to volcanic plumes (Edner *et al.* 1994, Weibring *et al.* 1998). Rather than utilising a natural source of radiation, the system fires a laser source tuned to a specific narrow frequency band of interest, into the plume. The radiation is back-scattered by aerosols and particles and collected by the instrument. IR absorptions at the chosen frequency are measured by comparison with the back-scattered energy received from a second laser tuned to a similar, but different, frequency to the side of the peak. The lasers must be re-tuned to different frequencies in order to detect absorptions of other molecules of interest. DIAL can be used to construct complex two- or three-dimensional plume concentration profiles. However, as figure 1-13 shows, the equipment is almost prohibitively bulky for useful measurements in most volcanic situations.

Figure 1-13: The mobile DIAL unit used by the National Physical Laboratory for atmospheric pollution monitoring.

Smaller lasers than those used in conventional DIAL have been incorporated into a more portable system known as TDLS (tunable diode laser spectrometry) (e.g. Tittel *et al.* 2000). Although these lasers have much reduced ranges (up to 5 km compared with 10-15 km of DIAL), their small size makes them much more suitable for volcanic field applications. Theoretically, TDLS

has the advantage over FTIR of increased sensitivity, but its major disadvantage is that scanning the entire IR spectrum quickly is not possible (Finlayson-Pitts & Pitts 1986).

DOAS: Differential optical absorption spectrometry is a technique operating in the UV/visible region of the spectrum. The broad-band radiation source is generally a UV lamp with collimating mirror, although it can be the sun. The principle on which the measurement is based is very similar to that in the DIAL system: a narrow spectral band is examined, and the difference between the absorbance at some wavelength of interest and another wavelength on either side of the absorption peak is measured (Finlayson-Pitts & Pitts 1986). Rapid scanning of a monochromator across the spectral range allows near simultaneous detection of multiple species. DOAS is another technique common in pollution monitoring, and has been used to detect SO_2 at Mt Etna (Edner *et al.* 1994, Weibring *et al.* 1998). UV/visible absorption spectrometry is not as applicable to volcanoes as FTIR because many of the molecules of interest to volcanologists do not have specific absorptions in this part of the spectrum.

1.3.3 Satellite-based remote sensing techniques

Satellite-based remote sensing offers some considerable advantages over ground-based measurements: no limitation by size or danger of the eruption; synoptic viewing; rapid, repeated and systematic data acquisition; and cost-effective (post-launch) measurements at a number of volcanoes. Weighed against these benefits are the challenges of monitoring small volcanic plumes from space, the often highly complex retrieval algorithms needed in data processing, and the ambition to measure more gas species than only SO_2.

Considerable success has been achieved in using the Total Ozone Mapping Spectrometer (TOMS) on the Nimbus-7 and Meteor-3 satellites to map the atmospheric distribution of volcanic SO_2: the instrument and some applications are reviewed by Symonds *et al.* (1994). Primarily designed to determine ozone concentrations by measuring back-scattered solar ultraviolet radiance in six narrow wavelength bands, TOMS is able to take advantage of strong absorptions by SO_2 in the same part of the spectrum to measure SO_2 concentrations. TOMS provides a coarse spatial resolution of 47 km by 47 km at nadir. While it is well-adapted to obtaining estimates of bulk SO_2 from large dispersed stratospheric plumes, it has insufficient resolution to detect medium to small-scale quiescent plumes in the troposphere.

Bluth *et al.* (1993) estimated that TOMS successfully detected SO_2 from 55 out of 350 known eruptions between 1979 and 1992, and also identified several eruptions not known from ground studies. Despite its coarse resolution, TOMS measurements combined with other forms of satellite data can still provide insight into volcanic cloud/ atmosphere processes. Schneider *et al.* (1999) reported direct evidence from satellite data of the separation of the ash-rich and gas-rich parts of the plume from El Chichon in the days following its 1982 eruption.

Limb-sounding instruments (which look obliquely through the atmosphere, rather than straight down at the ground) are capable of detecting trace gases at much lower concentrations than the nadir pointing TOMS, but the footprints of these sensors are inevitably even larger. The microwave limb sounder (MLS) aboard the Upper Atmosphere Research Satellite (UARS) began operating three months after the 1991 eruption of Mt. Pinatubo, and immediately detected residual volcanic SO_2 (Read *et al.* 1993). Although superior to TOMS for SO_2 detectivity, the MLS is still only sensitive to gas at altitudes greater than 15 km: so tropospheric plumes remain inaccessible. In addition to SO_2 gas, the MLS can detect aerosol phase, and was used to monitor the global evolution of Pinatubo aerosols until 1993 (Lambert *et al.* 1997).

Image data from the aircraft-mounted thermal infrared multispectral scanner (TIMS) can provide virtually instantaneous measurements of SO_2 plumes at spatial resolutions as fine as 3 m (at nadir) (Realmuto *et al.* 1994, Realmuto *et al.* 1997). This is applicable to SO_2 from quiescent degassing or non-explosive eruptions, providing a bridge between COSPEC-scale and TOMS-scale datasets. Realmuto *et al.* (1997) presented measurements from Kilauea's East Rift Zone, obtaining good correlation with COSPEC estimates of SO_2 burden. A similar instrument (MIVIS) was used by Teggi *et al.* (1999) at Mt Etna, with similar success. Both of these authors view their airborne imaging spectroradiometers as prototypes of future spaceborne sensors, such as ASTER (the Advanced Spaceborne Thermal Emission and Reflectance Radiometer), which will collect data over virtually any volcano on Earth at least once every 16 days and was scheduled for launch in 1998. These examples illustrate convincing progress towards the long-term goal of replacing routine COSPEC monitoring with SO_2 measurement from space.

Since the review of Symonds *et al.* (1994), there has been progress in refining satellite-based infrared interferometric techniques, within the fields of atmospheric and meteorological research, which could also be used for volcanological applications. It is hoped that developments in satellite-based technologies will soon provide widespread capability for space remote-sensing of even small volcanic plumes.

1.3.4 In perspective

This brief review of gas measurement techniques illustrates the diversity of available information and also, fundamentally, that almost every method measures something slightly different. While conventional direct samples can be collected as gas exits the vent, and presumably reflect closest to the true magmatic gas composition, these analyses may not relate well to gases released during very active phases. Filter packs and airborne gas analysers are subject to the effects of spatial and temporal plume heterogeneities. Remote techniques sample an integrated path through the gas plume after some mixing and equilibration with the atmosphere has occurred. Satellite instruments currently monitor plumes after they have traversed a great vertical extent in the atmosphere. The data collected by these different techniques are not directly comparable. As the

study of Weibring *et al.* (1998) showed, even fairly similar techniques used simultaneously side-by-side do not return the same answers because they are each affected to different extents by external factors, such as scattering of radiation.

A good deal of time must be spent on interpretation of data collected in these different ways to ensure its correct comparison. For safe and routine gas monitoring, remote-sensing methods will have a very important part to play. But it will be necessary to distinguish between the effects of plume-atmosphere interaction on plume compositions and those of volcanic origin. In Chapter 4, I consider the effects of plume-troposphere interaction at Masaya.

While techniques such as OP-FTIR promise to deliver a wealth of improved data on plume gas compositions, measurement of gas emission rates still presents great challenges. Currently, all estimates of emission rates depend on COSPEC measurements of SO_2 plume cross sections, combined with wind speeds. The potential for satellite-based measurements of both large and small (tropospheric) volcanic SO_2 emissions is likely to have significant future impact. Perhaps the best approaches in the development of gas monitoring will be integrated programmes in which different techniques are employed over the course of an eruption. Symonds *et al.* (1994) outline an idealised surveillance programme. Combined results would enable the individual techniques, as well as the volcano, to be better understood.

At present, there are no techniques, apart from conventional direct samples, that allow the simultaneous detection of the number of volcanic gases that is possible with ground-based OP-FTIR spectroscopy. That fact, coupled with its suitability for gas measurements during a range of volcanic activities and in a variety of different field configurations, ensures that OP-FTIR is set to play an increasingly significant role in future volcano monitoring. The recent deployment of a portable OP-FTIR spectrometer as an integral part of the Poseidon project for monitoring activity at Mt Etna (M. Burton, pers. com.) is evidence that this role is already being recognised.

1.4 Introduction to Masaya Volcano, Nicaragua

This thesis has a two-fold aim: first, to develop further the use of OP-FTIR in field monitoring of volcanic gases, and second, to use gas geochemical data to gain insight on degassing processes currently occurring at Masaya Volcano. Masaya is a natural laboratory at which to use OP-FTIR, because of its accessibility and its regime of reliable intense tropospheric gas emission. In this section, I will outline the characteristics of Masaya Volcano and its current activity, beginning with its tectonic setting and related aspects of geochemistry, then discussing Masaya's history of plinian eruptions, and ending with details of recent volcanic activity and the current episode.

1.4.1 Arc setting

Masaya is a low-lying (600 m a.s.l.) basaltic volcano on the Central American Volcanic Front, in Nicaragua (figure 1-14). The Central American Arc is the manifestation of eastward subduction of the Cocos and Nazca plates beneath the Caribbean. It has been the focus of both geochemical studies investigating the nature of subduction zone processes (e.g. Chan *et al.* 1999, Herrstrom *et al.* 1995, Reagan *et al.* 1994) and physical volcanology addressing structural parameters along the arc (e.g. Carr 1984, 1999, Stoiber & Carr 1973, Wadge 1984). Trends in geochemical parameters along the arc have been correlated with tectonic features, such as dip of subducted slab and overlying crustal thickness (Carr 1984, Carr *et al.* 1990, Leeman *et al.* 1994), with inferred regional asthenospheric mantle flow (Herrstrom *et al.* 1995), and with subduction zone temperatures (Chan *et al.* 1999).

Figure 1-14: Map of Nicaragua to show the location of Masaya Volcano, approximately 20 km south-west of Managua. Other Nicaraguan volcanoes are indicated by black dots.

Central American arc volcanoes have been noted for their particularly water-rich products (Roggensack *et al.* 1997, Sisson & Layne 1993). Nicaraguan lavas tend to show the greatest trace element subduction signal of the whole arc (Carr *et al.* 1990), with almost 100% sediment

subduction (Herrstrom *et al.* 1995), and large fluid additions to the sub-arc mantle (Feigenson & Carr 1993) (figure 1-15).

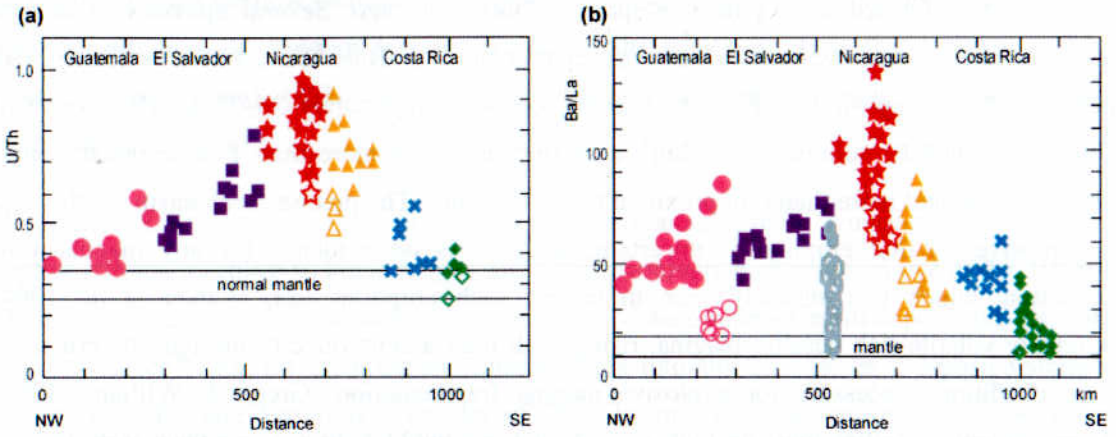

Figure 1-15: Geochemical variations along the Central American arc, figures from the MARGINS science plan (http://www.soest.hawaii.edu/margins), showing that the subduction signal is strongest in western Nicaragua (red stars). Filled symbols are samples from along the volcanic front; open symbols are back-arc or back-arc-like samples. (a) Regional variation in U/Th along the arc. U/Th is a useful tracer for sediment subduction in Central America because of the unusually high U content and U/Th of carbon-rich hemipelagic sediments on top of the Cocos plate. (b) Regional variation in Ba/La along the arc; Ba/La is another monitor for the subduction component.

The evolution of Masaya has been studied in detail by Walker (1993), and its stratigraphy by Williams (1983a), and Bice (1985). The oldest rocks correlated with a proto-Masaya have an age of 135 ka, and, since then, products from Masaya have been overwhelmingly basaltic or basaltic andesite, with little compositional variation. Major element variation in Masaya lavas has been attributed to open-system magmatic differentiation (combining fractional crystallisation and magma mixing) in a large shallow chamber (Walker *et al.* 1993). Masaya displays trace-element geochemical characteristics that are the most extreme along the Central American arc, with the highest $^{87}Sr/^{86}Sr$ values of any Central American basalts (Walker *et al.* 1993), and anomalous Li-Be-B enrichments (Chan *et al.* 1999, Leeman *et al.* 1994, Morris *et al.* 1990). These features may be related to sub-arc mantle heterogeneities, coupled with especially large slab fluid additions to the source of Masaya magmas and the open-system processes controlling the evolution of these magmas.

Two minor explosions from Masaya (on 24 October 1997 and 13 September 1998) ejected volcanic bombs over the rim of the crater. I have carried out geochemical analysis of these rocks, using both bulk (whole rock XRF) and point (electron microprobe) methods. These modern products have much the same basaltic (51 wt% SiO_2) composition as samples detailed in the literature (see Appendix for details of this analysis).

1.4.2 Structural setting and plinian eruptions

The currently active crater complex is situated within a 6 km by 11 km elongate caldera (figure 1-16) that was formed by a plinian eruption ~2500 years ago. Several episodes of unusual explosive basaltic eruptive activity have occurred at Masaya (Bice 1985, Williams 1983b). One such pyroclastic deposit (the Fontana Lapilli), dated approximately 35–25 ka (Walker *et al.* 1993), has a D.R.E. volume of 3.4 km^3, with thicknesses of more than 1 m across the entire Managua area, and more than 6 m proximal to the volcano. The precise mechanism for this type of explosive basaltic eruption is uncertain, as there is no evidence for any magma-water interaction, which is commonly seen to trigger such eruptions (c.f. Walker *et al.* 1984). Extremely volatile-rich basaltic magma, rising with high ascent velocity through the crust, can attain conditions necessary for explosive magma fragmentation (Gregg & Williams 1996). Magma ascent velocities must be high enough that gas bubbles do not segregate from the low viscosity basaltic melt and rise ahead, thereby preventing the build up of large overpressures. The magma must also be prevented from ponding at some shallow level within the crust from where degassing can occur.

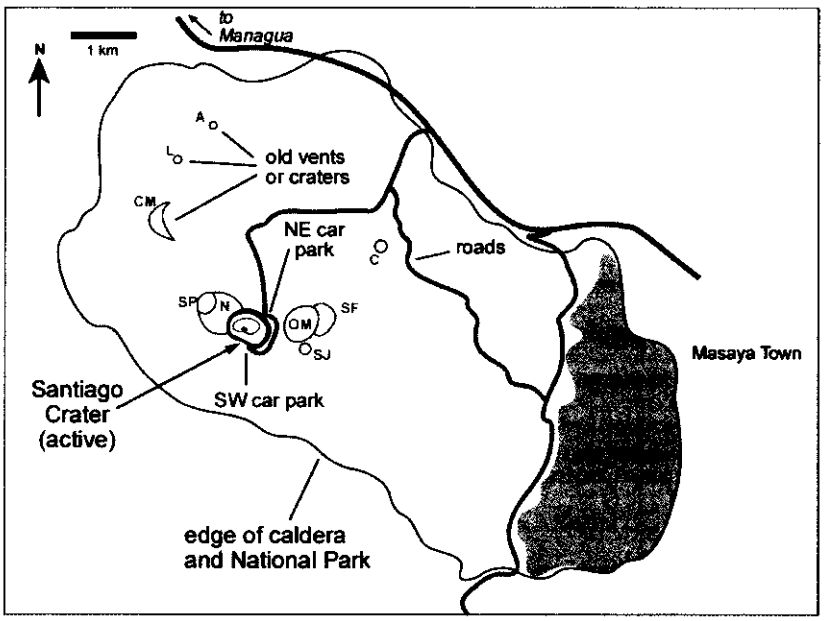

Figure 1-16: Scale map of Masaya caldera showing the currently active Santiago Crater and older cones and craters. Labels are: A=Arenal, L=La Luna, CM=Cerro Montoso, SP=San Pedro, N=Nindiri, OM=Old Masaya, SJ=San Juan, SF=San Fernando, C=Comalito.

Exactly what circumstances triggered the explosive eruptions in Masaya's history are unclear. Gregg and Williams (1996), suggest that faults crossing through Masaya and extending through the underlying lithosphere allowed gas-rich basaltic magma to rise rapidly from a deep source to the surface, without ponding. Masaya is, indeed, located near an arc segment boundary (Stoiber & Carr 1973) and on the intersection of tensional fractures and regional fault systems (Maciejewski 1998). Movement on faults could have opened a magmatic pathway to cause an

eruption, although volcanic activity at Masaya was unaffected by the large Managua earthquake of 1972 (Stoiber *et al.* 1986). Recent behaviour of the volcano has been overwhelmingly passive: gas venting from a shallow chamber likely prevents the evolution of conditions towards another explosive eruption. A modern eruption similar to the largest of those that have occurred in Masaya's past would obliterate Managua, disrupt the entire region, and have major environmental effects.

Williams (1983b) estimated the exit velocity for the Fontana Lapilli eruption at 170 m s^{-1}, an eruptive column reaching 50 km in height, and a comparatively high eruption rate of 2 x 10^5 m^3 s^{-1}. Pyle (1989) reassessed the published isopach maps of the Fontana Lapilli deposit and estimated a slightly lower 44 km for the eruption column height into still air. Given a deposit volume of 3.4 km^3 (D.R.E.) and assuming a density of 2600 kg m^{-3}, the mass erupted over the 2 hour duration suggested by Williams (1983b), is approximately 9 x 10^{12} kg. The mean mass eruption rate was therefore 10^9 kg s^{-1}, and following Woods (1995), for an exit velocity of 170 m s^{-1}, I estimate that a minimum volatile content of 3 wt % is required to propel this eruption (figure 1-17). During the Fontana Lapilli eruption, therefore, a minimum of 240 Mt of volcanic gas (scaling the volatile content to the mass of erupted products) may have been lofted high into the atmosphere over a short period of time.

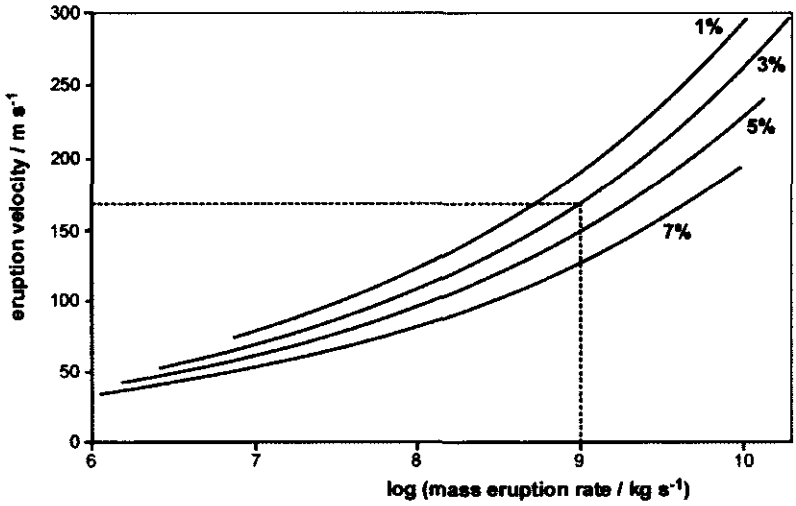

Figure 1-17: after Woods (1995). Relationship between magma volatile content (labelled), eruption velocity and mass eruption rate. For the conditions reported by Williams (1983b) for plinian eruptions from Masaya at least 3 wt % volatiles were required.

1.4.3 Recent volcanological history

The first historical records of volcanic activity at Masaya date from the early 1500s and the time of the Spanish Conquistadors. Oviedo and Fray Blas del Castillo (cited by McBirney 1956) described the appearance of the summit craters in 1529 and 1537, respectively, and both mentioned the existence of a lava lake within Nindiri Crater. The intermittent presence of lava

lakes seems to be a distinctive feature of Masaya's historic activity (McBirney 1956). A lava flow in 1670 resulted from a lava lake overspill from Nindiri (Walker *et al.* 1993). The last major lava eruption occurred in 1772 when a fissure opened at the base of the Old Masaya crater, and a 7 km flow ensued. Since that time effusive activity has been negligible. The smaller vents and spatter cones in the NW half of the caldera (see figure 1-16) appear to be the result of short-lived eruptive events (Maciejewski 1998), and all are inactive. Readers are referred to Maciejewski (1998), for detailed discussion of the evolution of volcanic features within the caldera.

The currently active crater, Santiago, along with the smaller San Pedro crater, was formed after a period of increased activity between 1850 and 1859, as the result of a large subsidence event (McBirney 1956). Since that time, the crater appears to have developed through pit collapses (Rymer *et al.* 1998), and all subsequent activity has been centralised in this crater. At least 6 episodes of strong degassing unassociated with major eruptions have occurred since 1850 (Table 1-1): high rates of degassing recommenced in late 1997 and continued to the time of writing. Despite the fact that the intermittent degassing behaviour of Masaya has been known for half a century, the mechanisms responsible for its timing and nature remain unclear.

Dates	Reference
1850–1859	1
1902–1906	1
1919–1927	1
1946–1959	1, 2
1979–1988	2, 3, 4
1993–1996	4
1997–present	This work

Table 1-1: dates of recorded degassing crises at Masaya. References: 1 McBirney (1956), 2 Stoiber *et al.* (1986), 3 Walker *et al.* (1993), 4 Rymer *et al.* (1998).

Recent activity at Masaya has been studied by Stoiber *et al.* (1986), and Rymer *et al.* (1998). Both studies utilised the good road network around Masaya (figure 1-18) to employ vehicle-borne COSPEC for measurements of the SO_2 emission rate, in 1980–82 and 1996–97, respectively. In addition, Stoiber *et al.* (1986) placed filter packs for sampling the gas plume both on the rim of Santiago crater and at distances downwind, and derived average emission rates of 14.8 kg s^{-1}, 9.6 kg s^{-1} and 0.2 kg s^{-1} for SO_2, HCl and HF. They considered that the emission rate of SO_2 from the volcano decayed exponentially with time after the onset of the degassing phase in 1979, and that gas ratios in the plume changed also. They explained these results in terms of a model of closed-system degassing of a large shallow magma body beneath Masaya. The question of whether the model of a closed magma body is applicable to Masaya is addressed in Chapter 5, which contains a fuller discussion of the data presented by Stoiber *et al.* (1986), compared with my observations of Masaya's gas plume in 1998 and 1999.

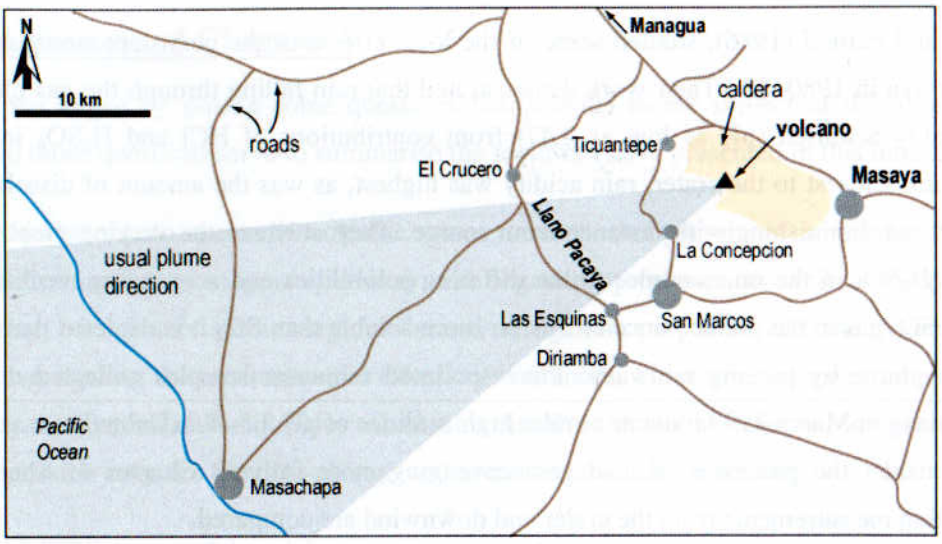

Figure 1-18: Regional map showing the road network around Masaya, and the usual plume direction, as blown by the prevailing north-easterly winds.

Rymer *et al.* (1998) concluded, on the basis of microgravity data, that the resumption of vigorous degassing activity in 1993 was caused not by a fresh magma intrusion but by convective overturn of magma to bring a gas-rich layer close to the surface. Their COSPEC measurements indicated a mean SO_2 emission rate of 6.9 kg s^{-1} in March 1996 and 3.8 kg s^{-1} in early 1997. The question of whether a convective overturn model can account for all the observations of degassing at Masaya is addressed in Chapter 6, where I discuss the results of Rymer *et al.* (1998) further, and consider other physical degassing models for Masaya.

Metaxian *et al.* (1997), monitored seismicity at Masaya in 1992 and 1993. Despite recording relatively few long-period events and volcano-tectonic earthquakes, they found the volcano was characterised by permanent seismic tremor. The source of the tremor was situated at shallow depth, directly associated with continuous degassing activity of the lava lake beneath the NE rim of Santiago crater. Their measurements spanned periods when the lava lake was not seen (1992) and when it was visible (1993) and they noted that the tremor persisted (although with reduced amplitude) even when the lava lake was not visible from the crater edge. They concluded that Masaya has an open magmatic system with shallow degassing magma bodies retained in the upper part of the volcano.

Colleagues from the OU, and Université de Montréal conducted COSPEC measurements of the sulfur dioxide emission rate in 1998 and 1999. Results on different days fluctuated significantly, but the mean for the period February to April 1998 was 21.4 kg s^{-1} (with maximum and minimum values of 41.9 kg s^{-1} and 7.8 kg s^{-1}), and for February to March 1999 was 20.7 kg s^{-1} (with maximum and minimum values of 47.0 kg s^{-1} and 14.5 kg s^{-1}) (Delmelle *et al.* 1999a, and pers. com.). These emission rate data are useful in combination with my observations of the gas composition, and I refer widely to them in Chapters 5 and 6.

Johnson and Parnell (1986), studied some of the local effects of the persistent strong degassing from Masaya in 1980–82. Their work demonstrated that rain falling through the gas plume was considerably acidified (pH as low as 2.47) from contributions of HCl and H_2SO_4 in varying proportions. Closest to the crater, rain acidity was highest, as was the amount of dissolved HCl, both of these diminishing with distance from source. They attribute the varying proportions of HCl and H_2SO_4 in the rain samples to the differing solubilities and scavenging mechanisms of HCl and SO_2 gas in the plume: since HCl is far more soluble than SO_2 it is depleted more rapidly from the plume by passing rainwater. Plume-polluted rainwater samples collected downwind from Masaya in March 1999 indicate similar high acidities of pH 3.5–4.0 (Delmelle *et al.* 1999b). I will consider the processes of acid gas scavenging more fully in Chapter 4, where plume composition measurements from the crater and downwind are compared.

1.5 Conclusions of Chapter 1

This chapter began by posing some questions fundamental to the subject of this thesis. Brief answers to those questions serve to summarise the reviews I have presented in this introduction:

(a) Motivations to measure volcanic gases include the pursuit of a greater academic understanding of magma chemistry and degassing processes, as well as the pragmatic goal of volcano monitoring for hazard mitigation purposes, and the wider aim of investigating the environmental effects of volcanoes. Since emitted gases are controlled by the sources and solubilities of volatiles dissolved in parent magmas, compositions and emission rates are likely to change with trends in a volcano's activity.

(b) OP-FTIR is a useful tool for gas monitoring for both practical and scientific reasons. It meets criteria for safe, useful and accurate remote gas measurements, and its flexibility of operation is a great advantage. Scientifically, extensive automation allows for rapid repeatable measurements, near real time analysis and observations on a temporal resolution previously impracticable. Since all species can be measured simultaneously, the instrument is well-suited to monitoring variations in gas ratios, which may be linked to changes in the final equilibrium pressure and temperature of degassing (such as magma movement or depressurisation), changes in the effective sources of volatiles (such as magma mixing or hydrothermal influx), reactions between hot gases and vent wall rocks, or secondary variations from in-plume effects (such as multiphase atmospheric oxidation reactions).

(c) Masaya Volcano provides an ideal location at which to use OP-FTIR since its active crater, and several locations downwind, are easily accessible by road, and offer suitable viewing geometries to use the instrument in a range of modes. Additionally, Masaya's consistent regime of strong passive gas emission provides a reliable and identifiable plume as a measurement target.

(d) Because of Masaya's characteristic intense degassing unaccompanied by eruption of lava, gas geochemical data are a vital source of information, and, coupled with data from geophysical techniques, provide insight on the processes occurring within the volcano. Additionally, the plinian eruptions in the past, which required volatile-rich magma sources and rapid gas exsolution, testify to the primary role of gases throughout the history of this volcano.

On the basis of these strong motivations to develop volcanic-gas monitoring by OP-FTIR, and the applicability of this technique to investigations at Masaya Volcano, I proceed by presenting the technique and data retrieval methodologies in some detail, before considering the results of field work at Masaya in the second half of the thesis.

CHAPTER 2
TECHNICAL ASPECTS OF OPEN-PATH FOURIER TRANSFORM INFRARED SPECTROSCOPY AT VOLCANOES

This thesis focuses on the application of ground-based open-path Fourier transform infrared spectroscopy to measurements of gases emitted by volcanoes. This is a relatively new application, although open-path spectroscopic techniques have been used in the fields of atmospheric chemistry and environmental pollution, from both ground-based (e.g. Herget & Brasher 1979, Marshall *et al.* 1994) and satellite platforms (e.g. Brown *et al.* 1996), for some years. In this chapter, therefore, I introduce the technique in detail, covering open-path FTIR in general before addressing the specific issues of its application to volcano monitoring, including a description of the MIDAC spectrometer used for my fieldwork, and the data retrieval procedure.

2.1 Introduction to Open-path Fourier transform infrared spectroscopy

Infrared spectroscopy has long been an indispensable tool for the chemical characterisation of unknown substances. This section covers the fundamentals of infrared spectroscopy before focusing on the Fourier transform technique specifically, including theoretical, instrumental and measurement analysis considerations.

2.1.1 Fundamentals of infrared spectroscopy

Infrared spectroscopy relies on the potential for molecules to emit or absorb infrared radiation due to changes in their vibrational or rotational state. The particular chemical environment of the molecule determines the frequency of energy absorbed or emitted as such a transition occurs: hence different molecular species have unique spectral signatures. The infrared spectrum of an unknown gas mixture contains lines that can be used to identify both its chemical composition and the concentrations of individual components. Readers are directed to Banwell (1972) for a review of the physical chemistry underpinning the technique of infrared spectroscopy. Some general principles are illustrated in figure 2-1.

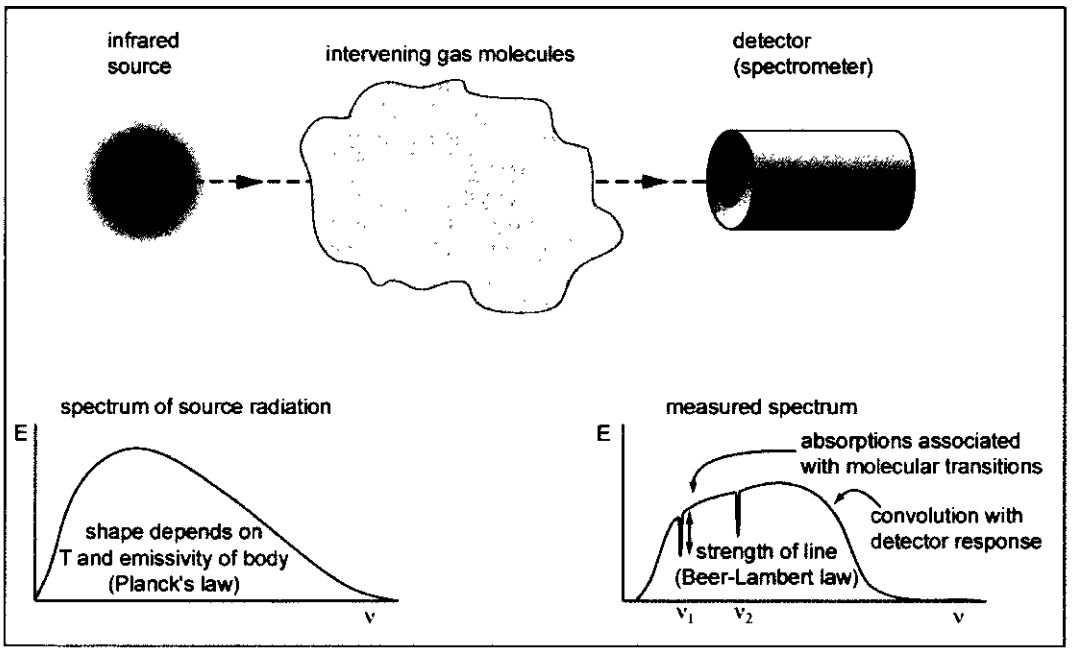

Figure 2-1: The fundamentals of infrared absorption spectroscopy. Gas molecules in the optical path between an infrared source and detector absorb energy at characteristic frequencies. The shape of the source function depends on the temperature and emissivity of the hot body, according to Planck's law. The measured spectrum is a function of the detector response curve as well as the amount and type of absorbing gases in the path. E is relative energy intensity and ν is frequency (wavenumbers).

Any infrared-active molecules in the path between the energy source and detector undergo vibrational and rotational transitions. If these molecules are hotter than the source, discrete

spectral lines will be seen in emission, but more commonly, molecules are colder and absorb energy from the source. Symbols used in the following discussion are summarised in Table 2-1.

Quantity	Symbol
Frequency of radiation (cm^{-1})	ν
Wavelength of radiation (μm)	λ
Intensity of incident radiation	I_o
Intensity of transmitted radiation	I
Transmittance	T
Absorption coefficient	ε
Concentration of absorber	C
Optical pathlength of measurement	L
Central frequency of absorption line	ν_o
Absorption linestrength	S
Lorentz line shape factor	f_L
Lorentz half-width (cm^{-1})	α_L
Doppler line shape factor	f_D
Doppler half-width (cm^{-1})	α_D

Table 2-1: Symbols used in section 2.1.1.

The intensity of an absorption line is related to the number of molecules responsible for it (i.e. the concentration of that species) through the Beer-Lambert law (where I_o is the intensity of the incident radiation of given wavelength, ε is the absorption coefficient (a constant for a given species at given wavelength), C is the concentration of the absorber and L is the pathlength through the absorbing material):

$$\frac{I}{I_o} = \exp(-\varepsilon CL) \qquad (2\text{-}1)$$

I/I_o is known as transmittance, T, and often given as a percentage. Within the literature, some authors prefer to use natural logarithms, while others use base-10 in their formulation of the Beer-Lambert law. This results in some confusion as to what exactly is meant when terms such as *absorption coefficient* are used, as its value will change. In this thesis, the form as in equation (2-1) will be accepted. Equation (2-1) assumes that the absorbing gas molecules are dispersed homogeneously along the measured optical path. Because measured absorption lines are subject to instrumental effects on line shape, deviations from the Beer-Lambert law are expected, these will be discussed in section 2.1.1.1.

The discrete regions of the infrared spectrum associated with energy transitions of gas molecules of interest at volcanoes are shown in figure 2-2.

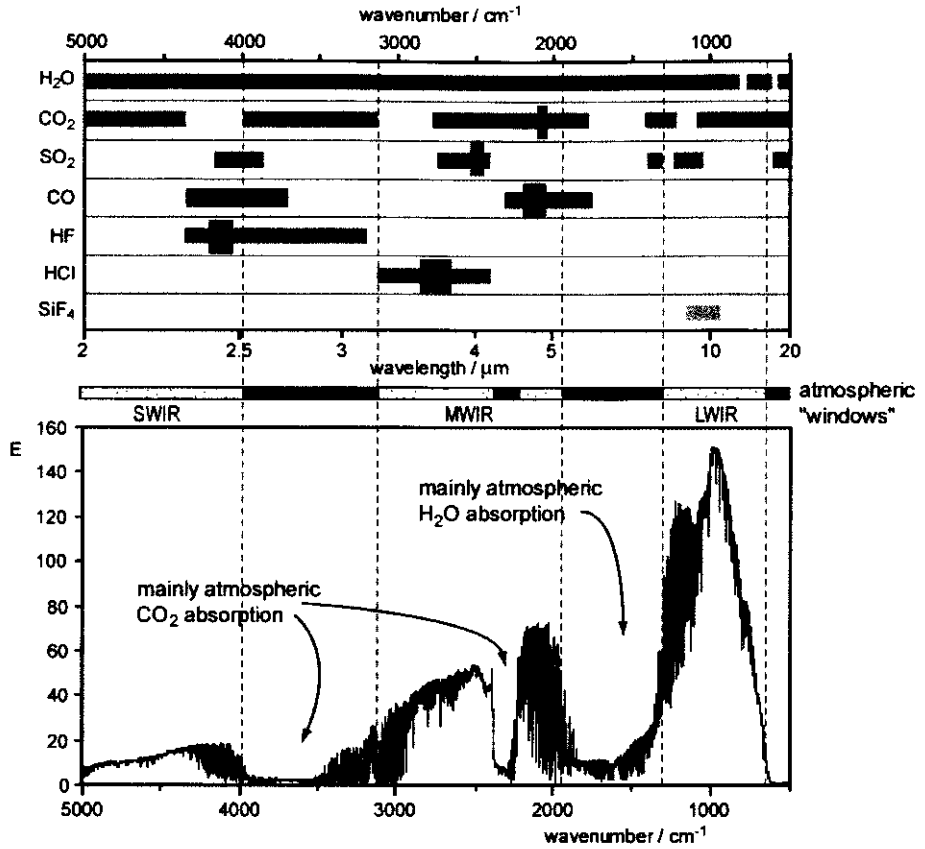

Figure 2-2: Lower half shows a typical spectrum collected at Masaya Volcano, with arbitrary units of energy intensity on the y-axis. Upper half shows the coverage of spectral line data for gases of volcanic interest in the HITRAN database (grey) and the smaller microwindows which are modelled in the retrieval for gas amounts (black). Open-path trace gas analysis relies upon detection of absorptions within the marked atmospheric windows (central bar) as opposed to those regions which are "black" due to H_2O and CO_2 lines.

Smaller, lighter molecules (e.g. HCl and HF) undergo transitions at higher energies (shorter wavelengths) than heavier molecules (e.g. SO_2). Lines associated with H_2O and, to a lesser extent, CO_2, occur throughout the infrared. In some wavebands, atmospheric absorptions due to these species can prevent any radiation from the source reaching the detector, even over path lengths of a few hundred metres. So-called "atmospheric windows" occur between major atmospheric absorption bands. Marked on figure 2-2 are windows in the long-wave IR (LWIR) between 700-1300 cm^{-1}, mid-wave IR (MWIR) between 2000-3200 cm^{-1}, with an opaque gap due to CO_2 at 2200-2400 cm^{-1}, and short-wave IR (SWIR) between 4000-5000 cm^{-1}. Detection of trace gases focuses on analysis of IR lines falling in these atmospheric windows.

2.1.1.1 Line shapes and deviations from the Beer-Lambert law

The theoretical shape of an absorption is determined by molecular properties, so that *S*, the line strength, is equivalent to the integral of the absorption coefficient for a given molecule over the frequency range of the transition responsible for it:

$$S = \int_0^\infty \varepsilon \, d\nu \tag{2-2}$$

Molecular collisions and random thermal motions result in broadening of the theoretical monochromatic lines across a range of frequencies. This broadening can be described mathematically by defining the absorption coefficient as a function of frequency away from theoretical line centre:

$$\varepsilon = S f(\nu - \nu_o) \tag{2-3}$$

where the function $f(\nu\text{-}\nu_o)$ is the normalised line shape factor.

Molecular collisions cause an energy exchange between molecules with the consequence that rotational and vibrational energy levels, and the absorption line itself, are effectively broadened. The degree of broadening is related to the frequency of collisions and therefore pressure and temperature. These effects are described in the Lorentz line shape factor, f_L:

$$f_L(\nu - \nu_o) = \frac{\alpha_L/\pi}{(\nu - \nu_o)^2 + \alpha_L^2} \tag{2-4}$$

where α_L is called the Lorentz half-width in cm^{-1},with pressure and temperature dependence:

$$\alpha_L(p,T) = \alpha_L(p_o,T_o) \times \left(\frac{p}{p_o}\right) \times \left(\frac{T}{T_o}\right)^n \tag{2-5}$$

and $\alpha_L(p_o,T_o)$ is the half-width at standard temperature and pressure. The value of the exponent, n, depends upon the nature of the molecules. Increasing both pressure and temperature results in broadening of absorption lines and therefore a reduced peak depth (figure 2-3(a)).

Random thermal motions also result in line broadening due to the Doppler effect. The Doppler line shape factor, f_D is given by:

$$f_D(\nu - \nu_o) = \frac{1}{\alpha_D \sqrt{\pi}} \exp\left(-\frac{(\nu - \nu_o)^2}{\alpha_D^2}\right) \tag{2-6}$$

where the Doppler half-width, α_D, is defined as:

$$\alpha_D = \frac{\nu_o}{c}\sqrt{\left(\frac{2kT}{m}\right)} \tag{2-7}$$

where c is the speed of light, k is the Boltzmann number and m is the molecular weight.

For altitudes up to approximately 25 km, Lorentz half-widths are broader than Doppler half-widths, in the infrared region of the spectrum. Above this, low pressures mean that Doppler broadening dominates. The two broadening factors can be convolved to form a single function, known as the Voigt line shape, applicable at all pressures. In the forward model algorithm described in section 2.3, the Voigt line shape is used.

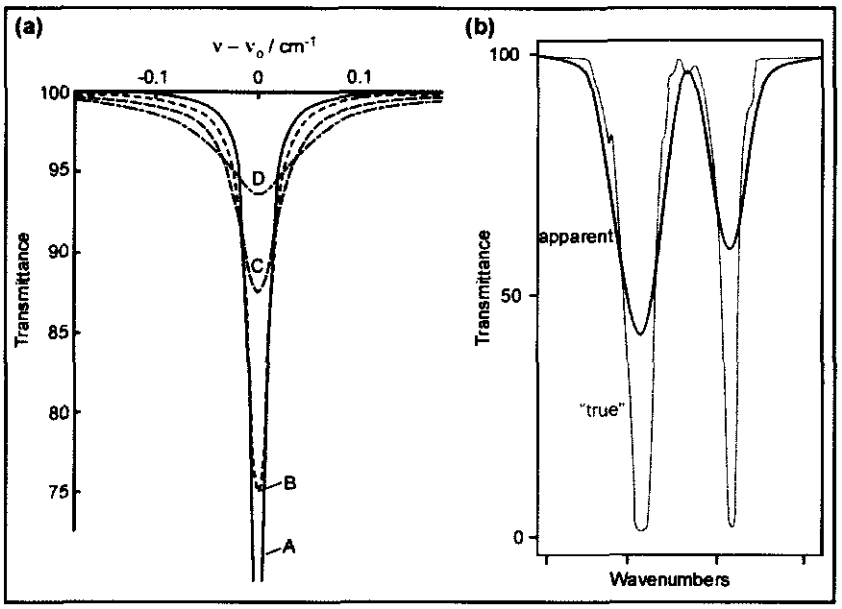

Figure 2-3: (a) adapted from Hanst and Hanst (1994). Spectral line shape as a function of pressure, according to equations (2-4) and (2-5). Curve A represents the lowest pressure and curve D the highest pressure. (b) The "true" spectrum (grey) was measured by a high-resolution instrument, while the apparent spectrum (black) was measured by an instrument with much lower resolution. The true transmittance is actually saturated for the line on the left, but the apparent spectrum belies any saturation. The integral across the line remains constant, so the instrumental broadening is accompanied by a reduction in peak height.

If an instrument could measure the theoretical line shape relating to a specific molecular energy transition, then the Beer-Lambert law (equation (2-1)) relating transmittance to concentration of the absorber holds true and the gas concentration can be simply calculated. However, apart from physical line broadening effects, instrumental effects usually result in measurement of an *apparent* absorption. In this case:

$$T_{app} \neq \exp(-\varepsilon CL) \qquad (2\text{-}8)$$

This effect is illustrated in figure 2-3(b). When absorption lines are measured by an instrument with considerably lower resolution than the theoretical line width, it results in smoothing of the spectral feature. Since the integral of ε across the whole line is constant, broadening of a line due to poor instrument resolution is accompanied by a reduction in peak depth. The measured peak no longer scales with concentration according to the Beer-Lambert law.

All of these effects must be accounted for in any analytical procedure, by correct fitting of instrumental line shape and well-constrained estimates of pressure and temperature, if gas concentrations are to be accurately retrieved from measured spectra.

2.1.2 Fourier transform spectroscopy

An introduction to the theory underpinning Fourier transform spectroscopy is provided by Griffiths (1975) and the following discussion owes much to that account. The central component of all FT spectrometers is the moving-mirror Michelson interferometer (figure 2-4). This device splits a beam of incident radiation into two paths, with varying optical path difference, and then recombines them to result in interference, which is measured by the detector. Intensity variations of the exit beam as a function of mirror position (i.e. path difference) are recorded. If the mirror scans at a constant speed, the amplitude of the signal arriving at the detector varies sinusoidally. This function is called the interferogram, and the cosine Fourier transform of the interferogram, after a number of corrections, is the observed spectrum, a plot of energy intensity as a function of wavelength (or frequency in cm^{-1}).

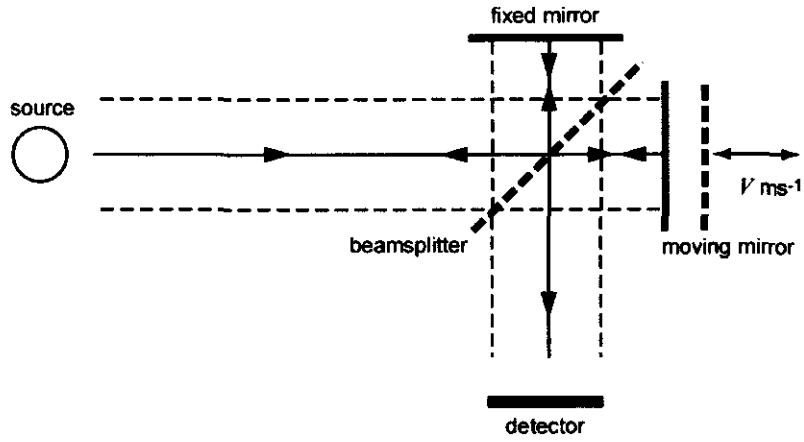

Figure 2-4: The Michelson interferometer. Incoming light is split into a through ray and a reflected ray by the beamsplitter. The reflected ray travels to the fixed mirror and returns. The through ray travels to the moving mirror (which translates at a fixed speed, *V*) taking a path that is equal to or longer than that of the reflected ray, depending on the mirror position. Recombination of the two rays, which are now out of phase by some amount dependent on the position of the moving mirror, at the beamsplitter results in interference fringes measured by the detector.

2.1.2.1 Mathematical description

The aim is to calculate the intensity of the incoming radiation as a function of frequency from a measurement which is the intensity of radiation reaching the detector as a function of path difference. Symbols used in the following descriptions are summarised in Table 2-2.

Quantity	Symbol
Frequency of incident radiation (cm^{-1})	ν
Wavelength of incident radiation (μm)	λ
Optical path difference between rays (cm)	δ
Amplitude of radiation entering spectrometer	$I(\nu)$
Amplitude of radiation modified by instrumental effects	$B(\nu)$
Amplitude of radiation reaching detector	$I'(\delta)$
Varying component of radiation reaching detector	$I''(\delta)$
Amplitude of measured interferogram	$I(\delta)$
Maximum optical path difference (cm)	Δ_{max}
Angle of divergence between central and off-axis rays	ϕ
Path difference between central and off-axis rays	l_ϕ

Table 2-2: Symbols used in section 2.1.2.

First consider a monochromatic beam of frequency ν passing through the interferometer. The energy arriving at the detector has amplitude that varies sinusoidally and is defined as:

$$I'(\delta) = \tfrac{1}{2} I(\nu) \{1 + \cos(2\pi\nu\delta)\} \qquad (2\text{-}9)$$

The varying component of this signal, $I''(\delta)$, is simply:

$$I''(\delta) = \tfrac{1}{2} I(\nu) \cos(2\pi\nu\delta) \qquad (2\text{-}10)$$

But the amplitude of the interferogram is not only proportional to $I(\nu)$, it is also affected by instrumental characteristics (beamsplitter efficiency, detector response, amplifiers, etc). So let $B(\nu)$ be the amplitude of incoming radiation, taking into account the effects of the instrument, and the interferogram is:

$$I(\delta) = B(\nu) \cos(2\pi\nu\delta) \qquad (2\text{-}11)$$

$I(\delta)$ is the signal received by the detector, but we want to find out $I(\nu)$ (or $B(\nu)$).

Now the form of the equation for $I(\delta)$ means that, by definition, $I(\delta)$ is the cosine Fourier transform of $B(\nu)$. Therefore, in order to determine $B(\nu)$ from the measurement of $I(\delta)$, we must take the Fourier transform (FT) of $I(\delta)$.

If the energy source is a continuum, or broadband, rather than monochromatic (ν), the interferogram in (2-11) must be represented by an integral:

$$I(\delta) = \int_0^{+\infty} B(\nu) \cos(2\pi\nu\delta)\, d\nu \qquad (2\text{-}12)$$

and the other half of the Fourier transform pair is

$$B(\nu) = \int_{-\infty}^{+\infty} I(\delta) \cos(2\pi\nu\delta)\, d\delta \qquad (2\text{-}13)$$

Because $I(\delta)$ is symmetrical about $\delta=0$, equation (13) is rewritten as

$$B(\nu) = 2\int_{0}^{+\infty} I(\delta) \cos(2\pi\nu\delta)\, d\delta \qquad (2\text{-}14)$$

Thus, by measuring $I(\delta)$ (or, in reality, $I(t)$, the variation in signal intensity at the detector through time as the mirror is translated at constant speed), we can calculate the whole spectrum of the incident radiation. If δ could be varied between 0 and $+\infty$ then the complete spectrum could be measured at infinitely high resolution. But because the mirror travel distance is necessarily limited, the resolution of the spectrum is also limited. Consequently, by Fourier transform spectroscopy, all frequencies are measured simultaneously, unlike the earlier diffraction-limited grating spectrometers, within a range controlled by the instrument's maximum mirror translation and the frequency-response of the detector in use.

2.1.2.2 Instrument resolution and line shape

Since the moving mirror cannot be translated an infinite distance, the interferogram is truncated after some finite value of δ. Let us call this maximum optical path difference, Δ_{max}. Restricting the interferogram in this way is the same, mathematically, as multiplying the entire interferogram, $I(\delta)$, by a Boxcar function, $D(\delta)$, which is equal to 1 between $\delta=0$ and $\delta=\Delta_{max}$, and equal to zero elsewhere. The measured spectrum is now

$$B'(\nu) = \int_{-\infty}^{+\infty} I(\delta)D(\delta) \cos(2\pi\nu\delta)\, d\delta \qquad (2\text{-}15)$$

Mathematically, multiplication and convolution are Fourier transform pairs: multiplication in the Fourier (δ) domain is equivalent to a convolution in the spectral (ν) domain. So the measured spectrum, $B'(\nu)$, is equivalent to a convolution of the FT of the complete interferogram, $I(\delta)$ ($-\infty<\delta<+\infty$), with the FT of the boxcar function, $D(\delta)$. Recalling that the FT of $I(\delta)$ is the true spectrum, $B(\nu)$, then:

$$\begin{aligned} B'(\nu) &= \mathrm{FT}[I(\delta)] \otimes \mathrm{FT}[D(\delta)] \\ B'(\nu) &= B(\nu) \otimes FT[D(\delta)] \end{aligned} \qquad (2\text{-}16)$$

The Fourier transform of the Boxcar function $D(\delta)$ is a sinc function, $J(\nu)$ (figure 2-5):

$$J(\nu) = 2\Delta_{max}\frac{\sin(2\pi\nu\Delta_{max})}{2\pi\nu\Delta_{max}} \qquad (2\text{-}17)$$

$$J(\nu) = 2\Delta_{max}\,\mathrm{sinc}(2\pi\nu\Delta_{max})$$

Convolution of the sinc function with the real spectrum results in smoothing of spectral lines to the resolution of the width of the sinc function, which is dependent upon Δ_{max}. Thus the nominal resolution of the spectrometer is inversely proportional to the maximum possible optical path difference, or mirror translation. In fact, as spectral lines separated by $(\Delta_{max})^{-1}$ cm^{-1} are completely resolved, the practical resolution can be better than this nominal value.

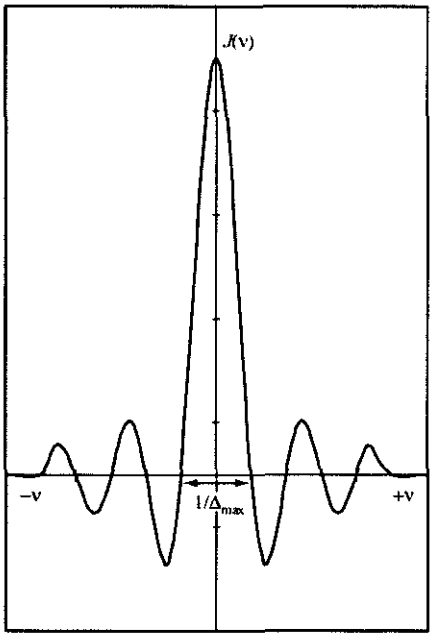

Figure 2-5: The form of a sinc function (equation (2-17)) that results from Fourier transform of the Boxcar function imposed by truncation of an interferogram at some finite optical path difference.

The pure sinc function shown in figure 2-5 represents the appearance of a single sharp line measured at a resolution less than the half-width of the line itself: the instrument has imposed a line shape onto the absorption. In practice, there are further contributions to the instrument line shape (ILS) recorded in the measured spectrum; these come from apodization functions and the effect of the instrument's finite field of view.

2.1.2.3 Apodization

The sinc function is not a very useful line shape because of the relatively large amplitude of the secondary maxima well away from the central frequency of the line. A mathematical function can be applied to the interferogram before its transformation with the aim of suppressing the amplitude of these sidelobes. Such a function is therefore termed an apodization function, $A(\delta)$,

and it weights the interferogram so that $A(\delta)$ is equal to 1 when the optical path difference is zero, and $A(\delta)$ is less than 1 elsewhere.

There are many forms of apodization function that could be used, but for all the spectra measured with the MIDAC instrument in this thesis, a triangular apodization function was applied. This is the most common form of apodization used in infrared Fourier transform spectroscopy because not only does it suppress the amplitude of the sidelobes, it also generates an ILS identical to that of an "old" diffraction-limited grating spectrometer. The triangular apodization function is described by:

$$A(\delta) = 1 - \left|\delta/\Delta_{max}\right| \qquad \text{for } -\Delta < \delta < +\Delta \qquad (2\text{-}18a)$$

$$A(\delta) = 0 \qquad \text{for } \delta < -\Delta \text{ and } \delta > +\Delta \qquad (2\text{-}18b)$$

The Fourier transform of this triangular function is a sinc^2 function. A single spectral line convolved with a sinc^2 function has similar appearance to figure 2-5, but with much reduced amplitude of the secondary maxima. The only drawback with apodization is a slight loss of resolution, although in the case of the MIDAC, this is relatively unimportant given the constraints of the maximum available optical path difference (Δ_{max}).

2.1.2.4 Finite field of view

Until this point, it has been assumed that the beam of radiation passing through the interferometer is perfectly aligned (e.g. in figure 2-4). In practice, there are always off-axis rays that can enter the spectrometer, and these will take a longer path than the central or aligned rays (figure 2-6). This problem occurs for two reasons, firstly, because it is impossible to produce a perfectly collimated beam of light, and secondly, because the spectrometer has a finite field of view (FOV). The effect of such off-axis rays is to cause ILS distortions, which must be accounted for in order to analyse measured spectra accurately.

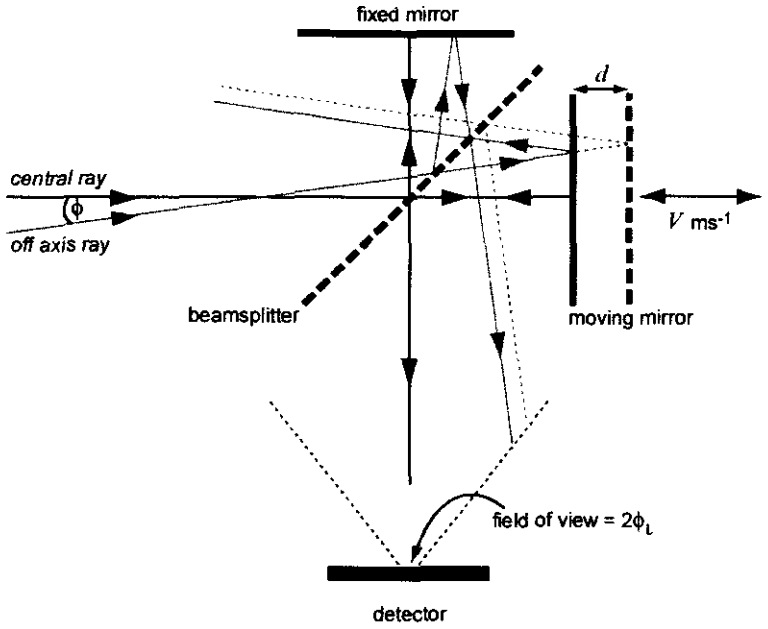

Figure 2-6: Paths taken by axial and off-axis rays through the interferometer to illustrate the effect of finite field-of-view.

When the mirror is moved a distance d, an off-axis ray at some divergence half-angle, ϕ, passes though the interferometer on a path which is longer than that of the central ray by a path difference, l_ϕ, of:

$$l_\phi = 2\frac{d}{\cos\phi} - 2d \qquad (2\text{-}19)$$

Because ϕ is small, this expression can be reduced, via a cosine expansion, to

$$l_\phi = d\phi^2 \qquad (2\text{-}20)$$

For monochromatic light at wavelength λ, as d increases, the off-axis ray will be out-of-phase with the central ray when

$$l_\phi = \frac{\lambda}{2} \qquad (2\text{-}21)$$

$$\text{i.e.,}\quad d\phi^2 = \frac{\lambda}{2}$$

Any further increase in d (i.e. further movement of the mirror) will add no further information to the interferogram, and the effect is to truncate the interferogram at some path difference less than Δ_{max}. This path difference, $2d$, gives the highest resolution, $\Delta\nu$ $(=(2d)^{-1})$, achievable with this half-angle, ϕ, for a wavelength, λ $(=\nu^{-1})$ (Griffiths 1975). So for a FOV limited to $2\phi_L$, the maximum achievable resolution is:

$$\Delta\nu = \nu\phi_L^2 \qquad (2\text{-}22)$$

Because there is a dependence of resolution on frequency in equation (2-22), the ILS does not remain constant across the infrared spectrum. It can also be shown (Griffiths 1975) that the apparent position, ν', of a spectral line theoretically at a frequency ν is affected by a FOV of $2\phi_L$, such that:

$$\nu' = \nu\left\{1 - \frac{\phi_L^2}{4}\right\} \qquad (2\text{-}23)$$

For incident radiation over a range of λ, the loss of information in the interferogram occurs over a range of frequencies, so that the end effect of a finite field of view is a multiplication of the interferogram with a sinc function.

A spectrometer's effective FOV is limited by its throughput. In the MIDAC instrument used in this thesis, the detector element controlled the FOV to a nominal 20 mrad. If the spectrometer optics become poorly aligned, or the source radiation is non-parallel, the effective field of view of the instrument will increase. This is because the detector's field of view is no longer uniformly filled. Clearly, the result will be an increased line width and poorer instrument line shape. These errors, if they arise, must be accounted for by accurate simulation of the ILS in spectral analysis.

2.1.2.5 Spectral analysis

Once the spectrum has been recorded, qualitative and/or quantitative analysis of its spectral features is needed. Absorptions characteristic of the major gases of interest at volcanoes (e.g. HCl, SO_2) can often be recognised directly in a raw spectrum collected over an open path up to 500 m in length. At longer distances (i.e. for solar spectra), absorptions relating to the greater number of molecules of atmospheric gases (especially H_2O and CO_2) in the path often obscure the spectral features of much smaller quantities of volcanic components. Quantitative analysis allows retrieval of gas concentrations from spectral features even when they are not obvious by visible inspection. I have used a forward modelling retrieval algorithm developed by M. Burton (pers. com.) to reduce raw infrared spectra to column amounts of absorbing gases: this retrieval is outlined in section 2.3.

Quantitative analysis in the literature often involves retrieval of absorbance spectra (ratioed spectra) calculated from the measurement spectrum divided by a reference background spectrum collected over the same path in the absence of sample gas (e.g. Hanst 1979). The advantage of using ratioed spectra is that background interference, such as atmospheric gas absorptions and instrument features, is eliminated, leaving a spectrum with increased sample signal to noise, but also increased measurement error. This procedure is successful in controlled environments. However, the ratio method is impossible for the analysis of solar spectra since suitable

background spectra cannot be collected. The optical path for solar measurements is constantly changing because the sun moves, and because H_2O concentrations in the atmosphere are highly variable. For the short path active measurements in this thesis it was also difficult to collect clean background spectra over exactly the same path as the measurements. The distribution of volcanic gas by the wind was unpredictable, and wind misalignments of the source and spectrometer resulted in a variable energy source function through a series of measurements. The use of an unsuitable background spectrum results in increased error and artefacts in ratioed spectra. In this thesis, only the raw single-beam spectra are manipulated, via the forward model and retrieval algorithm described in section 2.3.

2.1.2.6 A note on units

The most common unit for concentration used in gas phase tropospheric chemistry is the number of molecules per unit volume in cm^3. In terms of spectroscopic measurements, which integrate across the whole line of sight, gas concentrations are retrieved as the concentration-pathlength product responsible for the particular absorption being studied, and units are then molecules per cm^2. In contrast, the units for concentration used in the gas geochemistry and volcanology literature (and also for exposure limits) are most commonly parts per million by volume, or ppm. Gas concentrations integrated across a pathlength (in m) are then measured as ppmm. However, units involving ppm do not relate to a single absolute concentration of molecules because they are dependent on pressure and temperature, a fact that is overlooked in the literature.

In this thesis, all retrieved amounts are calculated in units of molecules per cm^2 (molec cm^{-2}), independent of pressure, temperature and pathlength. These values can then be converted for known pressure and temperature to the more familiar units of ppm or ppmm for comparisons with the literature. The equation relating ppm and molec cm^{-2} is:

$$X_i\,(molec/cm^2) = \frac{x_i\,(ppm)\,L(m)\,p_t\,(mb)}{T(K)} \times 7.243 \times 10^{14} \qquad (2\text{-}24)$$

The constant collects together Avogadro's number and the ideal gas constant together with pressure and length conversions (see Appendix for derivation).

A further discrepancy in the literature is involved in the manipulation of spectra. Often spectra are dealt with in units of absorbance (i.e. with peaks up), rather than in transmittance (peaks down). Absorbance (A) and transmittance (T) are related via the Beer-Lambert law (equation (2-1)) such that:

$$A = -\log_e T \qquad (2\text{-}25)$$

Raw spectra are plots of energy transmission, and both the retrieval scheme and all subsequent analysis involved in this thesis will manipulate spectra in transmittance.

2.1.3 Open-path measurement of passive infrared emission spectra

Although all of the data that I shall deal with in this thesis have been derived from *absorption* spectra, the potential of gas measurements by infrared *emission* spectroscopy should be appreciated (e.g. p317ff, Griffiths 1975). Whereas for absorption measurements an observer is constrained in the field to procure a suitable high temperature infrared source behind the plume gases, for emission measurements, a cold background only is required, allowing greater flexibility. In Chapter 3, emission features from volcanic SO_2 and HCl are identified in spectra collected using the volcanic vent as a passive source. While these have been problematic in terms of quantitative spectral analysis, they illustrate the fact that cold terrestrial or sky backgrounds could be used to view hotter volcanic gases in emission.

Measurement of gases using emission spectroscopy is well-known in application to jet-engine exhausts (e.g. Hilton *et al.* 1995), and Love *et al.* (1998) reported successful detection of volcanic SO_2 and SiF_4 in emission against the sky at Popocatepetl. For their measurements, they first collected a clear sky background spectrum upwind from the plume, and then pointed the spectrometer at plume gas to collect sample spectra. On subtraction of the sky background from that of plume plus sky, emission lines from the plume alone were revealed.

While constraints on plume viewing geometry are much reduced, infrared emission spectroscopy has limitations of its own. Wind systems around the summits or craters of volcanoes are notoriously erratic, and so it may be difficult to identify clean background spectra free of any volcanic gas contamination. For spectral features of the gas to be visible in either absorption or emission, there must be sufficient radiance contrast between the plume and background: this is guaranteed with the use of active or solar sources, but is often difficult to achieve with clear sky, or terrestrial backgrounds. Love *et al.* (2000) review the range of passive measurements that they have obtained using clear sky, cloud or ground backgrounds. Additional complexities in these data are the varying interplay of absorption and emission across the spectrum, and the varying contribution to background radiance from reflected sunlight.

Passive absorption spectra can be handled in the same way as the active and solar measurements on which this thesis focuses. With emission spectra, an absolute radiometric calibration of the instrument at the time of data collection is essential for quantitative retrievals (Love *et al.* 2000). Radiance spectra are simply obtained as plume spectra minus background, but an accurate knowledge of the gas temperature is required to calculate absolute column densities. However, because temperature uncertainty affects all gases similarly, while there are large errors in absolute column amounts, errors in gas ratios are much smaller. With only minor technical adjustments, the same instrument as used in this thesis (see section 2.2) was enabled by Love *et al.* (2000) for passive emission spectroscopy. This highlights the flexibility of portable field

spectrometers and their potential for an even wider range of operational modes than those used for the data presented here.

2.2 Application and Instrumentation

Routine collection and analysis of gas samples from volcanoes is required for integration of gas data into general volcano monitoring programmes. As outlined in Chapter 1, direct sampling techniques are far from ideal, not only for reasons of safety but also because a desirable temporal resolution of measurements is impossible to achieve. A worthwhile remote measuring technique should allow data collection from safe distances, applicability to phases of both explosive and passive degassing, measurement repeatability, fine (at least hourly) temporal resolution, rapid and quantitative data processing, and portability in order to respond to changes in the volcanic situation. Chapter 1 indicated how OP-FTIR spectroscopy goes some way to meeting these criteria. Perhaps the most attractive aspect of OP-FTIR spectroscopy for its application to volcano monitoring is its flexibility: not only is the field situation encountered at each volcano different, monitoring at a single location also frequently requires adaptability as volcanic activity changes or weather conditions or accessibility vary.

Although volcanic emissions had been detected by high-resolution static or airborne FTIRs for some time (e.g. Mankin & Coffey 1984, Mankin *et al.* 1992), Notsu *et al.* (1993) and Mori *et al.* (1993) were the first to apply a field portable open-path spectrometer to volcanology, at the Japanese volcanoes Asama and Unzen.

I have used the instrument that was first used by Francis *et al.* (1996b) at Italian volcanoes. In this section, I describe the field instrumentation, introduce the general procedure for making field measurements, and present some sample spectra.

2.2.1 The MIDAC spectrometer: elements of the instrument and field kit

The infrared spectrometer used to collect all the data discussed in this thesis is a commercial instrument developed by the MIDAC Corporation. Figure 2-7 illustrates the main components of the kit.

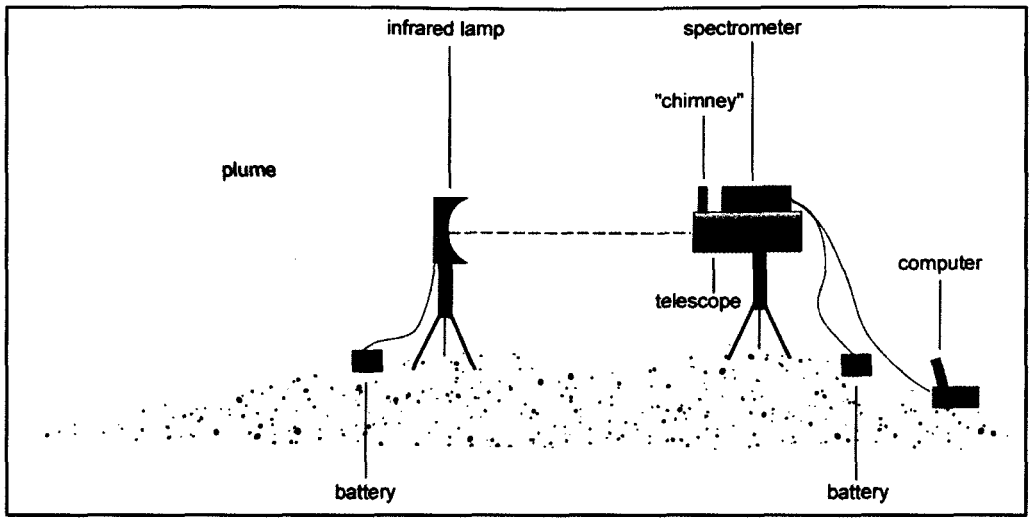

Figure 2-7: Illustration of a typical arrangement of the field instrumentation. The spectrometer and telescope are optically joined via the "chimney", which houses a set of 45° mirrors. The situation depicted here is in active mode, where an artificial energy source is placed behind the plume. The spectrometer and telescope combination can be tilted up or down on its tripod so that measurements may also be made in solar mode (with the sun as the source) or passive mode (with some terrestrial feature as the background energy source).

2.2.1.1 Infrared sources

Infrared absorption spectroscopy requires a source of incident infrared radiation from a body at higher temperature than the intervening gas sample. Aside from the portable artificial source depicted in figure 2-7, I have made use of the sun, and the hot volcanic vent as two alternative infrared energy sources in my fieldwork on Masaya. The main differences between these sources are their temperatures, and therefore the spectral energy distribution that they provide, and their path lengths, and therefore the amount of interfering absorption from atmospheric gases. The ideal source for measurement of gas absorptions must radiate at a temperature well above that of the gas and also provide energy distributed across the spectral range of interest.

MIDAC lamp: The artificial energy source is a 12 V silicon carbide glower operating at 1275 °C, at the focus of a 50 cm aluminium parabolic reflector. Since volcanic gas very quickly cools to ambient temperature on issue from a vent, the temperature differential between source and gas sample when the lamp is employed is easily sufficient, and the best quality absorption data that I have collected has been obtained using the lamp (active mode). The Planck curve for a black body radiating at 1275 °C is shown in figure 2-8: this source provides energy with good distribution across the spectral range of interest.

The lamp is designed to provide a collimated beam of radiation which can be collected by the telescope and passed through to the interferometer. Over distances of several hundred m (typical for Masaya field measurements), some background radiation also enters the telescope field of view, and, in practice, misaligned rays from both the lamp and the surroundings impair the

quality of the interferogram and hence the spectrum. In addition, repeated use of the lamp in harsh volcanic environments leads to degradation of the reflector surface by acid gases. However, the high quality of the data obtained from active measurements across the crater at Masaya affirms that sufficient high energy is reaching the spectrometer. The only noticeable effects in spectra may be a slightly reduced resolution, and a raised baseline at longer wavelengths due to emission from the atmosphere.

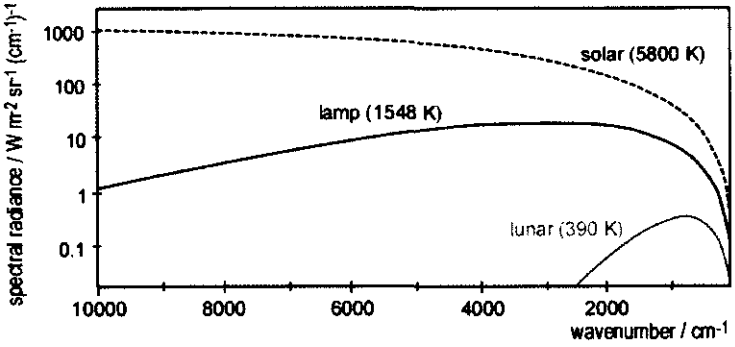

Figure 2-8: Blackbody spectral radiance emitted from sources radiating at different temperatures, calculated from the Planck function. Both the energy intensity and its spectral distribution vary with temperature.

Solar source: Depending on the viewing geometries available in the field, the solar disc (9.5 mrad FOV) can sometimes be used as an energy source for open-path FT spectroscopy (solar mode). Atmospheric scientists use the sun's radiation for almost all of their spectroscopic studies of the troposphere and stratosphere (e.g. Bell *et al.* 1998, Burton 1998, Mankin *et al.* 1992): the high temperature and intensity of the solar source allow measurements at very high spectral resolution well into the near infrared. For the purpose of volcanological application, solar radiation well surpasses the requirements of temperature differential and energy distribution for useful absorption measurements, but the long path length through the whole atmosphere has drawbacks.

Absorptions within the solar atmosphere (figure 2-9), along with those from gases present throughout the terrestrial atmosphere (notably H_2O and CO_2) result in many regions of the sample spectrum being severely contaminated or opaque. Visual inspection of raw spectra yields little qualitative information, but the solar absorptions and atmospheric contaminants can be modelled and accounted for within the retrieval procedure, so that good quality volcanic gas data are achievable. Solar radiation was frequently found to be too intense for the detectors, with signal saturation occurring if aluminium mesh attenuators were not used in front of the telescope. Adjustment of these attenuators allowed an optimum signal level to be achieved. Only if the sun was at a low angle and the volcanic gas optically thick was it possible to make measurements without the attenuators.

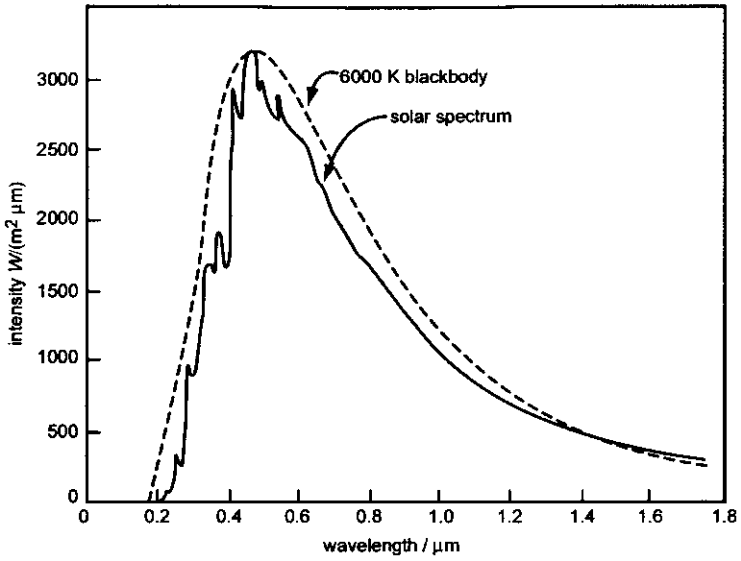

Figure 2-9: from Seinfeld (1986). The solar spectrum. Absorptions within the solar atmosphere itself result in deviations from a pure blackbody spectrum.

On rare occasions, thermal emission from the moon has been used in ground-based open-path FTS atmospheric measurements (Notholt 1994). This lunar source radiates at a maximum of 390 K in its centre during the full moon so that it's energy distribution is weak at higher frequencies compared with either the solar or artificial sources (figure 2-8). However, during one of the field campaigns at Masaya we were able to collect spectra successfully using the full moon as a source (Burton *et al.* 2001).

Passive terrestrial backgrounds: Theoretically, volcanoes should provide a range of hot terrestrial sources that could be utilised for FT spectroscopy, such as lava bodies, hot vents, or hot gases and erupted materials (passive mode). These kind of sources are the most difficult to characterise as their exact temperature is usually unknown, and they are likely to be transient. Mori *et al.* (1993) utilised energy from a hot lava dome at Mt Unzen as the source for their infrared measurements, and at Vulcano the hot fumarolic surface itself was employed (Mori *et al.* 1995). Oppenheimer *et al.* (1998b) used the hot lava dome at Montserrat. Terrestrial sources may radiate at almost any temperature up to about 1100 °C; for detection of IR absorptions at the shorter wavelengths (such as HCl at 3000 cm^{-1}) a source temperature of > 800 °C is preferable. For detection of absorptions at longer wavelengths (such as SO_2 at 1150 cm^{-1}), sun-heated wall rocks at little above ambient temperature may provide adequate energy (Oppenheimer *et al.* 1998a).

There are problems inherent in these passive terrestrial source measurements: if the temperature differential between source and gas is small or negligible, the gas may behave as an infrared emitter, rather than absorber. Complex situations may arise in which the path "sampled" by the spectrometer contains parcels of hot gases emitting IR radiation at their characteristic frequencies, then parcels of cooler gases absorbing radiation, and even parcels in which lighter

gas molecules are emitting while other heavier molecules are absorbing. Clearly the spectra arising from such a situation will be complicated and their analysis will require modelling of radiative transfer through multi-layer paths.

2.2.1.2 Spectrometer

The MIDAC spectrometer is normally used in conjunction with a 10-inch Newtonian telescope, to which it is optically joined by a system of mirrors located in the chimney. All mirrors in the telescope and interferometer are gold-coated. The telescope has a FOV of 3 mrad, compared to the 20 mrad FOV of the interferometer-detector combination, and so it collects incoming radiation and minimises the amount of off-axis energy reaching the optics. IR radiation entering the front ZnSe window of the spectrometer passes to a Michelson interferometer fitted with a ZnSe beamsplitter. A HeNe laser beam passing through the optics monitors the direction and velocity of the moving mirror. The recombined IR beam leaving the interferometer passes to a broad-band, liquid nitrogen cooled detector, which produces an electronic signal dependent on the intensity of the received radiation. One advantage of the MIDAC is its compact and compartmentalised arrangement: interchange from one detector module to the other is very straightforward and can be undertaken safely in the field. The spectrometer is capable of operating at nominal resolutions of 16 cm^{-1} up to 0.5 cm^{-1}, but I have only collected data using the highest resolution.

Parameter	**Value**
Highest nominal resolution	0.5 cm^{-1}
FOV of telescope	3 mrad
ZnSe windows and beamsplitter range	500–20000 cm^{-1}
FOV of spectrometer	20 mrad
MCT detector response	400–5000 cm^{-1}
Area of MCT element	0.01 cm^2
SNR for MCT detector	~7000
InSb detector response	1500–10000 cm^{-1}
Area of InSb element	0.00785 cm^2
SNR for InSb detector	~13000

Table 2-3: Some important instrumental parameters for the MIDAC spectrometer.

Two detectors with different response ranges (figure 2-10) were used for field measurements, a mercury-cadmium-telluride (MCT) operating in photoconductive mode, and an indium antimonide (InSb) in photovoltaic mode.

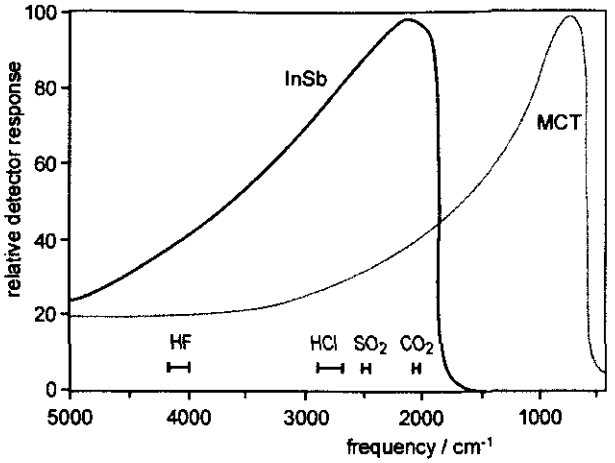

Figure 2-10: Comparison of the response ranges for the two detectors used in the spectrometer. The InSb is better over the region of interest for volcanic gases (2000–4200 cm^{-1}).

Ideally, the measured signal from a detector is linearly proportional to the incident flux of radiation. While this is true for InSb detectors, MCT detectors are widely known to show a non-linear response when illuminated (e.g. Abrams *et al.* 1994). Higher photon fluxes result in a recombination of charge carriers within the detector, and, regardless of illumination, series resistance can also cause the measurement to be nonlinear. This non-linearity is a problem in interferometric systems because of the large variation in photon flux experienced as the OPD goes through zero. It results in reduced spectral quality and zero-level offsets, causing systematic errors in retrieved concentrations of 3–4 % (Bell 2000). The problem is typically reduced by restricting the field of view, the aperture or the spectral range in order to restrict the incident photon flux, although these measures also result in reduced signal to noise. Because of non-linearities, measurements with the MCT are less reliable than those with the InSb.

The response of the MCT detector is minimal above 4000 cm^{-1}, resulting in very low signal-to-noise in the region of HF absorptions (4000-4200 cm^{-1}). The InSb has a higher signal to noise than the MCT, has none of the non-linearity problems, and has wavelength coverage sufficient to measure absorptions from the majority of volcanic gases. However, the SO_2 absorptions at 1150 and 1360 cm^{-1}, and the SiF_4 line at 1060 cm^{-1} are out of range for this detector. While SO_2 can be retrieved from an absorption at 2500 cm^{-1}, SiF_4 has no lines within the range of the InSb detector: this is unfortunate as SiF_4 detected at volcanoes may provide information on the vent temperature (Francis *et al.* 1996a). Measurements made using the MCT detector at Masaya afforded no evidence for the presence of detectable SiF_4 in the gas plume. For this reason, I have focused the analytical effort in this thesis on InSb data, which was also the most reliable in calibrated tests (section 2.4).

Each detector module includes its own pre-amplifier circuitry (figure 2-11). Since the amount of radiation incident on the detector varies depending on the source, the natural output signal also

varies. Movement of jumpers on a series of pins allows the pre-amp gain to be adjusted until an optimum electronic signal is output, regardless of the level of the input signal.

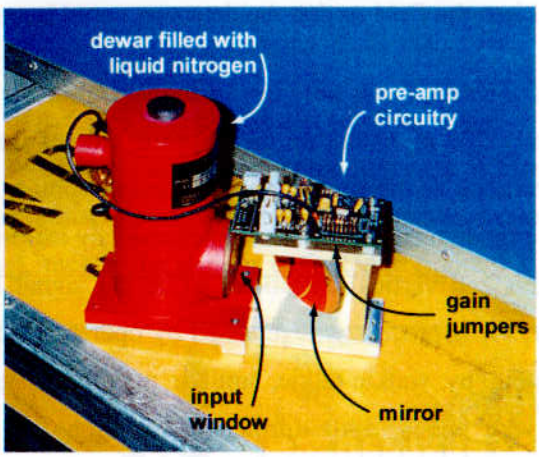

Figure 2-11: Photograph of a detector unit for the MIDAC spectrometer. The InSb and MCT detectors can be easily swapped in the field as each unit includes the relevant electronic circuitry for that detector.

2.2.1.3 Software

A laptop computer running commercially available Spectacle™ software (from LabControl GmbH, http://www.labcontrol.com/pro/work/specwin/winspec/index.html) was used to operate the spectrometer. Before measurements were collected, the alignment of source and spectrometer was optimised, and the signal level reaching the detector checked by a calibration of the interferogram. If needed, the signal level was varied by changing the resistance in the electronic pre-amplifier. A macro in the software allowed a given number of spectra to be collected automatically. A set of interferogram scans (usually 10) was coadded to improve signal to noise in the resultant interferogram. The software then automatically performed phase correction (which ensures that the zero path difference point of the interferogram is accurately located), and completed a fast Fourier transform, with selected apodization function. The data were saved on the computer's hard drive in .irs file format, which consists of one dimensional vectors with a 512 byte header containing the parameters and information required to display the spectrum, along with a descriptive text for that measurement. This whole process took between 30 s and 1 minute, before the next set of scans was collected. In this way, a set of 50 spectra was collected in under an hour. The saved spectra were processed through the retrieval algorithm at a later time.

2.2.2 Procedure in the field

The instrumentation is bulky (figure 2-7), and requires the use of a jeep or pick-up truck for transportation. Road (or air or boat) accessibility is a limitation on the use of FTS at volcanoes, although future development may result in decoupling the spectrometer from the telescope for some measurements, allowing much greater portability. Another portability issue concerns liquid nitrogen for the detectors. Once filled, the detector dewars have an estimated hold time of 12

hours. However, given the warm climate, and particularly during solar measurements when the dewars were tilted, the liquid nitrogen generally lasted for about half that time. A 1-litre flask of liquid nitrogen was carried into the field so that the detectors could be refilled.

At the summit of Masaya volcano, I was able to use the spectrometer for active measurements with the lamp approximately 500 m distant on the opposite side of the crater, and also in solar mode at the end of the afternoon as the sun dropped behind the plume. Alignment of the source and spectrometer for active mode measurements was achieved by making minimal movements of the tripod head in sideways and vertical directions while the signal level at the detector was monitored on the computer. This process was repeated by operators with both the lamp and the spectrometer, communicating by walkie-talkie, until a maximum signal level was obtained. Unless conditions were very windy, little further intervention for alignment was required, although if signal level in the displayed spectra suddenly dropped, alignment was one of the first things to be checked. Operation in solar mode required constant attention as the spectrometer followed the sun by manual tracking. In practice, this was achieved by watching an image of the solar disc on the inside telescope casing, and adjusting the tilt of the tripod to keep the image centred on the chimney aperture. Adjustments to the alignment were made during the phase correction and transformation process, rather than when the instrument was collecting scans. Further instrument development is underway to investigate coupling the spectrometer with a solar tracker, which would improve the accuracy of alignment with incoming solar radiation.

Once the spectrometer and source were aligned, the gain levels on the pre-amplifier were adjusted to provide optimum signal at the detector. The instrument was then ready to start data collection. A first trial spectrum was collected and inspected visually to ensure that transmittance levels appeared correct, that baselines in saturated regions were at zero, that there were no obvious spectral artefacts, and that there was some indication of absorptions from volcanic gas. The computer was set to collect a number of spectra (usually at least 50). The filename given to each spectrum followed an 8-digit pattern, indicating the IR source type, the detector in use, the date and the file number (e.g. ai233021.irs would specify spectrum number 021 collected on 23 March with the InSb detector and an active source).

Downwind, active measurements were made with the lamp and spectrometer a few hundred metres apart, but only very low quantities of gas were detected at ground level. Solar measurements were more successful downwind. Once the position of the plume overhead had been located, either visually or from the peak of COSPEC traverses made by colleagues (Delmelle *et al.* 1999a), the spectrometer was set up and tilted back manually until aligned with the sun. The spectrometer was able to function properly even at very high angles of tilt: the limit was set by the nitrogen-cooled detectors, which leaked liquid nitrogen at the greatest angles.

Solar mode measurements were successful as far away as the coastal roads at Masachapa, more than 30 km from the volcano.

2.2.3 Sample spectra

Depending on the choice of infrared source and detector, the shape of the resulting spectrum can vary. Figure 2-12 shows some raw measured spectra collected at Masaya Volcano. The spectra were analysed by retrieval in discrete microwindows, chosen to maximise the signal to noise for the gas under consideration, such as the regions indicated in figure 2-12(b) for HCl and SO_2.

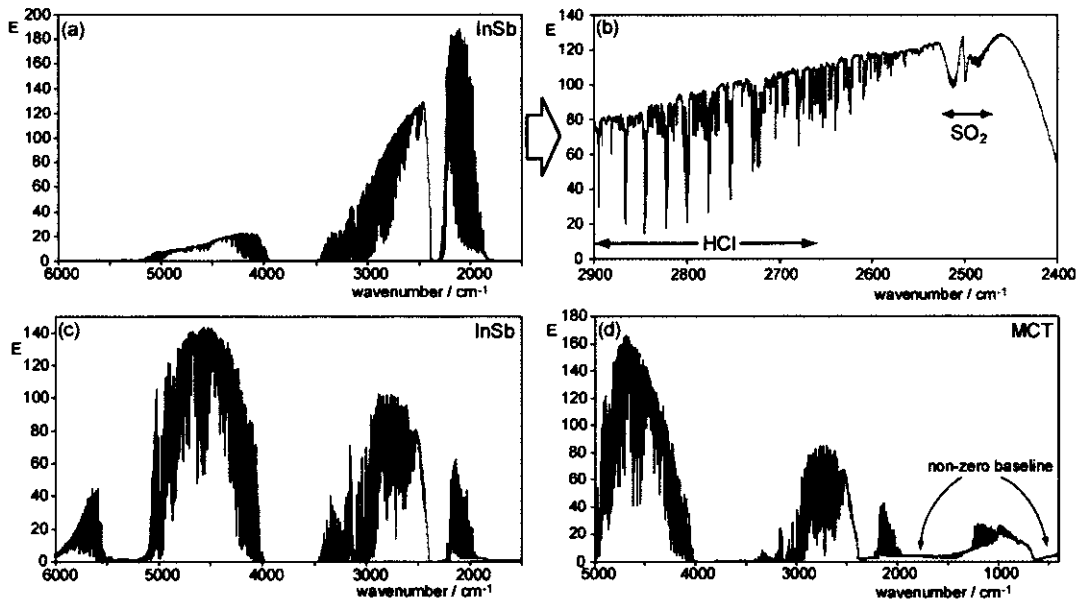

Figure 2-12: Raw measured spectra from Masaya volcano, with arbitrary units of energy intensity on the y-axes. (a) Lamp source (active) with InSb detector. Region containing retrieval microwindows for SO_2 and HCl is expanded into (b). When the solar source is used (c), the peak of the Planck curve (maximum energy intensity) has moved to higher frequencies. (d) Solar source with MCT detector. Note that the frequency range is different from (a) and (c), and erratic behaviour at low frequencies can be seen.

Problems of high photon fluxes affecting the behaviour of the MCT detector can be seen in figure 2-12(d). At frequencies below 600 cm^{-1}, the recorded energy should lie at zero as this is outside the response range of the MCT detector, whereas the measured spectrum shows a non-zero baseline. This can be corrected by attenuating the solar signal to reduce the number of photons reaching the chip. Problems of this kind can be minimised by careful operation of the spectrometer in the field. Saturation of the MCT detector chip in this way was not a problem for active measurements. With active MCT measurements, however, a different problem sometimes occurred. A non-zero baseline at low frequencies was observed, which resulted from the detection of background IR emission by the MCT. This baseline offset caused subsequent misanalysis of gas concentrations if it was unsubtracted prior to retrieval.

2.3 Spectral analysis procedure

Analysis of infrared spectra is a two-stage process consisting of data retrieval followed by interpretation. Section 2.1 showed how a measured spectrum is the result of absorption by gases coupled with instrumental effects. The retrieval problem is approached by constructing a forward model of an IR spectrum, and then tweaking it to achieve the best fit to the measurement. Data interpretation involves manipulating retrieved gas amounts into some understandable form.

2.3.1 Overview of data retrieval

Gas column amounts are retrieved by a forward model and optimal estimation procedure written in IDL, developed for this application by M. Burton (pers. com.). The methodology follows broadly that described by Burton (1998) for retrieval of stratospheric HCl and HF column amounts. This procedure is outlined in figure 2-13 and described in greater detail below.

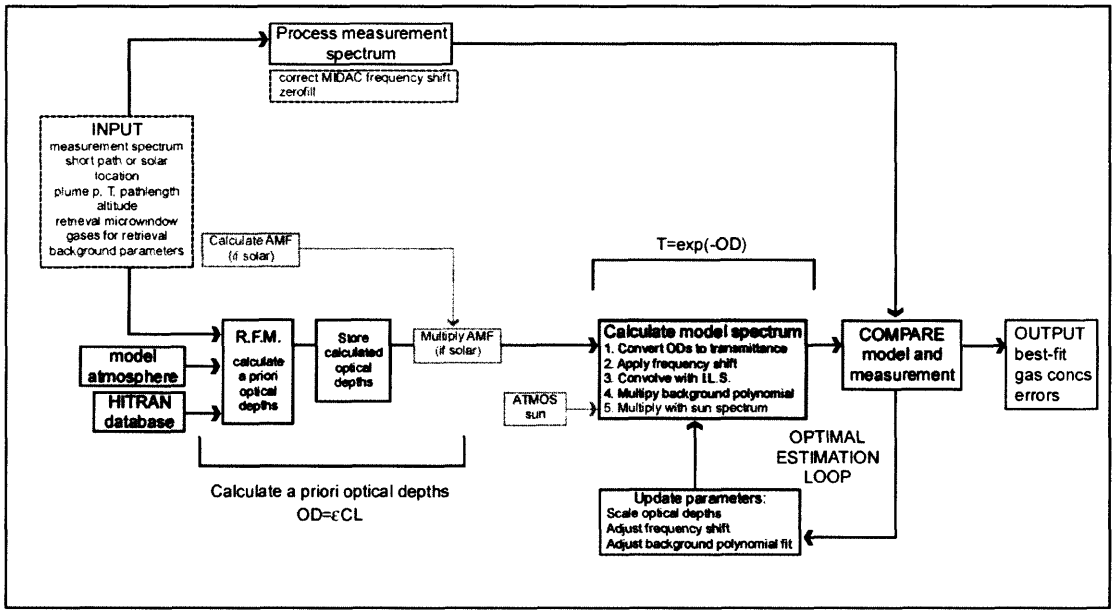

Figure 2-13: Flow chart outlining the main elements of the forward model and fitting procedure. The measurement spectrum is selected and choice of short-path or solar retrieval is made. *A priori* optical depths for the requested microwindow are calculated based on the input plume conditions and choice of model atmosphere, and using line parameters from HITRAN. For solar data, the *a priori* ODs are multiplied with the air mass factor appropriate for the measurement. The first forward model spectrum is calculated by converting the ODs to transmittance, applying a frequency shift, convolving with the ILS, multiplying with a background curve and, if solar data, with the correct portion of the sun spectrum. The forward model is compared with the measurement spectrum in the requested microwindow. The *a priori* ODs are then scaled, and the frequency shift and background curve adjusted slightly. A new forward model is calculated from the updated parameters and compared with the measurement. If the new forward model is a better fit, then the previous one is discarded, the new one held, and a second iteration of the loop proceeds. If the new one is worse than the previous, then it is discarded, the *a priori* model retained and the second iteration proceeds. Once the fit of model to measurement reaches a previously defined criterion, the retrieved parameters are output, and the ODs used in the best-fit are converted back to a *CL* product.

In brief, an infrared spectrum is simulated, in specified frequency microwindows, via a Fortran executable radiative transfer forward model using data from the HITRAN96 molecular spectroscopic database (Rothman *et al.* 1998), and, when appropriate, FASCODE-based model atmospheric profiles and a pure exoatmospheric sun spectrum (Abrams *et al.* 1996). The simulated spectrum is constrained by *a priori* values for volcanic and atmospheric gas concentrations: these are then allowed to vary through an optimal estimation algorithm (Rodgers 1976) and enhanced fitting procedure (Marquardt 1963) in order to generate the best fit to the measured sample spectrum. Convergence is attained when further iterations of the variable parameters produce no further improvement in the calculated cost function (i.e. goodness of fit) between model and measured spectrum. The gas amounts utilised in the best-fit spectrum, along with associated measurement errors pertaining to each retrieved gas, are recorded. Examples of fitted spectra are included in section 2.3.3.

The basis for any quantitative absorption spectroscopy, and therefore for the forward calculation of a model spectrum, is the Beer-Lambert law (equation (2-1)):

$$\frac{I}{I_o} = \exp(-\varepsilon \mathrm{CL}) \qquad (2\text{-}26)$$

The product εCL is also known as the optical depth (OD). A raw spectrum is a plot of I against ν. Thus there are several stages in the calculation of a forward model spectrum. I_o is modelled as a polynomial fit to the background curve in order to leave a flat 100% transmittance baseline. This background polynomial incorporates the effects of detector response and atmospheric attenuation leaving only the absorption lines. An array of optical depths is then calculated over the requested wavenumber range, and converted to transmittance.

There are some differences in approach for the analysis of solar data and active data, the most obvious of which is the different model of atmospheric path required in the two situations. For an active spectrum, a horizontal path is modelled at a single pressure and temperature, with uniform concentration of volcanic and atmospheric gases dispersed along it. For a solar spectrum, the IR transmittance throughout the whole atmosphere plus volcanic plume must also be modelled. In this case, the optical path is modelled in two stages: a 50 layer model atmosphere, defined by FASCODE pressure, temperature and concentration profiles (Clough *et al.* 1985), followed by a single pressure and temperature homogeneous volcanic plume layer. In both cases, optical depths for the relevant path profile are generated via the RFM, which was developed specifically for the purpose of vertical atmospheric measurements.

The retrieval returns a number which is a concentration-pathlength product, in molecules per cm^2 (molec cm^{-2}), responsible for the modelled absorptions. This can be understood with reference to the equation (2-26): ε is obtained from the spectral database, and the value of CL in the best-fit

model spectrum is returned. If plume dimensions are known (i.e. the plume-pathlength in the case of an active measurement), then this number can be converted to a gas concentration *sensu stricto*.

2.3.2 Input information and retrieval options

The retrieval is controlled by a single driver file, which contains input information and the user's decisions regarding the exact way that the retrieval should operate (Table 2-4). Pressure and temperature estimates for the volcanic plume are needed, as is a definition of the microwindow in which the spectrum will be retrieved. For active spectra (i.e. short path retrieval), an estimate of the pathlength constrains *a priori* volcanic gas concentrations. For the solar retrieval, the location of the measurement defines latitude and longitude, and hence, using time information from the data file itself, the air mass factor (AMF, i.e. $\sec\theta$, where θ is the angle of the sun above the horizon) for the measurement. The location also constrains the *a priori* gas concentrations to appropriate values. The gases required in the retrieval must be defined, some of which (usually atmospheric constituents like H_2O, CO_2 and CH_4) can be tied to values that were previously retrieved from a different region of the spectrum, while only those of particular interest in the current window are allowed to vary. Finally, a polynomial fit to the background detector response curve within the retrieval microwindow is needed: the number of parameters for this fit must be defined. Too few, and the background will be inadequately fitted, too many, and there is a risk that true absorptions may be fitted as part of the background. In practice, a polynomial of order between 3 and 5 was usually adequate.

Input parameter	Requirement
Location (for latitude and longitude), or choose short path retrieval	Always
Define which model atmosphere to use (held in file)	Solar only
Estimated Plume Pressure (mb)	Always
Estimated Plume Temperature (K)	Always
Estimated Plume Path Length (km)	Active only
Estimated Plume Altitude (km)	Solar only
Observer Altitude (km)	Solar only
Start wavenumber for retrieval microwindow	Always
Stop wavenumber for retrieval microwindow	Always
No. of parameters for background polynomial fit	Always
No. of gases for retrieval	Always
List of gas names for retrieval	Always
Number of gases to be constrained to *a priori* values	Always
List of gases to be constrained to *a priori* values	Always
Number of gases to be obtained from previously retrieved vmr file	Always
List of gases to be obtained from previously retrieved vmr file	Always
Flag for any output or input of retrieved VMRs	Always
Filename for output or input of retrieved VMRs	Always

Table 2-4: Input parameters needed to constrain the retrieval.

2.3.3 Sub-components of the retrieval scheme

2.3.3.1 HITRAN database

HITRAN (**HI**gh-resolution **TRAN**smission) is a line-by line compilation of spectroscopic parameters, widely recognised as an international standard. Since its first publication in 1973, it has undergone occasional updates to include new and improved data: the most recent edition, which is the one employed in the retrieval, was published in 1996 (Rothman *et al.* 1998). HITRAN was designed for accurate modelling of transmission and radiance from the microwave through ultraviolet spectral regions, with application to simulation and analysis of spectral observations in the terrestrial atmosphere as its primary motive. The database contains line positions and intensities, line-broadening parameters and pressure and temperature dependencies for vibrational and rotational energy transitions for 37 different molecules (including H_2O, CO_2, SO_2, HCl and HF). The data are a combination of high-resolution laboratory measurements and theoretical calculations, standardised to room temperature. Appropriate computer programming (such as the RFM employed in the retrieval) can select spectral parameters from HITRAN and calculate the energy transmittance expected at given temperatures and pressures for a given concentration of a particular species.

The HITRAN database has not yet reached its final and completed form. Much of the data are constantly being checked, revised and updated as higher resolution instruments are used for repeat measurements. The uncertainties on HITRAN line parameters are highly variable, and sometimes undefined (as in the case of SO_2 at the present time). For example, line intensities for the 2500 cm^{-1} SO_2 band included in the 1996 version are 36 % higher than those in HITRAN92 (Perrin *et al.* 1998). Line parameters for the HCl and HF transitions used in this thesis have not been modified since the previous version of HITRAN (Rothman *et al.* 1998) and have been quoted elsewhere with an accuracy of ±2 % (Paton Walsh *et al.* 1997). Because the data for line positions and intensities come from laboratory experiment, rather than a purely theoretical derivation, there is scope for continuing refinement as measurement technologies improve. However, HITRAN is currently the best available database for spectral transmission calculations, and is widely used. For the purpose of retrieving gas concentrations from our relatively low-resolution volcanic-gas spectra it is perfectly acceptable, as the analysis in section 2.4 and Chapter 3 demonstrates. An alternative spectral database covering a limited number of gases has been developed by NIST (http://www.nist.gov). In tests at the National Physical Laboratory, the NIST data for SO_2 appear more accurate than the HITRAN (section 2.4).

2.3.3.2 ATMOS solar spectrum

The infrared energy from the sun approximates closely to a blackbody radiating at about 6000 K, but it also includes solar absorptions as a result of the path through the solar atmosphere (figure 2-9). The ATMOS experiments, run by NASA's Jet Propulsion Laboratory, employed a high

resolution FT infrared spectrometer on board the Space Shuttle to collect solar occultation spectra of the Earth's atmosphere from space. In addition to the grazing atmospheric measurements, the experiment also produced many exoatmospheric near Sun centre absorption spectra that were averaged and used as backgrounds in the analysis of the terrestrial atmosphere measurements. The averaged high quality pure Sun spectra are available over the WWW (http://remus.jpl.nasa.gov) for public use in IR spectral analysis. The sun spectral data used in the current retrieval scheme are a composite of three spectra from three filter regions, covering most of the mid-infrared, which were collected during the November 1994 ATLAS-3 mission (Abrams *et al.* 1996).

The sun spectrum required some pre-processing before incorporation into the forward model (M. Burton, pers. com.). Since optical filters were used during the collection of the original data, the raw data have subsequently been high-pass filtered to remove the resulting low frequency structure. Additionally, the resolution of the instrument used in the ATMOS experiments was 0.01 cm^{-1} as compared to the 0.5 cm^{-1} resolution of the MIDAC; so the spectrum is convolved with the ILS suitable for our spectrometer.

2.3.3.3 RFM

The first stage in the simulation of the forward model spectrum (i.e. the calculation of optical depth) is carried out by the Reference Forward Model (RFM, version 4.0) which was developed by the Atmospheric, Oceanic and Planetary Physics group in the Department of Physics at Oxford University. This is a GENLN2-based (Edwards 1992) line-by-line radiative transfer model. A full description and downloadable algorithm is available on the WWW (http://www.atm.ox.ac.uk/RFM), along with a user's manual (Dudhia 2000).

The RFM takes the selected model atmosphere profile (containing pressure, temperature and gas concentration information) together with the *a priori* plume profile (containing pressure, temperature and gas concentration information) and calculates a line by line array of optical depths for the selected gases over the chosen retrieval microwindow. The requisite spectral line parameters (i.e. ε, the absorption coefficient) for the calculation are selected from HITRAN. The Voigt line shape is used to account for the effects of both Lorentz and Doppler broadening (equations (4) to (7)) across the temperature and pressure range relevant for the measurement.

The resulting line by line array of *a priori* ODs is then stored. For solar retrievals, this array is multiplied by the appropriate AMF. There are several steps in the final calculation of the model spectrum. First of all, the ODs are converted to transmittance, which is the basic spectrum. A small frequency shift is then applied and the spectrum is convolved with the ILS, which has been previously calculated (see section 2.3.4 for details of this calculation) and stored in a separate file. The result is multiplied with an order-n polynomial to fit the background response curve in

the microwindow. For a solar retrieval, the spectrum is finally multiplied with the relevant portion of the ATMOS sun spectrum. Thus the first forward model spectrum has been derived and the retrieval proper (i.e. the fitting procedure) can begin.

2.3.3.4 Fitting procedure

Once a forward model of the spectrum has been generated, an optimal estimation non-linear least squares algorithm is used to find the best fit to the measurement spectrum. Optimal estimation allows for the best fit within measurement error to be obtained. The method employed here was developed by M. Burton (pers. com.) and follows the Rodgers algorithm (Rodgers 1976) with Marquardt enhancement which caters for changes in step size in the iteration when nearing convergence. A mathematical description of the retrieval theory is presented in Burton (1998\ chapter 5), and will not be repeated here. The forward model and measurement spectra are compared, and a cost function, related to the goodness of fit between them is calculated. (The minimum of this cost function must be found for the best solution.) A weighting function is then constructed in order to achieve a small step away from the *a priori* solution: the weighting function scales the *a priori* gas optical depths, frequency shift and background response curve for the next iteration of the model spectrum. The cost function is recalculated for the new forward model: if it has reduced, this trial solution is accepted, the step size is decreased and the iteration is repeated. If the cost function increases, the trial solution is rejected, and a larger step size is used. Iteration continues until convergence is attained, or the maximum number of loops has occurred.

Elements other than the gas amounts can be varied in the retrieval solution matrix. Importantly, a frequency shift is fitted. This frequency shift is a common feature of FT measured spectra and generally arises as the result of beam divergence (i.e. FOV) within the spectrometer (Griffiths 1975). If needed, plume temperature can be estimated, providing that the ILS is accurately known.

One important advantage of this estimation procedure is that relative errors for each of the fitted components can be output along with the retrieved quantities. A solution covariance matrix is calculated for the retrieval algorithm results, and it is the diagonal elements of this matrix which represent the variance of each retrieved parameter. The measurement error required to derive the covariance matrix is defined as the standard deviation of the residual, which is the forward model minus the measurement. The calculated variances therefore include contributions from forward model error (chiefly from the choice of ILS), noise in the measurement, the information content of the measurement for each parameter, and the degrees of freedom. Information content depends upon the choice of microwindow (for signal and number of available spectral points), and the degrees of freedom are reduced as the number of parameters for retrieval increases.

Retrieved errors are minima. The calculation implicitly assumes that line parameters and the forward model calculation are free of error, that the instrument is linear and there are no offsets from the zero intensity level, that the retrieval microwindow has no effect on the results, and that there is no crosstalk between a gas and any other factor in the spectrum. These assumptions are, to a greater or lesser degree, untrue. The retrieved errors can provide a first estimate of the uncertainty associated with the retrieved amounts, but further information derived from full sensitivity analyses and extra laboratory measurements is needed to constrain the error contribution from other sources. Section 2.4 is a calibration of the instrument and retrieval using laboratory measurements. Chapter 3 includes an analysis of the errors associated with retrieval of Masaya field spectra.

2.3.4 General procedure

Over the course of two field campaigns at Masaya, more than 6000 raw IR spectra were collected. Because of this large amount of data, I had to use a systematic method of retrieving gas amounts from bulk sets of spectra, which could reflect widely varying concentrations. This general procedure is outlined below; when odd or interesting features were revealed in the retrieved data, I checked the retrieval on smaller numbers of spectra under closer inspection. Chapter 3 is a detailed examination of practical retrieval issues relating specifically to the Masaya data.

2.3.4.1 Confirming the correct ILS

The instrument line shape (ILS) imposed onto each absorption is dependent upon the maximum optical path difference of the spectrometer, the effective field of view, and the chosen apodization function. If any of these factors change, then the definition of the ILS used in the forward model must also be changed in order for correct fitting and retrieval. Many circumstances can be envisaged under which the ILS of the MIDAC spectrometer could be affected: violent movements during transport, regular interchanging of the detectors, removal and reattachment of the spectrometer unit from the telescope, removal and reattachment of the "chimney", or subjection to acidic volcanic gases could all result in gradual misalignments within the instrument, or degradation of the mirror surfaces. Misalignments or degradation of the quality of the source radiation generally cause an increase in the effective FOV, with the end result of a broadening of the ILS. Section 2.4 includes a calibration of the ILS as it was in March 2000.

As the first stage in data analysis, it was important to check that the model ILS provided a good fit. Each model ILS was created via a short executable programme, given a choice of apodization function (always triangular in this thesis), a maximum optical path difference and a field of view constraint. The programme takes the Fourier transform of an array of spectrum points, truncates the transform (i.e. effectively an interferogram) according to the instrument resolution (OPD),

and then applies an apodization function (c.f. equation (2-18)). A correction for the broadening resulting from a finite field of view is made; an inverse Fourier transform is applied to return the array to the spectral domain, and, finally, a file containing the ILS line parameters is output.

This calculated ILS function is convolved with the calculated transmittances to create the forward model spectrum. In order to check whether the calculated ILS provided a good fit, the retrieval was performed on a few spectra over 2699-2705 cm^{-1}, a window containing weak H_2O and HCl lines, to compare the shape of the peaks in the model and measured spectra. If the fit was unsatisfactory, a different ILS (calculated with a different FOV) was tried, until the best match to the peaks was achieved. Large datasets could then be analysed systematically using the newly defined ILS, but a careful check on the performance of the retrieval was maintained, to watch for further deviations in ILS.

2.3.4.2 Retrieval parameters

The effect that variations in the choice of microwindow and background polynomial fit can have on retrieved amounts from the Masaya data is covered in Chapter 3. Microwindows were chosen to contain one or more prominent transitions of the target species, while the signal of interfering species was kept to a minimum. Table 2-5 summarises the usual choice of parameters for retrievals from MIDAC spectra.

	Molecule	Microwindow (cm^{-1})	Background polynomial	Gases retrieved	Constraints
active	HCl	2690–2900	3	HCl, H_2O, CH_4	Output H_2O
	SO_2	2480–2520	4	SO_2, H_2O, CO_2	H_2O to previous retrieved
	HF	4000–4180	4	HF, H_2O	None
	CO_2	2075–2080	3	CO_2, H_2O	None
solar	HCl	2690–2900	3	HCl, H_2O, CH_4, N_2O	Output H_2O
	SO_2	2480–2520	4	SO_2, H_2O, CO_2, CH_4, N_2O	H_2O to previous retrieved, CO_2 to global average
	HF	4030–4180	4	HF, H_2O, CH_4	None

Table 2-5: Parameters used for the retrieval of gas amounts from MIDAC spectra.

HCl was retrieved from the P-branch of its fundamental ro-vibrational absorption in a microwindow from 2690-2900 cm^{-1}: this window contains eight doublets (for the two natural Cl isotopes) of varying strength, essential for systematic bulk analysis of spectra that could reflect widely different gas concentrations. For the highest concentrations of HCl, all except the weakest lines at the long wavelength end of the window are saturated, but with an accurate choice of ILS, these saturated lines should be correctly fitted. Atmospheric gases H_2O, CH_4 and N_2O have significant absorptions in this window; so these are fitted simultaneously with HCl. An order 3 polynomial is used to fit the background response curve. A typical short path retrieval of HCl is shown in figure 2-14(a).

A window centred on the combination $\nu_1+\nu_3$ band at 2500 cm^{-1} was chosen for the SO_2 retrieval. Although it is weaker than the SO_2 bands at 1150 and 1360 cm^{-1} (ν_1 and ν_3, respectively), the 2500 cm^{-1} line is the only one within the spectral range for the InSb. This band lies in a region that is relatively free from atmospheric contamination (unlike that at 1360 cm^{-1}). In data collected with the MCT detector, there was often a discrepancy in retrieved SO_2 concentrations from the 2500 cm^{-1} band and the 1150 cm^{-1} (e.g. section 2.4). This has been attributed to problems of background emission at longer wavelengths, which results in underestimates of the gas amount retrieved from the band at 1150 cm^{-1}.

The microwindow from 2480–2520 cm^{-1} includes the line centre and part of the wings providing variation in line strength (figure 2-14(b)). Atmospheric gases H_2O, CO_2, CH_4, and N_2O have significant absorptions in this window, and H_2O was constrained to the amount retrieved in the HCl microwindow. For solar retrievals, CO_2 was fixed to an *a priori* value determined by the air mass factor of the spectrum and the choice of model atmosphere, assuming a global CO_2 concentration of 364 ppm. An order 4 polynomial was used to fit the background response curve.

HF fundamental absorption lines occur above 4000 cm^{-1} in a region strongly affected by atmospheric absorptions. A window between 4000 and 4180 cm^{-1} containing 6 HF lines was used for short path retrievals (figure 2-14(c)), but in solar spectra atmospheric absorptions saturated the region up to approximately 4030 cm^{-1}, and so the microwindow for solar retrievals was truncated. H_2O and CH_4 were fitted simultaneously and an order 4 polynomial was used to fit the background response curve.

Volcanic contributions to CO_2 and H_2O concentrations may be inferred from short path measurements (see below). H_2O amounts are retrieved accurately from unsaturated lines in the HCl microwindow. CO_2 was retrieved from the weak line centred on 2077 cm^{-1}, in a small microwindow from 2075-2080 cm^{-1} (figure 2-14(d)). This window was chosen because it contained the maximum variation in CO_2 signal, and returned the smallest retrieved errors and most accurate amounts (compared to global atmospheric average) in tests of a range of microwindows. H_2O was fitted simultaneously, and an order 3 polynomial was used to fit the background.

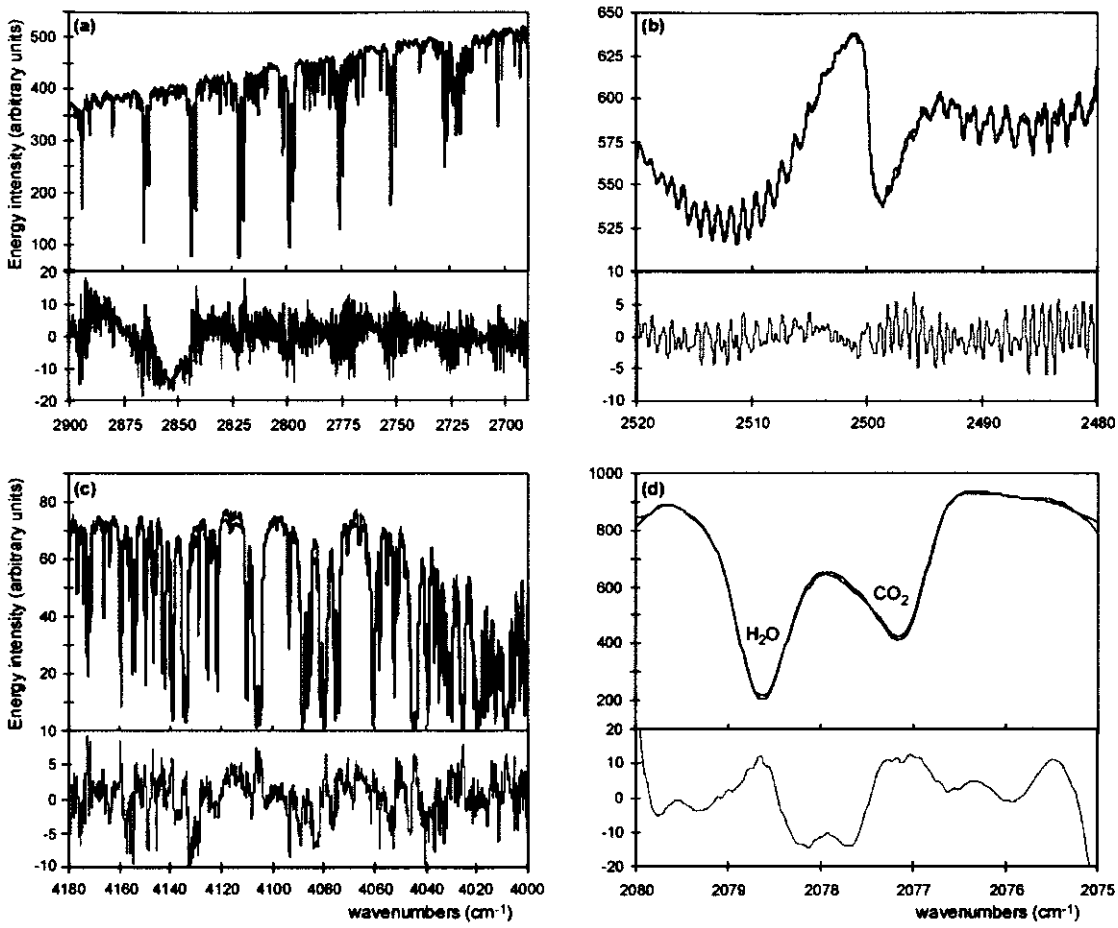

Figure 2-14: Typical retrieval microwindows from a short path measurement collected on 24 February 1998 at Masaya Volcano. Note the different scales in each. Figure shows measurement (red line), fit (black line) and residual (lower windows). (a) Eight striking HCl doublets are obvious in this window; other lines are H_2O and CH_4. (b) The SO_2 $\nu_1+\nu_3$ combination band shows a typical PQR contour. (c) Individual HF lines are impossible to make out due to the extreme H_2O contamination in this window. (d) The weak CO_2 line centred at 2077 cm^{-1} lies on the edge of a H_2O line at this resolution.

2.3.5 Data interpretation

The absolute column amounts of gas retrieved from each individual spectrum are not, alone, very informative. Large variations in absolute amount from one spectrum to the next can occur as a consequence of the wind blowing the plume around, or discontinuous puffing from the crater. Of much more use are gas concentration ratios, which can be derived from an individual spectrum or from a set of spectra. Retrieved amounts for target species are plotted against each other (e.g. HCl versus SO_2): each data point represents one spectrum. The average concentration ratio for the dataset is calculated from the gradient of the regression line through the points. Figure 2-15 illustrates this simple data treatment.

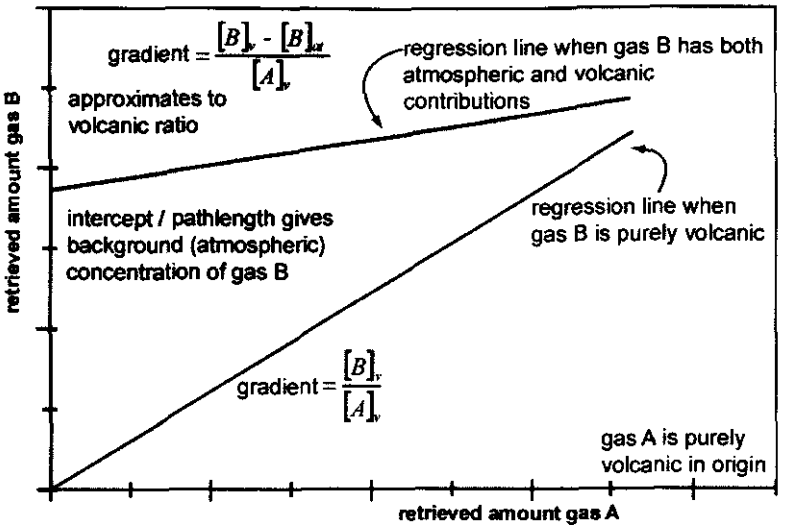

Figure 2-15: Illustration of the information obtained from scatter plots of retrieved gas amounts from a set of spectra. For a pair of gases which are both purely volcanic in origin, the regression line trends through the origin and its gradient gives the volcanic molar concentration ratio. If one of the gases is present in both the atmosphere and the volcanic gas, the regression line is actually a mixing line whose gradient approximates to the volcanic gas ratio (see text for explanation). The intercept is a measure of the background ambient (non-volcanic) contribution of that gas.

When pure volcanic gases (i.e. SO_2, HCl, HF) are plotted against each other, the regression line should trend through the origin. If gases also present in the atmosphere (i.e. CO_2, H_2O) are plotted against a pure volcanic component, then the regression line does not go through the origin, and the intercept represents the background atmospheric concentration of the gas. In this case, the regression line is a mixing curve between the concentrations in pure volcanic gas and the atmosphere. The ratio of the two components in pure volcanic gas is approximated by the gradient of the regression line if concentrations in pure volcanic gas are considerably higher than in the atmosphere.

For a pair of plume components, A and B, where A is a species present only in the volcanic gas, and B is a species present in both volcanic gas and the atmosphere, consider measurements of column amounts of the gases across an optical path, length l. Let the measured amount of A be a molec cm^{-2}, and the measured amount of B be b molec cm^{-2}. Let molecules of volcanic gas occupy a fraction, x, of the path length. Then:

$$a = xl[A]_v \tag{2-27}$$

$$b = xl[B]_v + l(1-x)[B]_{at} \tag{2-28}$$

where square brackets indicate concentration and the subscripts v and at represent volcanic gas and ambient atmosphere, respectively.

Rearranging equation (2-27) to substitute for x in equation (2-28) gives:

$$b = a\frac{[B]_v}{[A]_v} + l[B]_{at} - a\frac{[B]_{at}}{[A]_v}$$

which simplifies to:

$$b = a\frac{([B]_v - [B]_{at})}{[A]_v} + l[B]_{at} \qquad (2\text{-}29)$$

Equation (2-29) defines the mixing curve on a plot of b against a, and is of the form $y = mx + c$. So the intercept on the b axis is the background atmospheric concentration of B multiplied by the optical pathlength of the measurement. The gradient, m, of the regression line on a graph of b against a is a constant, which depends upon the relative concentrations of the species A and B in the volcanic gas and the atmosphere:

$$m = \frac{[B]_v - [B]_{at}}{[A]_v} \qquad (2\text{-}30)$$

If the concentration of B in the atmosphere is very much smaller than the concentration of B in pure volcanic gas, then the gradient of the regression line approximates to $[B]_v/[A]_v$ the ratio of these species in the volcanic gas. For CO_2, its concentration in the atmosphere is an average of 365 ppm, whereas its concentration in gas emitted from volcanoes similar to Masaya is at least 1.5 %, and possibly about 2.4 % (Giggenbach 1996, Symonds *et al.* 1994). Since the atmospheric CO_2 concentration is almost two orders of magnitude smaller than its concentration in volcanic gas, the gradient of the regression line on plots of retrieved CO_2 against retrieved SO_2 approximates closely to the ratio of these components in pure volcanic gas.

In calculations of ratios from retrieved amounts, it is important to estimate the associated uncertainty. Errors calculated in the retrieval algorithm provide a minimum estimate of the uncertainty associated with the retrieved amounts, although they do not include allowance for uncertainty in temperature, pressure and line parameter data. For SO_2, HCl and HF, concentration ratios for each individual spectrum can be calculated. The retrieved errors, taken as minima, can be propagated through to give an error estimate on the calculated ratio. For a set of spectra, it is possible to derive a weighted mean for the ratio, along with its standard deviation, from the individual calculated ratios and their errors. In practice, this calculation was unnecessary during the analysis presented in this thesis, since there was no systematic relation between error and calculated ratio, and the weighted mean was very little different from an unweighted mean calculated for the same set of data. My preferred data treatment was with scatter plots and regression lines as these gave a visual indication of how the retrieval had performed for the two gases over the whole dataset.

Uncertainties arising from temperature and pressure estimates, and the line parameter data used in the retrieval, must be considered separately. These estimates result in a systematic error on the retrieved amounts, affecting all species in a similar way. For smaller subsets of spectra, error on calculated gas ratios is significantly less than the error on individual absolute gas amounts and so these uncertainties may be neglected in the assessment of short time-scale relative variations. A discussion of errors specific to the Masaya data is presented in Chapter 3.

Gas concentration ratios calculated from retrieved amounts are ratios of the number of gas molecules, i.e. they are molar ratios. In this thesis, all quoted gas ratios are molar, unless otherwise stated. Frequently, in the volcanology literature, gas compositions may be reported as ratios by mass. Care must be taken to make equivalent comparisons and conversions as necessary.

If SO_2 mass emission rates are known from alternative means, such as COSPEC, then concentration ratios with SO_2, converted to mass ratios, can be used to estimate gas emission rates for any of the other detected species. Where volcanic H_2O and CO_2 are measured, the gas analysis comes close to 100 % of the total sample by mass. In this case, there is enough information from the combination of OP-FTIR and COSPEC measurements to define a total volcanic gas composition and emission rate, to a good approximation.

For active measurements, where the path length is known, the retrieved column amounts can be converted to true absolute concentrations. However, these figures are minima as the volcanic plume always occupied less than about two-thirds of the entire pathlength, at Masaya.

2.4 Sensitivity analysis of Instrument and Retrieval

(This section has been submitted as a paper to the *Journal of Geophysical Research*)

Following two field seasons at Masaya Volcano (February-March 1998 and March 1999), I collected a set of spectra with the MIDAC under controlled conditions in order to assess the performance of the instrument and the retrieval. A detailed sensitivity analysis of the MIDAC had not been performed for the whole period that it has been in use for field measurements, since January 1996. I ran a series of measurements over two days in March 2000 at the National Physical Laboratory (NPL) using gravimetrically-prepared primary gas standard mixtures, to obtain calibrated IR spectra. Out of the three non-atmospheric gases relevant to Masaya (SO_2, HCl, HF), SO_2 is the least reactive and was chosen as the test gas, since it could be pumped into a static gas cell and left without problems of reaction or adsorption onto the cell walls. Calibrated tests with the hydrogen halides would require the gas mixture to be pumped continuously through a gas cell. In addition to an error budget analysis for SO_2 measurements, I also undertook tests to determine the instrument line shape (ILS) using a carbon monoxide gas standard, since in the field data some variability in ILS had been apparent.

2.4.1 Collection of calibrated data

The normal field kit was used at NPL: the only differences in arrangement between this and active measurements at Masaya were the much shorter pathlength and the containment of gas in a cell rather than free in the atmosphere. However, the usual difficulties of atmospheric contamination were present since the path included some distance through free air. The spectrometer-telescope combination was mounted on a tripod and fixed in line with a 25 cm diameter gas cell and the lamp (figure 2-16). The total path length from the telescope to the lamp was 2.10 m.

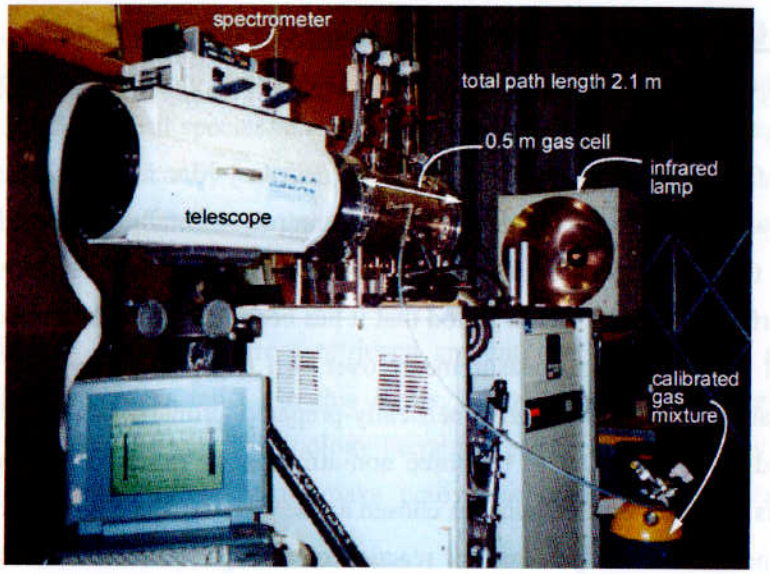

Figure 2-16: Arrangement of instrument and gas cell for measurements of calibrated gas mixtures at the National Physical Laboratory.

2.4.1.1 Specifications of the gas cell

The gas cell had a 0.5 m path length between ZnSe windows wedged at 0.5° to eliminate fringing effects. The window surfaces had no anti-reflective coating, reducing transmission despite the short path between instrument and lamp, so that the gain required to obtain sufficient signal at the detector was relatively high. A range of primary gas standards was available for the experiments (Table 2-6).

Species	**Nominal concentration (ppm)**	**Exact concentration (ppm)**	**Gas mixture**	**Cylinder number**
SO_2	250	248.108	SO_2/air	S 119
SO_2	2 500	2 405.46	SO_2/N_2	S 111
SO_2	10 000	10 002.957	SO_2/air	S 116
SO_2	20 000	21 738.14	SO_2/N_2	115875
CO	1 000	1 010.34	CO/N_2	NPL 723

Table 2-6: Details of the primary gas mixtures used for the tests; concentrations are in volumetric ppm.

For each set of measurements, the gas temperature was monitored by a probe (0.1 °C resolution) calibrated at NPL. However, because the probe was in direct contact with gas in the inflow pipe, not with the gas in the cell, it may have recorded temperatures up to 2 °C different from the cell gas temperature. During the course of the measurements, I checked the digital reading of pressure monitored on the gas cell against a calibrated pressure gauge. The results are shown in figure 2-17. The direct pressure measurements were then corrected by applying the equation of the best-fit curve, and corrected pressure readings are quoted in Table 2-7.

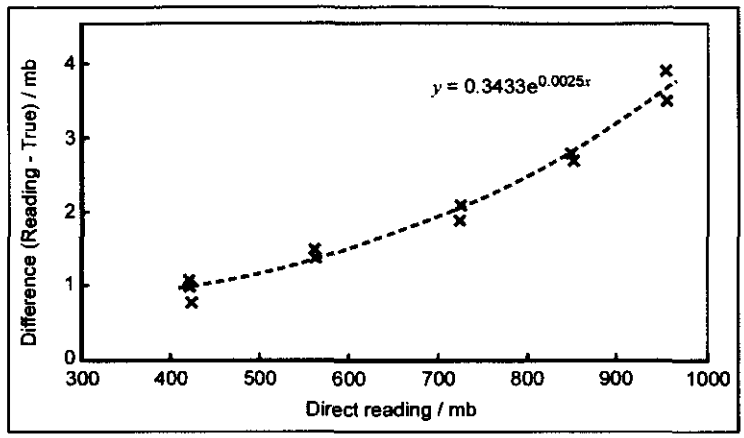

Figure 2-17: Calibration of the pressure monitor on the NPL gas cell. Direct readings were corrected using the equation of the best-fit curve through the calibration points.

2.4.1.2 Measurements

Table 2-7 contains details of the calibrated spectra collected. First of all, the gas cell was evacuated and allowed to stabilise, and some background spectra were collected. These spectra contain atmospheric absorptions (i.e. H_2O and CO_2) from the path through the air outside the cell, along with spectral features relating to the characteristics of the cell windows and the instrument itself.

For SO_2 measurements, the gas cell was filled to pressures just less than ambient with the calibrated SO_2 in air or N_2 mixture and allowed to stabilise, before pressure and temperature were recorded and 6 spectra collected. The detector was switched, and a further 6 spectra collected. The lowest concentration was used first, working up to the highest, to minimise contamination by SO_2 left over from previous runs.

For an empirical determination of the spectrometer's ILS, measurements of a carbon monoxide standard were made. The measured line shape of the CO lines is given by the convolution of the ILS with the true line shape of the CO lines. Because CO lines are relatively narrow (especially at low pressure) compared to the resolution of the spectrometer, the resulting line shape in the measured spectrum is almost entirely the function of convolution with the ILS. The gas cell was filled to a pressure just less than ambient with the primary gas mixture of CO/N_2, and 6 spectra were collected. Gas was then bled out of the cell in order to step down the pressure. When the pressure stabilised, further spectra were collected. The pressure was decreased over 4 or 5 steps in this way to a minimum of about 400 mb until no further narrowing of the CO lines was observed, as instrument broadening effects began to dominate over pressure-broadening. The gas cell was then re-evacuated, the detector changed, and the measurements repeated.

Set	Filenames[1]	Detector	Gas conc[2] (ppm)	Mean P[3] (mb)	Mean T[3] (K)	Gas conc[4] (molec cm^{-2})	Type
SO_2 calibration spectra (with telescope)							
1a	ai233001-005	InSb	-	2.65	289.7	0	b.g
1b	ai233006-010	InSb	-	0.86	289.7	0	b.g.
2	ai233011-020	InSb	248.108	964.19	290.8	2.97908×10^{17}	SO_2
3	am233001-008	MCT	248.108	964.73	292.9	2.95939×10^{17}	SO_2
4	am233009-013	MCT	-	0.86	293.6	0	b.g.
5	am233014-019	MCT	2405.46	972.66	293.3	2.88930×10^{18}	SO_2
6	ai233021-026	InSb	2405.46	972.46	293.2	2.88921×10^{18}	SO_2
7	ai233027-032	InSb	10002.957	968.55	293.5	1.19540×10^{19}	SO_2
8	am233020-025	MCT	10002.957	968.40	293.2	1.19665×10^{19}	SO_2
9	am233026-031	MCT	21738.14	963.30	293.5	2.58418×10^{19}	SO_2
10	ai233033-038	InSb	21738.14	962.80	292.9	2.58770×10^{19}	SO_2
CO spectra (with telescope) for ILS test							
11	ai243001-004	InSb	-	0.76	291.3	0	b.g.
12	ai243005-010	InSb	1010.34	970.72	292.2	1.21551×10^{18}	CO
13	ai243011-016	InSb	1010.34	904.18	292.5	1.13102×10^{18}	CO
14	ai243017-022	InSb	1010.34	755.92	293.4	9.42658×10^{17}	CO
15	ai243023-028	InSb	1010.34	645.37	293.7	8.04117×10^{17}	CO
16	ai243029-034	InSb	1010.34	517.34	293.6	6.44821×10^{17}	CO
17	ai243035-040	InSb	1010.34	400.96	292.4	5.01813×10^{17}	CO
18	am243001-004	MCT	-			0	b.g.
19	am243005-010	MCT	1010.34	949.13	294.4	1.17959×10^{18}	CO
20	am243011-016	MCT	1010.34	844.44	294.9	1.04770×10^{18}	CO
21	am243017-022	MCT	1010.34	718.82	295.0	8.91686×10^{17}	CO
22	am243023-028	MCT	1010.34	560.15	295.0	6.94745×10^{17}	CO
23	am243029-034	MCT	1010.34	418.92	295.2	5.19225×10^{17}	CO
Cell absent spectra (free atmosphere)							
24	am243035-037	MCT	-			0	atm
25	ai243041-043	InSb	-			0	atm
CO spectra (telescope absent) for ILS test							
26	ai243044-049	InSb	1010.34	420.57	296.2	5.19505×10^{17}	CO
27	am243038-043	MCT	1010.34	420.71	296.3	5.19602×10^{17}	CO

Table 2-7: Details of the spectra recorded during calibration experiments at NPL. Notes [1] Files are named sequentially in the last 3 characters, so set 1a consists of the 5 spectra numbered 001 to 005. [2] The true gas concentration in ppm is the NPL primary gas mixture. [3] Pressures and temperatures recorded here have been corrected according to their calibrations. [4] The true gas concentration in molec cm^{-2} is calculated from equation (24).

2.4.1.3 Calculation of "true" gas amounts in the cell:

Uncertainty in the calculation of the actual gas concentration in the cell arises from two principal sources. Firstly, because the thermometer probe was not in direct contact with the gas inside the cell, the temperature has ± 2 °C (i.e. ± 0.7 %) uncertainty on the measured value (T). Secondly, the cell and telescope were probably not perfectly aligned so that the path length (L) through the gas was greater than the nominal 0.5 m. The maximum increase in path length before

misalignment became visually obvious was 0.8 cm (a 10° misalignment from the centre line) or 1.6 %. The combination of these uncertainties resulted in the range of errors given in Table 2-8 for the calculated "true" gas amounts. Thus the nominal true gas concentrations were considered within the error bounds of +2.3 % and –0.7 %.

Cause of error	**Error in calculated concentration (%)**
T+0.7% and L	-0.7
T and L	0
T-0.7% and L	+0.7
T+0.7% and L+1.6%	+0.9
T and L+1.6%	+1.6
T-0.7% and L+1.6%	+2.3

Table 2-8: Error bounds in calculation of "true" gas amounts.

2.4.2 Results and data treatment

A series of retrievals of the measured spectra was performed. Firstly, the low-pressure CO spectra were used to define the ILS for both the InSb and MCT detectors. Although this step allowed the subsequent sensitivity analysis for SO_2 retrieval to be conducted, the ILS appropriate now is unlikely to be exactly the same as that appropriate for analysis of Masaya field data. Secondly, SO_2 spectra collected with the InSb detector were retrieved with systematic alterations to the input parameters for a thorough error analysis. InSb data are the focus of this investigation because I have used them more extensively in this thesis than MCT data. Reasons for the preference for InSb have already been outlined: it doesn't suffer from non-linearities in detector response, and has a greater sensitivity than the MCT. Thirdly, low concentration SO_2 spectra were used to estimate detection limits in this test situation. Fourthly, I have made a quantitative comparison of retrievals of SO_2 amounts from the different SO_2 absorption bands: at 2500 cm^{-1} (comparing InSb and MCT detectors), and at 1360 and 1150 cm^{-1} (MCT only). Finally, the results of these controlled tests are discussed in the context of application to real field data.

2.4.2.1 Instrument Line Shape tests

The MIDAC spectrometer has a nominal resolution of 0.5 cm^{-1}. However in field spectra collected in 1999 and more recently, the resolution appeared worse: the ILS, which is convolved with the real spectrum, had changed. The low pressure CO spectra were used for empirical determination of the current ILS.

The CO band at 2000–2250 cm^{-1} is a wide feature consisting of many very narrow lines (figure 2-18). Measurement of the spectrum at low pressure resolves a line shape which is the result of a very narrow line convolved with the ILS of the spectrometer. A good fit to the measured spectral line can only be achieved if the correct ILS is used in the retrieval.

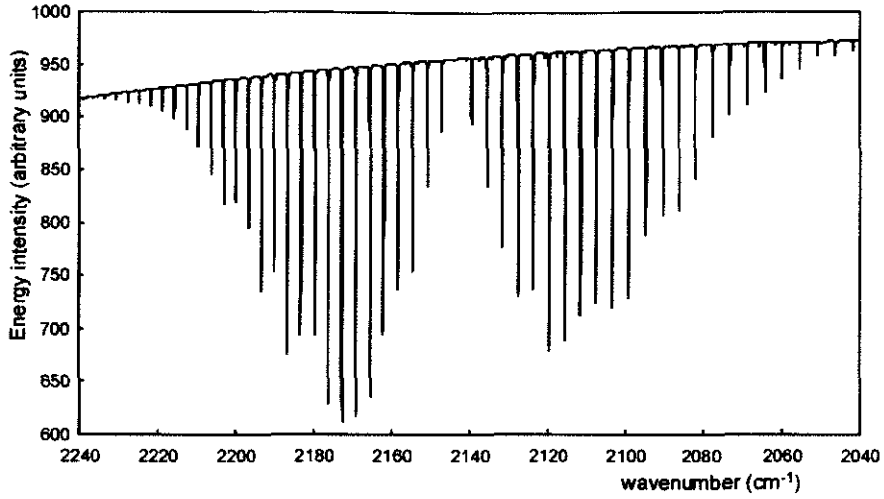

Figure 2-18: A spectrum of carbon monoxide with a single line at 2082 cm^{-1} highlighted.

Figure 2-19 shows the CO line at 2082 cm^{-1} measured by InSb and MCT detectors, when the gas was at pressures of 401 and 419 mb, respectively, together with fitted spectra for the same pressure. For each retrieval, all parameters were kept the same except for the input ILS, which was recalculated each time, using a triangular apodization function for a specified maximum OPD and FOV constraint centred at 2900 cm^{-1}, as described in section 2.3.4. The nominal values specified by MIDAC are 1.9 cm maximum OPD and 20 mrad FOV for the spectrometer. Most of the variation in ILS is attributed to changes in the effective FOV. These can arise if any of the mirrors involved in collecting and focusing the radiation on the detector is misaligned, or if the source radiation includes off-axis rays. Since the detectors are frequently switched, the spectrometer unit is sometimes separated from the telescope, and the "chimney" has also been removed on several occasions, it is possible that the optical path is no longer in perfect alignment. Additionally, the surface of the parabolic mirror in the lamp has been degraded by exposure to acid volcanic gas and windblown dust, so that the source collimation has deteriorated.

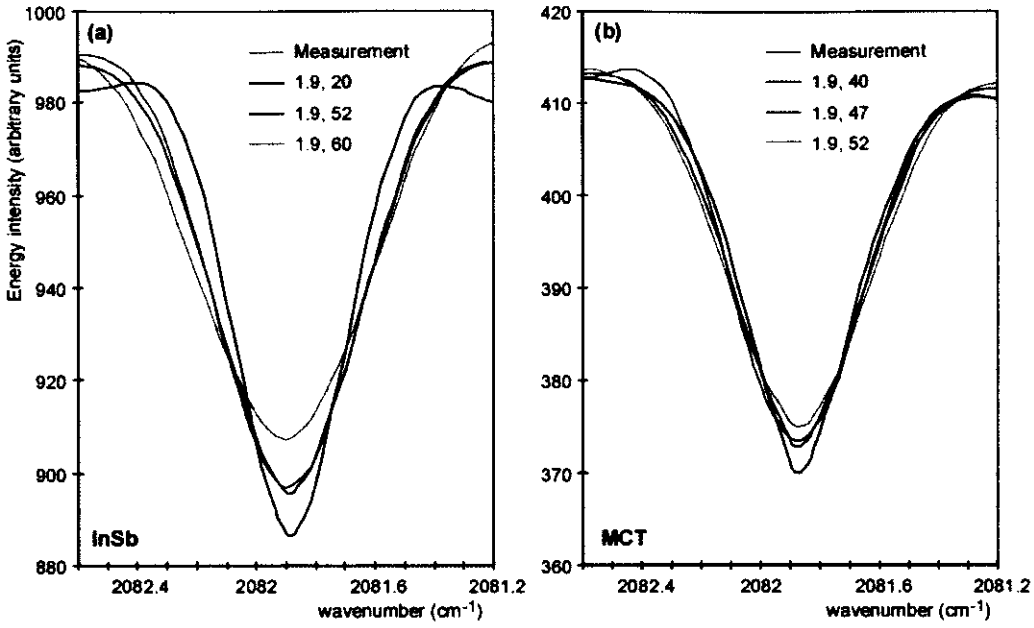

Figure 2-19: Retrievals of the CO line at 2082 cm^{-1} measured by (a) InSb (p=401 mb) and (b) MCT (p=419 mb) detectors. Different ILS were used for each fit, and are labelled on figure as "maximum OPD in cm, FOV in mrad".

For the nominal maximum OPD of 1.9 cm, the FOV was increased stepwise from the nominal value of 20 mrad. Reduced OPDs of 1.8 cm and 1.7 cm were also tried. For each newly calculated ILS, the 6 lowest pressure calibrated spectra were retrieved. Smaller adjustments to the ILS were made in order to find the best possible fit. The results are shown in Table 2-9.

OPD / cm	FOV / mR	Mean retrieved amt / molec cm^{-2}	Mean retrieved error	Error of retrieved : true
1.9	20	4.264×10^{17}	0.152	-0.1503
1.9	40	4.915×10^{17}	0.150	-0.0207
1.9	45	5.274×10^{17}	0.148	0.0509
1.9	47	5.416×10^{17}	0.148	0.0793
1.9	50	5.638×10^{17}	0.148	0.1236
1.9	52	5.799×10^{17}	0.148	0.1556
1.9	60	6.130×10^{17}	0.152	0.2215
1.8	50	5.830×10^{17}	0.148	0.1618
1.7	50	5.951×10^{17}	0.148	0.1858

Table 2-9: Results of variation of ILS on retrieval of low pressure CO line at 2082 cm^{-1} measured with the InSb detector. The true calibrated amount of CO was 5.02×10^{17} molec cm^{-2}.

As seen in figure 2-19(a), the nominal ILS was far too narrow to fit the measured peak. When a field of view of approximately 50 mrad was tried, the fit was much improved, and the mean retrieved error decreased. The fit varied negligibly if the OPD was changed from 1.9 down to 1.7 cm with the FOV fixed at 50 mrad. The closest fit to the peak and the best residual was found with an ILS calculated from a 1.9 cm OPD and a 52 mrad FOV. However, both the broad shoulders and broad apex of the peak could not be fitted simultaneously: the best fit ILS still has an apex which is slightly too pointed.

Interestingly, the ILS that produced the best fit to the peak did not result in the most accurate retrieved amount for this single peak (Table 2-9). However, when this optimum ILS was used to fit CO and H_2O across the whole band from 2050-2220 cm^{-1}, the mean amount retrieved for the 6 spectra was 5.031×10^{17} molec cm^{-2}, only 0.25 % different from the calculated true amount. Discrepancies may arise because of uncertainty in the HITRAN96 line parameter database. Alternatively, the resolution of the MIDAC spectrometer is not fine enough for accurate retrievals based on one narrow peak only. Because the low resolution ILS cannot be precisely modelled, it causes errors in the retrieved amount. The effect is not so pronounced across a broader microwindow containing a number of lines of different strengths: in this case, the fit is constrained by a greater number of spectral points across the whole band structure and inaccuracies in the ILS on individual peaks are less significant.

The ILS for measurements with the MCT detector was harder to fit (figure 2-19(b)). The ILS that was best for InSb data produced peaks which were too broad for the MCT. The best fit for the MCT low pressure CO peak was found with an ILS using a 47 mrad FOV, although this fit was less satisfactory than the fit for the InSb data. It is not surprising that the MCT and InSb detectors have different ILS, since contributions to the ILS come from the detector itself, as well as from the source radiation and spectrometer optics.

In subsequent analyses of InSb SO_2 spectra I used an ILS constructed from a 1.9 cm OPD and 52 mrad FOV. MCT analyses use an ILS with a FOV of 47 mrad. The ILS determined here was not used in analysis of field data: for spectra collected at Masaya in 1998 a FOV constraint of 20 mrad was used, while for 1999 data the FOV was 40 mrad, with maximum OPD remaining at 1.9 cm.

2.4.2.2 SO_2 retrieval: microwindow and background polynomial

The 6 spectra containing approximately 10000 ppm SO_2 (i.e. 5000 ppm.m which is typical for medium-to-high concentrations measured at Masaya's summit) were retrieved using a range of frequency microwindows, as shown in Table 2-10, and varying the number of parameters used in the background polynomial fit from 3 to 5. The measured pressure and temperature were used together with the ILS defined above. For all of the SO_2 retrievals, both H_2O and CO_2 were fitted simultaneously with SO_2. For this short path, the atmospheric gases CH_4 and N_2O were not present in quantities significant enough to require fitting.

frequency microwindow (cm^{-1})	**background polynomial**	**mean retrieved amount (molec cm^{-2})**	**mean retrieved error**	**ratio of retrieved/true**
2490-2510	3	1.22217×10^{19}	0.0555	1.022
2490-2510	4	1.21467×10^{19}	0.0658	1.016
2490-2510	5	1.21567×10^{19}	0.0665	1.017
2480-2510	3	1.22667×10^{19}	0.0446	1.026
2480-2510	4	1.22333×10^{19}	0.0456	1.023
2480-2510	5	1.22533×10^{19}	0.0507	1.025
2480-2520	3	1.22833×10^{19}	0.0425	1.028
2480-2520	4	1.22650×10^{19}	0.0440	1.026
2480-2520	5	1.22683×10^{19}	0.0443	1.026
2470-2520	3	1.22683×10^{19}	0.0450	1.026
2470-2520	4	1.22583×10^{19}	0.0451	1.025
2470-2520	5	1.22783×10^{19}	0.0471	1.027
2470-2530	3	1.23467×10^{19}	0.0492	1.033
2470-2530	4	1.23667×10^{19}	0.0491	1.035
2470-2530	5	1.23583×10^{19}	0.0493	1.034

Table 2-10: Results of repeated retrievals using different frequency microwindows and background polynomial fits. The true amount was 1.1954×10^{19} molec cm^{-2}. The preferred choice of parameters are those in row 8; see text for discussion.

If the line parameter database used to construct the forward model were perfect, then the best retrieval parameters would be those that returned closest to the true amount. HITRAN96 does, however, contain uncertainties, although the error associated with SO_2 line parameters is unquantified. Instead, the preferred retrieval parameters were selected on the basis of the smallest retrieved error, and error in the HITRAN database was assessed separately at a later stage.

The results in Table 2-10 show that retrieved error is a minimum for the 2480–2520 cm^{-1} microwindow, regardless of the number of parameters used in the background fit. This window contains the central part of the SO_2 $\nu_1+\nu_3$ band, so that SO_2 signal is strong while the signal from interfering species is minimised. The retrieved error reduces as window size is increased because of the greater amount of information available for the fit (i.e. more spectral points), and then increases as window size increases further as interfering signal from species other than SO_2 becomes significant.

Smaller microwindows are more sensitive to changes in the order of the polynomial used to fit the background response curve. Since the Q branch has little fine structure, smaller windows on the SO_2 feature are easier to fit erroneously with the polynomial curve. Within the 2480–2520 cm^{-1} microwindow the order of background polynomial made no visible difference to the fits, and little difference to the retrieved amount and error. An order 4 background polynomial was chosen because it resulted in fewer correlations in the retrieval solution matrix and convergence to a retrieval over fewer loops of the algorithm. It is emphasised, however, that this choice of background polynomial is of only minor consequence.

The greatest deviation in retrieved amount due to varying microwindow and/or background fit from the preferred retrieval parameters was +0.8 % and –1.0 %, comparing row 8 with rows 14 and 2, respectively, in Table 2-10. Error bounds of ±1.0 % were therefore assigned to choice of microwindow and background polynomial for retrieval of SO_2 at this concentration level. I retrieved the full concentration suite of InSb SO_2 spectra once using the optimum window and background, and then again using a "worst case scenario" of 2470-2530 cm^{-1} microwindow with 4 background parameters. The difference in retrieved amounts from these two situations was taken as an estimate of the error associated with bad choice of microwindow and background polynomial (Table 2-14).

2.4.2.3 SO_2 retrieval: the effects of errors in ILS

I ran the retrieval on each group of spectra with different SO_2 concentrations, specifying the correct pressure and temperature, using the 2480-2520 cm^{-1} window, with 4 background parameters, and using the ILS calculated from 1.9 cm OPD and 52 mrad FOV. I then repeated the retrieval with only the ILS changed, using the nominal 1.9 cm OPD and 20 mrad FOV. The results are shown in Table 2-11.

ILS (opd, fov)	**True amount / molec cm^{-2}**	**Mean retrieved amount / molec cm^{-2}**	**Mean retrieved error**	**Ratio nominal /optimum**
1.9, 52	2.98×10^{17}	3.1457×10^{17}	0.2079	
1.9, 52	2.89×10^{18}	3.0274×10^{18}	0.0496	
1.9, 52	1.20×10^{19}	1.2265×10^{19}	0.0440	
1.9, 52	2.59×10^{19}	2.5625×10^{19}	0.0444	
1.9, 20	2.98×10^{17}	3.1923×10^{17}	0.1801	1.015
1.9, 20	2.89×10^{18}	2.9640×10^{18}	0.0444	0.979
1.9, 20	1.20×10^{19}	1.2060×10^{19}	0.0387	0.983
1.9, 20	2.59×10^{19}	2.5210×10^{19}	0.0383	0.984

Table 2-11: Results of retrieval of SO_2 amounts using different ILS. Final column gives the ratio of amounts retrieved using the nominal ILS to those retrieved using an ILS of 1.9 cm OPD and 52 mrad FOV.

The CO tests showed that the use of a higher resolution ILS in the retrieval than provides the best fit to the data results in underestimated quantities, and that if the ILS is degraded to worse resolution than fits the data, then the quantities are overestimated. For the SO_2 retrieval, there was little difference between the fit provided by the 1.9 cm 52 mrad ILS and the fit provided by the nominal 1.9 cm 20 mrad ILS (figure 2-20, and column 4 in Table 2-11). However, there was some difference in retrieved amount, with the nominal ILS generally resulting in lesser quantities than the optimum ILS. The difference in retrieved amounts using the different instrument line shapes was between 1.5 and 2.1 % depending on concentration, and this was used as an estimate of the error caused by a bad choice of ILS.

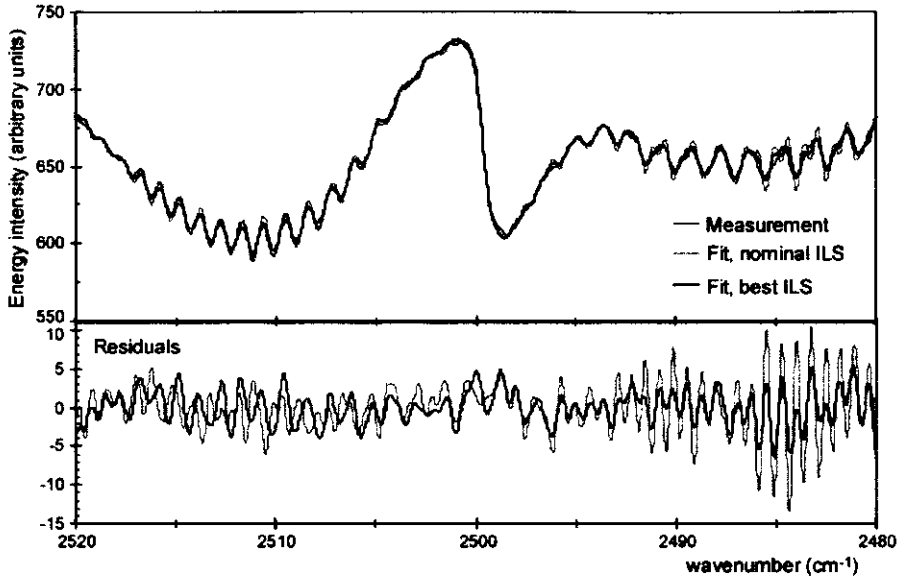

Figure 2-20: Measurement and fitted spectra (upper plot) for the SO_2 retrieval using the nominal and supposed best ILS, and their residuals (lower plot).

2.4.2.4 SO_2 retrieval: the effect of error in input pressure

The retrieval was performed retaining the same best ILS and retrieval window, and the correct temperature for each set of spectra, but varying the input pressure from 300 mb below the true pressure to 200 mb above the true pressure (which was approximately 970 mb). This simulates a pressure range equivalent to about zero to 3 km altitude. The test was repeated for each SO_2 concentration level. Results are shown in Table 2-12.

Input P (mb)	True amount	Mean retrieved amount	Mean retrieved error	Error (wrong P : correct P)
664	2.9791×10^{17}	3.0770×10^{17}	0.204	-0.022
764	2.9791×10^{17}	3.0975×10^{17}	0.206	-0.015
864	2.9791×10^{17}	3.1115×10^{17}	0.208	-0.011
964	2.9791×10^{17}	3.1457×10^{17}	0.208	0.000
1064	2.9791×10^{17}	3.1538×10^{17}	0.210	0.003
1164	2.9791×10^{17}	3.1717×10^{17}	0.212	0.008
672	2.8892×10^{18}	2.9528×10^{18}	0.049	-0.025
772	2.8892×10^{18}	2.9780×10^{18}	0.049	-0.016
872	2.8892×10^{18}	3.0028×10^{18}	0.049	-0.008
972	2.8892×10^{18}	3.0274×10^{18}	0.050	0.000
1072	2.8892×10^{18}	3.0512×10^{18}	0.050	0.008
1172	2.8892×10^{18}	3.0750×10^{18}	0.050	0.016
669	1.1954×10^{19}	1.1998×10^{19}	0.043	-0.022
769	1.1954×10^{19}	1.2085×10^{19}	0.043	-0.015
869	1.1954×10^{19}	1.2173×10^{19}	0.044	-0.007
969	1.1954×10^{19}	1.2265×10^{19}	0.044	0.000
1069	1.1954×10^{19}	1.2358×10^{19}	0.044	0.008
1169	1.1954×10^{19}	1.2448×10^{19}	0.044	0.015
663	2.5877×10^{19}	2.5085×10^{19}	0.044	-0.021
763	2.5877×10^{19}	2.5270×10^{19}	0.044	-0.014
863	2.5877×10^{19}	2.5442×10^{19}	0.044	-0.007
963	2.5877×10^{19}	2.5625×10^{19}	0.044	0.000
1063	2.5877×10^{19}	2.5810×10^{19}	0.045	0.007
1163	2.5877×10^{19}	2.6002×10^{19}	0.045	0.015

Table 2-12: Variation in retrieved amount at different SO_2 concentration levels when pressure input into the retrieval is changed.

The retrieved amounts showed a systematic dependence on pressure, although the mean retrieved errors showed negligible variation. A 300 mb decrease in pressure resulted in 2.1–2.5 % reduction in retrieved amounts from that retrieved with the correct input pressure, and a 200 mb increase in pressure resulted in 0.8–1.6 % increase in retrieved amount. The reason for such pressure dependence is the effect of pressure on the Lorentz lineshape (c.f. figure 2-3(a)). With increasing pressure, the line-width is broadened and the maximum peak height is suppressed, for a given concentration of absorber. Although the broad ILS of the spectrometer masks these effects visually, there is an impact on calculated concentrations.

For a given field location, such as Masaya, the ambient ground-level pressures were 943–954 mb at Santiago crater summit, 915–923 mb downwind on the Llano Pacaya, and 990–994 mb downwind at the coast. However the important pressure constraint is plume pressure. Whilst for active measurements this will be the same as the measured ambient pressure, for solar measurements where the plume may be at up to 1 km a.s.l., the pressure will be less. A height of 1000 m corresponds to an atmospheric pressure of about 900 mb, compared with approximately

950 mb at 600 m at the volcano's summit. The results show that a pressure variation of 100 mb causes up to 1 % error in the retrieved amount; so the maximum 50 mb uncertainty expected at Masaya would cause about 0.4 % error (Table 2-14). Inaccuracies on this scale in input pressure are therefore relatively unimportant.

2.4.2.5 SO_2 retrieval: effect of errors in input temperature

A similar procedure to the previous investigation into pressure effects was implemented, but this time the input pressure for each retrieval was kept at the correct value while input temperature was changed over a range ± 20 °C from the correct temperature. Results are shown in Table 2-13.

Input T (K)	True amount	Mean retrieved amount	Mean retrieved error	Error (wrong T : correct T)
271	2.9791×10^{17}	2.9369×10^{17}	0.211	-0.066
281	2.9791×10^{17}	3.0421×10^{17}	0.209	-0.033
291	2.9791×10^{17}	3.1457×10^{17}	0.208	0.000
301	2.9791×10^{17}	3.1601×10^{17}	0.159	0.005
311	2.9791×10^{17}	3.2341×10^{17}	0.208	0.028
273	2.8892×10^{18}	2.8504×10^{18}	0.050	-0.058
283	2.8892×10^{18}	2.9382×10^{18}	0.050	-0.029
293	2.8892×10^{18}	3.0274×10^{18}	0.050	0.000
303	2.8892×10^{18}	3.1186×10^{18}	0.049	0.030
313	2.8892×10^{18}	3.2120×10^{18}	0.049	0.061
274	1.1954×10^{19}	1.1560×10^{19}	0.044	-0.057
284	1.1954×10^{19}	1.1910×10^{19}	0.044	-0.029
294	1.1954×10^{19}	1.2265×10^{19}	0.044	0.000
304	1.1954×10^{19}	1.2638×10^{19}	0.044	0.030
314	1.1954×10^{19}	1.3018×10^{19}	0.044	0.061
273	2.5877×10^{19}	2.4160×10^{19}	0.045	-0.057
283	2.5877×10^{19}	2.4887×10^{19}	0.045	-0.029
293	2.5877×10^{19}	2.5625×10^{19}	0.044	0.000
303	2.5877×10^{19}	2.6378×10^{19}	0.044	0.029
313	2.5877×10^{19}	2.7155×10^{19}	0.044	0.060

Table 2-13: Variation in retrieved amount at different SO_2 concentration levels when temperature input into the retrieval is changed.

The retrieved amounts showed a systematic dependence on temperature, although the mean retrieved errors showed negligible variation. A ± 20 °C change in temperature resulted in approximately ± 6 % change in retrieved amount. As before, this correlation is explained by the temperature dependence of the spectral lineshape. The effects of increasing temperature on the lineshape are similar to the effects of increasing pressure, and temperature also affects the overall band shape. So for a given concentration, calculated amounts vary with temperature.

For fieldwork at Masaya, I encountered ambient temperatures in the range of 25–40 °C for daytime measurements, and 19 °C for lunar measurements. Over the course of one set of spectra

(approximately an hour) temperature never varied by more than 2 °C, but temperature often varied by 5 °C over the course of a day. However, it is the plume gas temperature, and not the ambient temperature, which is important. For active measurements at Santiago crater, depending on wind conditions and the amount of mixing within the crater, the plume gas temperature was probably up to 10 °C hotter than ambient. For solar measurements, as the plume was higher and had longer to equilibrate with the atmosphere, its temperature was probably less than ambient ground level temperatures. If a single average input temperature of about 30 °C were used in the retrieval of all the daytime spectral data, it could have error margins of ± 10 °C. The consequent error in the retrieved amount is roughly ± 3 % (Table 2-14). While this is a more significant error than that due to pressure uncertainties, it cancels out to some extent when ratios of retrieved concentrations for two components (such as SO_2 and HCl) are considered.

2.4.2.6 SO_2 retrieval: error analysis summary

From systematic tests on calibrated SO_2 spectra, I have been able to assess the errors associated with the retrieval over a range of concentration levels. Results from Tables 2-10 to 2-13 are summarised in Table 2-14.

Source of uncertainty	**Error in retrieved amount (%)**			
SO_2 conc in ppm	250	2400	10000	21000
Microwindow and b.g polynomial	1.2	0.4	0.8	0.4
Wrong ILS (using nominal)	1.5	2.1	1.7	1.6
50 mb error in input pressure	0.5	0.4	0.4	0.4
10 °C error in input temperature	3.3	3.0	3.0	2.9
Total (added in quadrature)	3.9	3.7	3.6	3.4
Uncertainty in line parameters (HITRAN)	3.6	3.6	3.6	3.6
Mean retrieved error	20.8	5.0	4.4	4.4
Accuracy of retrieved : true (best parameters)	5.6	4.8	2.6	-1.0

Table 2-14: Summary of errors associated with retrievals of SO_2 concentrations. Values in the first 4 rows have been derived from Tables 2-10, 2-11, 2-12 and 2-13, respectively. Uncertainties in the HITRAN96 database were estimated from a comparison with an alternative spectral database (see text). The retrieved error contains some contribution from ILS, microwindow and background polynomial within its calculation.

The "worst-case" total external error that could result from poor choice of retrieval microwindow, background fit and ILS and errors in plume pressure and temperature estimates is less than 4 %. Uncertainties associated with the HITRAN96 line parameter data for SO_2 are unquantified in the database itself. A 5.7 % discrepancy in SO_2 absorbance at 2500 cm^{-1} exists between HITRAN96 and an alternative spectral database from NIST (N. Davies, pers. com.). The NIST data are quoted with an uncertainty of ± 2.1 % at 95 % confidence, implying that error on the HITRAN data must be at least 3.6 %. This value is taken as a reasonable estimate of the uncertainty on HITRAN96 SO_2 line parameters for the $\nu_1+\nu_3$ band. Thus, the total error associated with factors outside the retrieval is of similar order to the error on the line parameters

used in the forward model. In practice, the external error is likely to be less than the total calculated here, as care was taken to use the best ILS possible in the retrieval of field data, and temperature estimates were probably better constrained than a 10 °C uncertainty.

In all cases, error output from the retrieval algorithm ("retrieved error") is greater than the total external error, and the high error for the lowest concentration reflects the fact that the signal to noise ratio in these spectra was low.

When the best choice of input parameters is used, the accuracy of retrieved amounts reflects a combination of line parameter and measurement (i.e. retrieved) error. Figure 2-21(a) shows retrieved amounts plotted against the true SO_2 concentrations, along with the errors associated with each retrieval. The difference in retrieved amount from true concentration is barely discernible on an x-y plot over a range of concentrations similar to that encountered in Masaya field data. For the lowest concentration, the relative standard deviation of retrieved amounts is almost 8 %, but standard deviation rapidly reduces with increasing concentration to 0.3 % at the high end of the range. Mean retrieved amounts are equal to the true concentrations to within 5 %, except for the lowest concentration spectra. However, there is a systematic decline in the error of retrieved to true amounts as concentration increases so that the highest concentration is underestimated (figure 2-21(b)).

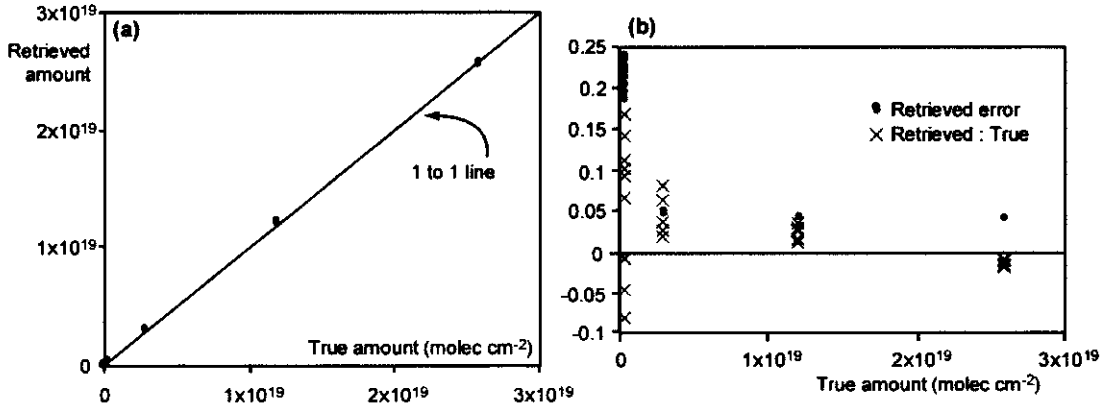

Figure 2-21: Compare with quantities summarised in Table 2-14. (a) Retrieved amounts plotted against the calculated true concentrations, and a one-to-one line for comparison. (b) Relative errors associated with the retrieval plotted against true concentration. The retrieved error is output along with retrieved quantities. The error between retrieved and true amounts is simply the difference divided by true concentration.

This trend is explained by the combination of two effects. At lower concentrations, the retrieval tends to maximise the strength of the SO_2 signal, resulting in overestimates, which reduce in scale as the actual SO_2 signal increases. At higher concentrations, problems associated with an imperfect ILS are exaggerated. Owing to convolution with the broad ILS, absorption features that appear only "strong" in the measured spectra are, in reality, saturated to varying degrees (c.f. figure 2-3(b)). If the ILS used in the retrieval is inaccurate, there is great scope for error when the

saturated spectral feature is fitted. However the cumulative error incurred in these two processes is only +5.6 % at the low concentration end (most of which can be attributed to noise in the spectra) and –1.0 % at the high concentration end.

The retrieved error declines from 20 % for the lowest concentration measurements to 4.4 % for the two highest concentration measurements. Although calculated to give a minimum estimate of the uncertainty associated with the retrieval, these retrieved errors are always slightly larger than the accuracy of the retrieved amount (figure 2-21(b)). It is therefore reasonable to take the retrieved errors as a conservative estimate of the uncertainty associated with SO_2 amounts derived using an accurate choice of retrieval parameters, temperature and pressure, despite uncertainty in the line parameter database.

In summary, the retrieval for SO_2 has performed well. The greatest individual contribution to uncertainty is associated with the estimate of plume temperature, although the 10 °C allowance in Table 2-14 is generous. The choice of ILS presents another significant uncertainty, generally in the region of 2 %. The retrieved error is more than enough to cover the bounds of accuracy.

2.4.2.7 SO_2 retrieval: approximate detection limits

I quantified detection limits for SO_2 retrieval in this test situation from the results of the retrieval run on spectra containing no SO_2 and the lowest SO_2 concentration (sets 1 and 2 in Table 2-7).

The mean retrieved SO_2 from 10 spectra collected when the gas cell was evacuated was 4.694×10^{15} molec cm^{-2} ($\sigma = 9.488 \times 10^{16}$ molec cm^{-2}), using optimum input parameters. The standard deviation is much greater than the mean retrieved amount, and so the possible error at zero concentration of SO_2 is approximately 10^{17} molec cm^{-2} (40 ppm m at room temperature and pressure). This provides some measure of the absolute minimum detection limit for SO_2 in active spectra, using the $\nu_1+\nu_3$ band at 2470–2530 cm^{-1}. The relatively stronger SO_2 bands below 2000 cm^{-1} are likely to have lower detection limits.

The mean retrieved SO_2 from 10 spectra of the lowest calibrated SO_2 concentration of 2.979×10^{17} molec cm^{-2} (120 ppm m at room temperature and pressure) was correct to within 5.6 % of the true amount (Table 2-14), showing that this was above the detection limit. Detection limits are expected to be higher in the less-controlled circumstances of field data collection than under the conditions of low humidity, short pathlength and easy alignment for these calibration spectra. For field data, SO_2 concentrations of more than 2.5×10^{17} molec cm^{-2} (equivalent to 100 ppm m at room temperature and pressure) should be measurable with high accuracy.

2.4.3 Comparison of different detectors and different SO_2 bands

2.4.3.1 Comparison of MCT and InSb for the 2500 cm^{-1} SO_2 absorption

The spectra collected using the MCT detector were retrieved using the optimum ILS and the microwindow and background polynomial determined in section 2.4.2. Results are shown in figure 2-22.

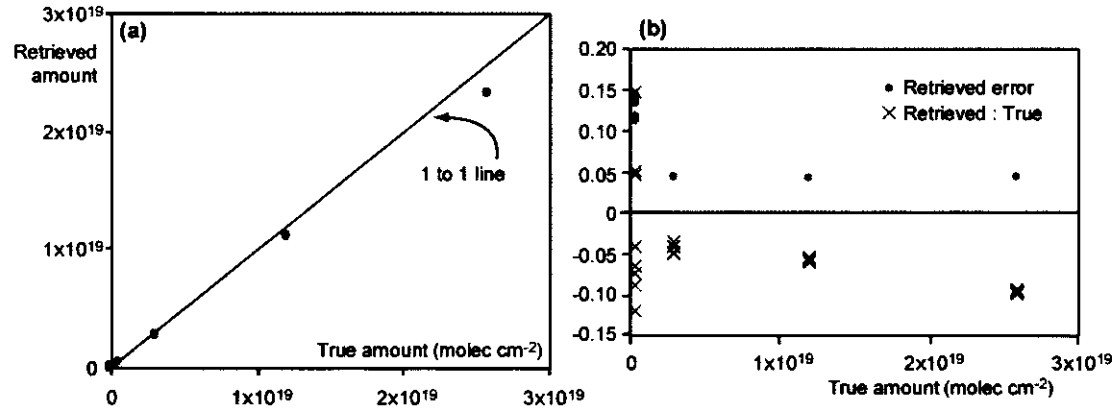

Figure 2-22: (a) Retrieved amounts from the 2500 cm^{-1} band in MCT spectra plotted against the calculated true concentrations, and a one-to-one line for comparison. (b) Relative errors associated with the retrieval plotted against true concentration. The retrieved error is output along with retrieved quantities. The error between retrieved and true amounts is simply the difference divided by true concentration.

The retrieved amounts from the MCT spectra are substantially worse than those retrieved from InSb data. The mean retrieved amount is always less than the true concentration, and at the highest concentration, the amount is underestimated by about 10 %. However, the retrieved errors for the highest two concentrations are about 4 %, confirming that the residuals from the retrieval are similar for InSb and MCT. The underestimation is likely to be linked to the ILS used in the retrieval, which was more difficult to fit for the MCT than the InSb. In addition, non-linearities in its response and a generally worse sensitivity contribute to a poorer performance by the MCT detector than that by the InSb.

This test confirms that even under the best measurement conditions and when the closest attention is paid to the parameters used in the retrieval, data collected with the MCT detector are harder to retrieve accurately than those collected with the InSb. While most gases of volcanological interest absorb radiation within the range of response of the InSb detector (e.g. SO_2, CO_2, HCl, HF, H_2S, CO, H_2O), there is at least one for which it is necessary to use MCT. SiF_4 has a strong absorption at 1060 cm^{-1}, and, when it is detected, can provide useful information about the temperature of gases exiting the vent (Francis *et al.* 1996a). Owing to the large number of spectra collected at Masaya, I have been able to focus on InSb data only for most of the analysis in this thesis. There was no indication of SiF_4 absorptions in spectra collected with the MCT detector (Chapter 5).

2.4.3.2 Retrieval of SO_2 using bands at 1150 cm^{-1} and 1360 cm^{-1}

SO_2 has spectral bands at lower frequencies (c.f. figure 2-2), which are stronger than the feature at 2500 cm^{-1}. These bands are beyond the response range of the InSb detector (~6000-1500 cm^{-1}), but can be detected using the MCT. The ν_3 band at 1360 cm^{-1} is the strongest, but this overlaps with a very strong H_2O absorption, so that except for the very shortest path lengths, the region is "black" and no information can be retrieved. For the spectra collected at NPL, this region was not saturated, although numerous strong H_2O lines occurred throughout. Figure 2-23 shows a microwindow from 1290–1410 cm^{-1} for five spectra of the different SO_2 concentrations. By comparison with the spectrum containing no SO_2, the strong SO_2 absorption is clearly seen, but only for the lowest concentration is the band free from saturation. Additionally, the pervasive H_2O lines make the SO_2 retrieval in this window difficult.

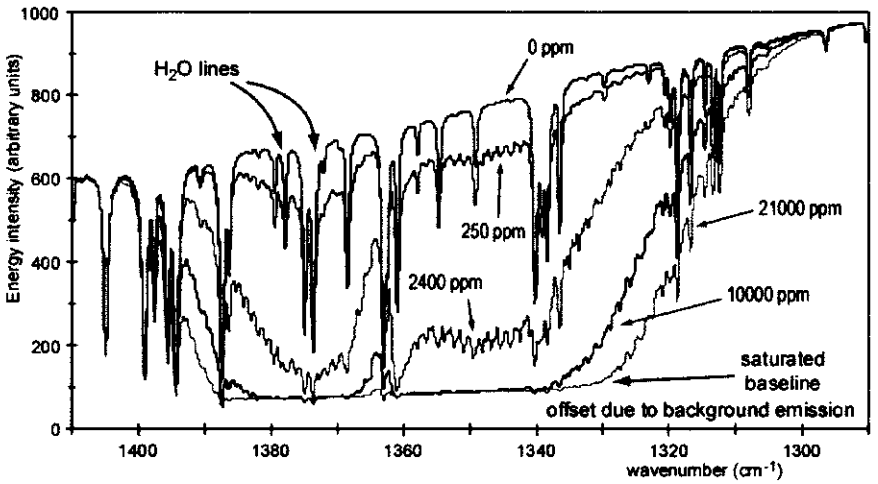

Figure 2-23: Microwindow centred on the SO_2 ν_3 band for five spectra containing nominal amounts of 0, 250, 2400, 10000 and 21000 ppm SO_2, as indicated. Numerous H_2O lines occur across this window, which is black for longer path lengths. The absorption for 2400 ppm (purple) is already beginning to saturate. Notice that the baseline is offset from zero in saturated regions: this is due to background emission at these frequencies.

An offset of the saturated baseline from the zero transmission level is apparent in figure 2-23. This arises as a result of background room temperature IR emission and from instrument self-emission, which is minimal at shorter wavelengths (e.g. above 2000 cm^{-1}), but significant at these longer wavelengths. If this offset is not subtracted prior to retrieval in affected regions, then retrieved amounts will be significantly underestimated, with increasing error for stronger lines. The effect is even more pronounced in the region of the 1150 cm^{-1} band.

The ν_1 band at 1150 cm^{-1} is nine times weaker than ν_3, but falls in a relatively clear atmospheric window. I ran the retrieval in a microwindow at 1110–1190 cm^{-1} chosen so that interfering CO_2 and CH_4 were avoided below 1100 cm^{-1} and above 1190 cm^{-1}, respectively. Results are shown in figure 2-24.

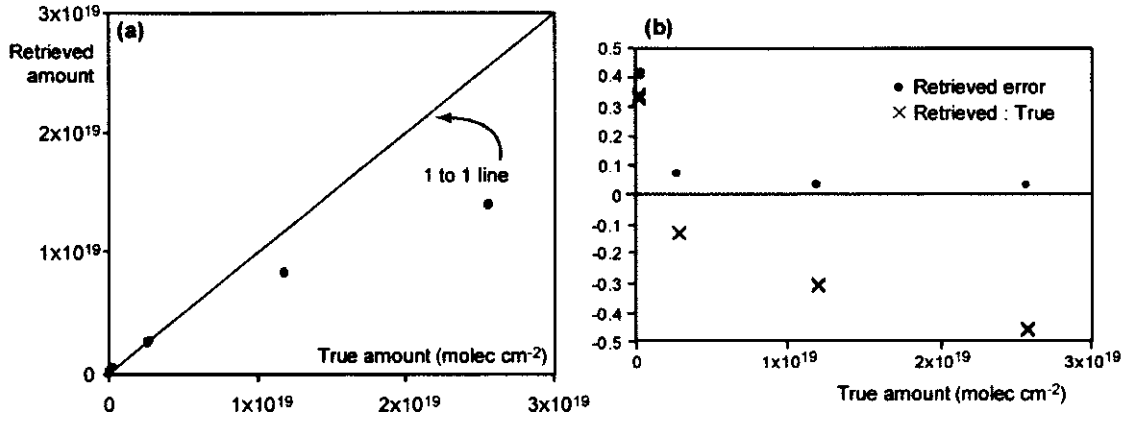

Figure 2-24: (a) Retrieved amounts from the 1150 cm^{-1} SO_2 band in MCT spectra plotted against the calculated true concentrations and a one-to-one line for comparison. (b) Relative errors associated with the retrieval plotted against true concentration. The retrieved error is output along with retrieved quantities. The error between retrieved and true amounts is simply the difference divided by true concentration.

Retrieval of the 1150 cm^{-1} SO_2 band resulted in severe underestimation, by up to nearly 50 %, of the true gas amounts at higher concentrations, while the retrieved errors remained small (figure 2-24). This discrepancy may result partly from misfit of the ILS, but it is due mainly to ambient background emission and instrument self-emission, which is at a maximum at these wavelengths. In the NPL measurements, emission from the gas cell placed between lamp source and spectrometer also contributes to the detected signal. Given the Planck curve for a room temperature black body (shown schematically in figure 2-25), the offset around 1150 cm^{-1} could be as much as 25 %. The overestimation of the lowest gas concentration in this window is the outcome of the retrieval fitting SO_2 to an irregular background curve when the SO_2 signal is at, or below, detection limit.

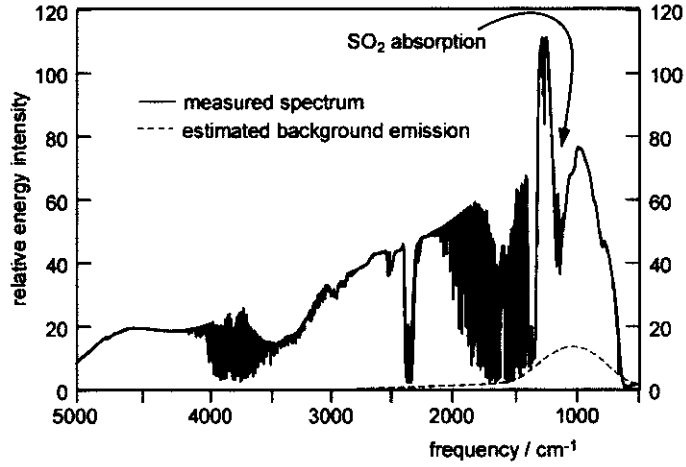

Figure 2-25: Spectrum measured with the MCT detector at NPL, with approximately 10000 ppm SO_2 in the gas cell. The strong SO_2 band at 1150 cm^{-1} is indicated, and a schematic room temperature Planck curve shows how background emission in the long wave IR could cause the baseline offset. The saturated ν_3 band between 1300 and 1400 cm^{-1} should lie at zero transmittance.

The offset can be corrected by collecting a background spectrum when the hot source (i.e. IR lamp) is absent, and then subtracting this emission spectrum from sample spectra. Unfortunately, this essential measurement was not made during the data collection at NPL. There is no way retrospectively to correct this effect accurately if it is found in previous field data and no background emission spectrum was collected at the time. Taking a ratio of a sample spectrum to a spectrum containing no gas compounds the problem, since the offset is present in both measurements. Close inspection of MCT spectra in saturated regions acts as an alert to this danger.

Retrieved amounts are summarised in Table 2-15, which compares MCT retrievals for the three different bands, and the InSb retrievals at 2500 cm^{-1}. SO_2 retrievals from the 1360 cm^{-1} and 1150 cm^{-1} bands were severely affected by saturation and background offsets. If the background emission could be removed, detection of SO_2 using the ν_1 band is likely to be much more satisfactory. SO_2 retrieval from the 2500 cm^{-1} band in the MCT spectra was sufficiently accurate for only the two lowest concentrations, before errors became significant. This behaviour may be the result of detector non-linearities as well as an inaccurate ILS. The InSb retrievals at 2500 cm^{-1} were more satisfactory, considering the whole concentration range, confirming my decision to use InSb field data preferentially in this thesis.

True amount / molec cm^{-2} (MCT)	**Retrieved/True (MCT)**			**Retrieved/True (InSb)**
	2500 cm^{-1}	1360 cm^{-1}	1150 cm^{-1}	2500 cm^{-1}
2.959×10^{17}	0.981	0.906	1.333	1.056
2.889×10^{18}	0.955	(0.683)	0.868	1.048
1.197×10^{19}	0.941	---	0.691	1.026
2.584×10^{19}	0.902	---	0.538	0.990

Table 2-15: A comparison of retrieval accuracy using the different SO_2 bands and detectors. The 1360 cm^{-1} absorption was saturated for the higher concentrations.

2.4.4 Comparison with an alternative retrieval algorithm

The calibrated InSb spectra were analysed by N. Davies (NPL) via a non-linear least squares algorithm (Davies 1999). The HITRAN96 line parameter database was used so that the performance of the two algorithms could be compared. The routine used a triangular apodization function and an OPD of 1.9 cm, but rather than constraining the ILS with a fixed FOV factor, Davies included the FOV component as a free parameter in the retrieval. Concentrations (in ppm) were retrieved from the single beam spectra, with the background curve fit by a second-order polynomial having fixed *a*, *b* and *c* parameters. The lowest concentration measurements were discarded because the absorption was close to the noise. Initially a microwindow from 2400–2600 cm^{-1} was used; the retrieval was then repeated fitting half of the SO_2 band in a window from

2400–2500 cm^{-1}. Finally, the NIST spectral database was employed in the algorithm to investigate the impact of line parameters on the retrieval. All results are given in Table 2-16.

Spectrum	True conc.	Retrieval 1		Retrieval 2		Retrieval 3	
	/ ppm	Conc. / ppm	% Diff	Conc. / ppm	% Diff	Conc. / ppm	% Diff
ai233021	2405.46	2823.47	+17.4				
ai233027	10002.97	11230.00	+10.9	10429.89	+4.1	10543.13	+5.4
ai233033	21738	23413.98	+7.7	21461.93	-1.3	22020.59	+1.3

Table 2-16: Results from the NPL analysis of the calibrated InSb spectra. Retrieval 1 used the HITRAN database with microwindow 2400–2600 cm^{-1}; retrieval 2 used the HITRAN database with microwindow 2400–2500 cm^{-1}; retrieval 3 used the NIST database with microwindow 2400–2600 cm^{-1}. See text for full details of the retrievals.

In summary, the performance of the NPL retrieval algorithm was less satisfactory than the retrieval employed in this thesis, and described in section 2.3. Comparative results for the accuracy of retrieved amounts using the M. Burton algorithm are +4.8 %, +2.6 % and –1.0 % for concentrations of 2405.46 ppm, 10002.97 ppm and 21738 ppm, respectively (from Table 2-14). Reasonable confidence can therefore be placed in results obtained using the retrieval algorithm described in this thesis.

2.4.5 Conclusions, and implications for the assessment of field data

Measurements of SO_2 and CO primary gas standard mixtures at NPL allowed the sensitivity of the instrument and retrieval to be thoroughly investigated. The best ILS determined from low pressure CO spectra were calculated using a maximum OPD of 1.9 cm, with FOV constraint of 52 mrad for the InSb detector and 47 mrad for the MCT detector. The increase in FOV from the nominal value of 20 mrad for the spectrometer is attributed to degradation of the lamp reflector coating resulting in off-axis rays in the source radiation, and to small misalignments within the spectrometer itself, causing further problems with off-axis radiation.

Tests on the InSb SO_2 spectra were used to quantify the range of error associated with input parameters in the retrieval. On the basis of smallest retrieved error, a microwindow from 2480–2520 cm^{-1} gave the best results, while the order of background polynomial was of relatively little consequence for this microwindow. A deviation of 0.5–1.2 % in retrieved amounts was possible with a worse choice of microwindow. The use of the nominal ILS parameters rather than those derived from the CO spectra resulted in 1.5–2.1 % deviations in retrieved amounts. An error of 50 mb in input pressure caused 0.4–0.5 % difference in retrieved amounts, while an error of 10 °C in input temperature caused 2.9–3.0 % difference to the retrieved amounts. The total error associated with these external factors ranged from 3.4 % for the high concentration measurements to 3.9 % for the low concentration measurements, because the ILS and microwindow have a greater effect when signal in the measurement is smaller.

Uncertainty in the HITRAN96 line parameter database for the SO_2 $\nu_1+\nu_3$ band was estimated at ± 3.6 %, a similar value to the total worst-case external error. The retrieval accuracy was better than 5 % for all except the lowest concentration spectra. In general, the retrieval returned overestimates, but at the high concentration end it underestimated the amounts, due to inaccuracies in the ILS exacerbated by near-saturated lines. Errors output from the retrieval algorithm were conservative enough to cover the bounds of accuracy in retrieved quantities, and were substantially greater at low concentrations due to the low signal to noise in these measurements. Estimates of detection limits for SO_2 indicated that, in field data, concentrations of 2.5×10^{17} molec cm^{-2} (100 ppm m at room temperature and pressure) should be measurable with high accuracy.

In addition to unquantified problems of detector non-linearity, the ILS for spectra collected using the MCT detector was harder to fit than the InSb ILS, with the consequence that retrievals of MCT data were worse than retrievals of InSb data. For the 2500 cm^{-1} band, the retrieval returned quantities that underestimated the true amounts by up to 10 %. At 1150 cm^{-1}, the underestimates were up to 48 % because of the secondary issue of unsubtracted background emission in the spectra. This highlights that it is essential to correct for instrument self-emission and background emission for accurate analysis of active or passive measurements at these longer wavelengths. The strong 1360 cm^{-1} band suffered from saturation in all but the lowest concentration spectra.

The greatest inherent problem in data retrieval is accurate quantification of the ILS. Uncertainties associated with estimates of plume temperature are on a similar scale to the uncertainties in line parameters and the retrieval accuracy. Although this quantitative sensitivity analysis pertains only to SO_2 retrievals, there are some broader implications extending to data reduction in general. Absorption lines for HCl and HF are simpler than the broad SO_2 feature. This means that the effect of a misfit in ILS may be more pronounced in retrievals of HCl or HF. The problem can be offset in two ways. Firstly, if a single HCl peak is examined, then the ILS that fits best can be used in subsequent retrievals. Secondly, if a broad window containing a number of lines of varying strength is retrieved, the fit to the overall band shape will help in obtaining an accurate retrieval. These principles have been incorporated into the general procedure outlined in section 2.3.

Aside from the specifics of the retrieval for different types of spectra and different gases, there is also some variation in the quality of the spectral data that are used in the forward model. Table 2-17 is a summary of the uncertainties relevant to transitions of the five gases of interest in this thesis. The HITRAN96 database itself does not include a quantitative summary of all potential uncertainties. Errors associated with the SO_2 line parameter data for the $\nu_1+\nu_3$ band were estimated above.

Molecule	% uncertainty in HITRAN96	Reference
SO_2	± 3.6 %	This study
HCl	1 % < *e* < 2 %	HITRAN96
HF	2 % < *e* < 5 %	HITRAN96
CO_2	2 % < *e* < 5 %	HITRAN96
H_2O	undefined	HITRAN96

Table 2-17: Estimates of the uncertainties, *e*, in spectral line parameters in the HITRAN database for transitions of interest in this thesis.

Solar data present a greater challenge in retrieval than active data. Owing to the presence of strong atmospheric absorptions, it is difficult to look closely at volcanic gas absorptions in the raw spectra, and therefore difficult to assess a good choice of ILS directly. Additionally, strong atmospheric absorptions mean that the signal-to-noise ratio for the volcanic gases is lower, and retrieved errors are higher, than for short path data. This is of particular importance in spectra collected at some distance downwind from the volcano, where the plume is higher and more dispersed and SO_2 amounts were at or below the detection limit estimated here. Chapter 3 is a discussion of issues relating specifically to the retrieval of Masaya field data.

Although large uncertainties can be envisioned in dealing with field data, the results in Chapters 3, 4 and 5 attest that the real situation is far from bad. My chosen method of data reduction, by means of plotting retrieved amounts on x-y scatter graphs, provides a clear visual indication of the quality of the data retrievals. Where there is a large scatter of data points or regression lines do not trend through the origin (in the case of pure volcanic gases), the results can be viewed with an appropriate measure of caution.

Conclusions of Chapter 2

The composition of target gas mixtures can be measured by infrared spectroscopy. The transmission of infrared radiation by gas molecules is linked to the gas concentration via the Beer-Lambert law. Actual measured lines show deviations from this relationship as they are affected by pressure, temperature and instrument resolution. Fourier transform spectroscopy uses the Michelson interferometer to record an interferogram, a measurement of energy intensity as a function of path difference. The spectrum is a Fourier transform of the interferogram convolved with the instrument lineshape, which depends upon the maximum optical path difference and field of view of the spectrometer, and an apodization function. Measured spectra can be analysed by the ratio method, or by a forward model and fitting routine for raw single beam spectra, such as that employed in this thesis.

OP-FTIR spectroscopy is an almost ideal remote tool for gas monitoring on active volcanoes, particularly because of its flexibility. The MIDAC instrument used in this thesis was initially developed for measurements using an active lamp or passive source, but is also suitable for solar measurements. The spectrometer is rugged, compact and portable, and its compartmentalised design allows for interchange between an InSb and MCT detector in the field. The InSb detector provides better sensitivity, spectral coverage and results than the MCT. The instrument's portability is limited by the need for liquid nitrogen to cool the detectors. Field measurements at Masaya Volcano required alignment of the lamp and spectrometer across the crater, or alignment of the spectrometer with the sun.

Data reduction consists of the retrieval of column amounts of gas from the measured spectra via a forward model and fitting procedure followed by interpretation of the retrieved amounts. The forward model is constructed using the Reference Forward Model with line parameter data from HITRAN96, convolved with a calculated instrument line shape, and multiplied with the ATMOS solar spectrum if necessary. The background is fitted with a polynomial curve. The fitting procedure is an optimal estimation non-linear least squares algorithm that returns the best-fit gas amounts and errors on each retrieved parameter. Spectra are analysed in discrete microwindows, which are chosen to maximise the signal from the target species while minimising errors. Retrieved amounts are displayed on scatter plots and gas ratios are derived from the gradient of the regression line. Uncertainty on the ratios was estimated to be approximately 10 %. In intercomparison of data, adequate consideration of both the concentration range and gas ratios should be made.

Results from an empirical sensitivity analysis were encouraging. Retrieval of SO_2 from active OP-FTIR spectra collected at volcanoes can be achieved with high accuracy, but much future work is needed to constrain the sensitivity with which other species (especially HCl, HF and CO_2) may be measured.

CHAPTER 3
RETRIEVAL ISSUES RELATING TO MASAYA FIELD DATA

While a general methodology for the systematic retrieval of field spectra can be fairly simply developed in theory (Chapter 2), a closer inspection of the individual spectra reveals significant inconsistencies which are difficult to deal with in practice. This chapter addresses retrieval issues that have arisen during processing of Masaya field data for this thesis.

The Masaya datasets are vast (more than 6000 spectra) and include spectra of widely differing gas concentrations collected using several different IR sources, and at different locations. Aside from distinctions in spectral energy distribution between spectra collected using different sources, there are other unexpected discrepancies in the data. Between 1998 and 1999 there was an increase in the proportion of background noise in the spectra, and the appropriate ILS to use in forward models also changed. In consecutive spectra, there were sometimes unpredictable variations in line shape, most likely related to variations in the energy source function, but these have been difficult to correct for in any systematic way, without significantly increasing computational time by fitting the ILS in every retrieval. In spectra collected at the summit of the volcano, gas concentrations were frequently so high that some HCl absorption lines were saturated. Choice of retrieval input parameters, namely retrieval microwindow and order of background polynomial, had consequent effects in retrieved amounts and gas ratios. Standard retrieval protocol has differed slightly for solar and active spectra.

Retrieved errors have been a useful indication of the success of the retrieval. However, the behaviour of the retrieved error as input parameters were changed, or for spectra with different amounts of gas, was sometimes complex. Interpretation of data collected downwind requires careful assessment of uncertainty in spectra of low gas concentrations. Quantitative treatment of data collected using passive (i.e. hot vent) sources presents the greatest challenge as the temperature of both gas and source seems to change rapidly and unpredictably.

Initial discussion of retrieval issues focuses on data collected with the IR lamp as this displays spectral features most clearly and is the easiest to interpret. Subsequently the discussion is widened to include data collected in solar mode, and the final part of the chapter is an analysis of data collected using the hot volcanic vent.

3.1 Consistency in field spectra

A systematic retrieval procedure relies upon individual measured spectra being consistent in shape and quality, with only the gas amounts (and degree of frequency shift and background curvature) varying from one to the next. With high-resolution static spectrometers, the assumption of such consistency between one spectrum and the next is well founded: the source of radiation (frequently the sun) is reliable, the instrument itself is clean and well-aligned, and the long optical path difference results in production of high quality interferograms. For the low-resolution portable field spectrometer used at volcanoes this may not be the case.

Exposure to harsh volcanic environments degrades lamp reflector coatings; dust and acids can coat interferometer mirrors and surfaces; repeated bumpy transportation of the instrument may leave components slightly out of alignment. These factors result in off-axis rays and internal reflections, and consequently increased background noise and/or degradation of the effective instrument line shape from the nominal theoretical resolution over time. Additionally, the actual energy source function reaching the spectrometer is subject to variation caused by wind-induced misalignments and changing concentrations of absorbers and scatterers in the optical path. So, the measured line shapes may vary even in consecutive spectra.

3.1.1 Background noise

Active spectra collected in 1999 show a marked increase in background noise compared with the 1998 spectra. Figure 3-1 shows a portion of the HCl band. Regions of the spectrum such as 2758-2764 cm^{-1}, which are close to a flat background line in the 1998 spectra, have developed a sinusoidal character in the 1999 spectra. This type of spectral noise is known as ringing or channelling and is the result of internal reflections within the spectrometer. A reflection within the instrument causes a spike in the interferogram and consequently a sine wave in the spectrum itself. This deterioration in performance between the 1998 and 1999 field trips could have a number of root causes: dirt and misalignments within the optical path will both provide scope for internal reflections.

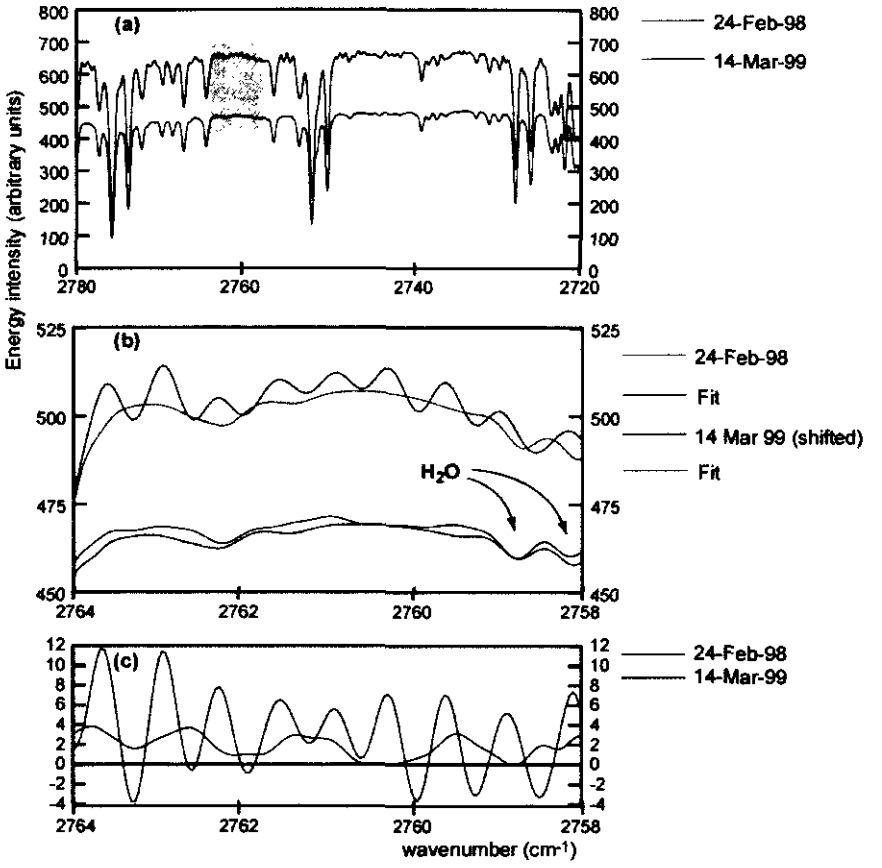

Figure 3-1: Raw spectra from 1998 and 1999 with fits and residuals. (a) The two spectra here contain similar gas concentrations, and absorptions from H_2O and HCl are obvious. Both spectra were collected using the lamp source across Santiago crater. (b) The panel in (a) magnified, with the 1999 spectrum shifted down to maximise the energy scale. The increased sinusoidal background noise in the 1999 spectrum compared with the 1998 spectrum masks two small H_2O peaks close to 2758 cm^{-1}. (c) Residuals from retrieval of the spectra. The sinusoidal nature of the background noise in the 1999 spectrum is even more apparent.

For spectra in which the gas concentrations are high, the presence of increased spectral noise results in an exaggerated residual (such as in figure 3-1), but absorption lines are strong enough that the retrieval still performs well. If gas concentrations are low, or a window with very weak lines only is chosen, then the retrieval attempts to fit the noise. The retrieved error on the HCl fit over 2720-2780 cm^{-1} for both of the spectra in figure 3-1 was the same, at 4.2 %. Despite the difference in noise, the strong HCl lines ensured a precise fit. The observation of increased spectral noise in the 1999 spectra means that a change in instrument line shape should also be expected between the two campaigns, since the cause of increased internal reflections will also increase the effective FOV of the measurements. The fits depicted in figure 3-1 were constructed from different ILS for the two spectra, an effective FOV of 20 mrad for 1998, but 40 mrad for 1999.

3.1.2 Lineshapes

In tests at the National Physical Laboratory in March 2000, reduced pressure carbon monoxide spectra allowed the ILS to be examined directly (Chapter 2), and tests on SO_2 spectra showed that the use of a bad ILS resulted in up to 2.1 % difference in the retrieved amounts. Accurate description of the ILS in field spectra is difficult because of pressure-broadening effects on absorption lines. A general impression of whether an adequate ILS is being used in retrievals can be gained from visual inspection in a number of frequency ranges. Of the gases measured at Masaya, HF has the narrowest lines and would theoretically be the best absorption to view to study the ILS. However, HF lines are in a region of the spectrum which is heavily contaminated by H_2O absorptions, and the only HF line which is not severely overlapped by H_2O at the resolution of the MIDAC is a weak line at 4174 cm^{-1}. HF is also the least abundant of the volcanic gases and so is often present in only low concentrations. HCl lines are also relatively narrow, and suffer from less H_2O contamination. Frequently the concentration of HCl in spectra is so high that saturation of the lines complicates the retrieval. A relatively weak pair of HCl lines at 2702 cm^{-1} does not overlap with H_2O and can be used to check the ILS.

If the ILS used in the retrieval is a good fit to reality, then saturated HCl lines, as well as weaker ones, should be fitted well. For this reason it is instructive to watch a broad band HCl retrieval between say 2690-2900 cm^{-1} to see if residuals across the band are uniform. A poorly modelled ILS results in residual spikes over HCl lines, often changing from negative at one end of the band to positive at the other end of the band.

3.1.2.1 Evidence for varying ILS from 1998 to 1999

Active spectra collected in 1998 were generally fitted well using an ILS generated from the nominal 1.9 cm OPD and 20 mrad FOV. Figures 3-2 and 3-3 show two sets of retrievals, which differ only in the ILS used in the forward model, run for two spectra collected a year apart. In figure 3-2, the best fit to the 1998 spectrum is generated using the nominal ILS. In figure 3-3, there are strong residual peaks when the 1999 spectrum is retrieved using the nominal ILS. Residuals are reduced when the broader ILS from a 40 mrad FOV was used, but in 3-3(d), it is clear that even with this ILS the HCl lines are not fitted perfectly, and perhaps an even broader ILS would perform better.

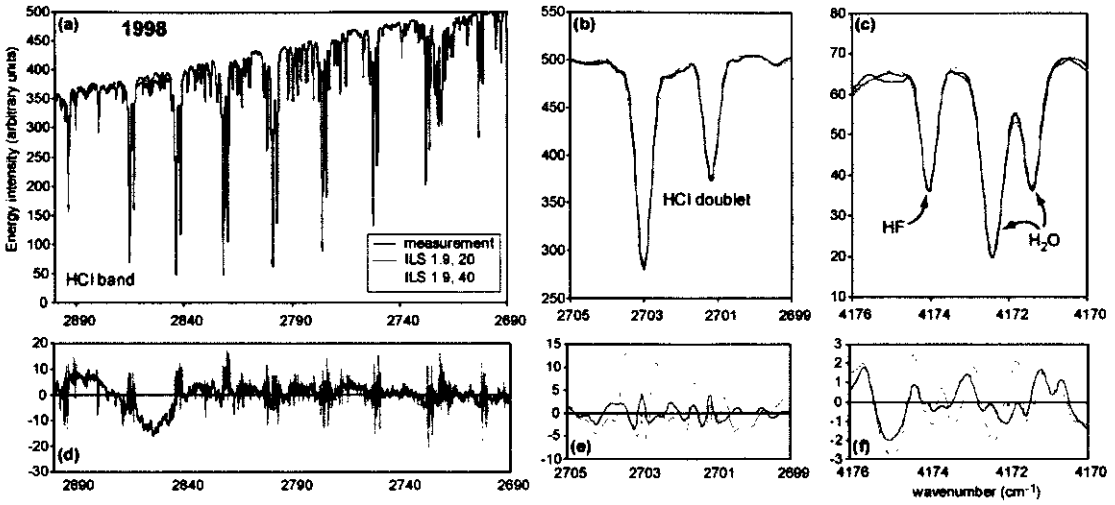

Figure 3-2: Retrievals run using two different ILS for the 24 February 1998 spectrum number ai242005. (a), (b) and (c) show fits overlying the measurement in three microwindows, for a broad portion of the HCl band, a single pair of HCl lines and a single HF line, respectively. The residuals shown in (d), (e), and (f) attest to the better fit provided by the ILS which used a 20 mrad FOV (black line). The model ILS is not perfect, though, as some residual peaks remain in (d). Retrieved amounts and errors are summarised in Table 3-1.

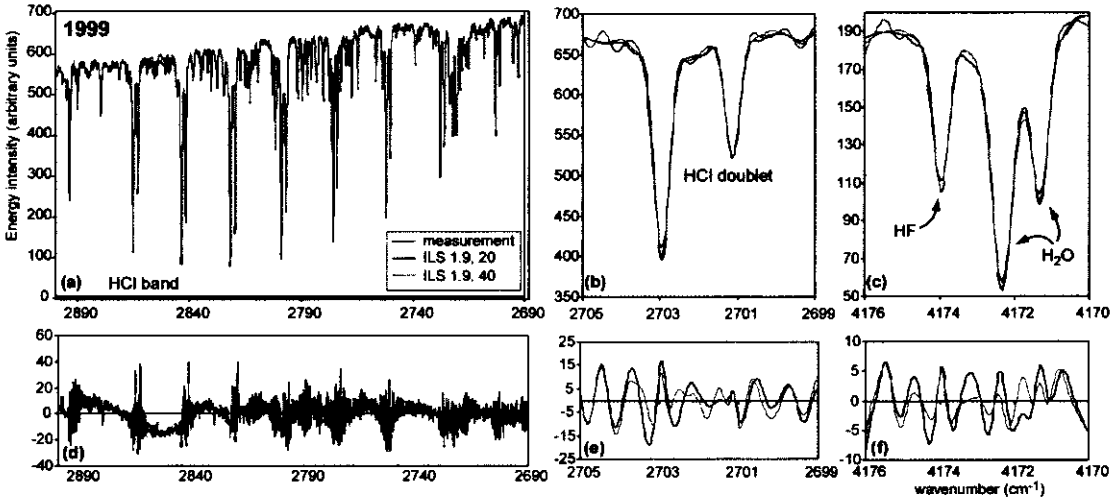

Figure 3-3: Retrievals run using two different ILS for the 14 March 1999 spectrum number ai143055, displayed in a similar way to figure 3-2. The measurement overlain by the two fits is shown in three microwindows in (a), (b) and (c), for a broad portion of the HCl band, a single pair of HCl lines and a single HF line, respectively. The residuals shown in (d), (e), and (f) attest to the better fit provided by the ILS which used a 40 mrad FOV (grey line), in contrast to the 20 mrad ILS used for the 1998 measurement in figure 3-2. The residual peaks in (d) show that possibly an even broader ILS should be used. Retrieved amounts and errors are summarised in Table 3-1.

The differences in retrieved amounts caused by changing the ILS used in these retrievals are summarised in Table 3-1. Although the best residuals in figures 3-2 and 3-3 are visually obvious, the retrieved errors do not correlate with this observation: for both the 1998 and 1999 spectra the retrieved error is smaller when the broader ILS is used. The retrievals over small (6 cm^{-1}) microwindows are more susceptible to changes in ILS than those over a broader microwindow,

with the change in ILS causing more than 30 % difference in amount for the 1999 single HF line. There is greater uncertainty associated with retrievals of the 2702 cm^{-1} HCl line and the 4174 cm^{-1} HF line because these are weak lines within the absorption bands for each species, and also because narrow windows contain fewer spectral points with which to constrain the fit. Whereas measurements from high-resolution instruments with well-characterised instrument line shapes can be accurately retrieved using single, narrow lines (e.g. Burton 1998), it is safer with the lower-resolution MIDAC to retrieve concentrations for HCl and HF using several lines together, as this minimises the effect of the badly characterised ILS. The best choice of microwindow for HCl retrieval is further complicated by saturation in the strongest lines, this saturation varying in consecutive spectra as gas concentration changes (section 3.2.1.1).

	microwindow	2690–2900 cm^{-1}		2699–2705 cm^{-1}		4170–4176 cm^{-1}		
	background polynomial	3		3		3		
	retrieved gases	HCl, H_2O, CH_4		HCl, H_2O		HF, H_2O		
	ILS	**ret HCl**	**HCl err**	**ret HCl**	**HCl err**	**ret HF**	**HF err**	**best resid**
1998	1.9, 20	1.08×10^{19}	0.02957	1.18×10^{19}	0.1051	2.42×10^{18}	0.2064	y
	1.9, 40	1.11×10^{19}	0.02894	1.40×10^{19}	0.1047	3.11×10^{18}	0.1982	
	% diff	2.97		18.39		28.40		
1999	1.9, 20	1.02×10^{19}	0.02623	8.63×10^{18}	0.1064	1.94×10^{18}	0.2391	
	1.9, 40	1.06×10^{19}	0.02561	1.03×10^{19}	0.1053	2.57×10^{18}	0.2264	y
	% diff	3.94		19.67		32.87		

Table 3-1: Retrieved amounts (in molecules per cm^2) and errors from the retrievals depicted in figures 3-2 and 3-3. Retrievals of single absorption lines are more affected by choice of ILS than broad-band retrievals.

Providing that more than one line is fitted, and that a relatively good choice of ILS is made, then Table 3-1 indicates that the retrieved amounts will be within 3-4 % error. In practice, I used a 20 mrad FOV for the 1998 measurements and 40 mrad for those from 1999. Attempts to achieve a greater level of accuracy in the ILS were unnecessary because the ILS could change from one spectrum to the next in a set of consecutive measurements as described below.

The possible causes for general deterioration of the instrument line shape are related to both the IR source and the spectrometer. Given the harsh environments in which it is used, and the amount of travelling that it has undergone, the MIDAC appears surprisingly robust. The ILS has changed only slightly (although noticeably) from the nominal parameters, despite all the factors which could affect it.

3.1.2.2 Evidence for varying ILS in consecutive field spectra

Superimposed on the gradual deterioration of the ILS from 1998 to 1999 there are further inconsistencies in the spectra. In a series of spectra collected consecutively using the IR lamp source, three kinds of variation are visible. The *first* is variation in the strength of absorption lines, which is expected as the wind blows different amounts of volcanic gas into the optical path. The *second* is variation in the strength of the energy signal reaching the detector, seen as changes in maximum energy intensity for the full spectrum. This is attributed to variable misalignment of lamp and spectrometer caused by the wind, to the varying amounts of absorbing and scattering particles in the optical path, and perhaps also to temperature pulsing of the plume itself. There may be a trade-off in the choice of optimum pathlength, with longer paths providing higher absorption signal since they contain more gas molecules, while shorter paths ensure less variation in the received source energy. The *third* is small differences in absorption lineshape, seen most obviously in the residuals from consecutive spectra in a systematic retrieval. Figure 3-4 shows measurements and residuals for three consecutive spectra collected on 24 February 1998.

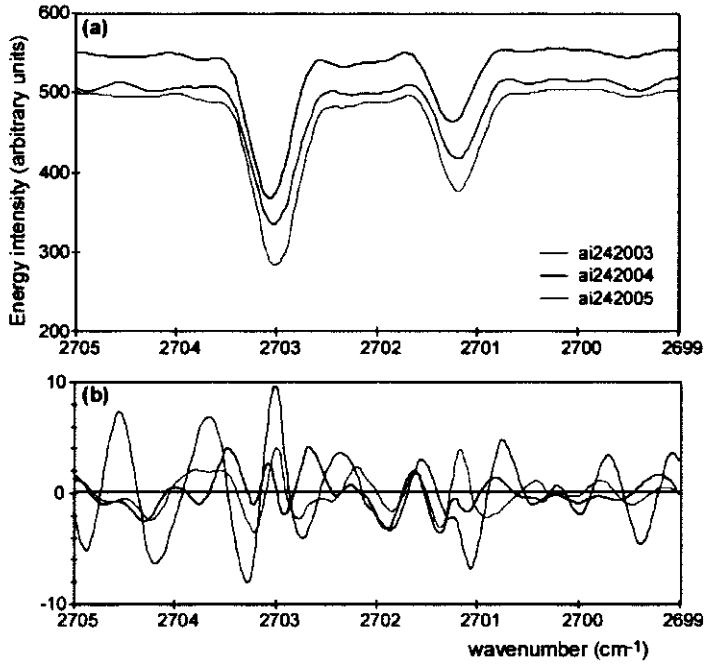

Figure 3-4: Three consecutive spectra, for which the total collection time was about two minutes, collected on 24 February 1998 using the active source. (a) Microwindows of the raw measurements, at different levels because the energy intensity was varying. The HCl band is used because it shows individual lineshapes more clearly. (b) Residuals from a retrieval using an ILS calculated from 1.9 cm OPD and 20 mrad FOV. Differently shaped residuals indicate that the effective ILS is different for each spectrum.

This "random" variation in lineshape is difficult to understand. While some variation in the average temperature of gas seen by the instrument is likely on these timescales, temperature is unlikely to have a visual impact on the broad lineshape imposed by the instrument. Conceptually, it is possible to provide reasons as to why the ILS itself could vary in consecutive spectra, chiefly because the energy function reaching the detector is liable to changes due to wind misalignments

and variable optical path. However, despite attempts to link the visual variations in residual with either, or both, maximum energy intensity in the spectrum or gas concentration, I have been unable to find a convincing correlation. Small changes to the FOV constraint used in the ILS can produce improvements in the residual for a given spectrum, but for subsequent spectra, the residuals may be made worse by this same change. In general, watching the residuals during a systematic retrieval provided a good indication as to how well the chosen ILS was performing; only if similar residual peaks appeared consistently was there a need to change the ILS in use.

3.2 Retrieval Parameters

Practical considerations in the retrieval of infrared spectra include not only dealing with inconsistencies encountered in the raw data, outlined above, but also coping with the uncertainty introduced with choice of input parameters for the retrieval procedure. The two factors with greatest impact are choice of retrieval microwindow and polynomial fit to the background curve within the chosen window. Microwindow is of particular significance for HCl and HF. Background polynomial fit has little bearing on retrieved amounts of SO_2, HCl and HF, but affects the CO_2 retrieval significantly. These issues are discussed in the subsections below.

Estimates of the external parameters temperature and pressure are required as input information in the retrieval. SO_2 calibration tests (Chapter 2) showed that pressure varying over the range encountered for all the different measurements at Masaya Volcano introduced less than 0.5 % error in retrieved gas amounts. For this reason, a single pressure was used in all retrievals for spectra of a similar nature (i.e. 950 mb for active summit, and other appropriate values for solar summit, active downwind and solar downwind). The temperature of the volcanic gas could not be measured accurately. For active summit measurements the gas was up to 10 °C warmer than ambient and so a single temperature of 305 K was used in all active summit retrievals. Estimates of the correct temperature to use in solar retrievals are subject to greater uncertainty, but 295 K was used for summit solar measurements and 290 K for downwind solar measurements.

3.2.1 Microwindows

The microwindow used for the SO_2 retrieval was confirmed by the calibration tests in Chapter 2. For HCl and HF, the optimum choice of retrieval microwindow was harder to determine, for several reasons. Both of these gases have discrete absorption lines of varying strengths across broad regions of the infrared spectrum. The lines often overlap with H_2O absorptions, and in the case of HCl, saturation of the strongest lines occurs for high gas concentrations. No calibration spectra for these gases were available. Retrieved amounts and errors for HCl and HF are dependent upon which portion of each band was chosen for the retrieval. In the following subsections I discuss the effect of different microwindows on the retrieval of these gases.

3.2.1.1 HCl retrieval choice of microwindow

HCl lines occur across the entire region from 2600 to 3200 cm^{-1}. Lines within the R branch between 2600 and 2900 cm^{-1} are much less affected by problems of H_2O contamination than the P branch, and so this region is favoured for HCl retrievals. The relative intensity of the lines varies across the branch with strongest lines around 2790-2850 cm^{-1} and weaker lines below 2760 cm^{-1}. Each line is a doublet owing to the natural abundance of ^{35}Cl to ^{37}Cl in a ratio of roughly 3:1. If the absorption is not saturated, then the relative intensities of the isotopic lines in each doublet should be in roughly 3:1 proportions. Figure 3-5 shows a measurement of the R branch.

Comparison of the isotopic proportions observed in the weak lines with those of the stronger lines reveals an apparent discrepancy. This effect has two causes. The first is that the lines are not measured at infinite resolution, which results in reduction of intensity. The second is that the stronger lines in the middle of the band are affected by saturation: the stronger ^{35}Cl line is "clipped" more than its corresponding ^{37}Cl line. If isotopic proportions appear to vary across the HCl band then possible saturation is indicated.

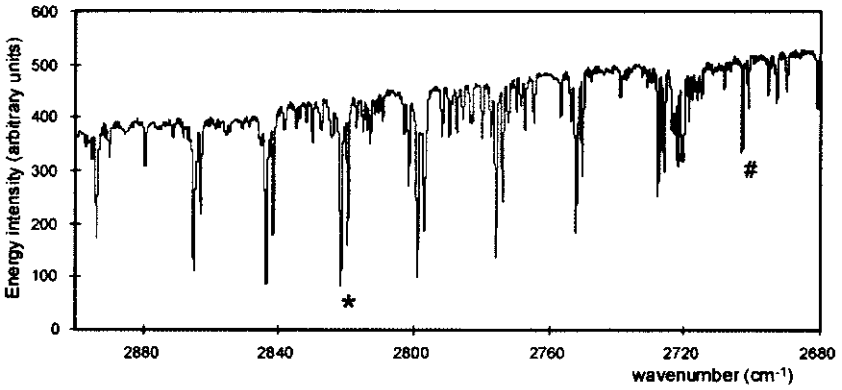

Figure 3-5: Field measurement (raw single-beam spectrum) collected using the active source at Masaya Volcano on 24 February 1998 showing most of the R branch of the HCl absorption band. HCl doublets are obvious and the additional absorptions are H_2O lines. Weak HCl lines are marked in blue and strong lines in red. Comparing the doublets marked with a # and an asterisk, a difference in relative intensity of the $H^{35}Cl$ line and the $H^{37}Cl$ line can be seen, with the asterisked doublet showing an apparently higher proportion of ^{37}Cl to ^{35}Cl owing to "clipping" (saturation) of the stronger line.

This illustrates a difficulty in dealing with the variable and often high gas concentrations encountered in measurements at the summit of Masaya. In raw spectra, the strongest HCl lines are frequently affected by saturation, but the weakest HCl lines provide little constraint for the retrieval (equivalent to a lower signal to noise). The problem is demonstrated in figure 3-6. A retrieval utilising only weak lines returns higher gas amounts than a retrieval using only strong lines (figure 3-6(b)), with the result of a maximum 7 % difference in SO_2/HCl ratio. A retrieval across a broad window is intermediate between the two. The retrieval on weak lines has a smaller correlation coefficient than the other two, indicating greater scatter in data points arising from the weaker "signal" in these lines.

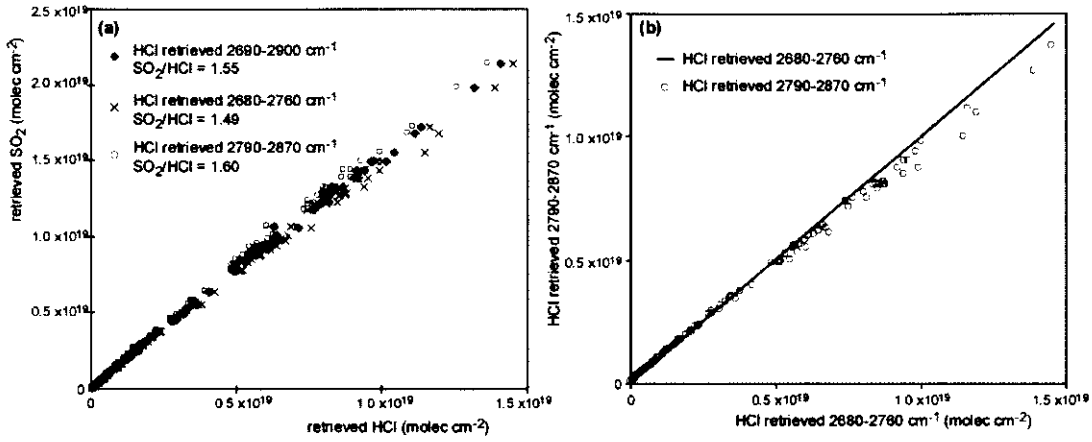

Figure 3-6: (a) A plot of retrieved amounts of SO_2 and HCl from 90 spectra collected on 28 February 1998. HCl was retrieved over three different microwindows. A broad window from 2690-2900 cm^{-1} returned amounts shown as filled diamonds. A window (e.g. the blue curve in figure 3-5) containing only weak HCl lines from 2680-2760 cm^{-1} returned amounts shown as blue crosses, while a window (e.g. the red curve in figure 3-5) containing only strong HCl lines returned amounts shown as red open circles. Using only strong lines results in smaller retrieved amounts than using only weak lines, with the broad microwindow an intermediate. There is greater scatter in the results using the weak lines reflected in a smaller correlation coefficient for this trend, and arising because the relative signal in weak lines is less. The difference in SO_2/HCl ratio calculated from the blue crosses and the red circles is 7 %. (b) HCl retrieved using only strong lines plotted against HCl retrieved using only weak lines. Retrievals of the strong lines result in underestimates at the higher concentrations, because of saturation.

The SO_2/HCl ratios calculated in figure 3-6(a) were 1.55 for the 2690–2900 cm^{-1} window, 1.49 for the 2680–2760 cm^{-1} (weak lines) window, and 1.60 for the 2790–2870 cm^{-1} (strong lines) window, with standard errors of 0.0053, 0.0069, and 0.0055, respectively. At the level of statistical calculation, these ratios are different, but considering the scale of error associated with the retrieval (approximately 5 %, following section 2.4), the numbers are equal, within error of the intermediate value.

Since there are no calibration spectra available to confirm which microwindow returns the most accurate gas amounts, it seems most sensible to use the broad microwindow in order to balance out problems associated with using either strong or weak lines only. If the ILS used in the forward model is accurate, then saturated lines should be fitted well in the retrieval along with weaker lines. Residuals indicate when the fit across the band is poor since residual peaks remain over some lines and not others. This may be due to small changes in ILS from one spectrum to the next as well as saturation effects. However, problems associated with fitting saturated lines cannot be very severe since the points on SO_2-HCl plots do not curve off towards constant HCl at high concentrations.

3.2.1.2 HF retrieval choice of microwindow

The P branch of the HF absorption band consists of 6 narrow lines in the region from 3990-4180 cm^{-1} (figure 3-7). This region is strongly contaminated with H_2O lines and at the resolution of the

MIDAC spectrometer, all but one of the HF lines are inseparable from neighbouring H_2O. The only line that does not overlap with H_2O is at 4174 cm^{-1}, but this is a very weak absorption. Saturation of the HF lines is not a problem as it was for HCl, since typical amounts of HF are much less. However the water contamination of most of the lines increases uncertainty on the retrieved amounts so that retrieved errors are 4-5 times greater for HF than for HCl.

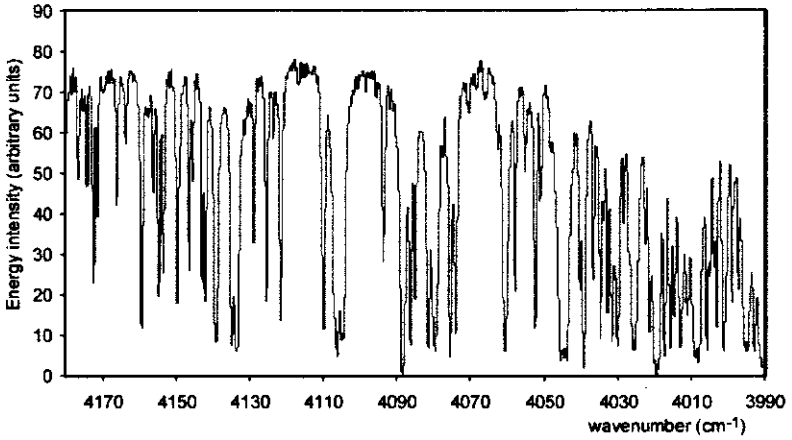

Figure 3-7: A portion of a field spectrum collected at Masaya Volcano on 24 February 1998, containing 6 HF lines at approximately 4000, 4038, 4075, 4110, 4142 and 4174 cm^{-1}. All other lines are H_2O absorptions. The line at 4174 cm^{-1} highlighted in red is the only one which does not overlap with H_2O lines at this resolution, but unfortunately this is the weakest line in the band.

The microwindow used for HF retrieval strongly affects the retrieved gas amounts, as shown in figure 3-8, where HF retrieved using different windows is plotted against retrieved HCl. A broad window containing the whole branch from 4000-4180 cm^{-1} results in the strongest correlation with retrieved HCl. A window from 4170-4176 cm^{-1} containing the least contaminated HF line results in higher retrieved amounts and a weaker correlation, arising because the weak line provides relatively little constraint on HF, and the narrow window provides little constraint on neighbouring H_2O. Use of this window provides erratic results: for some datasets it resulted in amounts that were similar to or less than those retrieved with the broad window. An intermediate window from 4050-4150 cm^{-1} containing 3 strong HF lines results in lower retrieved amounts.

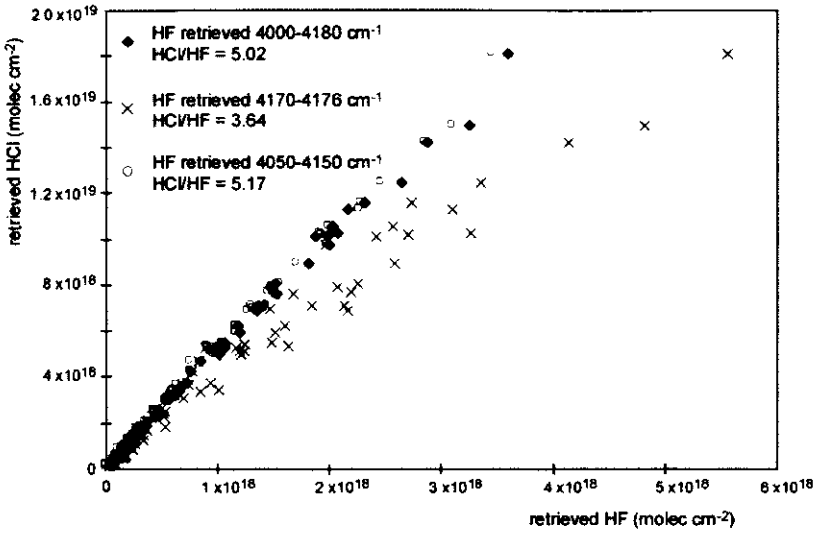

Figure 3-8: A plot of retrieved amounts of HCl and HF from 75 spectra collected on 14 March 1999. HCl was retrieved using a window at 2690-2900 cm^{-1}. HF was retrieved over three different microwindows. A broad window from 4000-4180 cm^{-1} returned amounts shown as filled diamonds. A window from 4170-4176 cm^{-1} containing the one least-contaminated HF line returned amounts shown as blue crosses, while a window from 4050-4150 containing strong HF lines returned amounts shown as red open circles. The results using the single weak HF line show much greater scatter, which is reflected in a smaller correlation coefficient for this trend. There is only a small difference between the retrievals using the broader windows, although the correlation coefficient for the 4000-4180 cm^{-1} window is marginally better.

Since no calibration spectra are available to confirm which is the most accurate HF retrieval, I have chosen to use the broad 4000-4180 cm^{-1} window in systematic spectral analysis. The least-contaminated line at 4174 cm^{-1} should be included, despite the fact that on its own it cannot constrain the retrieval adequately, and by making use of the stronger HF lines in the rest of the branch, the signal to noise is maximised.

3.2.2 Background curve polynomial fit

The background response curve within the selected retrieval microwindow is fitted using a low-order polynomial curve. If the background polynomial is allowed too many parameters then correlations within the retrieval matrix can arise. For relatively broad microwindows, the polynomial order makes little difference to the retrieved amounts: a third order curve is used for the HCl retrieval and fourth order for the HF retrieval. SO_2 is retrieved over a much smaller window (2480-2520 cm^{-1}), but a fourth order polynomial is used here because it is in a region close to the strong CO_2 band at 2300-2400 cm^{-1}.

For very small windows, the background curve used in the model can strongly influence the retrieved amount. CO_2 was retrieved over 2075-2080 cm^{-1} because this window contained the maximum variation in CO_2 signal from the line centred at 2077 cm^{-1}, and returned the smallest retrieved errors and most accurate amounts (compared to global atmospheric average) in tests of

a range of microwindows. The best visual fit between raw spectrum and model was achieved using an order 3 background polynomial (figure 3-9).

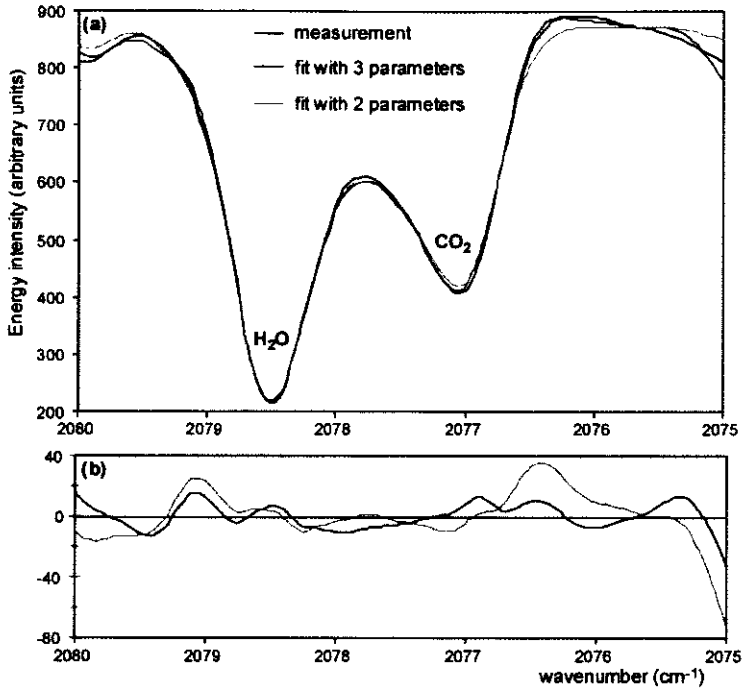

Figure 3-9: (a) A portion of a spectrum collected on 14 March 1999 at Masaya volcano (measurement is red curve). The weak CO_2 line at 2077 cm^{-1} is contaminated by H_2O absorptions, and so both are fitted. Two retrievals were run during which all variables were kept the same except for the background polynomial fit. The black line is the fit using an order 3 polynomial to fit the background curve, and the grey line is the fit using an order 2 polynomial. (b) Residuals from the fits in (a), using same colour key. The residual from the order 3 background fit is better. Retrieved amounts of CO_2 are greater using the order 3 polynomial.

Although the visual difference in fits using the different polynomials is only small, there is a significant difference in the retrieved amounts, shown in figure 3-10.

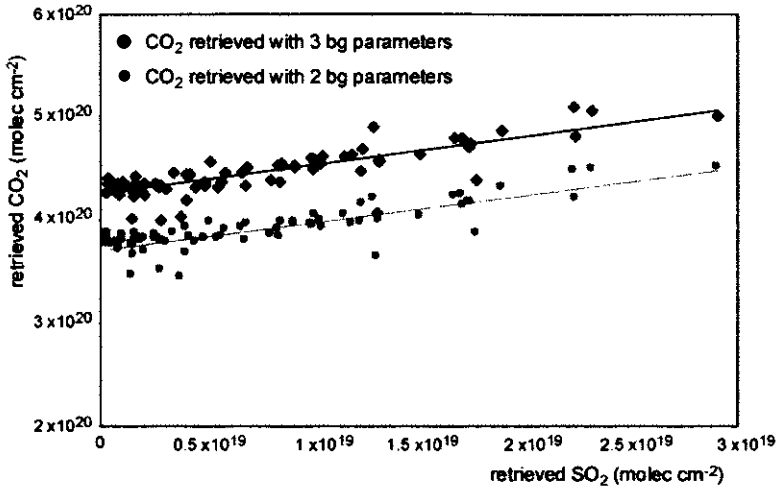

Figure 3-10: Retrieved amounts of CO_2 and SO_2 for 75 spectra collected on 14 March 1999. Although the visual difference between the fits in figure 3-9 is only small, there is a significant difference in the amounts of CO_2 retrieved depending on the order of polynomial. The intercept on the CO_2 axis indicates that the atmospheric CO_2 concentration calculated from these data is 316 ppm for the order 2 retrieval and 362 ppm from the order 3 retrieval. The global atmospheric average is approximately 365 ppm.

An independent test confirms that the retrieval using a third order polynomial is better. The background CO_2 concentration can be calculated from the intercept on the CO_2 axis on a graph like figure 3-10. The background CO_2 concentration implied by the data retrieved using the order 2 polynomial is much less than the global atmospheric average, whereas the retrieval using the order 3 polynomial implies a background concentration much closer to the expected value. The CO_2 data presented in this thesis were retrieved using a third order polynomial fit to the background.

3.2.3 Retrieval parameters for spectra collected using the solar source

Spectra collected using the solar source differ from active spectra in that the path length through the atmosphere is much longer, although the amount of volcanic gas in the optical path is similar. This results in much stronger contamination from absorption lines of atmospheric gases, while the volcanic "signal" is unchanged. Atmospheric gases such as CH_4 and N_2O cause significant absorptions in the solar spectra, whereas they are present in such small quantities in the short path active spectra that they were neglected in those retrievals. The long path through the atmosphere makes retrieval of the volcanic CO_2 component from solar spectra impossible. Additionally, there are sun absorptions present in the measurement, which are modelled in the retrieval from a portion of the ATMOS sun spectrum.

The same microwindow, 2690-2900 cm^{-1}, as that used in the short path retrieval was used for solar retrievals of HCl. Much stronger atmospheric contamination was visible, and both CH_4 and N_2O were fitted along with HCl and H_2O in this window.

For SO_2, the window from 2480-2520 cm^{-1} was used, and CH_4 and N_2O were fitted along with SO_2, H_2O and CO_2. H_2O absorptions in this window were constrained from the amounts retrieved in the HCl window, and CO_2 absorptions were calculated from the appropriate AMF assuming an atmospheric concentration of 365 ppm.

The microwindow for HF from solar spectra was reduced to 4030-4180 cm^{-1}, compared with the 4000-4180 cm^{-1} window used in short path retrievals. The longer atmospheric path means that H_2O absorptions frequently saturate the spectrum up to about 4030 cm^{-1}. Throughout this window, and especially for high AMF, saturated atmospheric absorptions resulted in loss of information, and consequently greater scatter in retrieved HF from solar spectra. CH_4 was also fitted in this window.

The same ILS as that used in contemporaneous active measurements was used for the solar retrievals. Although any internal misalignments contributing to the ILS are constant in both measurements, it is unlikely that *exactly* the same ILS is appropriate for active and solar retrievals, due to their different source functions and signal levels. However, it is much more difficult to check the ILS on single lines in the solar data due to the high levels of atmospheric contamination. And, whereas the ILS was a significant contribution to the error in short path retrievals, for solar retrievals, the increased "noise" from atmospheric absorptions is a more important contribution to the error. Thus the use of the same ILS in both active and solar retrievals is justified.

The main difference resulting from retrieval of solar compared to active data was an increase in retrieved error, which is attributed to differences in atmospheric contamination between the two types of spectra. Retrieved errors are discussed below.

3.3 Retrieved errors

The retrieval procedure returns an error associated with the gas amount retrieved from each spectrum (section 2.2). The retrieved error is a measure of the confidence with which the best-fit forward model spectrum is equal to the measured spectrum. Mathematically, the error is calculated from the standard deviation of the residual across the microwindow, but a number of factors influence this. Signal-to-noise in the measurement is important and this depends upon background noise (which varies in different regions in the spectrum) and the strength of the absorption line of interest (which varies with amount of gas present, energy intensity and the nature of the line itself). The size of retrieval microwindow is important because this controls the number of data points available for the analysis. Increasing the order of polynomial chosen to fit the background increases the error in the retrieval (see Chapter 2, Section 4). Finally the choice of ILS affects the shape of the forward model and contributes to the residual. As well as the retrieved error, there are further uncertainties in estimates of plume temperature and pressure and associated with the line parameter data (HITRAN96) used to construct the forward model.

In this section, I assess how the retrieved errors behave for the range of data encountered in the thesis. Estimates of plume temperature and pressure, and uncertainties in the line parameter data are additional contributions to the error associated with the retrieved amounts, and are assessed separately.

3.3.1 Retrieved error from active spectra

For active measurements at the summit of Masaya, the retrieved errors are inversely proportional to retrieved amounts of gas, as shown in figure 3-11.

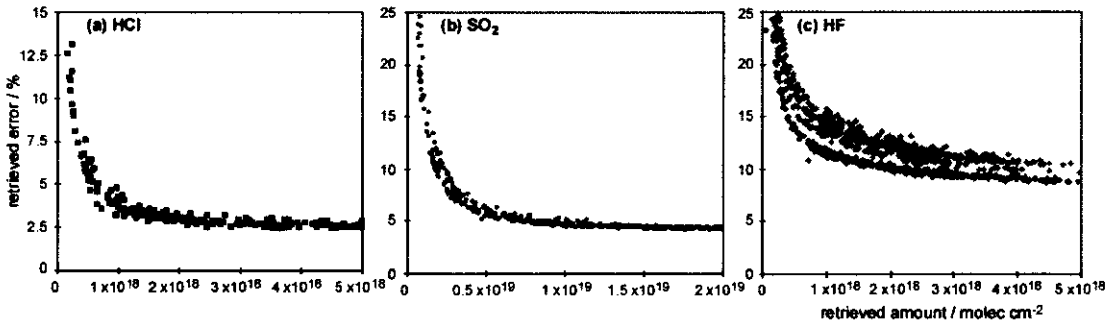

Figure 3-11: Retrieved errors as percentages plotted against retrieved gas amounts in molec cm^{-2} for (a) HCl, (b) SO_2, and (c) HF. Note changes in scale. The data in this figure are from spectra collected using the lamp at the summit of Masaya volcano in 1999, and have been selected to demonstrate the trends. The greater scatter of the HF data reflects the strong contamination by variable concentrations of atmospheric H_2O in this band. 1998 data follow the same trends.

The pattern is the same regardless of gas species: for very low gas concentrations, the error is high, tending towards numbers greater than 100 %, off the scale of figure 3-11. As gas

concentration (and therefore signal to noise in the spectra) increases, the error reduces, tending towards a constant value which is dependent upon the gas in question. This pattern provides a method for estimating detection limits (Table 3-2).

	Detection limits (molec cm^{-2}) within errors of:			**Smallest retrieved error**	
	20 %	10 %	5 %	Error (%)	Amount (molec cm^{-2})
HCl	1×10^{17}	3×10^{17}	7×10^{17}	2.5	$> 3 \times 10^{18}$
SO_2	8×10^{17}	2×10^{18}	8×10^{18}	4	$> 1 \times 10^{19}$
HF	4×10^{17}	3×10^{18}	---	10	$> 3 \times 10^{18}$

Table 3-2: Summary of the errors and retrieved gas amounts for Masaya active field measurements.

Within 10 % error, HCl has a detection limit of 3×10^{17} molec cm^{-2}, SO_2 has a detection limit of 2×10^{18} molec cm^{-2}, and HF has a detection limit of 3×10^{18} molec cm^{-2}. The differences in these limits can be attributed to a combination of line strength (the HCl and HF absorptions are stronger lines than that for SO_2) and contamination by atmospheric lines (the HF lines are strongly contaminated by H_2O absorptions). In 1998, 64 % of the active data fell below the 10 % error limit for SO_2 and 82 % of the data fell below that limit for HCl. In 1999 the statistics were apparently better: 92 % of the data fell below the 10 % error limit for SO_2 and 99 % of the data fell below that limit for HCl. The reason for this apparent improvement was that a greater proportion of the spectra in 1999 contained high gas amounts. As the gas concentrations increase (figure 3-11), the error tails off to constant values of 2.5 % for amounts greater than 3×10^{18} molec cm^{-2} for HCl, 4 % for amounts greater than 1×10^{19} molec cm^{-2} for SO_2, and 10 % for amounts greater than 3×10^{18} molec cm^{-2} for HF.

Retrieved gas concentrations for measurements made downwind in active mode were typically less than 1.8×10^{17} and 3.5×10^{17} molec cm^{-2} for HCl and SO_2 respectively, quantities which fall outside the 10 % error detection limit. The smallest retrieved errors from downwind active measurements of HCl and SO_2 were 15 % and 50 %, respectively. Despite the high error values, retrieved amounts of HCl and SO_2 correlated well (e.g. figure 3-15, below).

Retrieved amounts of H_2O and CO_2 in active data showed relatively little variation because the atmospheric contribution of these gases to the optical path was much greater than the volcanic contribution. Similarly, the retrieved errors for these two gases show much less variation than that for the pure volcanic gases. Retrieved error for H_2O from active spectra was 3-4 % on average, while that for CO_2 was 20 %. The high error value for CO_2 reflects both the fact that the CO_2 line at 2077 cm^{-1} is relatively weak, and that it also overlaps with H_2O lines.

3.3.2 Retrieved error from solar spectra

Retrieved errors from solar spectra (figure 3-12) follow a similar trend to the active spectra, but larger error values and greater scatter reflect the increased "noise" due to stronger atmospheric absorptions.

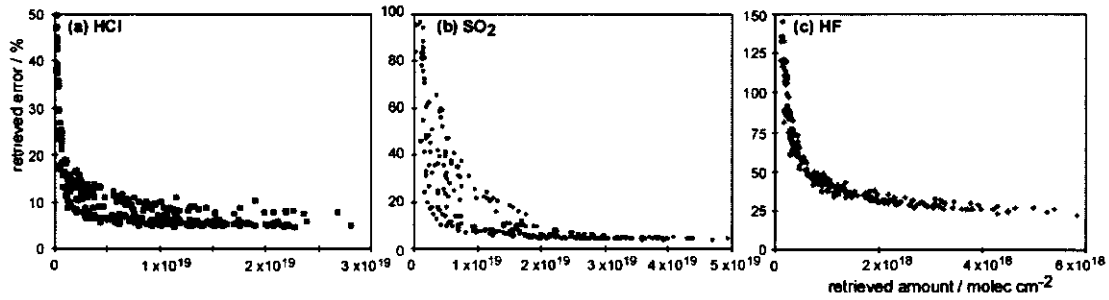

Figure 3-12: Retrieved errors as percentages plotted against retrieved gas amounts in molec cm^{-2} for (a) HCl, (b) SO_2, and (c) HF. The data in this figure are from spectra collected using the solar source at the summit of Masaya volcano in 1999, and have been selected to demonstrate the trends. Compare with figure 3-11, and note different scales on axes.

For solar spectra, retrieved errors for SO_2 tail off to lower values than those for HCl: this is the opposite way round compared to the active spectra, and reflects the fact that there is less H_2O contamination in the SO_2 microwindow than in the HCl window. However, SO_2 errors are greater than HCl errors for low concentrations because of the weaker SO_2 line strength. Table 3-3 shows that detection limits for these solar data are much higher than for the active data summarised in Table 3-2. Solar HF retrievals are always subject to very large error due to the near saturation of that band by H_2O absorptions.

	Detection limits (molec cm^{-2}) within errors of:			**Smallest retrieved error**	
	20 %	10 %	5 %	Error (%)	Amount (molec cm^{-2})
HCl	8×10^{17}	4×10^{18}	1.8×10^{19}	5	$> 1.8 \times 10^{19}$
SO_2	5×10^{18}	1×10^{19}	2×10^{19}	4	$> 3 \times 10^{19}$
HF	---	---	---	25	$> 4 \times 10^{18}$

Table 3-3: Summary of the errors and retrieved gas amounts for Masaya solar field measurements.

Solar spectra collected downwind from Masaya typically contained less than 1×10^{19} molec cm^{-2} of SO_2 and less than 5×10^{18} molec cm^{-2} of HCl due to dispersal of the plume. Retrieved errors for these downwind measurements were higher than those from measurements at the volcano's summit, as expected for much lower gas concentrations.

Retrieved gas amounts from solar spectra have much higher associated errors than retrievals from active data because of the greater atmospheric path length and stronger interfering absorptions. For higher resolution instruments, the problem would be less severe since there would be less overlap of specific lines.

3.3.3 Error summary

Section 2.4 demonstrated that, for SO_2 at least, a 10 °C change to the temperature used in the retrieval could cause up to 3.3 % difference in the absolute retrieved amounts. Pressure estimates had a lesser effect, with a 50 mb change resulting in 0.5 % difference in retrieved amount. The same estimates of temperature and pressure were used in retrievals for the different gas species in any given set of spectra. Any error in the estimate of T and P will affect retrieved amounts of the different gases systematically, so that when gas ratios are considered, the effect will partly cancel out.

Estimates of the errors associated with the HITRAN line parameter database were also discussed in Chapter 2 and suggested to be ± 1–2 % for HCl, ± 2–5 % for HF, and ± 3.6 % for SO_2. Line parameter error is systematic for all retrieved amounts and results in calculated gas ratios being offset from the true volcanic composition by some systematic value.

A conservative combined error estimate for temperature, pressure and line parameter sources for a calculation of SO_2/HCl ratio can be determined by summing the separate contributions in quadrature. For the values suggested above, it is 5.3 %. The combined effect of the retrieved errors is variable depending on gas concentration, and whether the spectra are active or solar. For active data, the systematic error from temperature, pressure and line parameters is likely to be greater than the combined retrieved errors, whereas for solar data, retrieved error may be more important. Ultimately, the total error associated with retrieved SO_2/HCl ratios should be similar to or less than 10 %, and slightly more for ratios involving HF or CO_2. If gas concentrations are very low, then the uncertainty associated with a calculated ratio increases correspondingly.

3.4 Implications for analysis and interpretation of retrieved data

This chapter has highlighted a number of difficulties associated with the retrieval of gas concentrations from field data. The choice of input parameters, such as retrieval microwindow and order of background polynomial, affects the gas amounts retrieved. More fundamentally, because the quality of the measured spectra is not perfectly consistent, and the apparent lineshape changes, then gas amounts and ratios determined from systematic data retrieval have an associated random uncertainty. Retrieved errors reflect the "signal-to-noise" in the spectra, including noise from atmospheric absorptions, and are approximately equal in size to the systematic uncertainties associated with temperature, pressure and line parameter data.

Here, I comment on some implications of these uncertainties and the imperfect nature of the retrieval process. These implications are relevant to the detailed discussion of retrieved data in Chapters 4 and 5.

3.4.1 Scatter plots of retrieved gas amounts

The simple method of determining volcanic gas ratios from a set of retrieved data involves constructing scatter plots of the retrieved amounts of two different gases. In general, when data from sets of at least 50 spectra (collected over one observation period) are plotted up in this way, strong correlations are seen (R^2 greater than 0.9), and a tight fit to a straight line trend though the origin is defined (figure 3-13).

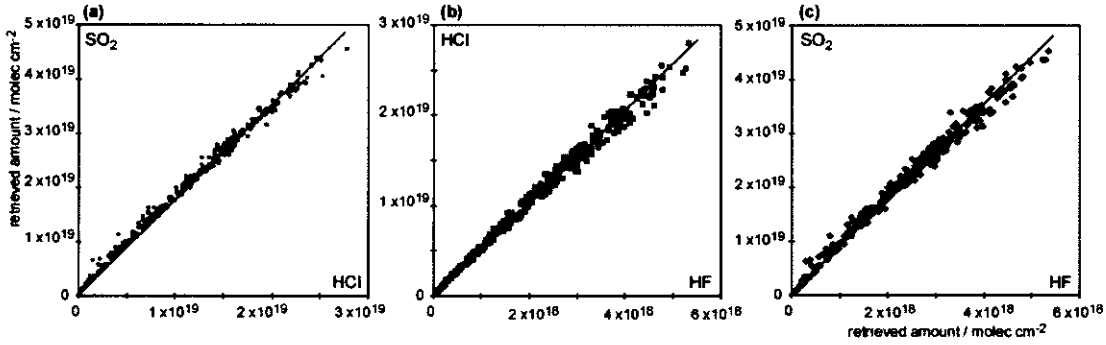

Figure 3-13: Scatter plots of retrieved amounts of gas (in molec cm^{-2}) for 320 spectra collected with the lamp source on 16 March 1999 at Santiago Crater. Each graph shows a least squares unweighted regression line forced through the origin. (a) SO_2 against HCl. Notice how points tend to scatter above the trend line at low concentrations and below the trend line at high concentrations. (b) HCl against HF. (c) SO_2 against HF, showing a similar distribution to (a).

However, on closer inspection, systematic variability in the scatter of points around the least squares regression line through the origin can be observed. In plots of retrieved SO_2 against HCl, points tend to scatter above the regression line at the low concentration end, and below the regression line at the high concentration end (figure 3-13(a)). This trend is present to a greater or

lesser extent in all similar graphs, but is much less pronounced in plots of retrieved HCl against HF (figure 3-13(b)).

If this curvature were confirmed as "real", then tropospheric mixing processes in the plume could be invoked to explain it. Instead, it cannot be isolated from some combination of uncertainties in the retrieval process. The problem appears to lie with retrieved SO_2 since the scatter in HCl-HF graphs is less polarised. Figure 3-13(a) has a similar appearance to figure 2-24 which plotted retrieved SO_2 against true concentration for calibrated tests of the MIDAC at the National Physical Laboratory. The SO_2 tests described in section 2.4 revealed that low gas concentrations were overestimated, while for concentrations greater than about 2×10^{19} molec cm^{-2} the retrieved amounts became underestimates. In that section, these errors were attributed to a tendency to maximise the SO_2 signal in the model at low concentrations when signal to noise in the measurement is low, coupled with an increasing effect, at high concentrations, of using an imperfect ILS to model high intensity lines.

One outcome of the trend observed in figure 3-13(a) is that if SO_2/HCl ratios are calculated from individual spectra, there is a weak correlation between ratio and retrieved gas concentration (figure 3-14). For this reason, I have been very cautious when considering apparent changes in gas ratio from one spectrum to the next. My preferred approach has been to derive average gas ratios across a range of concentrations, by means of regression lines, for sets of spectra. If ratios calculated from individual spectra are used, they are interpreted in the context of both the levels of gas in the spectrum and the other measurements collected at the same time.

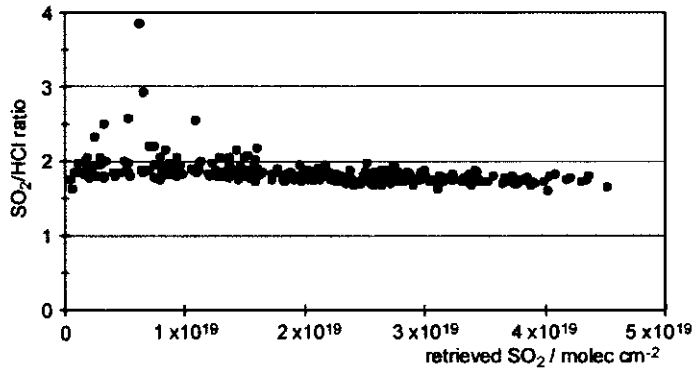

Figure 3-14: SO_2/HCl ratios calculated from the individual spectra used in figure 3-13 plotted against the retrieved SO_2 concentrations. There is a decrease in ratio at the higher concentrations for the same reasons as the trend in points away from the regression line of figure 3-13(a). See text for discussion.

Graphs involving retrieved HF show greater scatter of points overall, reflecting the higher errors associated with the HF retrieval (e.g. figure 3-11).

3.4.2 Retrievals of low gas concentrations

When spectra contain only weak gas absorptions, such as data collected downwind, relative errors are high. Strong trends between retrieved gas amounts are still achieved, despite large error bars constructed from the retrieved error (figure 3-15). This strong correlation is misleading because it inspires overconfidence in the value obtained for the SO_2/HCl ratio from a regression line.

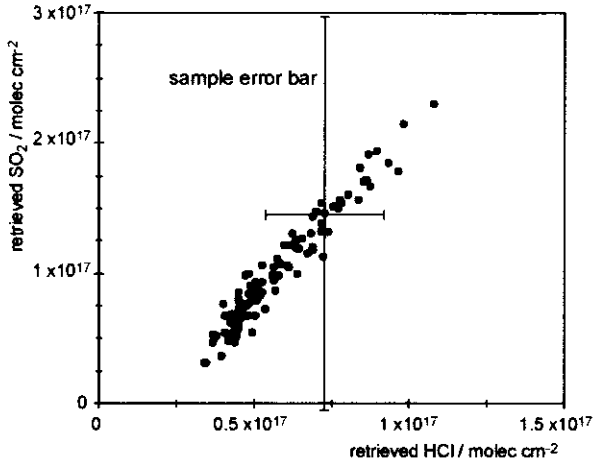

Figure 3-15: Retrieved amounts of SO_2 and HCl from 100 spectra collected with the active source 14 km downwind from Masaya Volcano on 11 March 1999. A typical error bar is shown.

The low amounts of SO_2 measured downwind using an active source are at the SO_2 detection limit estimated in Chapter 2 section 4 from the tests at NPL. The minimum detection limit in that section was estimated from the standard deviation of retrieved SO_2 for measurements when there was actually no SO_2 in the optical path, and was given a value of 10^{17} molec cm^{-2}. Yet the true detection limit for SO_2 must be lower than 10^{17} molec cm^{-2} since a strong trend is seen on plots such as figure 3-15. Figure 3-16 is one of the spectra from figure 3-15, and the SO_2 signal is just discernible above the noise although the retrieved amount was only 1.7×10^{17} molec cm^{-2}.

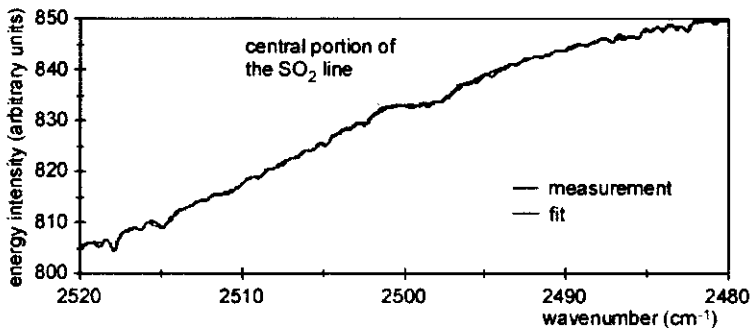

Figure 3-16: The SO_2 window in spectrum number ai113006 collected on 11 March 1999 using the active source. The SO_2 signal is still visible above the noise, although the retrieved amount of SO_2 is only 1.7×10^{17} molec cm^{-2}.

Although gas concentrations measured downwind are low, plots like figure 3-15 may still provide a good estimate of the SO_2/HCl gas ratio since the correlation is so strong. The offset of the regression line away from the origin is likely to be the result of a systematic offset in the retrieved amounts for SO_2 or HCl or both: the calculated ratio may, however, still be accurate. Low-concentration data collected downwind from Masaya Volcano are examined in greater detail in Chapter 4.

3.5 Spectra collected in passive mode

Volcanoes provide good locations at which to use IR spectroscopy since there are often sources of natural short-wave infrared radiation available, such as hot lava flows or domes (e.g. Mori *et al.* 1993). At Masaya Volcano, the central active vent was the hottest natural source available. Although pooled lava was not visible, strong incandescence suggested its presence at very shallow depth. In this section I discuss the results of spectra collected in passive mode at Masaya.

3.5.1 Collection of measurements

Passive measurements were made from the SW side of Santiago Crater for an unobstructed view of the vent (figure 3-17). During the night, a reflected glow within the vent was visible, implying temperatures similar to magmatic, about 1000 °C. The crater floor is about 150 m below the observation point, and so the path length for the measurements was approximately 200 m, given a viewing angle of about 45 ° from horizontal. Gas appeared to exit from the ~10 m diameter vent in "puffs", and then mixed rapidly with air, in a turbulent manner dependent upon strong convection within the crater and wind patterns.

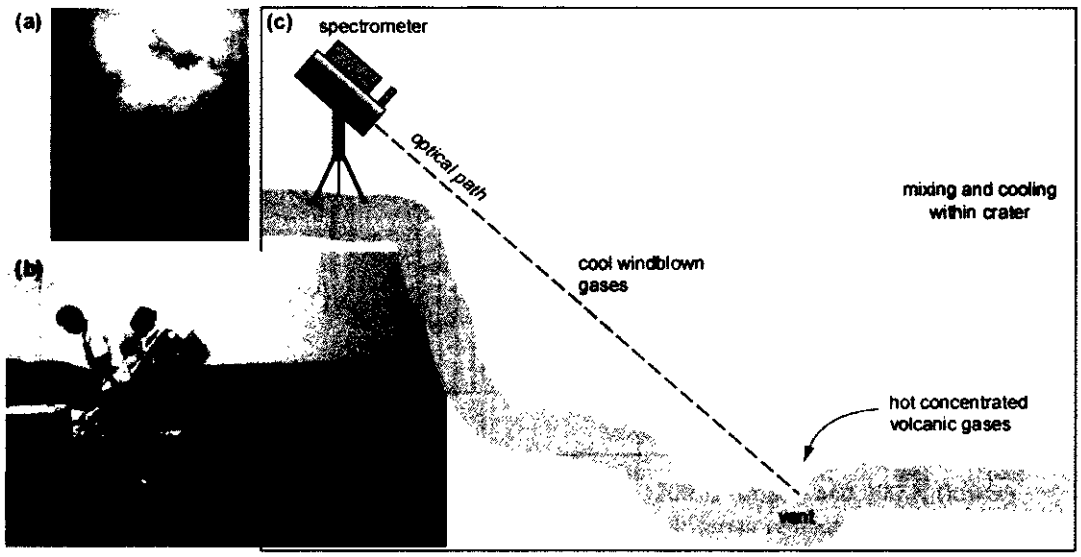

Figure 3-17: Collection of spectra at Santiago Crater using the vent as a passive IR source. (a) The active vent was about 10 m in diameter, issuing gas in "puffs". (b) Measurements from the crater rim in 1998. (c) Cartoon illustrating the geometry and conditions for passive data collection (not to scale). Turbulent mixing of the volcanic gas with air in the crater resulted in a highly variable distribution of gas along the optical path. *Photographs from the Peter Francis Collection.*

The high temperature source in the vent area may have been hot vent rocks, hot concentrated gases, reflected radiation from deeper in the conduit, or a combination of all three. Movement of the volcanic gas within the crater resulted in a rapidly changing distribution of gas along the optical path as spectra were collected: at times there was a clear view of the vent, at others clouds of gas obscured it.

Over the course of two field seasons at Masaya, I attempted passive measurements using other background sources, such as the interior crater wall and the clear sky. Spectra collected in these experiments were poor in quality: the volcanic gas in the optical path was too cool for IR emission, and the source radiation was too cool for gas absorptions.

3.5.2 Results from vent measurements

Because of the range of gas and temperature distributions possible along the optical path during passive data collection, individual spectra show a range of appearances, often changing markedly in consecutive measurements. The possibilities seemed to be derived from two end-member types of spectra, shown in figure 3-18.

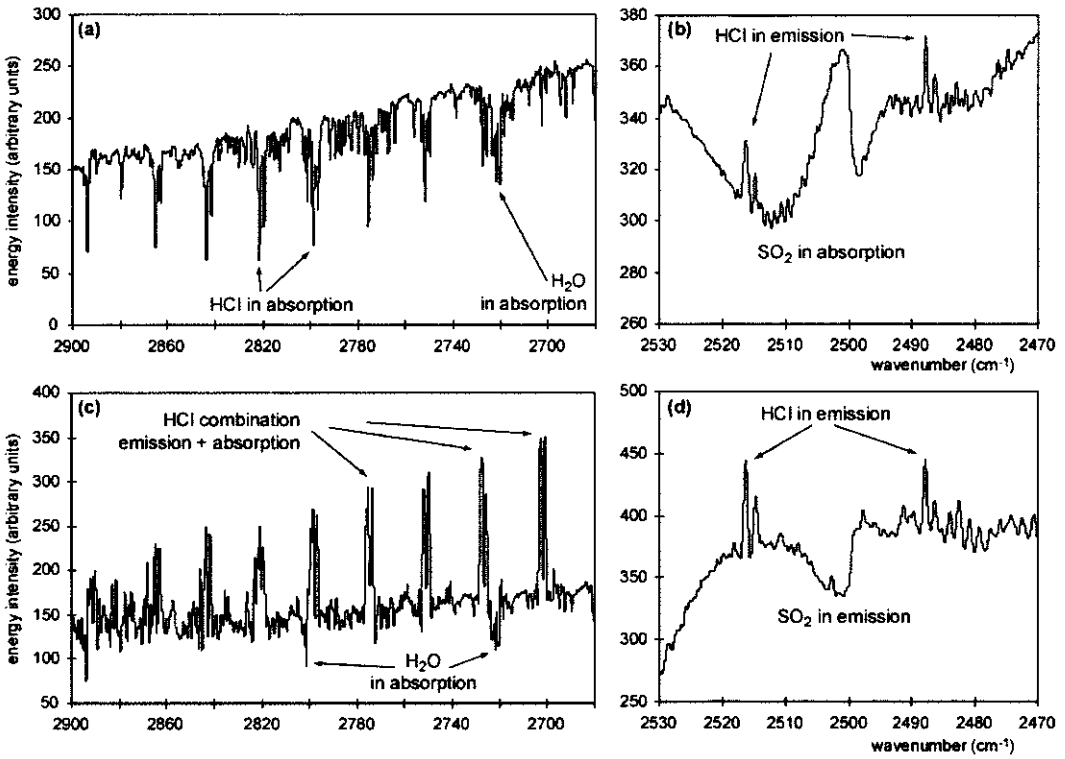

Figure 3-18: Typical spectra collected using the hot vent source. (a) and (b) are portions of spectrum number pi282006 collected on 28 February 1998, while (c) and (d) are portions of spectrum number pi203033 collected on 20 March 1998. (a) Absorption lines for HCl and H_2O are obvious, with little evidence for any emission. (b) The SO_2 feature is seen in absorption, but sharp HCl emission peaks are also present in this part of the spectrum. (c) There is evidence for H_2O lines in absorption, but very strong HCl emission lines occur across this band. (d) The SO_2 band is here seen in emission, with the sharp HCl emission peaks again obvious.

The spectrum shown in figure 3-18(a) and (b) is very similar in appearance to spectra collected with the active source, except for the presence of emission lines in the SO_2 microwindow. The spectrum in figure 3-18(c) and (d) is very different, with ubiquitous emission lines and the SO_2 band in emission. The differences between the two are associated with temperature changes of the source and the intervening gas.

When the vent source is relatively hot, and most of the gas along the optical path is relatively cold, then the volcanic gases absorb energy and spectra record lines in absorption. When the volcanic gases along the optical path are relatively hot (e.g. the wind has blown cooler plume out of the way), then they emit energy, and lines are seen in emission. Sometimes, lines at longer wavelengths (e.g. SO_2 at 2500 cm^{-1}) are seen in emission, while lines at shorter wavelengths (e.g. HCl around 2800 cm^{-1}) are in absorption, because the gas temperature is not quite high enough for emission at the shorter wavelengths to occur.

Spectra are complex because the population of individual lines varies with T, so that the spectral energy distribution within the HCl band is very different at 300 K compared to 1200 K (figure 3-19). In figure 3-18(b), absorption by cold SO_2 is dominant over emission by hot SO_2. However, at low (ambient) temperatures, HCl lines at these relatively long wavelengths are unpopulated; so absorption by cold HCl does not subtract from the hot HCl emission lines in this band.

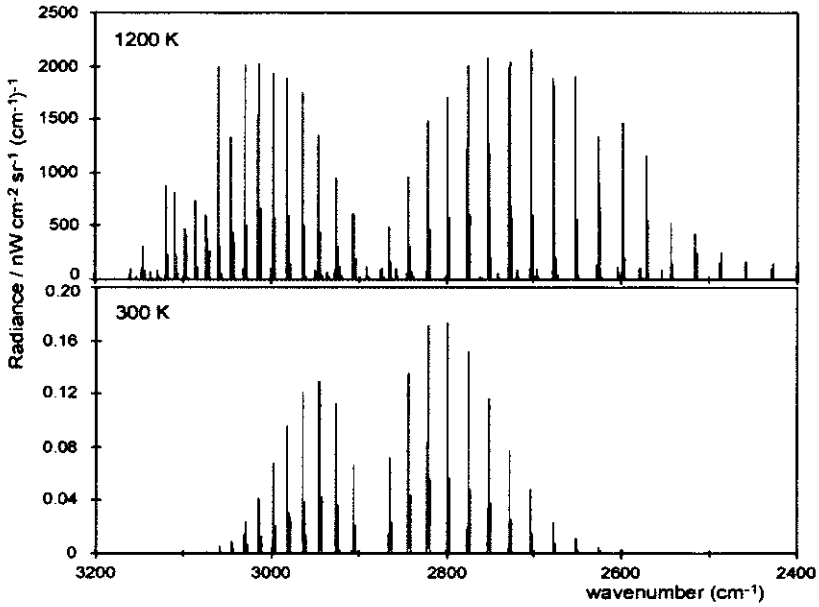

Figure 3-19: Pure HCl emission spectra simulated at 1200 K (upper) and 300 K (lower). Note the variation in spectral energy distribution at the different temperatures. HCl lines below 2550 cm^{-1} are only significantly populated when the temperature is greater than 500 K. Irregular line heights in the upper plot are the result of a finite number of sampling points across the spectrum, and not a function of temperature.

At its simplest, the spectral energy distribution seen in the passive measurements could be simulated through a three-layer model. First, calculate radiance from the hot vent (assumed to be black body), at temperature T_v. Second, calculate emission by hot gases, with column amount C_h at temperature T_h, and third, calculate absorption by cold gases, with column amount C_c at temperature T_c. Without some constraint on one or more of the temperatures, or the gas composition, it is difficult to retrieve a unique solution to fit the measured spectrum.

3.5.3 Discussion

While the spectra collected in passive mode can easily be used for qualitative identification of the major gas species, their quantitative treatment presents a much greater challenge. The retrieval scheme described in Chapter 2 has been developed for analysis of infrared absorption spectra, and cannot be used to fit lines in emission. Although the HCl and SO_2 absorptions, such as in figure 3-18(b), can be modelled, the sharp emission lines are not fitted at all. Furthermore, fitting absorptions in complex spectra such as these is subject to inherent ambiguities. The recorded spectral lines represent a combination of emission (near-vent) and absorption along the path. The gas amount retrieved is therefore not a simple measure of the number of gas molecules along the path, but the result of a balance between the number of molecules absorbing and the number emitting energy at that wavelength. Additionally, the proportions of molecules absorbing and emitting for SO_2 and HCl are unlikely to be exactly the same, affecting the gas ratio determined from a single spectrum.

In figure 3-20, a measured spectrum showing detail of HCl and SO_2 in emission is compared with a simple simulation of emission from a 3-component gas at 690 K, degraded to the resolution of the MIDAC spectrometer. The proportions of SO_2:HCl:H_2O were 1.6:1:100, typical for the gas composition at Masaya. Individual lines can be easily correlated across the two spectra. The hot gas exiting the vent is expected to be at near magmatic temperatures, and the 690 K used for the model, is well below expected values. This could have two explanations. The passive measurement is not a pure emission spectrum: it records also any subsequent absorption in the path. Moreover, the gas responsible for this spectrum may have moved away from the vent and cooled.

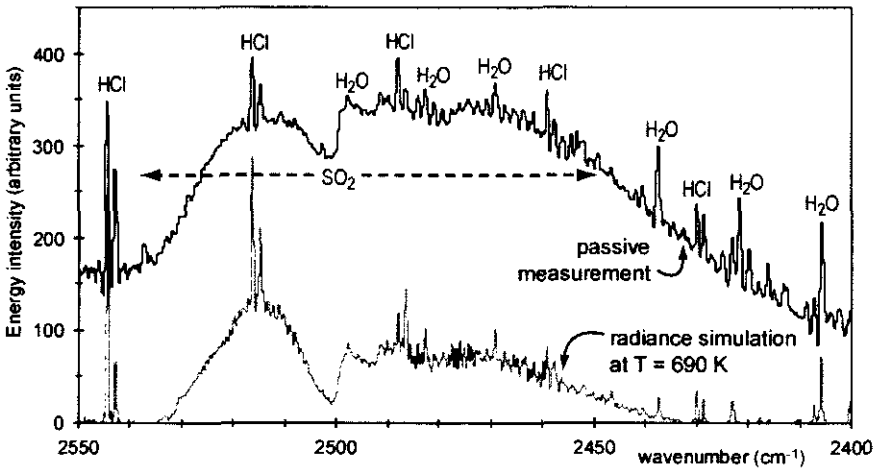

Figure 3-20: Comparison of a passive measurement collected on 20 March 1998 (spectrum pi203033) with a simple radiance simulation at 690 K for a gas mixture consisting of SO_2, HCl and H_2O in the proportions 1.6:1:100. Emission lines are correlated across the two spectra. The measurement spectrum has a background curve, while the model was calculated with a flat baseline.

The main difficulty with the passive measurements collected at Masaya was that the near-vent gas was hot and the vent source was not much hotter than the gas. For passive measurements where the source radiates at a much higher temperature than the gas in the path, (e.g. a glowing lava dome or a fresh lava flow), then difficulties associated with emission lines from the gas are much reduced. In that case, quantitative treatment of the spectra using the current retrieval algorithm would be more promising. A quantitative retrieval scheme to cope with data like those presented here would need to include more sophisticated modelling of radiative transfer along the optical path, to allow for variable-thickness layers of gas at variable temperatures.

3.6 Conclusions of Chapter 3

This chapter has covered practical issues arising from the retrieval of infrared spectra collected at Masaya Volcano. Uncertainties associated with the retrieval come from several sources:

(a) Background noise, which was greater in the 1999 spectra than the 1998 measurements.

(b) The estimate of ILS used in the forward model, when the line shapes vary in the measured spectra.

(c) The choice of microwindow for the retrieval (especially for HCl and HF) and the polynomial fit to the background curve (especially for CO_2).

(d) Signal to noise in the measurement, which is dependent upon gas concentration and the nature of the line itself.

(e) Estimates of plume pressure and temperature, and uncertainty in the HITRAN96 line parameter database.

(a) to (d) all contribute to the retrieved error. (e) must be estimated separately, and, for Masaya data, error associated with pressure, temperature and line parameters was shown to be less than 5.3 % in total.

I have shown that retrievals of solar and active spectra should return SO_2/HCl ratios within an average error similar to 10 %, providing that a range of gas concentration data is used in the determination of those ratios. For ratios involving CO_2 and HF the error will be greater.

The data collected in passive mode at Masaya cannot be adequately quantitatively treated with the current retrieval scheme, owing to the presence of emission features in the spectra. The passive data can be used for qualitative identification of major volcanic gases. For these data, future development of the retrieval scheme would require modelling radiative transfer through several gas layers at different temperatures along the optical path.

CHAPTER 4
MASAYA I:
THE IMPACT OF TROPOSPHERIC PROCESSES ON MEASURED PLUME COMPOSITIONS

The composition of a volcanic plume measured at some distance away from the vent reflects the composition of gas released from the magma modified by subsequent processes related to hydrothermal and atmospheric interactions. For this reason it is essential to consider the potential effect of atmospheric processes on measured compositions before the data are interpreted for their volcanological significance. At Masaya, incandescence within the open vent is strong evidence that gases are released directly from a magma-air interface at shallow depth, and so gas interaction with a hydrothermal system is largely irrelevant to this situation. This chapter focuses on the potential for variability in measured plume compositions arising as the result of atmospheric interaction alone, regardless of the behaviour of the volcanic source.

The range of processes that can modify the gaseous composition of the atmosphere includes not only gas-phase reactions, but also reactions on, in, or with suspended solid and liquid particles. This is a burgeoning field of research in its own right, carrying with it implications for the impact of particles released via anthropogenic pollution on the radiative balance of Earth and its climate. Many of the reactions of interest are still only poorly understood. With regard to the fate of tropospheric volcanic plumes, information about the processes and rates of removal of SO_2, HCl and HF from the gas phase is desirable.

In this chapter I will address the following questions for Masaya Volcano: If OP-FTIR measurements in different modes sample different paths through the plume, do they record the same composition, or is the plume modified locally by tropospheric processes? How comparable are OP-FTIR measurements made downwind and at the summit? Can downwind measurements be used to obtain volcanological information? Are repeated measurements for the same location affected by local meteorological variability, and if so, does this variability obscure volcanological information?

Finally, I summarise the impact of tropospheric processes on the plume compositions recorded at Masaya, and discuss the implications of this research for remote volcanic plume monitoring.

4.1 Atmospheric processes relevant to studies of tropospheric volcanic plumes

It is essential that remote monitoring of volcanic plumes is coupled with an understanding of the atmospheric processes which are initiated as the gases leave the volcanic vent: without this, it may be impossible to interpret the volcanological significance of gas measurements correctly. Apparent variations in measured gas compositions could reflect:

(a) Real, at-source variations in volcanic gas composition;

(b) Variation arising from mixing of gases from multiple source vents with different compositions;

(c) Variable rates of scavenging for different gas species due to tropospheric processes;

(d) Spatial heterogeneities in the plume, arising from (b);

(e) Artefacts produced by the retrieval, arising from non-linear performance across the measured concentration range, especially associated with large errors for low concentrations.

Process (b) can be discounted immediately, since, at Masaya, gases are clearly emitted from a single vent. Process (e), the reliability of the retrieval in dealing with Masaya field data, was discussed in Chapter 3, and some non-linearity in the SO_2 retrieval was noted. In the current chapter, I discuss potential variations arising from tropospheric scavenging, and assess the evidence in Masaya field data for whether processes (c) and (d) may contribute significantly to measurements.

In terms of tropospheric processes, passively degassing volcanoes are similar to power plants, in that both emit a characteristic cocktail of "pollutant" gases into the ambient atmosphere. Both are point sources and sustain plumes that disperse downwind. However, progress in quantifying the dispersal, reactions and deposition of anthropogenic pollutants (SO_2, NO_x, O_3, VOCs) is not immediately transferable to the realm of volcanic emissions, which involve a different mixture of components. Some studies have addressed atmospheric chemistry as it relates to volcanic gases directly (e.g. Bekki & Pyle 1994, Martin *et al.* 1986, Oppenheimer *et al.* 1998c, Pinto *et al.* 1989, Self *et al.* 1996, Tabazadeh & Turco 1993). In general, these have focused on the global atmospheric impact of gases released during large explosive eruptions, rather than the tropospheric impact of continuous passively degassing volcanoes.

Although H_2O and CO_2 are volumetrically the most important constituents of volcanic plumes, and relatively unreactive CO_2 is potentially an important tracer of the magmatic contribution to volcanic gases, their fate within the troposphere is of little interest because of their high ambient concentrations. However, the fact that large quantities of hot water vapour are present in

tropospheric volcanic plumes is likely to be significant to the fate of other volcanic components. The local humidity within the gas plume may be significantly higher than ambient, and volcanic effluent contains a range of potential condensation nuclei. Gas emitted from volcanoes often looks "cloudy", confirming condensation of liquid water droplets, with consequences for the fate of soluble species present in the plume.

In this section, I summarise the processes important in considering tropospheric volcanic plumes. I discuss the interaction of SO_2 and HCl with the surrounding atmosphere, and possible mechanisms and rates for the removal of acid gases from tropospheric plumes. Finally I suggest simple end-member models for tropospheric effects on measured plume compositions.

4.1.1 Tropospheric processes

Once released, volcanic gases are subject to a complex range of processes, summarised in figure 4-1. Both chemical and physical processes can occur, and the relative importance of individual reactions depends on the nature of the emitted gases and the nature of the local troposphere (in turn controlled by local meteorology).

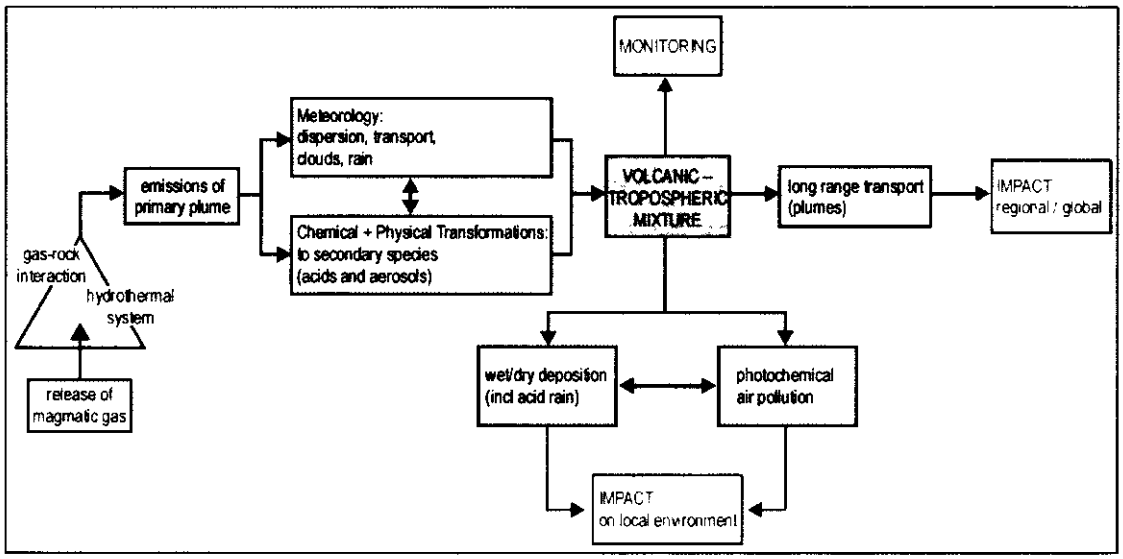

Figure 4-1: Processes affecting volcanic gases from emission to environmental impact, and the place of monitoring. The position of hydrothermal system interaction is illustrated although this appears unimportant at Masaya. Emissions from the volcanic source are usually a mixture of acidic gases, trace metals, and solid particles (ash). Two sets of processes can be identified, those that modify the in-plume composition, and those leading to deposition. Atmospheric interaction begins immediately the gases enter free air, which may be well before a plume leaves a crater. (modified from Finlayson-Pitts and Pitts (1986).)

Current research on chemistry in the troposphere is reviewed by Ravishankara (1997). Because the troposphere contains suspended solid and liquid particles, heterogeneous reactions (those occurring on the surface of a solid) and multiphase reactions (those occurring within an aqueous medium) are usually more important in altering gas composition than slower homogeneous gas

phase reactions. Although condensed water is likely to be the predominant form of suspended material, other substances (e.g. S-containing particles at various stages of evolution, sea-salt particles, soot, silicates, and organic aerosols) may also be important media for reactions. Apart from their direct involvement in reactions, suspended particles also control the available actinic flux, affecting photochemical processes. Rates of tropospheric heterogeneous and multiphase reactions are poorly known, needing a better understanding of the microphysics of particle formation for their constraint, and rely upon observation rather than prediction.

The tropospheric chemistry occurring within a volcanic plume will be complex. Rates of transformation and removal of gas species depend upon the availability of condensed water and solid particles in the plume, but also on the photochemical production of radicals (which in turn depends upon UV flux and the availability of oxidants such as H_2O_2 and OH), and the changing pH within water droplets.

4.1.1.1 Effect of meteorology

A volcano's physical setting, such as the edifice height and local topography, as well as its geographical situation, dictates patterns of local meteorology. Local weather conditions affect the fate of tropospheric plumes both directly, through dispersion and transport downwind, and indirectly, through factors such as temperature, humidity, fogs, cloud cover and the amount of sunlight reaching the plume. These factors constrain which chemical reactions are favoured: hydrolysis and photochemical processes in particular will be affected. Fog water droplets provide an aqueous medium for liquid-phase SO_2 to sulfate conversion, and a cycle of condensation on aerosols at night followed by evaporation during the day can dramatically increase the concentrations of pollutants in the droplets to result in low pH fogs.

Reactions occur over long distances as the gases are transported, so that acid deposition occurs over long ranges. At Masaya, a region of 900 km^2 is affected, and time-averaged concentrations of SO_2 exceeding 30 ppb are commonly observed under the plume up to 30 km away from the active crater (Delmelle *et al.* 1999a).

The balance between competing reactions depends largely on the weather. In terms of plume transport, wind speeds are important, but also if atmospheric inversion layers develop, then these can control the further dispersion of the plume. This is the likely situation with Masaya's plume: temperature inversions develop overnight, trapping the volcanic plume in a low level layer so that its deleterious effects on population and vegetation downwind are maximised during the night and early morning.

4.1.1.2 Chemical and physical reactions affecting SO_2

The ultimate destiny of sulfur gases is oxidation to sulfuric acid aerosols, or sulfates, which are subsequently rained out or deposited from the atmosphere. It is widely accepted (e.g. Ravishankara 1997) that this oxidation of SO_2 to sulfuric acid in the troposphere occurs predominantly as a multiphase reaction (i.e. in droplets) by attack from oxidants like H_2O_2 and O_3. Equations (4-1) to (4-4) show one possible scheme for SO_2 oxidation in cloud droplets, which was investigated by Chandler *et al.* (1988).

$$SO_{2(g)} \xleftarrow{H_2O} SO_{2(aq)} \tag{4-1}$$

$$SO_{2(aq)} \longleftrightarrow HSO_3^- + H^+ \tag{4-2}$$

$$HSO_3^- + H_2O_2 \longrightarrow SO_4^{2-} + H^+ + H_2O \tag{4-3}$$

$$\frac{d[SO_4^{2-}]}{dt} = k'[H_2O_2][SO_{2(aq)}] \tag{4-4}$$

They found that this oxidation was extremely rapid and estimated the rates constant *k'* from field measurements to be approximately 6×10^6 l mol^{-1} s^{-1}, almost an order of magnitude greater than similar estimates from laboratory studies. The fieldwork of Chandler *et al.* (1988) was carried out in the UK, and relates specifically to the interaction of SO_2 with mid-latitude orographic clouds; it is not, therefore, immediately transferable to the climatic situation of Masaya. The range of variation between field and laboratory measurements serves to highlight the requirement for more detailed research in this area.

Photodissociation of SO_2 in the gas phase to SO and O, which may be important higher up in the atmosphere, cannot occur in the troposphere because the necessary UV radiation does not penetrate this far. Other possible reaction routes for SO_2 oxidation are via organic radicals (although this is considered unimportant in the troposphere (Finlayson-Pitts & Pitts 1986)), via transition metal catalysis, or via homogeneous aqueous phase reactions.

Observations of power plant plumes (discussed by Finlayson-Pitts and Pitts (1986)) provide some insight into the rates and mechanisms of SO_2 oxidation. Because there is still little known in detail about the heterogeneous and multiphase reactions which occur, rates cannot be derived accurately from theory. Studies indicate that the oxidation rate could be up to 10 % per hour, but higher in fog or cloud. Rates also tend to be higher in summer than winter, suggesting the importance of photochemistry or temperature at some stage in the process. SO_2 oxidation rates increase when the gas is mixed with surrounding air containing photochemical oxidants. But significant SO_2 oxidation to sulfate still occurs at night, suggesting the importance of liquid phase reactions, and rates dramatically increase in the presence of liquid water or when there are humidities greater than about 75 %.

Martin *et al.* (1986) studied the plume chemistry of Mt Etna and observed a range of sulfur loss rates, and possibly very short residence times of aerosols, very likely influenced by variable weather and plume conditions.

Deposition of SO_2 directly onto surfaces occurs in competition with SO_2 oxidation. Under conditions where rates of oxidation are slow (i.e. dry and cool) and appropriate surfaces exist (e.g. a high concentration of dry particles in the plume, or ground level plumes) dry adsorption of SO_2 may become an important process in its removal from the gas phase.

4.1.1.3 Chemical and physical reactions affecting HCl

The most important property of HCl for tropospheric reactions is its solubility. The Henry's Law solubility constant for HCl is 2.5×10^3 mol l^{-1} atm^{-1} (equivalent to 2.53×10^5 mol m^{-3} Pa^{-1}) at 298 K, which is approximately three orders of magnitude larger than that for SO_2 (values quoted from Seinfeld (1986)). Because HCl is not a criterion air quality pollutant like SO_2, its tropospheric chemistry has received much less attention, despite the importance of chlorine in the stratosphere. However, because of its high solubility, its chemistry may be far simpler than that of SO_2.

Gas	H / mol l^{-1} atm^{-1}	H / mol m^{-3} Pa^{-1}	Reference
CO_2	3.4×10^{-2}	3.4	(Seinfeld 1986)
SO_2	1.24	126	(Seinfeld 1986)
HCl	2.5×10^3	2.53×10^5	(Seinfeld 1986)
	$2\times10^6/k_A$		(Sander 2000)
HF	$9.6/k_A$		(Sander 2000)

Table 4-1: Henry's Law constants for gases dissolving in liquid water at 298 K. For strong acids, the solubility is dependent on dissociation constant. Henry's Law constants represent physical solubility only: for species that participate in acid-base equilibria, the maximum that can be dissolved is greater than the value predicted by Henry's law. There is a lack of consensus as to exact values, see, for example, Sander (2000).

Multiphase reactions are likely to be more important than surface reactions, and the rate of HCl removal will be even more strongly affected by the presence of liquid water than SO_2 oxidation. Clouds, fog, or rain will significantly alter the composition of the remaining gas-phase plume due to HCl dissolution. A study of "acid rain" at Masaya (Johnson & Parnell 1986) found that rain-water pH was controlled by the amount of dissolved HCl, and while SO_2 was still available for dissolution at long distances downwind, proximal rainfall removed almost all of the HCl from the plume.

4.1.1.4 Deposition processes

Figure 4-1 indicated that deposition could occur by wet or dry processes. Dry deposition refers to the removal of particles or molecules at ground surfaces (e.g. soils, vegetation, water) via settling or sticking. Rates of dry deposition depend strongly on the nature of the surface: rates of acid

deposition increase strongly if, for example, leaf surfaces are wet. Dry deposition velocities also trend with the reactivity of the species involved: rates for HF (which has high absorptivity) are quoted as 1–4 cm s^{-1} while for SO_2 as 0.1–2 cm s^{-1} (Seinfeld 1986). Wet deposition refers primarily to precipitation events: particles or aerosols act as condensation nuclei and fall out with water droplets, while acids dissolve into water droplets in clouds and are subsequently removed during rainfall.

Tabazadeh and Turco (1993) assessed the wet deposition of HCl from a stratosphere-bound eruption plume following the Mt Pinatubo eruption. Once water began to condense, HCl was readily dissolved to form solutions of 1–5 wt % HCl. This process was very rapid, with an equilibrium determined by Henry's Law. Large volcanic eruptions often induce rainfall, and the dissolved HCl is thereby efficiently removed.

4.1.2 Simplified models and implications for OP-FTIR plume measurements

OP-FTIR spectroscopy is used primarily to measure the composition of the gas phase in the plume. Once a gaseous molecule has been converted to something else via any heterogeneous or multiphase process, it is effectively removed from the measurement, even if it has not yet been physically deposited from the plume. While rates of deposition are important in monitoring the potential plume impact downwind, in terms of observing changing plume chemistry, it is the rates of heterogeneous and multiphase reactions that are important. Of particular importance is the rapid rate of dissolution of HCl (and presumably HF) into any water droplets present. Water droplets may be present in the plume even if ambient humidities are low, due to the presence of a number of potential condensation nuclei and the extreme variations in pressure and temperature experienced by gas exiting a high temperature volcanic vent. The presence of water droplets or aqueous films is also crucial for tropospheric SO_2 oxidation, so there is competition between a number of possible reactions. As reactions occur, aqueous aerosol becomes increasingly acidified, affecting the balance of subsequent reactions and dissolutions, and eventually saturated with respect to further scavenging of acid gas molecules. Figure 4-2 summarises the factors involved in removal of acid gases by water droplets,

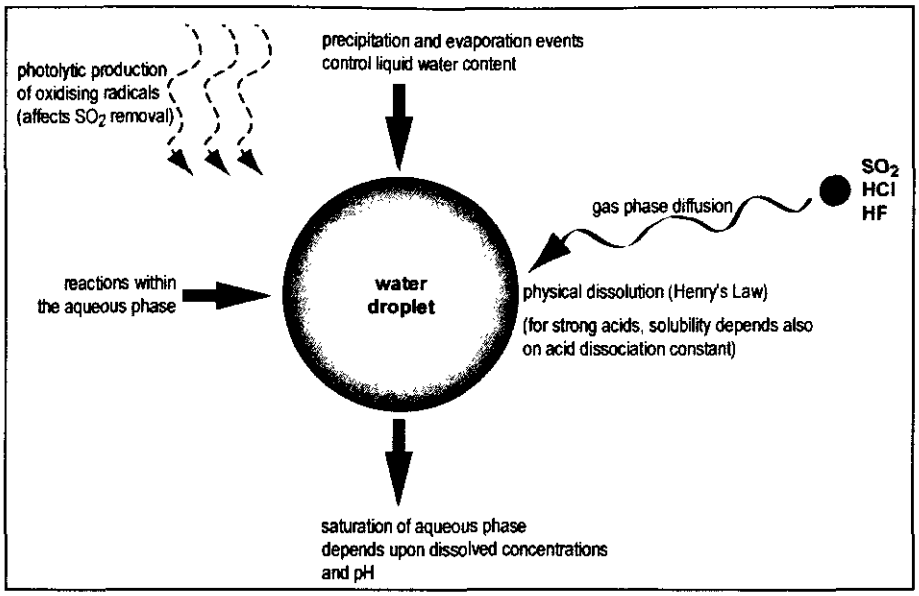

Figure 4-2: The complex interplay of factors relevant to aqueous removal of acid species from a volcanic gas plume. Reaction rates depend upon diffusion, liquid phase reactions and solubilities. Local meteorology controls atmospheric water content, and affects gas-phase diffusion. A range of other possible catalysts and reaction pathways are available in the real troposphere.

At one extreme, consider a volcanic plume emitted into an environment with almost unlimited condensed atmospheric water. Scavenging from the gas phase will be unlimited and controlled by the rates of reaction for different species. Rates for HCl and HF, which have higher physical solubilities, are likely to be faster than those for SO_2, which relies upon chemical reaction in preference to physical dissolution. The measured gas phase composition will reflect the relative rates of scavenging, so that SO_2/HCl or SO_2/HF ratios increase as the plume ages.

At the other extreme, in a perfectly dry environment, no aqueous removal processes are possible. Reactions on the surfaces of solid particles may also be precluded as they are thought to involve thin aqueous or organic films. Dry deposition of HF is relatively rapid, compared to SO_2, but otherwise, in this situation there may be only slow change in the gas phase composition as the plume ages.

For a situation in which limited condensed water is available for tropospheric reactions, the crucial factor is how rapidly the available water becomes saturated. There may be rapid removal of soluble species initially as plume water condenses on exit from the volcanic vent. Subsequently, the gas phase composition may remain constant and change only through slower dry deposition processes or in short-lived precipitation events. This intermediate situation is likely to be normal for Masaya, with rapid reactions and dissolutions occurring as the plume convects within the crater until aqueous aerosol is saturated, but with little subsequent gas phase compositional change as the plume ages and disperses downwind. A different set of reactions

may become important as the plume disperses over the Pacific Ocean and mixes with the marine boundary layer.

In the rest of this chapter, field measurements from Masaya are assessed in order to delimit the role that tropospheric processes may play in contributing to compositional variations in the data.

4.2 Comparison of active and solar mode summit data

Spectra were collected at Santiago Crater using both the active lamp source and the sun. Measurements collected in these two ways sampled different optical paths (shown in figure 4-3). Retrieved plume compositions are not expected to be the same if rapid tropospheric chemistry is occurring as the gas exits the crater, or if significant spatial heterogeneities exist within the plume.

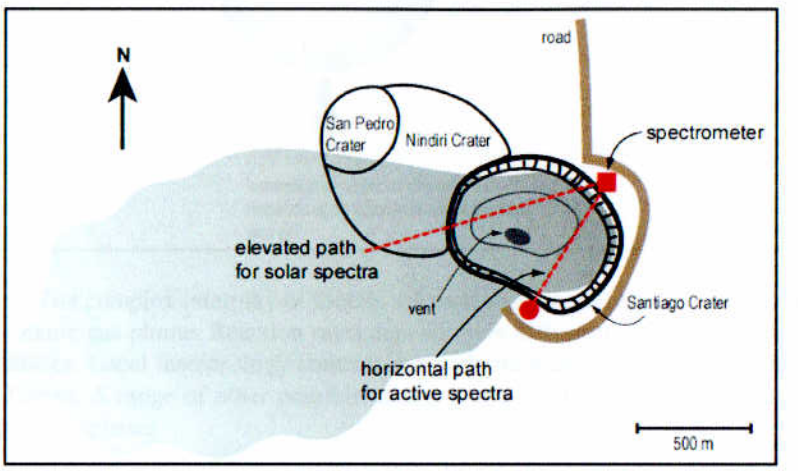

Figure 4-3: Sketch map of the summit of Masaya volcano to show the different paths through the plume sampled by solar and active measurements.

Solar measurements were collected towards the end of the afternoon when the sun dropped behind the plume, creating an appropriate viewing geometry. Active measurements were not restricted by time of day, but on a few occasions the path indicated on figure 4-3 was unsuitable because the wind was more northerly and the lamp source would have been immersed in volcanic gas.

4.2.1 Measurements on a single day, 23 February 1998

On 23 February 1998, 50 active spectra were collected across Santiago Crater at 13:00–13:30 h, followed by 50 solar spectra collected at 15:50–16:20 h. The active path mainly sampled the edge of the plume, while the solar path intersected denser parts of the plume. Figure 4-4 shows retrieved amounts of SO_2, HCl and HF from the two datasets. Higher gas amounts were retrieved from solar spectra than from active spectra, as a result of an optical path through the core of the plume.

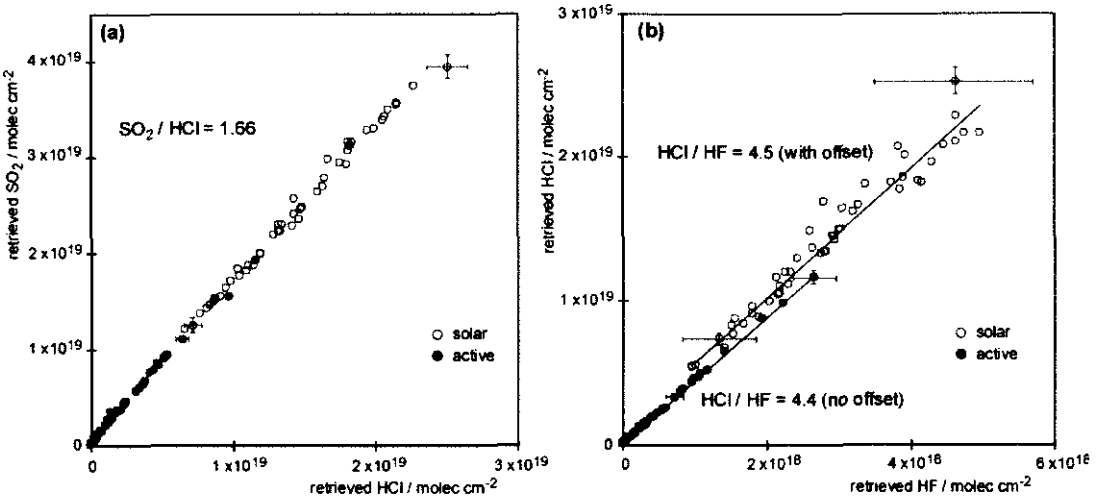

Figure 4-4: Retrieved amounts from spectra collected on 23 February 1998 at Santiago Crater, using solar (open circles) and active (filled circles) sources. (a) SO_2 plotted against HCl, (b) HCl plotted against HF. Some typical error bars are indicated: these are calculated from the relative error returned with each retrieval. Retrieved errors are greater for the solar data than the active data. While in (a) the regression lines for solar and active data are indistinguishable and trend through the origin, in (b) the regression line through the retrieved solar data has an intercept to positive HCl (see text for discussion).

The SO_2/HCl ratios derived from the gradients of regression lines through the two datasets in figure 4-4(a) are the same, at 1.66. Regression lines trend through the origin, indicating sound retrieval of both SO_2 and HCl from both datasets. The SO_2/HCl ratios calculated from individual spectra are also very consistent (figure 4-5).

Figure 4-4(b) shows some discrepancy in retrieved HCl and HF between the active and solar data. While the regression line for the active data trends through the origin, that for the solar data has an intercept on the positive HCl axis. This offset arises from poorly constrained HF retrievals when the spectra are strongly contaminated by atmospheric H_2O, also indicated by the larger HF retrieved error bars. HF is underestimated by about 6 % in the solar retrievals because of H_2O saturation in that spectral region: the regression line intercepts the negative HF axis at approximately 3×10^{17} molec cm^{-2}. The low HF retrieved from the solar spectra results in high HCl/HF ratios calculated from individual spectra, compared with the active results (figure 4-5). However, the ratios calculated from the regression lines on figure 4-4(b) for the two datasets, compensating for the underestimated solar HF, are the same within error, at 4.4 and 4.5 for the active and solar data, respectively.

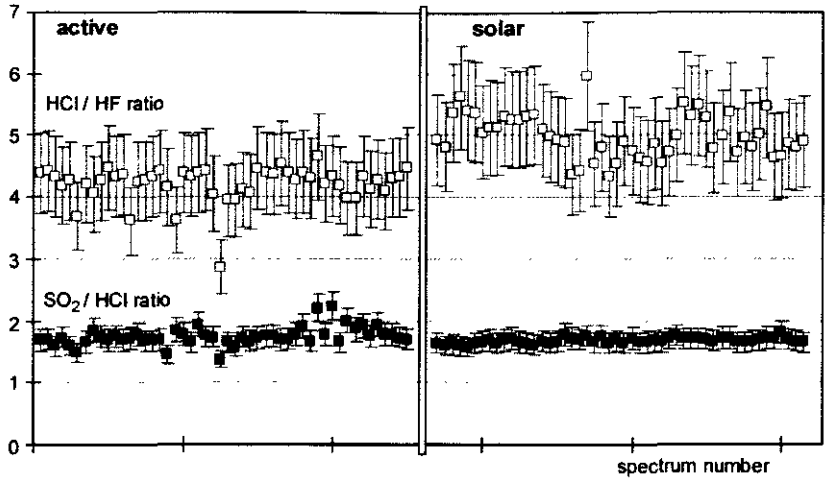

Figure 4-5: SO_2/HCl (filled squares) and HCl/HF (open squares) ratios calculated from individual spectra, plotted against spectrum number. Error bars are ± 15 % on the HCl/HF ratios, and ± 10 % on the SO_2/HCl ratios. The increased scatter in SO_2/HCl ratio for active data compared to solar data is due to the lower gas concentrations (lower signal to noise). HCl/HF ratios calculated from solar spectra are consistently higher than those from the active data because HF is underestimated in retrieval of the strongly H_2O contaminated solar spectra (see text).

This comparison of active and solar data collected on the same afternoon at Santiago Crater has demonstrated the importance of plotting retrieved amounts on scatter graphs in order to consider results in context and to identify spurious retrievals. Ratios derived from individual spectra can be misleading if strong background contamination affects the accuracy of the retrieval. Within error, the gas compositions indicated from the two types of measurement are the same. There is no evidence from these data for spatial plume heterogeneities or rapid in-plume chemistry affecting the gas composition above the crater.

4.2.2 All active and solar summit data

Consistent results from active and solar summit data were obtained throughout both field campaigns in 1998 and 1999. Figure 4-6 shows retrieved amounts of SO_2, HCl and HF plotted for both active and solar data in 1998. The same problem with the solar HF retrieval is apparent, but ratios are very comparable for the two sets of measurements.

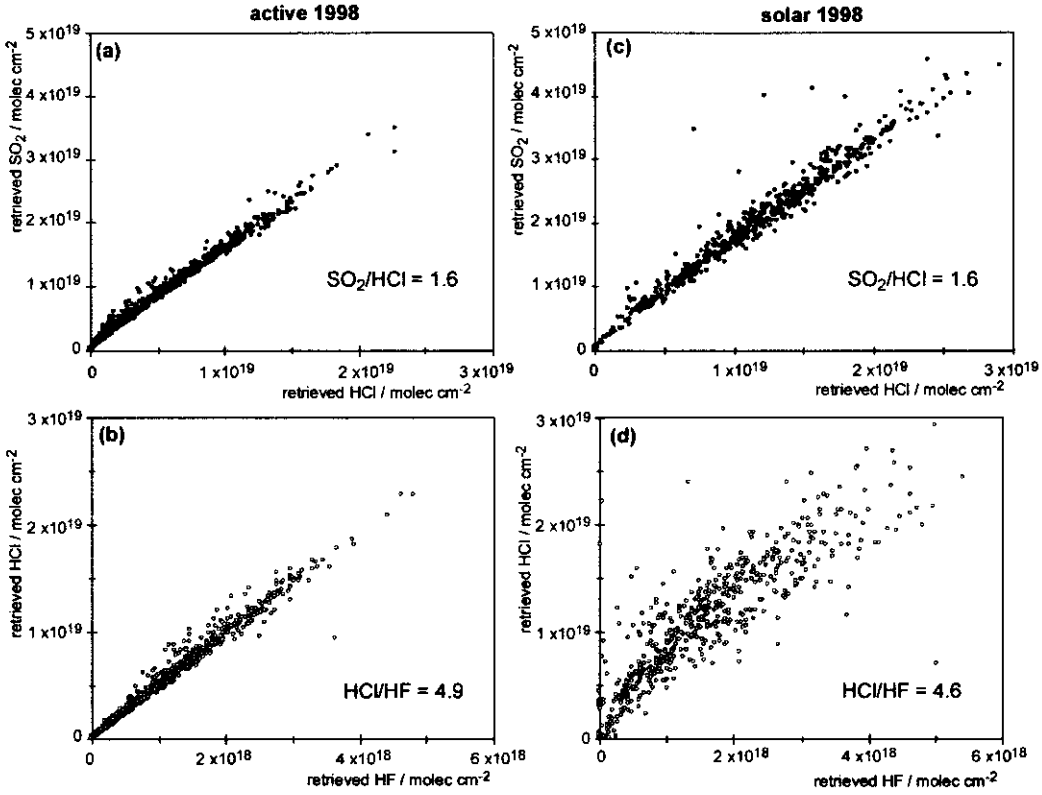

Figure 4-6: Retrieved amounts from all summit active (a) and (b) and solar (c) and (d) data collected in February–March 1998. (a) and (c) show retrieved SO_2 plotted against retrieved HCl; (b) and (d) show retrieved HCl and HF. Notice that in (d) a similar trend to that in figure 4-4(b) due to underestimated solar HF is apparent. Gas ratios are calculated as the gradient of best regression lines which are unconstrained to go through the origin.

For 1999, correspondence between active and solar measurements was similar to that seen in 1998, with SO_2/HCl ratios of 1.6 and 1.8 for active and solar data, respectively, and HCl/HF ratios of 5.1 and 5.0. Given the fact that these ratios represent averages for data collected over a period of 5 weeks in 1998, and 2 weeks in 1999, the consistency in gas composition recorded in figure 4-6 is striking. Weather systems in Nicaragua during the dry season are relatively stable, but ambient temperature, humidity and wind speed still showed some variability over the measurement period. However, regardless of these variations in conditions, the results indicate that the plume composition above Santiago Crater is stable.

4.2.3 Conclusions from summit measurements

Comparison of results from solar and active measurements at Santiago Crater on a single day, and over the course of two field campaigns, has confirmed two points. First, measurements collected in active and solar mode are directly comparable (over the same range of concentrations), and similar results are retrieved. The only discrepancy lies with the HF retrieval, since solar data are more affected by H_2O contamination in the relevant spectral region. If retrieved HF amounts are interpreted carefully, then mistaken conclusions can be avoided.

Second, the SO_2-HCl-HF gas compositions derived from both the solar and active data are very consistent, despite different optical paths through the plume and small changes in weather over the measurement period. The plume appears to be compositionally well-mixed, and relatively unaffected by potential rapid tropospheric chemistry above Santiago Crater. Any processes occurring in this region must affect all three species equally so that no compositional variation is detected, an unlikely scenario. Alternatively, tropospheric processes occurring as the volcanic gas enters the atmosphere may be confined to within the crater itself. Strong convection and rapid mixing are visible within the crater, so that an equilibrium mixture has been established by the time the plume exits at the top of the crater and is measured. Any further chemistry would require plume dispersion and ageing, and mixing with more tropospheric water.

4.3 Comparison of summit and downwind observations

Plume measurements both downwind and at the summit of the volcano were possible on several days during the two field campaigns. These measurements had a dual purpose: first, to delimit the downwind range at which high quality volcanic-gas spectra could be collected; and, second, to determine whether there was any change in gas composition resulting from tropospheric processes as the plume was carried downwind and dispersed.

In this section, I have selected examples from four different days covering different distances downwind, different gas concentrations, and both solar and active modes. Maximum retrieved amounts downwind are typically an order of magnitude lower than maximum amounts at the crater due to plume dilution and dispersion. Difficulties in dealing with the low concentration downwind data are highlighted, and conclusions about the role of scavenging processes and the use of OP-FTIR at long distances downwind are drawn. Only SO_2 and HCl are considered since amounts of HF are well below detection limit in the downwind data.

Figure 4-7 shows where the spectra discussed in this section were collected. Active measurements recorded the near ground-level gas composition in that location. For solar spectra, unless measurements were made around noon, the composition represents a slant path through the plume in the sun's direction. In general, solar spectra were collected in the afternoon, which meant that there was some contribution from plume further downwind (i.e. in a south or west direction).

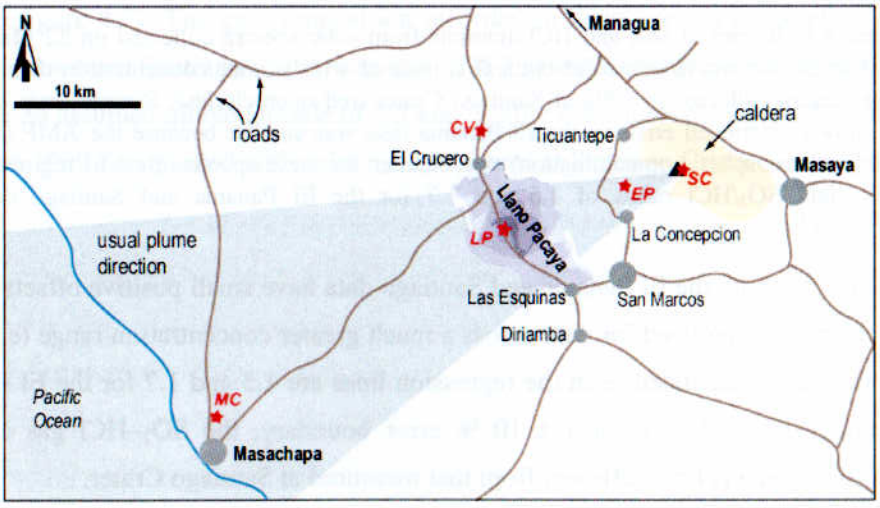

Figure 4-7: Map of the area surrounding Masaya Volcano. The central grey region marks out the usual plume swath. The Llano Pacaya is a region of high land (approx. 1300 m a.s.l.) downwind from the volcano (approx. 600 m a.s.l.) continually under attack from volcanic gases. Some of the more significant towns are marked, and red stars mark the locations from where spectra were collected. Code: SC=Santiago Crater, EP=El Panama, CV=Casa Vieja, LP=Llano Pacaya, MC=Masachapa.

4.3.1 Solar spectra from El Panama, 22 March 1998

225 solar spectra were collected between 1100 and 1600 h on 22 March 1998 from a locality called El Panama, a village on high ground above the western caldera wall, approximately 5 km downwind from Santiago Crater. Because the sun was at near-zenith for many of these measurements, retrieved errors are generally lower than those for summit measurements, despite the lower gas concentrations, because the atmospheric path is shorter and background contamination in the spectra is less. Retrieved amounts of HCl and SO_2 from the downwind spectra are compared with retrieved amounts of similar concentrations and error selected from the entire set of summit solar measurements for 1998 in figure 4-8.

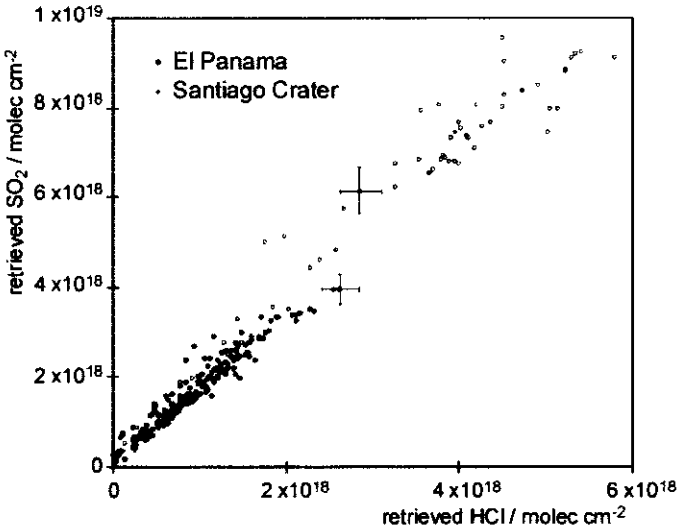

Figure 4-8: Retrieved SO_2 and HCl amounts from solar spectra collected on 22 March 1998 at El Panama (black solid circles) compared with similar concentration data for solar spectra collected in 1998 at Santiago Crater (red open circles). Sample error bars are shown. Retrieved error on the El Panama data was smaller because the AMF (and therefore atmospheric contamination) was smaller for these spectra. Best-fit regression lines yield SO_2/HCl ratios of 1.5 and 1.7 for the El Panama and Santiago data, respectively.

Regression lines for both the El Panama and Santiago data have small positive offsets on the SO_2 axis: these offsets go unnoticed for data across a much greater concentration range (e.g. figure 4-6(c)). SO_2/HCl ratios calculated from the regression lines are 1.5 and 1.7 for the El Panama and Santiago data, respectively. Given a ± 10 % error boundary, the SO_2–HCl gas composition measured at El Panama is little different from that measured at Santiago Crater.

The plume gas above El Panama is approximately 10 minutes "older" than that above Santiago Crater, for an average wind speed of 8.5 m s^{-1}. While rates for SO_2 oxidation to sulfate aerosol in water droplets are generally reported as "extremely rapid" (e.g. Chandler *et al.* 1988), and dissolution of HCl should also be fast, the rate constant for gas-phase oxidation of SO_2 is about 24 hours (Eatough *et al.*, 1994). Multiphase processes are therefore expected to have time to occur as the Masaya plume travels from Santiago to El Panama, but homogeneous gas phase

reactions will take much longer. Since there is no discernible compositional change, there are two possible explanations. First, rates of removal of gaseous SO_2 and HCl via multiphase processes may be approximately equal in this situation, so that the SO_2/HCl ratio in the gas phase remains approximately constant. Second, there may be insufficient condensed water vapour within the dispersing plume to provide sites for downwind dissolution of HCl or multiphase oxidation of SO_2.

This second explanation is favoured. Within and above Santiago Crater, the plume often has a very "cloudy" appearance, due to condensing water vapour, but as it disperses downwind, the plume becomes hazier, implying a lower concentration of water droplets. Convection and mixing of the warmer volcanic gas with the ambient atmosphere is strong within Santiago Crater, but much less as the plume moves downwind in temperature equilibrium with its surroundings. Thus, condensed water droplets may quickly become saturated within the crater, but as the plume moves downwind, the remaining gaseous SO_2 and HCl has little contact with fresh condensed water, while existing plume water droplets may re-evaporate.

4.3.2 Solar spectra from El Panama, 12 March 1999

In 1999, solar spectra were again collected from El Panama, but between 1600 and 1730 h, later than the 1998 measurements. At this time of day, the sun was lower in the sky (at elevation angles from 25 ° to 7 ° by the end of data collection), the atmospheric path was longer (so retrieved errors were higher), and the spectrometer was aligned in the direction of the Llano Pacaya (see figure 4-7). The gas composition recorded in these spectra is therefore of plume at greater distances from Santiago Crater than the 1998 El Panama measurements, approximately 9 to 18 km for an assumed plume altitude of 1.5 km. Figure 4-9 shows SO_2 and HCl retrieved from the 12 March 1999 data plotted with solar measurements at Santiago Crater for comparison.

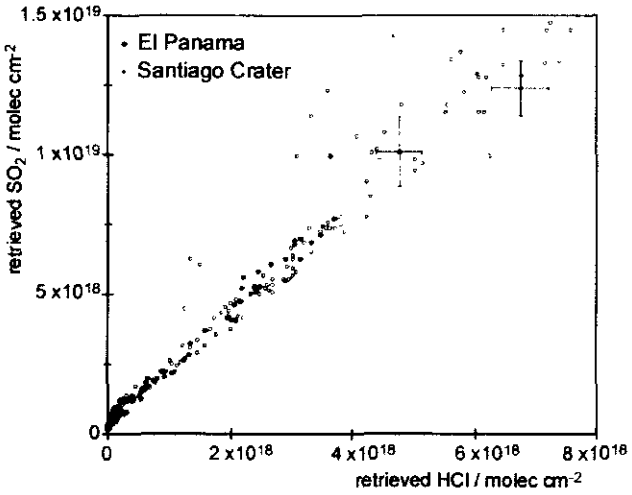

Figure 4-9: Retrieved SO_2 and HCl amounts from solar spectra collected on 12 March 1999 at El Panama (black solid circles) compared with similar concentration data for solar spectra collected in 1999 at Santiago Crater (red open circles). Sample error bars are shown. Best-fit regression lines yield SO_2/HCl ratios of 2.1 and 2.0 for the El Panama and Santiago data, respectively.

The SO_2/HCl ratios derived from figure 4-9 are 2.1 and 2.0, calculated from the regression lines for the El Panama and Santiago data, respectively. As previously, these numbers are the same, within error. Despite the fact that the plume sampled by this set of measurements from El Panama could have travelled for approximately 45 minutes from Santiago Crater, mixing with the troposphere has had little effect on the relative concentrations of SO_2 and HCl in the gas phase. Any changes in gas composition up to 15 km downwind are undetectable by this method.

4.3.3 Solar spectra from Casa Vieja and Masachapa, 17–18 March 1998

On 17–18 March 1998, logistics permitted four sets of solar spectra to be collected in order to compare gas compositions measured at two different distances downwind with the composition measured at Santiago Crater. On 17 March, the wind direction was unusually south-easterly, and so measurements were made from a locality called Casa Vieja, approximately 15 km NW of Santiago Crater. 50 spectra were collected at Casa Vieja between 1300–1415 h, and then 35 spectra were collected at Santiago Crater between 1655–1735 h. On 18 March, the wind was back to its normal direction, and 80 downwind spectra were collected between 1235–1500 h close to Masachapa, approximately 40 km SW of Santiago Crater. 35 spectra were collected on return to Santiago, between 1655–1735 h. Retrieved amounts of SO_2 and HCl from these data are plotted in figure 4-10. Approximate plume ages at Casa Vieja and Masachapa, given average wind speeds of 8.5 m s^{-1}, were 30 minutes and 1.5 hours, respectively.

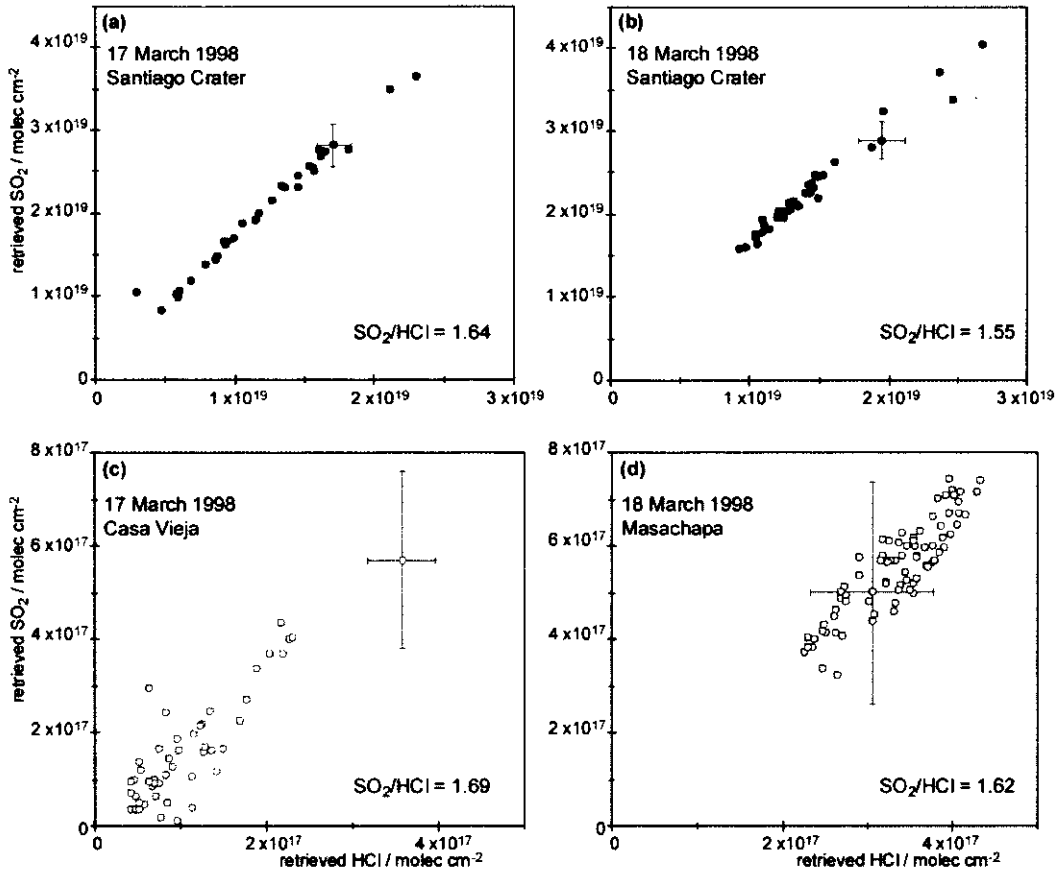

Figure 4-10: Retrieved SO_2 and HCl amounts from solar spectra collected downwind (open circles) and at the crater (solid circles) in 1998: (a) 17 March at Santiago Crater, (b) 18 March at Santiago Crater, (c) 17 March at Casa Vieja, and (d) 18 March at Masachapa. Sample error bars calculated from retrieved errors are shown. SO_2/HCl ratios were calculated as the gradient of regression lines fitted to the data. Note different scales.

Measurements at Santiago Crater on both days confirmed SO_2/HCl gas ratios of about 1.6. On both days, the downwind SO_2/HCl ratios were slightly higher than those derived from summit data, but the difference was insignificant. Within the bounds of error, all four datasets verify the same SO_2–HCl gas composition, despite the fact that the retrieved amounts vary by almost two orders of magnitude. Although retrieved errors are substantial for the low concentration downwind measurements (figure 4-10(c) and (d)), these data are still reliable, with R^2 correlation coefficients of 0.8.

In general, solar data collected even up to 40 km from the volcano (i.e. a plume age of approximately 1.5 hours) shows very little evidence for the influence of tropospheric processes on plume gas composition. Downwind measurements have inherently low gas concentrations and high associated errors, and would be unsatisfactory as the *only* information on volcanic gas composition. Nevertheless, these data show that for the Masaya situation, spectra collected at some distance are a reliable proxy for at-crater sampling.

4.3.4 Active spectra on the Llano Pacaya

14 km south west from Masaya volcano, the land rises steeply to form a broad ridge called the Llano Pacaya at approximately 1300 m a.s.l. (see figure 4-7). The volcanic plume leaves Santiago Crater at 600 m a.s.l., and is blown by northeasterly Trade winds directly into, and over, the Llano Pacaya ridge. Active spectra were collected on the Llano Pacaya to investigate the near-ground level plume composition.

30, 100 and 50 spectra were recorded on 3, 10 and 14 March 1998, respectively. Path lengths between lamp and spectrometer were approximately 300 m. Retrieved amounts of SO_2 and HCl are plotted in figure 4-11. Retrieved amounts at similar concentration levels from active spectra collected on 3 and 9 March 1998 at Santiago Crater are shown for comparison.

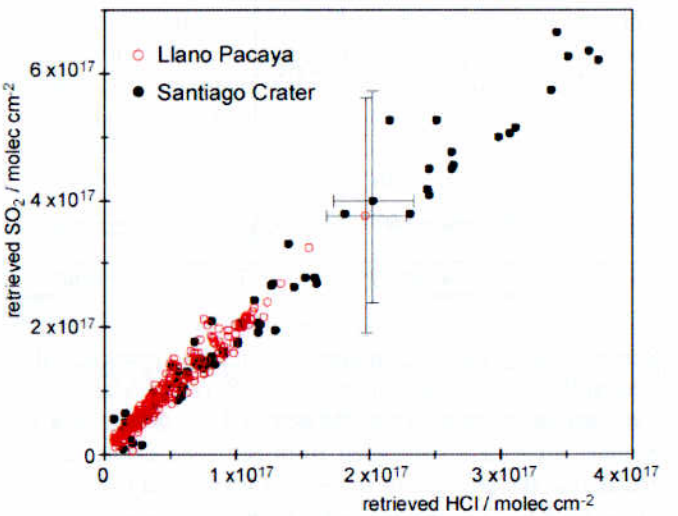

Figure 4-11: Retrieved SO_2 and HCl from active spectra collected on the Llano Pacaya on 3, 10 and 14 March 1998 (red open circles) compared with similar concentration data for active spectra collected at Santiago Crater on 3 and 9 March 1998 (black solid circles). Sample error bars calculated from the retrieved error are shown. Regression lines yield SO_2/HCl ratios of 1.9 and 1.7 for the Llano Pacaya and Santiago data, respectively.

The downwind and summit data are almost indistinguishable on figure 4-11. SO_2/HCl ratios of 1.9 and 1.7 calculated from the gradient of regression lines through the Llano Pacaya and Santiago Crater data, respectively, are the same, within error. The relative proportions of SO_2 and HCl in the gas at ground level 14 km downwind are unchanged from the proportions measured above Santiago Crater. This result implies either that SO_2 and HCl are deposited from the plume at approximately equal rates, or that deposition as the plume gas comes into contact with vegetation is negligible. Delmelle *et al.* (2001) indicate that dry deposition onto the land may remove up to 10 % of the total emitted SO_2 and HCl from the plume during transport downwind from Masaya Volcano. These authors confirm the implication of the data in figure 4-11, that the removal of both HCl and SO_2 by dry deposition does, indeed, occur at a similar rate at Masaya.

The maximum retrieved amounts of SO_2 and HCl from the Llano Pacaya active spectra are 4×10^{17} molec cm^{-2} and 2×10^{17} molec cm^{-2}, respectively (figure 4-11). These values are equivalent to 0.6 ppm and 0.3 ppm for the 300 m pathlength. Time-averaged SO_2 concentrations over 4-week periods in 1998 and 1999 of greater than 0.09 ppm were derived by Delmelle *et al.* (1999a) for the core of Masaya's plume at the Llano Pacaya, using a network of diffusion tubes and PbO_2 sulfation plates. The values derived from the OP-FTIR measurements compare well, since these represent a temporary maximum. At night, ground-level concentrations are expected to be higher as a result of atmospheric inversions trapping the plume at low altitude. Long term exposure to such levels of acid gases is considered detrimental to the health of the local population (Baxter *et al.* 1982, Baxter *et al.* 1990).

4.3.5 Conclusions from downwind measurements

Active and solar spectra collected at distances between 5 and 40 km from Santiago Crater have been used to determine downwind SO_2/HCl gas ratios. There has been no consistent difference between summit and downwind gas compositions: all the data point to negligible changes in gas composition as the plume disperses. The favoured explanation has been that negligible oxidation of SO_2 or dissolution of HCl occurs as the tropospheric plume travels downwind, under the daytime conditions in which measurements were made. A greater concentration of available free condensed atmospheric water, such as during the rainy season or periods of low cloud, could provide the appropriate environment for heterogeneous and multiphase chemistry, and the measured plume gas composition might then be expected to change.

The absolute amounts retrieved from downwind solar spectra represent column amounts along a slant path through the plume at that location. Absolute concentrations at any given point are controlled not only by the source gas emission rate, but also by patterns of plume dispersion, which in turn are affected by wind speeds, turbulence and atmospheric stratification. While retrieved amounts at discrete locations therefore have little useful plume information alone, in the future, solar spectra collected at different points along a transect under the plume may be integrated to provide a plume concentration cross section.

For active field spectra, SO_2 detection limits were estimated at 10^{17} molec cm^{-2} (Chapter 3): most of the data presented in figures 4-8 to 4-11 represent concentrations above that limit. For the solar measurements, retrieved error also varied considerably with AMF and the amount of background contamination in the optical path. While the errors associated with the low concentration downwind measurements preclude them from providing satisfactory plume data alone, in conjunction with comparable data collected at the summit, these spectra prove insightful.

4.4 Short timescale variability in summit measurements

Spectra collected in active mode at Santiago Crater (see figure 4-3) provide a rich dataset in which to examine the short timescale behaviour of the plume composition. Sets of approximately 50 spectra spanning a 30-minute period were usually collected, but on a few occasions longer occupations were achieved. In addition, variability from one day to the next could be examined.

Small variations in weather, either as the result of the normal diurnal pattern, or as local weather systems fluctuated, may contribute to the type and rate of tropospheric processes that affect the volcanic plume. Since water is the most important substance for tropospheric reactions, changes in atmospheric water content are likely to be significant. Temperature is also a critical parameter as the saturated vapour pressure of water in air depends strongly on temperature and determines the proportion of liquid phase water available. The gas phase composition recorded in active spectra at Santiago will directly reflect rapid processes occurring within and above the crater, as well as the source composition.

4.4.1 Active spectra on 16 March 1999

At Masaya night-time weather patterns are very different from the daytime: temperatures drop and relative humidity rises, and frequently inversion layers trap the volcanic plume at low altitude. On 16 March 1999, an early start was made in order to examine any variation in plume composition at Santiago Crater with the change from nocturnal to diurnal weather patterns. Light rain prevented measurements before about 0800 h; so the data set consists of 320 spectra spanning the period from 0825 to 1245 h. SO_2, HCl, HF, H_2O and CO_2 were retrieved from the spectra, and figure 4-12 shows retrieved amounts and gas ratios through time.

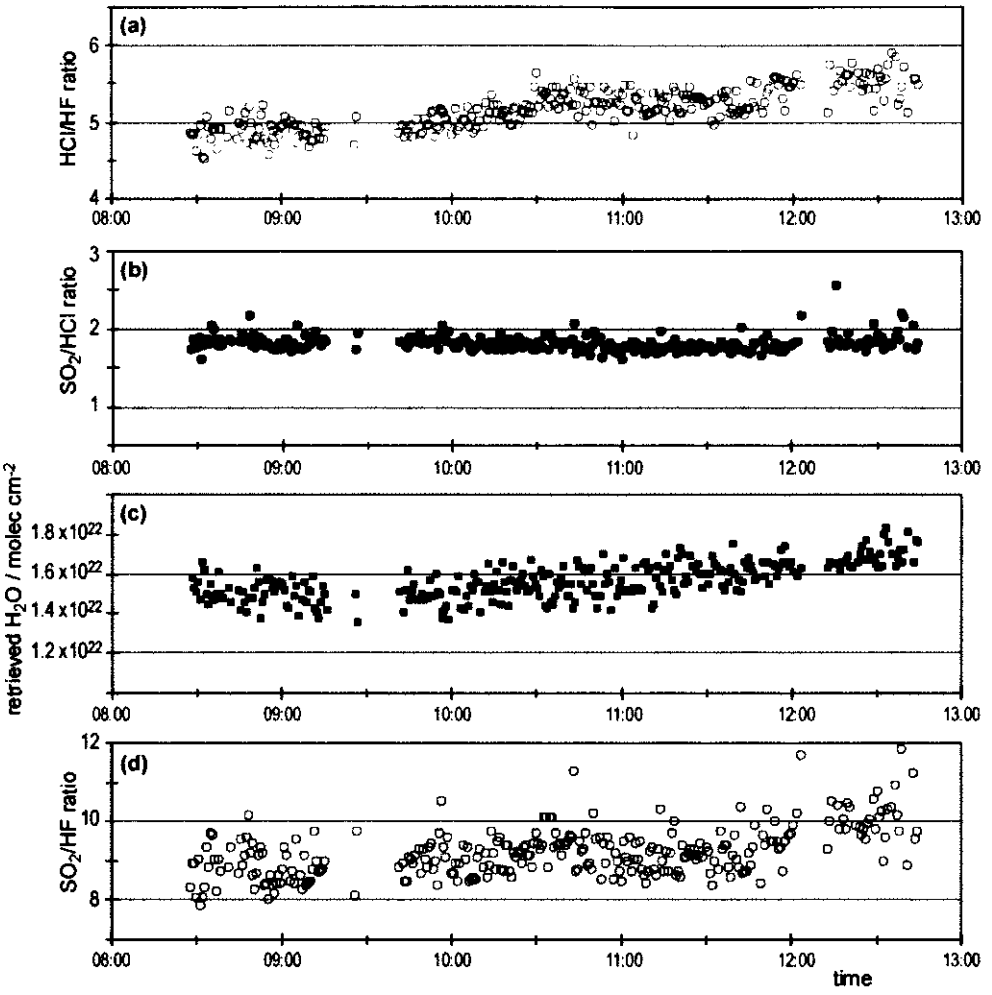

Figure 4-12: Gas ratios and retrieved H_2O from active spectra collected at Santiago Crater on 16 March 1999. (a) HCl/HF, (b) SO_2/HCl, (c) retrieved H_2O, and (d) SO_2/HF through time. The data gap around 0930 h represents a period of low gas and instrument realignment and calibration.

Retrieved amounts of volcanic gases (SO_2, HCl, HF) covered a consistent range for the duration of the measurements. Gas ratios plotted in figure 4-12 were calculated from individual spectra and some variability is revealed in the time-series. While the SO_2/HCl ratio remained roughly constant, a gradual increase in the HCl/HF ratio from approximately 4.8 at 0920 h to 5.5 at 1245 h is apparent (figure 4-12(a)). Over the same period, the retrieved water vapour in the optical path shows an increase from approximately 1.4×10^{22} molec cm^{-2} to 1.75×10^{22} molec cm^{-2} (figure 4-12(c)). Retrieved amounts of volcanic gases do not show this increase, and so the change in H_2O concentration is attributed to a change in the background atmospheric water vapour content.

Contemporaneous meteorological data (Table 4-2) from a portable weather station confirm an increase in background atmospheric water vapour (calculated via equation (4-5)). Ambient temperature rose from 23 °C to 29 °C between 0920 h and 1245 h, while relative humidity fell from 42 % to 36 %. Because the saturated vapour pressure for water is strongly dependent on temperature, the actual ambient water vapour concentration increases by 20 % despite the

measured decrease in relative humidity. Although this trend of increasing water vapour is confirmed, the absolute values calculated for the ambient water vapour concentration are difficult to compare directly with the retrieved amounts because of additional quantities of volcanic water present in the optical path.

$$H_2O(ppm) = \left(\frac{R.H.}{100} \times \frac{S.V.P.}{P_{ambient}} \right) \times 10^6 \qquad (4\text{-}5)$$

Time	Temp / °C	R.H. / %	Pressure / mb	S.V.P. / mb	Calculated H_2O / ppm
0920	23	42	956	28.1	12 345
1245	29	36	954	40.1	15 132

Table 4-2: Meteorological data for 16 March 1999. Saturated vapour pressure (S.V.P.) at the relevant temperatures from tables in Houghton (1986). Ambient atmospheric water content was calculated for the measured meteorological parameters and these values of S.V.P. using equation (4-5).

The increase in HCl/HF ratio through time seen in figure 4-12(a) is linked to the increase in ambient water vapour. SO_2/HF ratio also increases (figure 4-12(d)), while SO_2/HCl is roughly constant, so that the different ratios are caused by changing proportions of HF in the plume relative to the other volcanic gases.

4.4.2 Active spectra on 24–25 February 1998

Active spectra were collected at Santiago Crater between 1615–1640 h and 1000–1030 h on 24 and 25 February 1998, respectively. Weather conditions for the two measurement periods were different. On 24 February, active measurements were not possible during the morning due to an unusual wind direction: during the afternoon observation period the temperature was approximately 32 °C with relative humidity at 35 %. On 25 February temperature was 29 °C and relative humidity 51 % for the morning measurements. Retrieved gas amounts from the two sets of spectra covered similar ranges, and are plotted in figure 4-13.

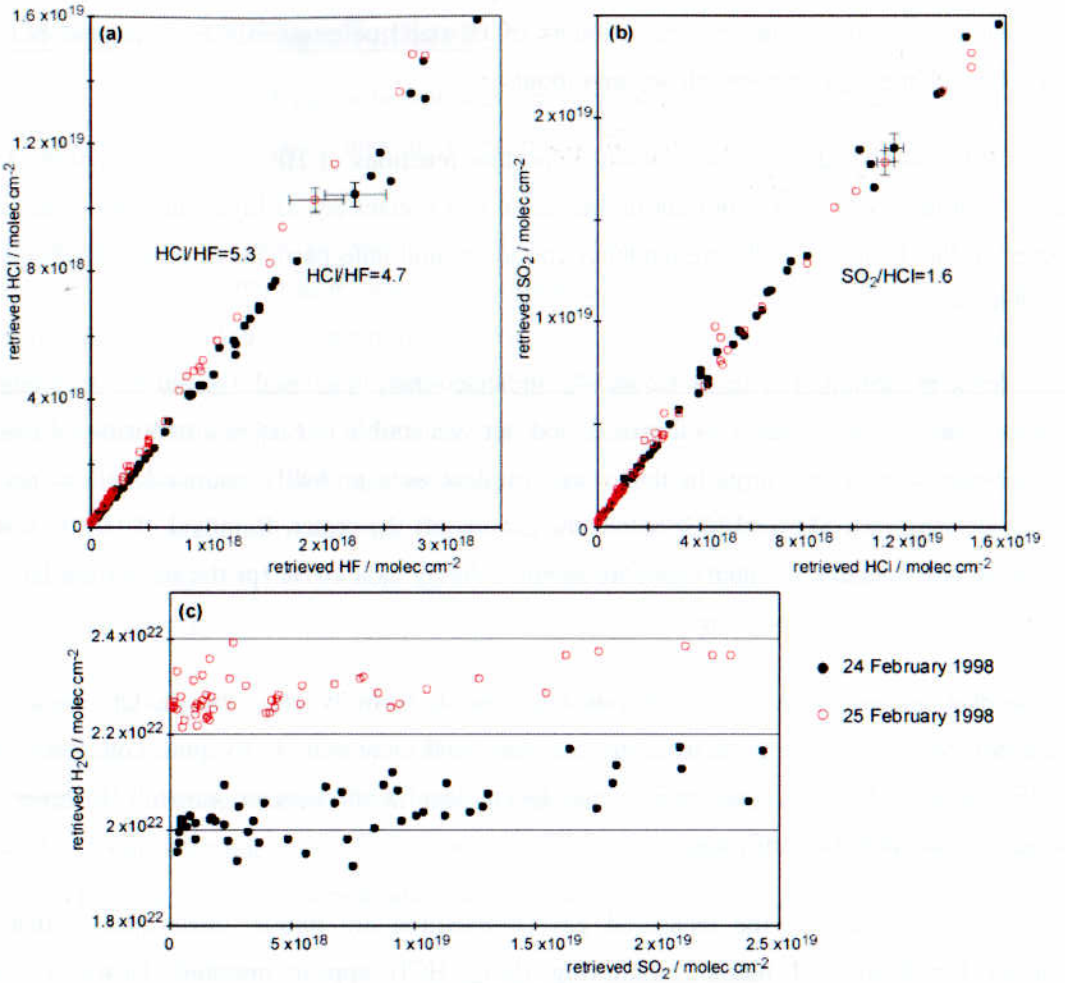

Figure 4-13: Retrieved data from active spectra collected on 24 (black solid circles) and 25 (red open circles) February 1998. (a) HCl against HF, with ratios given by the gradient of the regression lines, and sample error bars. (b) SO_2 against HCl, with a ratio of 1.6 for both datasets, and sample error bars. (c) H_2O against SO_2, showing higher background atmospheric water vapour on 25 February.

Different HCl/HF ratios of 4.7 and 5.3 were obtained from the 24 and 25 February data, respectively, while SO_2/HCl ratios were the same, at 1.6. The background atmospheric water vapour concentrations derived from the intercept on figure 4-13(c) were approximately 2.0×10^{22} molec cm^{-2} and 2.3×10^{22} molec cm^{-2} for 24 and 25 February respectively. As in the data from 16 March 1999, the higher HCl/HF ratio on 25 February is linked to a higher background water content. The difference in HCl/HF ratio over the two days is controlled by a change in the relative proportions of HF in the gas phase, confirmed by the constant SO_2/HCl ratios but an increase in SO_2/HF ratio (not shown).

4.4.3 Conclusions from short timescale summit measurements

Meteorological variability has been found to have a limited effect on the plume gas composition measured at Santiago Crater. The controlling variable seems to be atmospheric water vapour content. While relative proportions of SO_2 and HCl in the gas phase are consistent regardless of

local weather conditions, the relative amounts of HF, and consequently HCl/HF and SO_2/HF ratios reflect changes in atmospheric water vapour.

There is little published information about important reactions of HF in the troposphere. Apart from its high reactivity, two important properties of this species are its high solubility (reactivity) in water (Table 4-1), and its strong tendency for adsorption onto particles or other molecules via hydrogen bonds.

The evidence presented in sections 4.2 and 4.3 indicated that, in general, the plume, once outside the crater, was compositionally well-mixed, and not susceptible to further compositional change via tropospheric reactions. In particular, water droplets were probably saturated with respect to further reactions with SO_2 and HCl before the plume left the crater. Removal of HF by further dissolution into condensed water therefore seems unlikely as a cause for the increasing HCl/HF ratio with atmospheric water content.

Because of its electronic structure, HF molecules readily form hydrogen bonds. One suggestion for the link between HF removal from the gas phase and increased H_2O vapour concentration is that HF undergoes H-bonded adsorption onto H_2O molecules and aqueous aerosol. However, this mechanism has yet to be confirmed.

Meteorological effects on the measured gas composition are minor: those species that are important for downwind plume monitoring (SO_2, HCl) appear immune. However, more substantive changes in local weather are likely to induce larger scale alterations in plume chemistry. Remote measurements of volcanic plume composition should be examined for their dependence upon atmospheric variables before firm interpretations of the source composition are made.

4.5 Conclusions and Implications

This chapter has illustrated that a complex range of processes can modify the gaseous plume composition once it is released into the troposphere. Specific tropospheric heterogeneous and multiphase reactions of relevance are still relatively ill-defined, especially for HCl and HF, which, unlike SO_2, are not pollutants which are routinely monitored for air quality. Local meteorology exerts an effect as it controls atmospheric water content, the available sunlight flux, and plume dispersion. SO_2 oxidation to sulfate is more rapid via multiphase processes than in the gas phase in the troposphere, and where condensed water content is high, this process can be extremely rapid. HCl is expected to be removed predominantly by dissolution into water droplets. For the volcanic situation like that at Masaya, the balance and rates of processes may be controlled by the availability and size distribution of water droplets and particles in the plume: once saturation with respect to acid gases is reached then there is little scope for further compositional change.

Three points have arisen out of the data presented in this chapter. First, the gas composition above Santiago Crater is essentially well-mixed and stable. Second, the composition measured downwind is indistinguishable from that measured at the summit; and third, over short timescales, local atmospheric water content affects only the proportion of HF in the plume. The discussion relating to these observations is summarised in figure 4-14, and below.

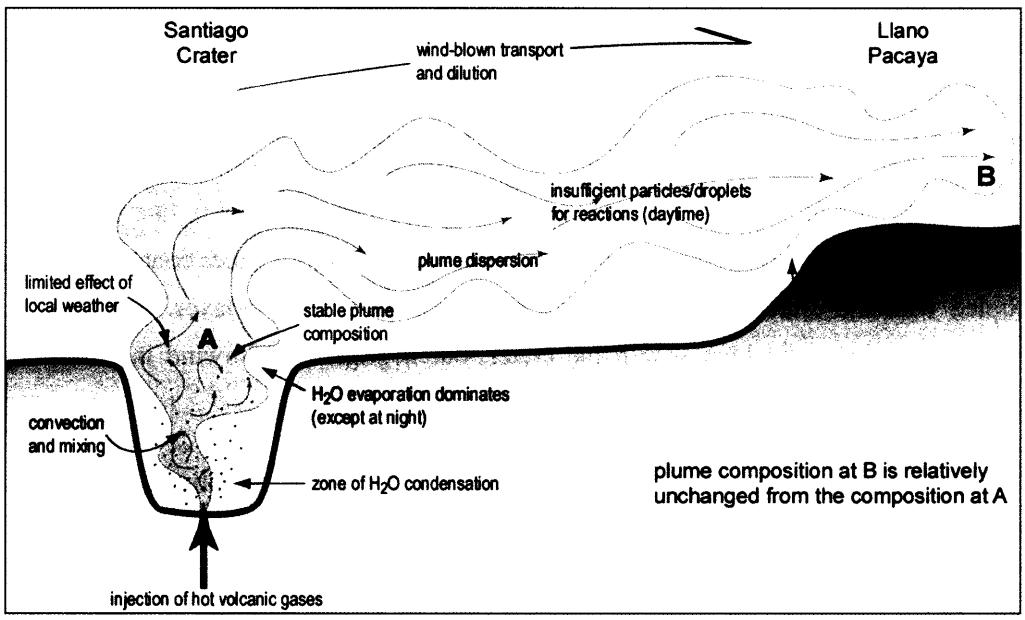

Figure 4-14: Cartoon illustrating the tropospheric processes affecting Masaya's plume for the field conditions experienced during data collection. This description is valid only for daytime observations during the dry season, with similar volcanic behaviour. Rapid tropospheric chemistry is likely to occur within the crater where water vapour is condensing, but nowhere else, as evaporation becomes the dominant process. Cloud or rain interaction with the plume could have severe impact with significant wet deposition of components. As the plume continues downwind to the Pacific, interaction with the marine boundary layer may encourage different scavenging processes.

Conclusions about tropospheric processes

(a) Rapid tropospheric chemistry within the crater is favoured by a number of factors. Temperature and compositional gradients, established as hot volcanic gases are injected into the base of the crater, induce strong convection, and are likely to result in condensation of at least some volcanogenic water vapour. Water droplets and other particles come into contact with large volumes of gas as mixing continues, providing great opportunity for reactions. Local weather also influences the ambient water content. Rates and extent of heterogeneous and multiphase processes depend upon competition between several species able to dissolve in, or react with, water. Reactions continue until the water droplets are saturated, or too acidic for further reaction, or begin to evaporate as they move up through the crater and disperse. High emission rates mean that water saturation occurs long before all of the volcanic gas has been scavenged.

(b) Beyond the crater, evidence suggests that little chemistry occurs to modify the plume composition. A regime of wind-blown dispersion operates, and since ambient humidity is low, water droplets tend to vaporise during the day. The ash burden in Masaya's plume is negligible, and so, once remnant water droplets have evaporated and the particle distribution is diluted, there is little scope for heterogeneous or multiphase chemistry as the plume travels downwind. Dry deposition as the plume reaches the Llano Pacaya is negligible, during the day: damp vegetation at night may encourage higher rates.

(c) Depletion rates of SO_2 from the plume are negligible over the range of field measurements. In contrast, Oppenheimer *et al.* (1998c) show that at other volcanoes tropospheric SO_2 depletion rates are variable and sometimes fast. The significant downwind variation in SO_2 from Soufriere Hills Volcano (Montserrat) reported by these authors is likely related to the moist atmosphere (orographic clouds) and potentially high liquid water content of the plume, coupled with the effect of interaction with the marine boundary layer. For Masaya, SO_2 depletion rates may be high within the crater, but negligible downwind in the absence of liquid water in the atmosphere.

(d) The scenario suggested in figure 4-14 is relevant only for the conditions under which the field data were collected, and cannot be extended beyond these limits. During the night, there is potential for a very different regime, since low temperature and high relative humidities favour formation of water droplets, and inversion layers may trap the plume at low levels. During periods of low cloud or in the rainy season, acid dissolution into water droplets and wet deposition will increase dramatically: at these times the downwind gas composition may be very different from that monitored at Santiago Crater. Rain falling through the plume becomes significantly acidified (Delmelle *et al.* 1999b, Johnson & Parnell 1986): this process will considerably modify the composition of the gas remaining in the plume.

Implications for remote plume monitoring

(a) Under the conditions for the field measurements presented in this thesis, OP-FTIR spectra collected downwind from Masaya volcano are representative of the at-crater volcanic SO_2–HCl plume composition. However, at distances greater than approximately 5 km, plume dispersion means that HF concentrations are below reliable detection. Consistent measurement of the plume downwind is a reliable volcano-monitoring tool since any changes in SO_2/HCl ratio under these conditions are more likely to be volcanological than plume chemistry-related.

(b) At other volcanoes, or during different times of year at Masaya, it is essential that near-vent and downwind variability is thoroughly investigated. Downwind plume monitoring can only be used to assess volcanological changes if variations arising from plume chemistry are minimal, or at least well-understood.

(c) High error can be associated with the low concentrations retrieved from downwind spectra. Best results are obtained by maximising column amounts and minimising atmospheric contamination in the spectra. This can be achieved by using solar mode operation with a viewing geometry in which the spectrometer is pointed toward the volcano rather than away downwind, and by measurement at low AMF. Long active paths through the plume, obtained by the use of carefully positioned retro-reflectors, may provide an alternative.

(d) While plume compositions may appear stable and consistent over timescales of weeks or months, small-scale short-term variability can arise as a result of local weather changes. Relationships between measured gas compositions and meteorological variables must be defined before short-term patterns can be confidently linked to the behaviour of the volcano.

CHAPTER 5
MASAYA II:
A VOLCANOLOGICAL INTERPRETATION OF GAS COMPOSITIONS MEASURED 1998–1999

Chapters 3 and 4 have addressed the potential influence of retrieval artefacts and tropospheric processes on the gas measurements at Masaya Volcano. There, I concluded that the recorded gas compositions are representative of the volcanic source, and any variations are more likely to have volcanological causes than be the result of plume-atmosphere interaction. This chapter provides a volcanological interpretation of the gas data.

During 1998 and 1999, when the fieldwork was carried out, Masaya was undergoing a period of intense passive degassing (which has continued up to the time of writing). Apart from two minor explosions, which ejected lava bombs over the rim of Santiago Crater, this period has seen no eruption of magma. Gas is emitted from a single vent at the floor of the crater, and although the lava surface is obscured from view, some reflected incandescence is visible, indicating a magma-air interface at very shallow level.

This chapter will focus on spectra collected in active mode at Santiago Crater (figure 5-1) as these are the highest quality data and retrieved amounts have lower errors than retrievals from solar mode spectra. These spectra are assumed to represent most closely the vented gas composition. Although the gas composition may have evolved between leaving the magma-air interface in the vent and sampling at the crater rim, there has been little evidence to suggest extensive atmospheric modification of the gas composition prior to measurement (Chapter 4). The extent of any such modification is unquantifiable with these data, but is unlikely to be very significant since large amounts of reactive HF are still present in measurements. The gas composition itself and any temporal changes in ratios therefore reflect a combination of source compositions and shallow magmatic processes.

Figure 5-1: Photo of active measurements at Santiago Crater: view along the optical path from the spectrometer.

The full retrieved gas composition data set from the 1998 and 1999 field campaigns is presented below. The full complement of SO_2, HCl, HF, H_2O and CO_2 is discussed. The temporal stability of the gas ratios is examined at different timescales. A representative Masaya gas composition is compared with published gas geochemical data from other volcanoes. Typical emission rates for all five gases are calculated, and implications for the magma degassing mechanism are considered. Finally, a previous gas study at Masaya is assessed in the light of my findings, and constraints are placed on models for the degassing system.

5.1 Presentation of retrieved gas data

Raw single beam spectra collected in active mode at Santiago Crater contain clear spectral features of SO_2, HCl, HF, CO_2 and H_2O. Although these five gases are invariably the major components of volcanic emissions, traditional volcanic gas analyses report a range of minor species in addition (e.g. Allard 1983, Giggenbach 1996, Symonds *et al.* 1994). As well as noble gases, these include molecules such as H_2S, CO, COS, SiF_4, and HBr, which are all "infrared-active". Previous OP-FTIR studies of volcanic plumes have identified the carbon species (Mori & Notsu 1997, Oppenheimer *et al.* 2001a), and SiF_4 (Francis *et al.* 1996a, Love *et al.* 1998, Love *et al.* 2000, Maciejewski 1998), but none has constrained minimum detection limits for these species. H_2S has yet to be confirmed in volcanic infrared spectra: the H_2S feature consists of many weak lines in the range 1200–1300 cm^{-1}, a region which is usually severely contaminated by atmospheric water absorptions.

SiF_4 has a strong and distinctive absorption feature located at 1010–1050 cm^{-1}; amenable to measurement by an MCT detector. The presence of SiF_4 in volcanic emissions is associated with low temperature degassing and attributed to the reaction between silica in vent wall rocks and gaseous HF (Rosenberg 1973, White & Hochella 1992), through equation 5-1:

$$SiO_2 + 4HF \leftrightarrow SiF_4 + 2H_2O \qquad (5\text{-}1)$$

The equilibrium constant for this reaction is strongly temperature dependent, so that production of SiF_4 is negligible at magmatic temperatures but becomes more abundant with falling temperature (Rosenberg 1973). So measured SiF_4/HF ratios have been used to derive the effective equilibrium temperature for volcanic gas in contact with silicate rocks (Francis *et al.* 1996a, Love *et al.* 1998, Love *et al.* 2000).

In MCT spectra collected at Santiago crater there was no evidence for SiF_4. Even when spectra were ratioed to remove background absorptions, while the nearby SO_2 line centred at 1150 cm^{-1} was clearly seen, SiF_4 was absent. This is unsurprising, since at Masaya, observation of an incandescent glow within the active vent indicates that gases are released from a magma-air interface at shallow depth, at near magmatic temperatures. Additionally, relatively high concentrations of HF have been measured in the plume. For HF partial pressures measured in the plume of approximately 10^{-1}, and temperatures of 800–1200 °C, molar SiF_4/HF ratios of 0.01 to 0.0001 are predicted (from figure 1 of Rosenberg 1973), indicating that SiF_4 would be well below detection limit by OP-FTIR. Since HF plume concentrations measured by OP-FTIR methods may be affected by tropospheric transport prior to sampling, the evaluation of equilibrium gas temperatures using such remotely measured SiF_4/HF ratios may be less reliable than that using directly sampled and thermodynamically restored gas compositions.

CO has a strong spectral feature consisting of many narrow lines in the region 2000–2250 cm^{-1} (see figure 2-18), while COS is a broad band feature at 2030–2080 cm^{-1}; so both are detectable with the InSb. Raw active spectra from Santiago Crater showed no evidence for spectral features from either of these gases since the region is strongly contaminated by atmospheric absorptions. When the background was ratioed out, resultant absorbance spectra contained no visible indication of CO or COS either, although volcanic H_2O and CO_2 lines remained.

Volcanic gas ratios for SO_2, HCl and HF are easily obtained either directly from individual spectra, or from the gradient of regression lines through scatter plots of amounts retrieved from a set of spectra. Volcanic CO_2:SO_2 or H_2O:SO_2 ratios cannot be derived from individual spectra since these record the total amount of atmospheric plus volcanic CO_2 and H_2O. Instead, these ratios must be approximated by the gradient of regression lines on scatter plots of retrieved amounts for a set (see figure 2-15). This section begins by concentrating on the acid gases, and considers the temporal stability of gas ratios as well as the average composition. The second part focuses on the CO_2 and H_2O content of the volcanic gas, along with apparent variations in the background concentrations of these two. Finally, I derive a total gas composition, assuming negligible contributions of species that have gone undetected by OP-FTIR.

5.1.1 SO_2–HCl–HF compositions

The acid gases SO_2, HCl, and HF are relatively easily identified in volcanic plumes since their background atmospheric concentrations are negligible. Relative proportions of these gases have been used to trace changes in volatile source and magma composition (Edmonds *et al.* 2001, Oppenheimer *et al.* 2001b), to monitor trends between magmatic and meteoric/hydrothermal input to the gas phase (Martini 1996, Symonds *et al.* 1996), and to track changes in the depth of the degassing source (Pennisi & Le Cloarec 1998). Additionally, routine monitoring of these ratios could potentially follow the degree of degassing of a single magma batch through time (Stoiber *et al.* 1986), variations in vent temperature (Mueller 1970), or changes in sulfur speciation.

Path amounts of SO_2 were retrieved from raw active spectra in a microwindow at 2480–2520 cm^{-1}, following the procedure outlined in Chapters 2 and 3. HCl and HF were retrieved similarly in windows at 2690–2900 cm^{-1} and 4000–4180 cm^{-1}, respectively.

5.1.1.1 Gas ratios and maximum column amounts

Retrieved amounts of SO_2, HCl and HF from all the active mode spectra collected at Santiago Crater during the field campaigns in 1998 and 1999 are displayed on scatter plots in figure 5-2. Linear regression lines through the data indicate average ratios in 1998 of 1.55 and 4.90 for SO_2/HCl and HCl/HF, respectively, and in 1999 of 1.63 and 5.06. Regression lines in figure 5-2

all have R^2 correlation coefficients of 0.99, although this value does not take into account the error associated with each data point.

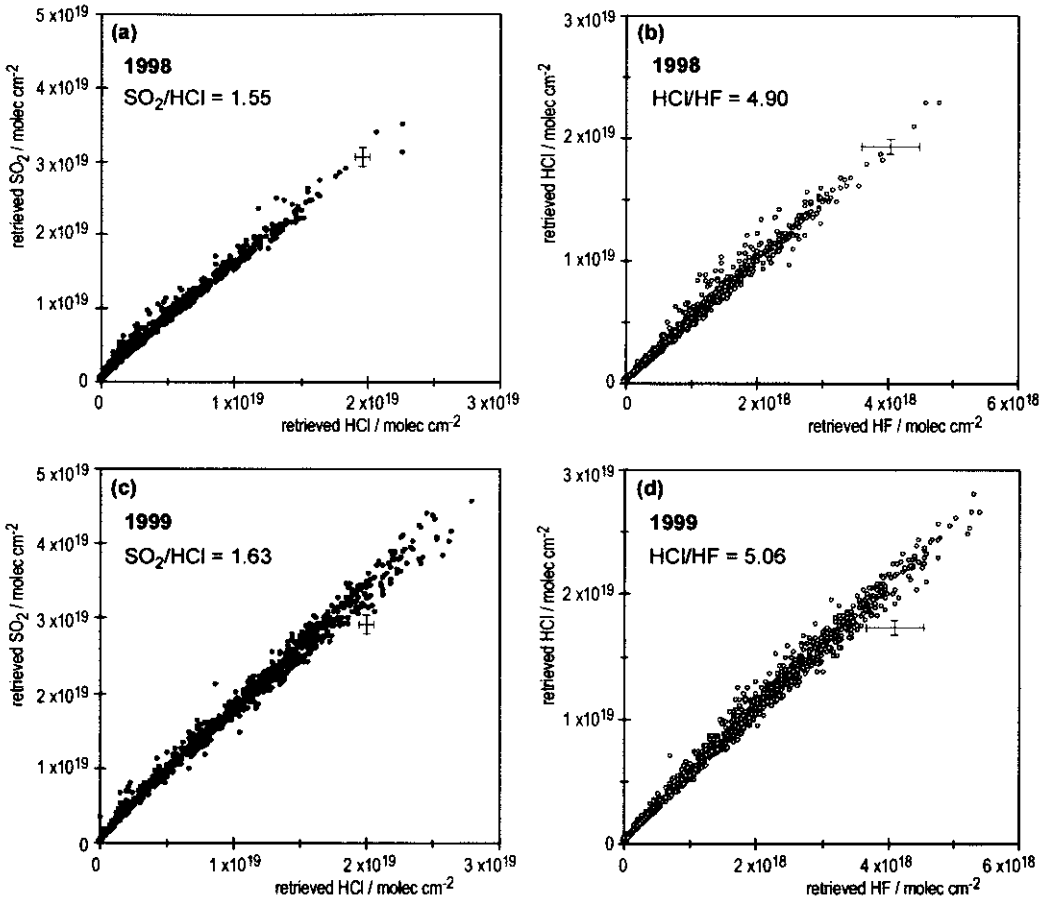

Figure 5-2: Retrieved amounts of SO_2, HCl and HF from all active mode spectra collected at Santiago Crater on 22 February to 24 March 1998 (a and b) and 8 to 16 March 1999 (c and d). SO_2 against HCl plotted in (a) and (c); HCl against HF plotted in (b) and (d). Example error bars were calculated from typical retrieved errors.

In order to assess the range of variation for these average ratios, the mean and standard deviation of the ratios calculated from each individual spectrum (i.e. for each data point in figure 5-2) can be derived. These are shown in Table 5-1. The mean ratios are slightly different from the regression line gradients in figure 5-2 because of small offsets from the origin of the lines on the scatter plots, but these differences are minor in relation to the calculated standard deviations, which are a little over 10 % of the mean. Average SO_2/HCl or HCl/HF gas ratios for Masaya are thus best quoted with 10 % error bounds. This bound, derived empirically, is similar to that estimated at the end of Chapter 3 section 3 from a consideration of retrieved errors.

	SO_2/HCl		**HCl/HF**	
	Mean ratio	S. D.	Mean ratio	S. D.
1998	1.76	0.32	4.87	0.75
1999	1.76	0.21	5.32	0.56

Table 5-1: Statistical mean and standard deviations of ratios calculated from each individual spectrum represented in figure 5-2.

Given ± 10 % error on the average gas ratios, neither SO_2/HCl nor HCl/HF were significantly different in 1999 compared to 1998. In March 2000, preliminary gas ratios derived from active spectra were again little different, at 1.6 and 6.1 for SO_2/HCl and HCl/HF, respectively, with some of the change in ratios attributed to poor signal to noise arising from degradation of the lamp (H. Duffell, pers. com.). Such a consistency in gas composition, although striking, is perhaps unsurprising since volcanic activity has been steady and similar during all the periods of field measurement.

The maximum retrieved gas amounts on figure 5-2 set an upper limit on the absolute concentrations in the plume gas above Santiago Crater. From visual observation at the time of measurement, the plume typically occupied about half of the total 518 m optical path between spectrometer and lamp, or less. If the plume path length was approximately 260 m, the 4.5×10^{19} molec cm^{-2}, 2.7×10^{19} molec cm^{-2} and 5.2×10^{18} molec cm^{-2} of SO_2, HCl and HF, respectively, recorded in 1999 are equivalent to concentrations of 76 ppm, 46 ppm and 9 ppm, at typical Masaya pressure and temperature. Given the heterogeneity visible in the plume, concentrations in parts may have been substantially higher. For comparison, commonly accepted 15-minute exposure limits are 5 ppm for SO_2 and HCl, and 3 ppm for HF (Raffle 1994). Tourists, National Park staff and volcanologists alike can therefore be exposed to potentially harmful levels of these acid gases if engulfed by the plume at Santiago Crater.

5.1.1.2 Temporal study of ratios

The average SO_2/HCl and HCl/HF gas ratios derived from the full suite of active spectra may hide smaller compositional variations occurring over shorter timescales. Daily average ratios from the active spectra collected at Santiago Crater in 1998 and 1999 are shown in figure 5-3. The averages were calculated from the gradient of regression lines on scatter plots of retrieved amounts for each set of measurements, and represent periods of between 30 minutes and almost 5 hours. The standard deviations of ratios derived from each individual spectrum were used as a measure of the error on any given day.

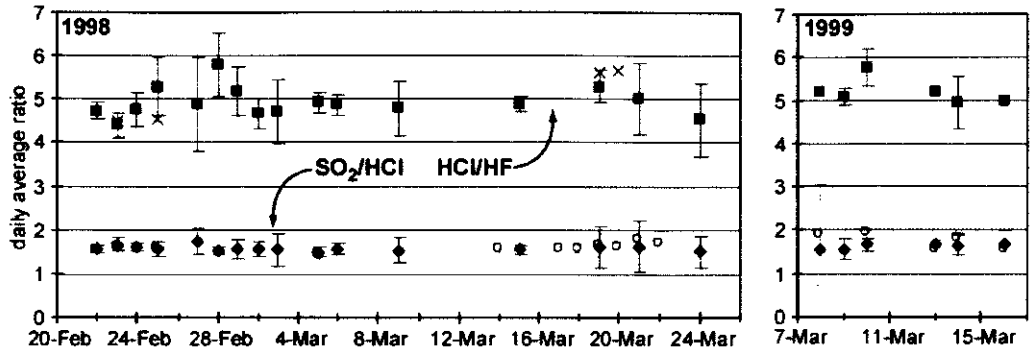

Figure 5-3: Daily average ratios of retrieved amounts from active mode spectra at Santiago Crater. HCl/HF ratios are shown as black squares; SO_2/HCl ratios are black diamonds. Error bars (black) are calculated as the standard deviation of individual ratios for that day. For comparison, daily average ratios from solar spectra are shown as red open circles for SO_2/HCl and red crosses for HCl/HF, with some error bars in grey. The larger error bars are associated with days when either gas concentrations in the spectra were low, or there were fewer data, or both.

Daily average SO_2/HCl ratios in figure 5-3 are strikingly uniform through both field campaigns, and comparative average ratios from solar data are also consistent. Variation over the timescale of about a month, and from one year to the next, is less than the variance in measurements on any single day. Given the larger error on HF retrievals, the HCl/HF ratios are also remarkably stable. Although some of the apparent variation in HCl/HF ratios may result from real fluctuations in source composition, the data are inconclusive. HF in the plume is more susceptible to local meteorology than HCl or SO_2 and so apparent variation may also arise from this cause.

Whatever small-scale fluctuations in measured compositions may be hidden within the daily averages, figure 5-3 confirms that a characteristic feature of Masaya's degassing regime is its compositional stability. Models for the persistent volcanic activity sustained at Masaya since its last reactivation in 1993, and possibly throughout the historic period, must allow for emission of gas of an unchanging composition. Essentially, this involves extended degassing of a constant magma composition under similar conditions of pressure and temperature for at least the duration of these measurements.

5.1.1.3 Variations on the shortest timescales

While variability in gas composition over monthly and yearly timescales has been insignificant, it is possible that the composition may be modified at much shorter timescales (minutes), as a consequence of processes of gas release from the magma. A set of 300 active spectra was collected at Santiago Crater between 1030 h and 1500 h on 9 March 1999, in order to investigate fluctuations in measured gas compositions over this period. SO_2/HCl and HCl/HF ratios calculated from each individual spectrum are shown in figure 5-4.

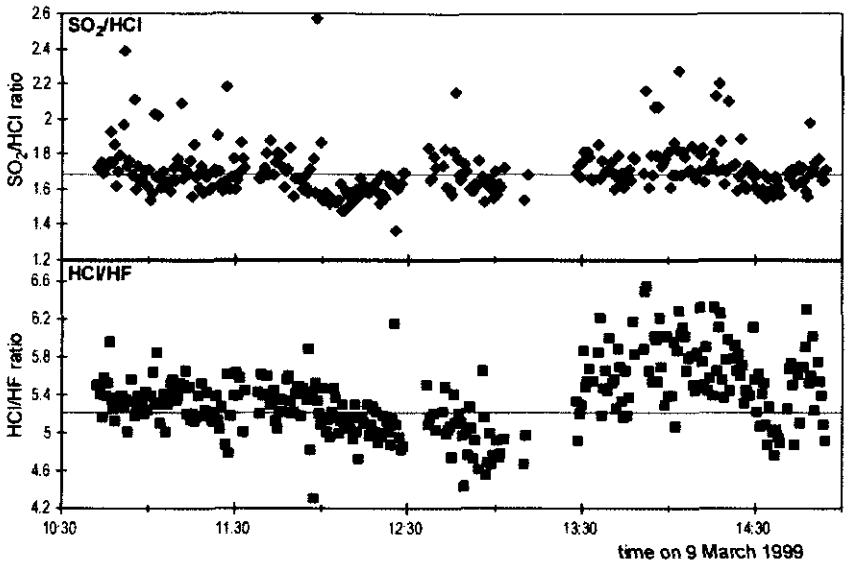

Figure 5-4: SO_2/HCl and HCl/HF ratios calculated from individual active spectra collected on 9 March 1999 at Santiago Crater. Also shown are lines representing averages for the data set. The data gap around 1315 h is related to a computer crash during measurement collection.

Both SO_2/HCl and HCl/HF ratios show some small changes through the period of measurement. However, this apparent temporal variation could be related to changing amounts of gas in the optical path and artefacts caused by non-linear performance of the retrieval across the concentration range (see Chapter 3 section 4, and figure 3-14). Calculated SO_2/HCl ratios are shown plotted against retrieved SO_2 in figure 5-5, to investigate this relationship.

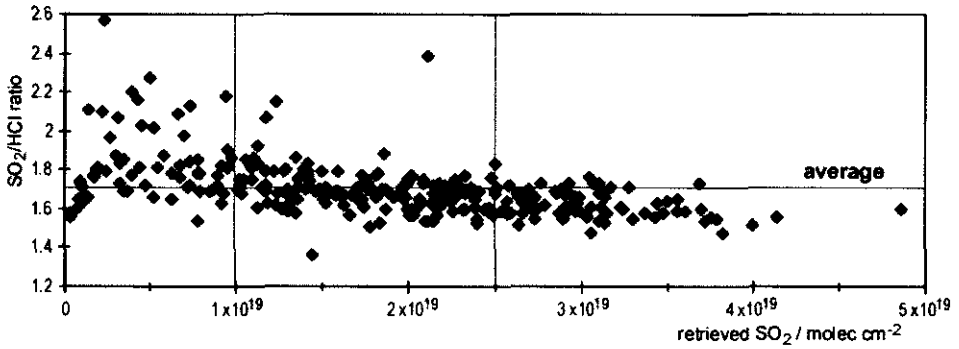

Figure 5-5: Calculated SO_2/HCl ratios for data from 9 March 1999 plotted against retrieved SO_2. Vertical lines divide the three concentration subsets examined in the text.

As in figure 3-14, there is a marked decrease in SO_2/HCl as gas concentration increases. This is likely a retrieval artefact, and so the data were subsequently examined in three concentration subsets, in order to determine whether the range in ratio at any given concentration followed a coherent pattern through time. 64 spectra had retrieved SO_2 below 1×10^{19} molec cm^{-2}: this "low" concentration subset also had the greatest range of ratios, related to larger relative error on these measurements. 157 spectra fell in the "mid" concentration range with retrieved SO_2

between 1×10^{19} and 2.5×10^{19} molec cm^{-2}. The "high" concentration set consisted of 80 spectra with retrieved SO_2 greater than 2.5×10^{19} molec cm^{-2}.

Figure 5-6 shows the data from figure 5-4 redrawn and coded into the three concentration subsets. For both SO_2/HCl and HCl/HF the greatest scatter of points can be attributed to the low subset, as expected due to higher relative error. A coherent pattern in SO_2/HCl ratio through time remains in both mid and high subsets, with ratios in the high subset offset to slightly lower values. In particular, there is a dip in SO_2/HCl ratio around 1200 h, a return to higher values around 1330 to 1400 h, and then another dip at the end of the observation period around 1430 h. The high subset shows a more consistent HCl/HF ratio over time than the mid subset, for which the HCl/HF ratio is especially irregular after about 1330 h. However, even within the high subset, the HCl/HF ratio seems to follow a similar pattern to that demonstrated by the SO_2/HCl ratio.

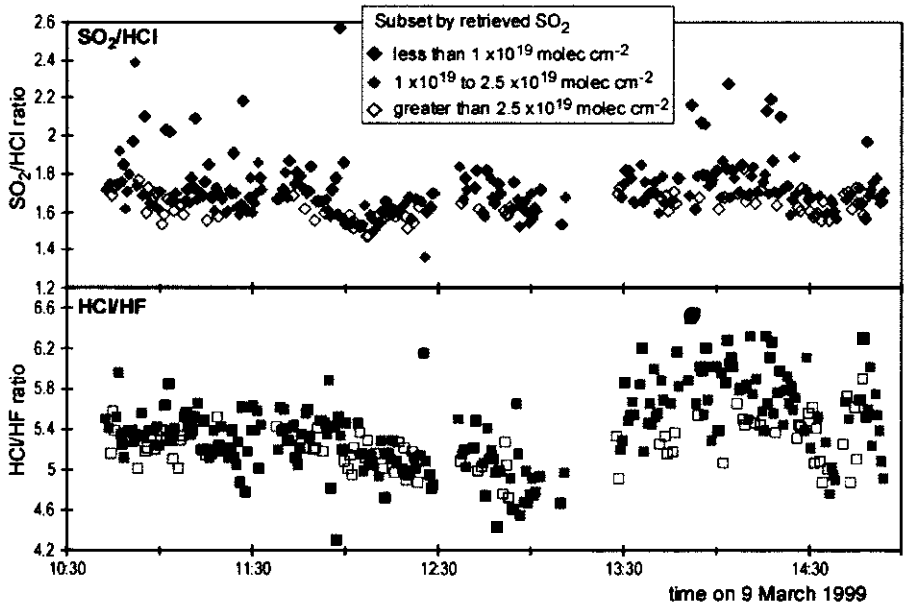

Figure 5-6: SO_2/HCl and HCl/HF ratios calculated from individual active spectra collected on 9 March 1999 at Santiago Crater. Data are subsetted according to the amount of retrieved SO_2. Colour coding for the HCl/HF data is the same as for SO_2/HCl.

Ambient weather was steady, showing fluctuations of only 2 °C in temperature and 6 % in relative humidity during the observation period. Variability in gas ratios over this timescale is therefore unlikely to be related to meteorological factors, although this cannot be ruled out completely. While some of the remaining variation may be related to retrieval artefacts, the synchronised changes in SO_2/HCl and HCl/HF could signal real source variations in volcanic gas composition.

Since the gas composition at Masaya remains steady overall, short-term variation may be linked to short-lived processes of gas release. Gas is released from the surface of lava lakes by bubbles bursting through the lava-air interface and exhaling gas in gusts (Tazieff 1983, 1994). Similarly,

gas is emitted from Masaya's active vent in "puffs", which may be related to bubbles bursting at the shallow magma surface. Such intermittent gas release may tap pockets of gas which have resided in shallow parts of the volcanic system for variable lengths of time, developing individual compositional character relative to their "age". Processes such as shallow degassing-induced crystallisation as well as continual exsolution of more soluble volatiles like Cl and F could contribute to this effect. Alternatively, the small-scale compositional fluctuations may reflect the natural range of variation in equilibrium gas compositions produced by this style of shallow persistent degassing, arising from exsolution at various depths and the relative rates of gas bubble rise and magma ascent.

5.1.2 CO_2–H_2O–SO_2 compositions

H_2O and CO_2 are generally the two most abundant components of volcanic gases, often constituting about 95 mol % of the total. Because carbon dioxide is readily exsolved from magmas and remains relatively inert during exhalation into hydrothermal or atmospheric systems, it is a useful marker of the magmatic contribution to volcanic emissions. While scrubbing of SO_2 in crater lakes (Oppenheimer 1996) can lead to misleadingly low measured SO_2 emissions (Doukas & Gerlach 1995), CO_2 emission rates are more reliable. C/S ratios in magmatic gases from arc volcanoes are generally in the range 1 to 10 (Poorter *et al.* 1991), while the global average CO_2/SO_2 molar ratio for passive volcanic plumes is approximately 2.2 (Williams *et al.* 1992).

CO_2 and H_2O in volcanic gases are inherently difficult to measure by remote methods due to their high natural tropospheric abundances: comparatively small volcanic anomalies are effectively "drowned out" by atmospheric contributions to the measurement. While OP-FTIR measurements in solar mode cannot be used to derive volcanic CO_2 and H_2O due to the long atmospheric path, active spectra (or passive vent measurements) may be suitable. One way to cope with the high background CO_2 in the spectra is by the method of ratioing a spectrum containing volcanic gas to a clean background spectrum so that only the volcanic contribution to the CO_2 absorption remains in the calculated spectrum (e.g. Mori & Notsu 1997). The difficulties associated with this method have already been outlined (Chapter 2 section 1). Instead, in this thesis, total amounts of volcanic plus atmospheric CO_2 have been retrieved from raw spectra, and the volcanic contribution is assessed by means of comparison with retrieved SO_2, assumed to be of purely volcanic origin. CO_2 was retrieved in a narrow window centred on a peak at 2077 cm^{-1}. The procedure for retrieval of volcanic water was similar, and H_2O was retrieved over the 2690–2900 cm^{-1} microwindow at the same time as HCl.

5.1.2.1 CO_2 retrieved

CO_2 was successfully retrieved from spectra collected in active mode at Santiago Crater. Retrieved amounts are plotted against retrieved SO_2 for 1998 and 1999 in figure 5-7. Retrieved errors associated with CO_2 are typically 15–20 %, because the peak at 2077 cm^{-1} is relatively weak and overlaps with a water line. Given the scale of potential error, the correlations shown in figure 5-7 are relatively strong. Strictly, a regression line through the data is a mixing line between atmospheric and volcanic CO_2–SO_2 compositions, with the intercept representative of the atmospheric CO_2 concentration. However, as discussed at the end of Chapter 2 section 3, the gradient of the regression line approximates well to the volcanic CO_2/SO_2 ratio because the absolute CO_2 concentration in volcanic gas is much higher than the absolute atmospheric concentration. So the average volcanic CO_2/SO_2 ratio of the volcanic plume at Santiago Crater was 2.2 and 2.3 in 1998 and 1999, respectively, within approximately ± 15 % error.

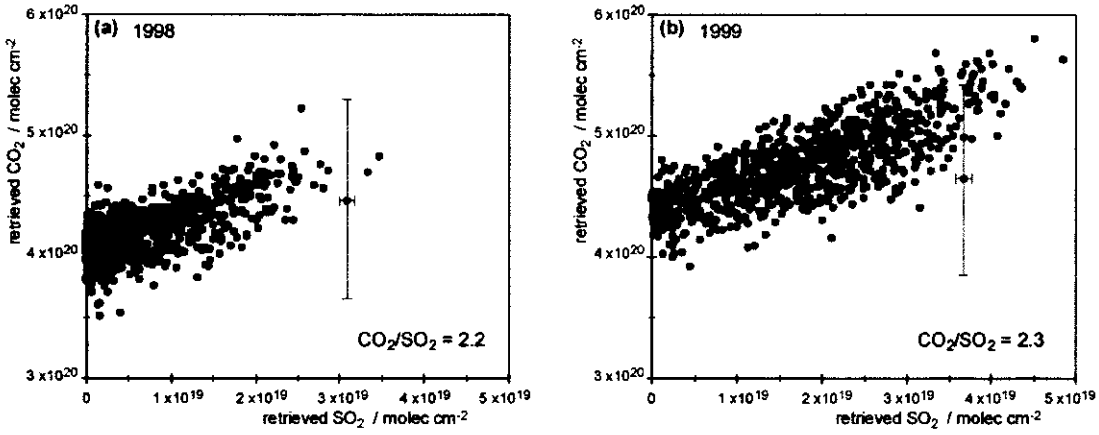

Figure 5-7: Retrieved amounts of CO_2 and SO_2 from active spectra collected at Santiago Crater for (a) 22 February to 24 March 1998, and (b) 8 to 16 March 1999. The intercept of a regression line on the CO_2 axis represents background atmospheric CO_2 concentration over the optical path, while the gradient approximates to the volcanic CO_2/SO_2 ratio. Typical error bars are shown: the error on CO_2 is approximately ± 15–20 %, but this appears exaggerated on the reduced scale of the graphs.

The difference in range of retrieved SO_2 in 1999 compared with 1998 on figure 5-7 is not related to a change in emission rates, but is simply because more of the spectra collected in 1999 contained a high proportion of plume gas than in 1998. The broader distribution of data points on the CO_2–SO_2 plot compared to a similar plot for, say, retrieved SO_2 and HCl (e.g. figure 5-2a) reflects both the greater error inherent in the CO_2 retrieval and also some apparent daily variation in CO_2 intercept, rather than any significant daily variation in CO_2/SO_2 ratio. The overall average background CO_2 concentrations derived from figure 5-7 are 351 ppm and 368 ppm for 1998 and 1999, respectively, while daily average background CO_2 concentrations calculated from similar plots are in the range 330–370 ppm and 360–390 ppm. In comparison, the average atmospheric CO_2 concentrations measured at Mauna Loa were 367 ppm and 370 ppm, for February–March 1998 and March 1999, respectively (Keeling & Whorf 2000). The apparent change in background CO_2 concentration from the OP-FTIR data from 1998 to 1999 is unlikely to relate to

a significant change in regional atmospheric CO_2, although small local variations in background CO_2 due to time of measurement, diffuse flank degassing, or distribution of the volcanic plume cannot be ruled out. Instead, this apparent change is related to the retrieval, since the ILS was different for the two sets of measurements. A better fit to the ILS may have been achieved for the 1999 data, which is why the background CO_2 for that year is closer to the global atmospheric average.

The average CO_2/SO_2 ratios obtained from figure 5-7 mask small daily variations in ratio of 2.0–2.6 in 1998 and 1.8–2.8 in 1999. Some of this variation may reflect inaccuracy in the CO_2 retrieval, particularly on days when the H_2O column concentration was high as H_2O lines dominate the CO_2 retrieval microwindow. Daily variation in CO_2/SO_2 ratio and background CO_2 concentration is not significant, given the high error on the CO_2 retrieval. Similarly, the change in average CO_2/SO_2 ratio from 2.2 in 1998 to 2.3 in 1999 is negligible.

The maximum retrieved CO_2 from these active spectra is approximately 5.6×10^{20} molec cm^{-2}, equivalent to 480 ppm (figure 5-7b). Assuming that for this measurement the plume occupied half of the 518 m optical path, the CO_2 concentration in the plume above Santiago Crater was approximately 590 ppm, compared with a background atmospheric concentration of 368 ppm. This implies that the plume above Santiago Crater causes a local CO_2 anomaly of about 220 ppm above normal atmospheric abundances, equivalent to a 60 % increase. In comparison, Koepenick *et al.* (1996) found maximum volcanic plume CO_2 anomalies of 70 ppm (with average of 10 ppm) 1 km downwind from Oldoinyo Lengai in 1994, using LICOR, while 4–6 km downwind from Popocatepetl maximum volcanic plume CO_2 anomalies were only 3–4 ppm (Gerlach *et al.* 1997). The OP-FTIR measurements at Masaya show that, where possible, ground-based measurements of the higher plume CO_2 anomalies close to an active crater may provide more dependable data.

5.1.2.2 H_2O retrieved

The amount of water vapour in the optical path recorded in active spectra at Santiago Crater is strongly dependent on the background atmospheric concentration. The background water vapour in the troposphere varies as ambient temperature and humidity change. These variations in background water vapour are visible in figure 5-8, which shows retrieved H_2O plotted against retrieved SO_2, coded by date.

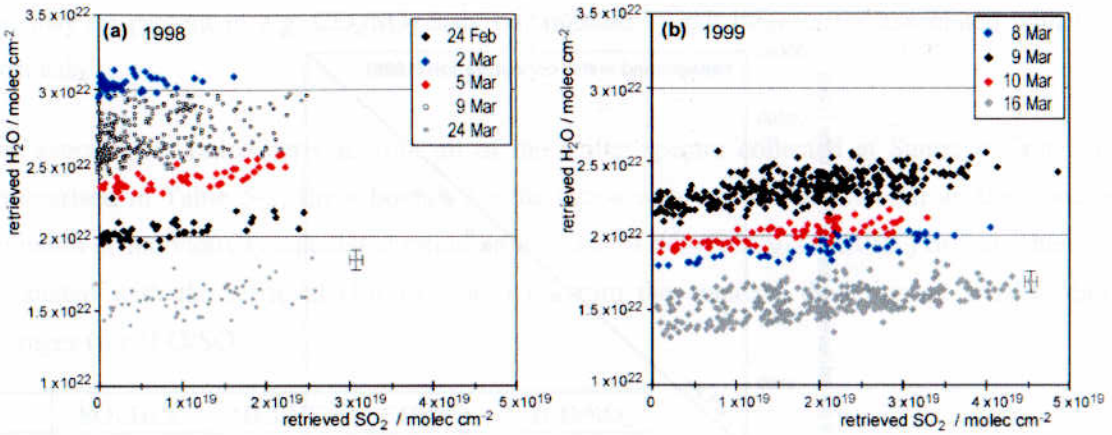

Figure 5-8: Retrieved amounts of H_2O and SO_2 from active spectra collected at Santiago Crater on selected days in (a) 1998 and (b) 1999. Data are coded according to date of collection. The intercept of a regression line on the H_2O axis represents the background atmospheric H_2O concentration over the optical path, while the gradient approximates to the volcanic H_2O/SO_2 ratio. Typical error bars are shown and are approximately ± 4 % on both H_2O and SO_2.

The most striking feature of figure 5-8 is the variability in background water concentrations apparent from day to day. Intercepts on the H_2O axis indicate that the background water content can range from 1.5×10^{22} molec cm^{-2} to 3×10^{22} molec cm^{-2}, equivalent to 12500 ppm to 25500 ppm across the 518 m optical path. This range of concentrations is explained by the wide range of ambient relative humidities (between 30 and 60 %) measured during fieldwork. Where spectra were collected over periods of more than an hour (9 March 1998, 9 and 16 March 1999) some diurnal variation in atmospheric water is obvious from the broad distribution of data points.

For measurements in 1999, accurate meteorological data at Santiago Crater were obtained using a portable weather station. Recorded values of ambient temperature, pressure and relative humidity, together with tabulated values for the saturated vapour pressure of water (Smithsonian Meteorological Tables quoted in Houghton 1986), can be used to derive an independent measurement of background atmospheric water content. A comparison of background water content derived from the two different methods is shown in figure 5-9. The background water content estimated from the OP-FTIR retrievals is systematically lower than the ambient value from weather measurements by approximately 10 %. While error associated with the meteorologically derived value may be ± 2%, and the error on the OP-FTIR retrieved value may be 7–10 %, a further contribution to the discrepancy may come from temperatures used in the calculations. The average temperature across the crater is potentially 5 °C hotter than ambient temperatures elsewhere: saturated vapour pressure increases with temperature, and therefore affects relative humidity.

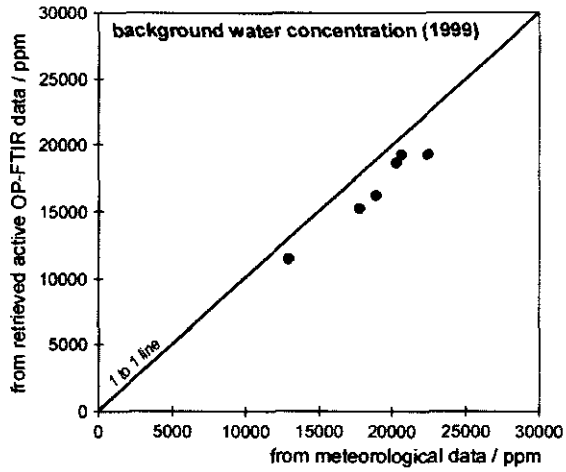

Figure 5-9: Comparison of estimates of background atmospheric water concentration derived from meteorological data (x-axis) or from the intercept on plots of retrieved H_2O against SO_2 from active OP-FTIR data. Each dot represents the average for data on one day. A one-to-one line indicates that values derived from the OP-FTIR data are systematically lower than the calculated values.

Given the extreme background variation in water content, the trends on figure 5-8 set by the proportion of volcanic H_2O: SO_2 are remarkably consistent. Daily average H_2O/SO_2 ratios were approximated by the gradient of regression lines through the data for each day. For more than half of the daily datasets in 1998 the R^2 correlation coefficient between retrieved H_2O and SO_2 was unreliably low. For those data where R^2 was above 0.5, the H_2O/SO_2 ratios ranged from 45 to 96 and 59 to 76 in 1998 and 1999, respectively. Because the maximum amount of water due to the presence of the volcanic plume is not very different from the background (plume absent) amounts, the gradient of a regression line is highly sensitive to small errors in the retrieved amounts. Since the 1999 data span a larger concentration range than the 1998 data, they are considered more reliable, and the average H_2O/SO_2 ratio is taken to be 66 ± 7 ($\pm 1\sigma$). Although this value can reasonably be used as representative of the H_2O–SO_2 composition of Masaya's volcanic plume, the variation in calculated H_2O/SO_2 ratios cannot be assigned to a volcanic cause since scatter in the retrieved data is too great.

5.1.3 Average Masaya plume composition and emission rates

The data retrieved from infrared spectra collected at Santiago Crater have shown little evidence for temporal variability of Masaya's plume gas composition. Although some variation in retrieved gas ratios, generally of the order of less than ± 10 %, was apparent, this has mainly been shown to be insignificant given the scale of uncertainties associated with the retrievals. At the shortest timescales (minutes and hours), some potentially real fluctuations in the SO_2–HCl–HF composition at source have been identified. These may be linked to processes of gas release from a subsurface lava lake. Such deviations in gas composition are only small (10 % change in ratio),

and may be present in e.g. CO_2/SO_2 also, but masked by the larger error associated with CO_2 retrievals.

The average gas ratios derived from all of the active spectra collected at Santiago Crater are summarised in Table 5-2. Error bounds for the ratios were calculated either from the standard deviation of individually calculated ratios (in the case of SO_2/HCl and HCl/HF) or from the error associated with the retrieval (for CO_2/SO_2) or from the standard deviation of reliable daily averages (for H_2O/SO_2).

	SO_2/HCl	HCl/HF	CO_2/SO_2	H_2O/SO_2
1998	1.6 ± 0.2	4.9 ± 0.7	2.2 ± 0.3	72 ± 25
1999	1.6 ± 0.2	5.1 ± 0.6	2.3 ± 0.3	66 ± 7

Table 5-2: Average molar ratios with error bounds for the plume above Santiago Crater in 1998 and 1999.

As previously discussed, minor components of volcanic gases such as H_2S, CO, COS, SiF_4 etc were below detection limit in these spectra. Since these species typically make up much less than 1 mol % of most measured gas compositions, the ratios in Table 5-2 can be used to derive a total plume composition, within good approximation (Table 5-3). During both field campaigns, colleagues from The Open University, the University of Montreal and INETER monitored the sulfur dioxide emission rate downwind (usually along the Llano Pacaya) by COSPEC (Delmelle *et al.* 1999a). Average SO_2 emission rates were little different over the two years, at 21.4 kg s^{-1} (1σ = 6.3 kg s^{-1}) and 20.7 kg s^{-1} (1σ = 5.6 kg s^{-1}) for February to April 1998 and February to March 1999, respectively. Although these average emission rates hide significant short-term variability in COSPEC measurements (discussed below), they can be used in combination with the OP-FTIR data to derive average total gas emission rates, also shown in Table 5-3.

	1998			**1999**		
	Mol %	**Mass %**	**Emission Rate / kg s^{-1}**	**Mol %**	**Mass %**	**Emission Rate / kg s^{-1}**
H_2O	95	87	430	94	86	380
CO_2	2.9	6.5	32	3.3	7.3	33
SO_2	1.3	4.3	21	1.4	4.6	21
HCl	0.82	1.5	7.6	0.89	1.6	7.4
HF	0.17	0.17	0.9	0.17	0.18	0.8
Total	100	100	500	100	100	450

Table 5-3: Average gas composition and emission rates of Masaya's plume above Santiago Crater in 1998 and 1999. All values quoted to 2 significant figures.

Emission rates in Table 5-3 are based on the mean sulfur dioxide emission rate calculated for the entire set of COSPEC measurements obtained by my colleagues during the 1998 and 1999 field campaigns. However, these averages were associated with standard deviations of 30 %, typical for COSPEC data (e.g. Stoiber *et al.* 1983), and with maxima and minima of 41.9 kg s^{-1} and 7.8 kg s^{-1} in 1998, and 47.0 kg s^{-1} and 14.5 kg s^{-1} in 1999 (P. Delmelle, pers. com., 1999). For a

single day, a series of consecutive COSPEC runs could return emission rates with larger standard deviations of up to 50 % (G. Williams-Jones, pers. com.), a variability also observed during a previous strong degassing episode at Masaya (Stoiber *et al.* 1986). Such variation in measured SO_2 flux, is due, at least in part, to artefacts of the measurement itself: wind speeds affect plume dispersion and the strength of the measured SO_2 signal, cloud cover controls the amount of available UV radiation, tropospheric transport results in turbulence perhaps exacerbated by airflow over the Llano Pacaya highland. The variability may also be part real: intermittent puffing of gas from the vent and crater controls emission rate at the shortest timescales. Earth tide may have some influence on gas emission at Masaya, as at Halemaumau (Connor *et al.* 1988), since there is evidence for tidal control for short-term microgravity changes (Delmelle *et al.* 1999a). If short-term variations in gas emission rate do occur, they are unaccompanied by significant changes in gas composition.

No compositional variations to suggest changes within the volcanic system have been detected on any scale. Volatile depletion of the magma source, changes in the magma composition, or movement of magma within the system, are all expected to result in changes in gas composition, and probably also emission rate. Instead, at Masaya, all the evidence points to great stability in the degassing regime leading to approximately constant compositions and emission rates over the observation period.

5.2 Discussion

While it is important to consider the results of these gas measurements at Masaya Volcano in the context of other published data, both for Masaya and other volcanoes world-wide, comparisons with data obtained by different measurement techniques are problematic. In particular, gas measurements by remote methods as compared to direct sampling may record the plume composition at later stages in its evolution. Unfortunately, there are only a few remotely-measured plume compositions in the literature for comparison.

In this section I discuss both the composition and emission rates from Masaya in the context of measurements from other volcanoes. I also critically examine a previous study of gases from Masaya (Stoiber *et al.* 1986) in the light of these new data. Finally the results are used to provide some constraints for physical models of Masaya's degassing regime, considered in more detail in Chapter 6.

5.2.1 Composition and emission rate

Masaya is unusual for volcanoes along the Central American Arc. The Nicaraguan volcanoes generally fall into two categories: relatively low-lying shield-like stratovolcanoes with many cones and craters located near fault zones, and relatively taller stratocones with one major central vent (van Wyk de Vries 1993). In contrast, the Masaya caldera is located within a larger, older caldera to the edge of a voluminous basaltic ignimbrite shield (Las Sierras): it is closer to a typical shield volcano than a stratocone. In terms of the measured gas composition, however, there are strong similarities between the OP-FTIR results and the few directly sampled compositions available for other Central American volcanoes. Table 5-4 presents gas data for Masaya and Momotombo (Nicaragua), Poas and Arenal (Costa Rica).

As at other arc volcanoes, all the gas compositions in Table 5-4 are relatively water rich (c.f. Symonds *et al.* 1994). Again, typically for passively degassing arc volcanoes, SO_2/HCl ratios are all in the range of 1 to 3, while CO_2/SO_2 ratios are generally in the range 1 to 4. Anomalous CO_2/SO_2 ratios are found for most of the Poas data, and the 1982 measurement for Momotombo, which was just one sample, rather than a mean composition. Poas gases are strongly influenced by the hydrothermal system which sustained a crater lake during the sampling periods in 1981–83. These compositions are significantly hydrated: their relatively low proportions of CO_2, generally magmatic in origin, indicate a strong contribution from a hydrothermal or meteoric source. The gas sample from 1992, which was very different from the earlier data, was collected from a fumarole on the dry crater floor, and showed clear evidence of direct magmatic contribution (Martini 1996).

Volcano	H_2O	CO_2	SO_2	H_2S	HCl	HF	other	Total	SO_2/ HCl	HCl/ HF	CO_2/ SO_2	Ref
Masaya 1998 (ave)	94.79	2.90	1.32		0.82	0.17		100.00	1.61	4.82	2.20	
Masaya 1999 (ave)	94.23	3.28	1.43		0.89	0.17		100.00	1.61	5.24	2.29	
Masaya 1980–82									0.9	>201		1
Momotombo 1978	93.00	4.70	1.20	0.02	0.40		0.71	100.03	3.00		3.92	2
Momotombo 1980 (mean)	97.44	1.45	0.42	0.23	0.17	0.02	0.46	100.18	2.4	11.06	3.48	3
Momotombo 1982	93.18	3.63	0.47	0.34	0.37	0.01	2.00	100.00	1.27	37.00	7.72	4
Momotombo 1983 (mean)	95.05	2.38	0.70	0.49	0.35	0.03	0.98	99.97	2.00	12.07	3.40	4
Momotombo 1985 (mean)	93.50	3.66	0.93	0.67	0.40	0.01	0.80	99.97	2.33	28.57	3.94	4
Poas 1981 (June)	95.79	0.82	1.77	0.02	0.91	0.09	0.58	99.98	1.93	9.72	0.46	3
Poas 1981 (July)	96.14	0.71	1.54	0.42	0.80	0.09	0.67	100.38	1.91	8.55	0.46	3
Poas 1981 (Aug)	96.35	0.95	1.34	0.01	0.69	0.08	0.58	100.00	1.93	8.62	0.71	3
Poas 1983	97.08	0.53	1.99	0.01			0.39	100.00			0.27	3
Poas 1992	88.46	4.89	3.94	1.34	1.30	0.03	0.03	99.99	3.03	45.04	1.24	5
Arenal 1982	94.00	3.00	2.22	0.054			0.5	99.77			1.35	6

Table 5-4: Total gas compositions in mol %, and molar gas ratios, for Masaya and other Central American Arc volcanoes. All data are from direct sampling methods, except for the OP-FTIR data presented in this thesis. Where there are gaps in the table, no data was available. Masaya data for 1980–82 were derived from filter pack measurements on the rim of Santiago Crater. Momotombo is a passively degassing Nicaraguan stratocone with summit fumaroles: direct magmatic contribution to the gases was confirmed by observation of glowing lava through crater cracks. Poas (Costa Rica) data for 1981–83 were collected from vigorously degassing dome fumaroles with a nearby crater lake; in 1992 the crater lake was absent. Gas emission from the active and summit craters of Arenal (Costa Rica) in 1982 accompanied basaltic andesite lava extrusion. References: 1 Stoiber *et al.* (1986), 2 Allard (1983), 3 Symonds *et al.* (1994), 4 Menyailov *et al.* (1986), 5 Martini (1996), 6 Casadevall *et al.* (1984).

In comparison with the average OP-FTIR Masaya compositions measured a year apart, gas data for Momotombo and Poas show a considerable lack of stability from one year to the next. This may reflect irreproducibility of the direct sampling technique more than real deviations in gas composition. A striking feature of the Masaya compositions in 1998–99 is the relatively high HF contents, and correspondingly lower HCl/HF ratios. This greater proportion of HF measured at Masaya could be real, and related to the high temperature very shallow open-vent degassing occurring at Masaya, in contrast to lower temperature fumarolic gas release at the other volcanoes, which provides opportunity for reaction and removal of HF before it is sampled. Alternatively, the lower HF recorded at the other locations may be the result of unquantified reaction of HF in sampling vessels. The apparent discrepancies between gas data collected in 1980–82 at Masaya and those presented in this thesis are discussed in detail below.

In Table 5-5, molar gas ratios derived from remote plume measurements at a range of volcanoes world-wide are compared. Apart from Pu'u O'o and Etna, all of the volcanoes in Table 5-5 are situated on arcs.

Volcano	SO_2/HCl	CO_2/SO_2	method	conditions	Ref
Masaya (1998)	1.6	2.2	OP-FTIR	passive degassing	
Masaya (1999)	1.6	2.3	OP-FTIR	passive degassing	
Unzen (Mar 1992)	0.7–1.6		OP-FTIR	dome degassing	1
Unzen (Jul 1992)	1.0–1.8		OP-FTIR	dome degassing	1
Soufriere Hills (Jul 1998)	1.6		OP-FTIR	dome degassing	2
Soufriere Hills (Jan 1999)	3.1		OP-FTIR	dome degassing	2
Vulcano (1993)	3.5–11.2		OP-FTIR	fumarolic degassing	3
Vulcano (1994)	0.8–1.4		OP-FTIR	fumarolic degassing	4
Etna (1994)	3.3–4.1		OP-FTIR	passive degassing	4
Etna (Jun 1997)	4.0		OP-FTIR	passive degassing	5
Etna (Oct 1997)	4.6		OP-FTIR	passive degassing	5
Popocatepetl (Feb 1997)	4.4–5.1		OP-FTIR	occasional minor ash eruptions	6, 7, 8
Popocatepetl (Jun 1995)		1.5–2.9	LICOR/ COSPEC	non-eruptive degassing	9
White Island (1996)	4.7		OP-FTIR	fumarolic degassing	8
Aso (1996)	40	3.5	OP-FTIR	fumarolic degassing	10
Redoubt (Jan 1990)		9.9	COSPEC	1 mo post-eruptive degassing	11
Redoubt (Jun 1990)		1.3–2.2	MIRAN/ COSPEC	6 mo post-eruptive degassing	11
Pu'u O'o (1995)		0.2	LICOR/ FTIR	degassing from lava lake / point sources	12

Table 5-5: Molar gas SO_2/HCl and CO_2/SO_2 ratios derived from remote measurements of volcanic plumes. Most of the measurements were made at volcanoes undergoing quiescent degassing or in the post-eruptive phase; Popocatepetl in 1997 was undergoing intermittent ash eruptions, and the January 1990 measurements at Redoubt were only a month after the climactic eruption. References: 1 Mori *et al.* (1993), 2 Oppenheimer *et al.* (2001b), 3 Mori *et al.* (1995), 4 Francis *et al.* (1995), 5 Francis *et al.* (1998), 6 Goff *et al.* (1998), 7 Love *et al.* (1998), 8 Love *et al.* (2000), 9 Gerlach *et al.* (1997), 10 Mori and Notsu (1997), 11 Casadevall *et al.* (1994), 12 Gerlach *et al.* (1998).

There are great similarities in the remotely-measured ratios. SO_2/HCl is generally in the range of 1 to 5. The wide range of SO_2/HCl ratios from Vulcano in 1993 covers measurements from five different fumaroles, for which the ratio was seen to vary significantly from one to the next (Mori *et al.* 1995). In 1994 a combined plume exiting the crater was sampled by Francis *et al.* (1995) using the spectrometer in active mode, providing a more reliable average plume composition. The high SO_2/HCl ratio obtained at Aso Volcano was for fumarolic degassing close to a crater lake (Mori & Notsu 1997): a considerable proportion of magmatic HCl may have been scavenged by the hydrothermal system.

CO_2/SO_2 ratios in Table 5-5 range between 0.2 and 10. There are fewer remotely measured CO_2 data owing to the difficulties associated with the high background atmospheric concentration. The measurements at Redoubt and Pu'u O'o were not strictly remote as airborne instruments were flown downwind from the volcanic source to collect in-plume gas samples. The Pu'u O'o

cone is situated on Kilauea's East Rift Zone, approximately 15 km away from the summit caldera, and CO_2/SO_2 gas ratios are severely affected by extensive early depletion of CO_2 via summit degassing, prior to magma reaching the ERZ (e.g. Gerlach & Graeber 1985). In general, convergent-, hotspot, and divergent-plate volcanoes show a similar range of CO_2/SO_2 ratios: this ratio is more strongly affected by the extent of degassing of the magma, with the more insoluble CO_2 readily depleted from the magma early on, as at Pu'u O'o (Symonds *et al.* 1994). In the same way, at Redoubt, six months into the post-eruptive phase the CO_2/SO_2 ratio was much reduced from the earlier figure, although there are greater uncertainties on these values.

Comparisons of volcanic gas emission rates, as well as compositions, are essential for understanding the volcanic system. Rates can be used to assess volumes of magma required to support the surface behaviour in order to provide constraints for possible physical degassing mechanisms. In general, quiescent degassing supports relatively low emission rates, while the highest emission rates occur during eruptive phases. Table 5-6 compares the emission rates derived from OP-FTIR and COSPEC measurements at Masaya in 1998 and 1999 with rates during the previous degassing episode in 1980–82, and with data for passively degassing volcanoes world-wide.

	Emission rates / kg s^{-1}				
Volcano	**SO_2**	**HCl**	**HF**	**CO_2**	**Ref**
Masaya (1998)	21.4	7.6	0.9	32.3	
Masaya (1999)	20.7	7.4	0.8	32.7	
Masaya (1980–82)	14.8	9.6	0.19		1
Etna (Jun 1997)	62.5	8.9	1.3	412.2	2, 3
Stromboli (1980–93)	4.6–9.3	0.7–1.5	0.02–0.05	33.6–67.1	4
Erebus (ave 1986–91)	0.49	0.35	0.17		5
Pu'u O'o (Sep 1995)	25			3.5	6
Mt St Helens (Jul 1980)	14.8	1.44	0.4	135.2	7
Redoubt (Jun 1990)	18.5	9.3		27.8	8, 9
Augustine (1987)	4.4	2.4	0.02	1.2	10
Global volcanism	412	13–348	1.9–190	2060–2490	11, 12, 13, 14

Table 5-6: Gas emission rates from passively degassing volcanoes. References: 1 Stoiber *et al.* (1986), 2 Francis *et al.* (1998), 3 D'Alessandro *et al.* (1997), 4 Allard *et al.* (1994), 5 Zreda-Gostynska *et al.* (1997), 6 Gerlach *et al.* (1998), 7 McGee *et al.* (1992), 8 Casadevall *et al.* (1994), 9 Gerlach *et al.* (1994), 10 Symonds *et al.* (1990), 11 Andres and Kasgnoc (1998), 12 Symonds *et al.* (1988), 13 Gerlach (1991), 14 Williams *et al.* (1992).

The data for Mt St Helens, Redoubt and Augustine volcanoes in Table 5-6 are from non-explosive phases following major eruptions. Etna is renowned for its prodigious degassing unassociated with major eruptive activity: in June 1997 there was mildly explosive activity in two of the summit craters and minor lava effusion from one. Stromboli undergoes persistent open-conduit degassing accompanied by minor explosions. Erebus has been passively degassing throughout the historic period and the data relate to quiet gas release from the surface of a slowly

convecting lava lake. Several point sources and an active lava lake released gas from Pu'u O'o during measurement of the data in Table 5-6.

The only higher SO_2 emission rates than those at Masaya in 1998–99 are from Etna and Pu'u O'o. Emissions of halogen gases from Masaya match those from Etna. While Stromboli's CO_2 emission rate is similar to that at Masaya, its SO_2 emissions are much weaker: this may relate to a dominant deep CO_2 rich source magma available at Stromboli (Allard *et al.* 1994).

Estimates of total gas emission rates for global sub-aerial volcanism are poorly constrained and cover broad ranges, especially for the halogen gases, which are rarely remotely monitored. The lower limits for global volcanic HCl and HF emissions are exceeded even by just the list of passively degassing volcanoes in Table 5-6.

A water emission rate of more than 400 kg s^{-1} measured at Masaya (see Table 5-3) is the highest reported quiescent steam output from a single volcano, although there are few data available for comparison. It is possible that a proportion of water in Masaya's plume has a meteoric, rather than magmatic, source, as shown for some other high temperature gas samples (e.g. Fischer *et al.* 1998). However, the stability of the average emission rates and H_2O/SO_2 ratios observed one year apart, together with observed gas release through an open-vent at surface levels, favour steady-state degassing of a magmatic source, with little meteoric contribution.

Along with Stromboli, and to a lesser extent Etna, Masaya's high gas emission rates are accompanied by negligible eruption of magma. Masaya is a type location at which to address questions associated with persistently active volcanoes (e.g. Allard 1997, Allard *et al.* 1994, Francis *et al.* 1993). How does magma replenishment take place? What is the ultimate fate of degassed magma? How does the conduit remain open? Models of Masaya's regime must provide for shallow level magma replenishment able to sustain high rate continuous release of magmatic volatiles, without eruption of lava (to be discussed in Chapter 6).

5.2.2 SO_2/HCl ratios at Masaya compared with an earlier study

Emission rates and composition of Masaya's plume were previously studied during an earlier episode of strong degassing, under conditions similar to those experienced for my fieldwork in 1998–99. Stoiber *et al.* (1986) quantified Masaya's plume composition in 1980–82 using plume filter samples and COSPEC measurements. Ground-based COSPEC traverses were mostly made along the Llano Pacaya, directly comparable to the COSPEC data collected in 1998–99. Filter packs able to collect SO_2, HCl, HF and HBr gases, sulfate, chloride, fluoride and bromide anions, were deployed both on the rim of Santiago Crater and at stations downwind.

Bromine and fluorine results were presented with caution, as they were close to detection limits, and the ion-chromatographic laboratory analysis may have been unreliable. I suspect that the

negligible HF concentration that Stoiber *et al.* (1986) obtained is at least partly related to the filter sampling and analytical methods, primarily through adsorption or reaction of HF in the collection apparatus. For this reason I concentrate on comparisons of sulfur and chlorine only in further discussion.

Stoiber *et al.* (1986) report total S/Cl mass ratios and H_2S/SO_2, SO_2/SO_4^{2-}, HCl/Cl^- ratios for 1980–82 (their tables 1 and 2), which are summarised in Table 5-7. They derive average emission rates of SO_2, HCl and HF of 14.8 kg s^{-1}, 9.6 kg s^{-1} and 0.2 kg s^{-1}, respectively (their table 4), assuming that all recorded sulfur and halogen species were originally present as SO_2 and hydrogen halide gases.

	Mass ratios			Molar ratios	
Species	**Average**	**No of samples**	**S. D.**	**Average**	**S. D.**
S_t/Cl_t	0.8	29	0.26	0.88	0.29
SO_2/SO_4^{2-}	90.5	5	55.6	135.7	83.4
HCl/Cl^-	29.5	5	11.4	28.7	11.0
HCl_t/HF_t	>367	5		>201	

Table 5-7: Mass ratios for species in Masaya's plume at Santiago Crater in 1980–82, from tables in Stoiber *et al.* (1986). Molar ratios calculated by simple mass-molar conversion. Standard deviations are for the averages for each set of samples listed in the tables. The total S/Cl ratio is an average for November 1980 to November 1982, whereas the other ratios span the period November 1980 to February 1981. An H_2S/SO_2 mass ratio of 0.00063 was also quoted based on very limited data.

Because the OP-FTIR data records gaseous molecules present above Santiago Crater, my results should strictly be compared with gas phase data, discounting contributions from aerosol. From the data reported by Stoiber *et al.* (1986), with appropriate mass-to-molar conversions, SO_2/HCl gas ratios can be calculated using the relationships:

$$S_t = SO_{2(g)} + H_2S_{(g)} + SO_4^{2-} \quad (5\text{-}2)$$

$$Cl_t = HCl_{(g)} + Cl^- \quad (5\text{-}3)$$

This leads to an average $SO_{2(g)}/HCl_{(g)}$ molar ratio for 1980–82 of 0.91, apparently lower than the ratios measured in 1998–99 (approximately 1.6). However, closer inspection of the gas data presented by Stoiber *et al.* (1986) reveals great variability between individual analyses: for example, even within the two months Jan–Feb 1981, S_t/Cl_t ranges 0.65–1.79, SO_2/SO_4^{2-} ranges 24.1–197 and HCl/Cl^- ranges 13.2–35.5. This scale of variation is at odds with the consistency in gas composition so far presented in this thesis, and indicates an inherent problem with reproducibility in the sampling method used by Stoiber *et al.* Not only is the filter pack method subject to the normal difficulties of reaction or absorption within containers associated with any form of invasive sampling procedure, it may also suffer from spatial and temporal heterogeneities in the plume. For comparison, the OP-FTIR technique at Etna (Francis *et al.* 1998, Oppenheimer

et al. 1998a) provided a more consistent and reliable plume composition than plume filter samples collected on the rims of Etna's active craters over the same period (Pennisi & Le Cloarec 1998).

The average $SO_{2(g)}/HCl_{(g)}$ molar ratio of the results of Stoiber *et al.* (1986) for 1980–82 should be quoted as 0.9 ± 0.6 (using 2σ error calculated from the average S_t/Cl_t ratios presented in their Table 1), but this may be far from representative of the true plume composition. Given this range of uncertainty, the results of Stoiber *et al.* are not significantly different from those presented here for 1998–99, and the gas vented from Masaya may not have changed substantially in composition in nearly 20 years.

5.2.3 Implications for degassing processes

The gas composition and emission rates measured by OP-FTIR in 1998 and 1999 place constraints on models for the degassing regime at Masaya during this period. The gas composition is similar to measurements at other passively degassing arc volcanoes, implying a significant contribution from subduction-related components to the volatile source (e.g. Alt *et al.* 1993, Sano & Williams 1996, Symonds *et al.* 1994). The average gas composition presented in this chapter has been shown to be primarily "magmatic" in nature. Since this composition has remained unchanged over the two measurement periods, it requires a constant source able to remain undepleted in terms of its volatile supply. The relatively high proportion of HF in Masaya's plume calls for shallow level near-complete degassing of magmas, directly into the atmosphere. Visual observations of the vent and negligible volatile contents in matrix glasses and shallowly trapped melt inclusions in recently erupted volcanic bombs support this assertion.

Average emission rates along with reasonable estimates of initial magma volatile contents can constrain the volumes of magma degassed during this period. Volcanic bombs erupted from Santiago Crater during minor explosions in October 1998 and September 1999 contained plagioclase as the predominant phenocryst in a vesiculated glassy matrix. Melt inclusions within these phenocrysts contained only low dissolved sulfur and chlorine contents (less than 100 and 400 ppm, respectively) when studied under electron microprobe (see Table 6-2, Appendix and Delmelle *et al.* 1999a), suggesting considerable melt degassing prior to entrapment. Matrix glass volatile contents were negligible.

Better estimates of parent volatile contents in the basaltic magma are available from published data for other arc volcanoes (e.g. Holloway & Blank 1994, Metrich *et al.* 1999, Papale & Polacci 1999, Roggensack *et al.* 1997, Sisson & Layne 1993). Typical melt concentrations of 1200 ppm (mass) S, 0.4 wt % CO_2 and 4–5 wt % H_2O are assumed for Masaya parent basalt. Coupled with average emission rates of 21 kg s^{-1} SO_2, 32.5 kg s^{-1} CO_2 and 410 kg s^{-1} H_2O, these concentrations

suggest that approximately 3×10^{11} kg of magma have been fully degassed over the 13 month period between my first and last gas measurements.

In order to sustain the rates and invariant composition of gas emitted from Masaya, magma must have been continuously replenished to shallow levels during those 13 months. The estimated mass of magma is equivalent to a volume of approximately 1×10^8 m^3, and suggests an average shallow level replenishment rate of 3 m^3 s^{-1} during that period. Interestingly, this number is similar to the average magma supply rate of at least 0.1 km^3 yr^{-1} during the last century, which Stoiber *et al.* (1986) suggest on the basis of completely different data and assumptions. In contrast, estimates of magma production rate over the last 300 years based on edifice sizes are $0.5–2 \times 10^{-3}$ km^3 yr^{-1} for the Masaya section of the Central American Volcanic Arc (Carr 1984, Carr *et al.* 1990, Wadge 1984). The discrepancy is due in part to the process of averaging over a period of time that includes both active and quiescent volcanic phases. Because my estimate is calculated from gas and volatile data, the difference may also be related to the possibility of "excess" gas emission, magma recycling, and decoupling of melt and volatiles in arc volcanic processes.

The ultimate fate of replaced degassed magma remains an unresolved question. The lack of eruption of any significant amount of lava at the same time as such prolific release of volcanic gas indicates that open-conduit conditions prevail at Masaya, so that pressure build-up and explosions are averted.

A more complete discussion of potential physical models for Masaya's degassing regime is presented in Chapter 6. The requirements for the system presented by the OP-FTIR spectroscopic study of the gas plume can be summarised as open-conduit steady-state degassing, supported by efficient gas transport and release at shallow levels. Stoiber *et al.* (1986) described a closed-system degassing model for Masaya, in which a period of degassing begins with high emission rates of SO_2 and maximum S/Cl values. They suggested that SO_2 emission rates and S/Cl ratios should decline over the course of a few years with S more rapidly outgassed from the magma body than Cl. Results from 1998–1999 show no such trend and do not support this model. Rymer *et al.* (1998) explained microgravity measurements at Masaya by a process of discontinuous magma convection, in which large scale convective magma overturn brings vesiculated gas-rich magma close to the surface. This kind of process could link with the open-system degassing that I envisage, so that the shallowest parts of the magma system undergo discrete overturns, while a steady-stream of volatiles is continuously received from depth.

5.3 Conclusions of Chapter 5

This chapter has assessed the volcanic gas data from Masaya in 1998–99 for the information that they provide about the current activity at this persistently active volcano.

(a) The results have shown that a generally overwhelmingly consistent gas composition is emitted from Masaya over all timescales, from minutes up to one month. Average molar ratios for SO_2/HCl, HCl/HF, CO_2/SO_2 and H_2O/SO_2 were 1.6, 4.9, 2.2 and 72, respectively, in 1998, and 1.6, 5.1, 2.3 and 66 in 1999. Other minor volcanic gas constituents were below detection limits. This composition may have been unchanged since a previous study in 1980–82.

(b) Small variations in SO_2/HCl and HCl/HF ratios on timescales of minutes to hours may be related to mechanisms of shallow gas release, if they are real.

(c) The in-plume concentrations of SO_2, HCl and HF above Santiago Crater were estimated at 76 ppm, 46 ppm and 9 ppm, respectively, levels which far exceed recommended health limits.

(d) Emission rates from Masaya derived from gas ratios and simultaneous COSPEC-measured SO_2 emissions were high compared to other passively-degassing volcanoes persisting over several years without major eruptive activity.

(e) Models for Masaya's degassing system were constrained to reflect pseudo steady-state high-temperature open-conduit degassing from an undepleted volatile source, requiring shallow-level magma replenishment rates of the order of 3 $m^3 s^{-1}$ during the observation period.

CHAPTER 6
MASAYA III:
PHYSICAL MODELS FOR DEGASSING

Masaya is one of a number of volcanoes whose activity falls into the category of persistent volcanism. The most famous example is Stromboli, but Mount Etna, Vanu'atu, and active lava-lakes such as those at Erta'Ale, Kilauea, Erebus and Nyiragongo are also included. The common characteristic of these volcanoes is sustained excessive degassing, relative to eruption rates of lava. Physical explanations for this behaviour have included both endogenous growth (Francis *et al.* 1993) and magma recycling (Harris *et al.* 1999). In this chapter I consider physical explanations for the gas emission sustained at Masaya in 1998–99.

Examining a previous episode of intense degassing at Masaya in 1979–85, Stoiber *et al.* (1986) suggested that gas emission resulted from essentially closed system degassing of a single batch of magma emplaced at relatively shallow depths beneath Santiago Crater. Rymer *et al.* (1998) suggested that resumption of activity at Masaya in 1993 was due to a process of large scale convective magma overturn, bringing gas-rich partly vesiculated magma to a broad region just below the floor of Santiago Crater. In this explanation, gas emission is the outcome of gas-melt separation in the bubbly magma layer, which gradually reduces in thickness.

Laboratory experiments have frequently been used to develop physical models for degassing at basaltic volcanoes. In this chapter I will discuss the application of two published models to Masaya's degassing behaviour. The first is a model for the generation and collapse of a foam layer at the roof of a basaltic magma chamber, which subsequently feeds gas emission at the surface (Jaupart & Vergniolle 1989, Vergniolle & Jaupart 1990). The second is a model for volcanic degassing maintained by magma convection in a conduit (Kazahaya *et al.* 1994, Stevenson & Blake 1998). These models have been chosen because they are particularly appropriate for the case when no magma erupts, and they consider surface degassing behaviour over relatively short timescales, rather than approaching the problem from the perspective of eruption triggers or magma chamber dynamics.

The chapter begins with a précis of the observations to be explained by a physical description. The published models are then considered in turn and applied using the data for Masaya. Finally a hybrid model is developed which can account for both the measured gas compositions and emission rates and also other published geophysical data relevant to the period of observation.

6.1 Summary of observations and questions

Volcanic activity has been described at Masaya since the arrival of the Spanish Conquistadors in the Sixteenth Century. Geological evidence suggests volcanism dating from 0.5–1 Ma, including periods of unusual basaltic plinian activity (Williams 1983b), the last of which resulted in formation of the present caldera less than 6000 years ago. Masaya is credited as the first volcano at which a lava lake was described (in McBirney 1956), with reference to one that persisted around 1529–1537. The most recent lava flows occurred in 1670, when a lava lake in the Nindiri Crater overflowed, and in 1772, from a fissure at the base of Old Masaya crater. Since around 1850 and the inception of Santiago Crater, activity has been centred in this one crater, with no significant eruption of material, but characterised by episodes of intense degassing, and pit collapses. A lava lake has briefly reappeared at the bottom of Santiago at various times, usually associated with crater floor collapses.

Although there is documentary support for variations in the intensity of degassing from Santiago since 1850, there is little reliable scientific evidence for *cycles* of behaviour. Even over the last 25 years, apart from the study of Stoiber *et al.* (1986) published work is relatively limited until Rymer *et al.* (1998) began consistent geophysical measurements in 1993. My focus in this chapter is therefore on the periods of intense degassing for which reliable data are available, and, in particular, during which my fieldwork was carried out. The relevant observations are summarised below.

The episode of intense degassing that was occurring at Santiago during field work in 1998 and 1999 (and continues at the time of writing) was characterised by COSPEC measured SO_2 emissions of more than 20 kg s^{-1}, a substantial increase over emissions of approximately 4 kg s^{-1} in 1997 (Delmelle *et al.* 1999a, Rymer *et al.* 1998). Rymer *et al.* (1998) indicate that activity in 1997 was the continuation of a phase which began with reactivation of a lava-lake and strombolian eruptions in mid-1993. A previous period of strong degassing, characterised by maximum SO_2 emissions of 14 kg s^{-1}, began in 1979 and lasted until the mid 1980s (Rymer *et al.* 1998, Stoiber *et al.* 1986), after which activity waned, and rockfalls and floor collapses were the major events recorded for Santiago Crater until 1993.

While measured SO_2 emission rates from Masaya have varied significantly over the last 25 years, it is difficult to separate the observed activity into distinct phases, and especially to identify repeated cycles on the basis of relatively sporadic observations. Given the uncertainty which rests even on details of recent activity, claims that five distinct periods of vigorous gas release separated by quiescent phases have occurred since 1850 (McBirney 1956, Stoiber *et al.* 1986) must be treated with caution, and cannot form the basis for a scientific model of cyclic degassing. Nevertheless, it is clear that magma resides close to the surface for extended periods of time at

Masaya, and that the ability to support continual high rate gas release for several years at a time is a characteristic feature of this volcano.

6.1.1 Observations

During fieldwork at Masaya in 1998 and 1999, I made three types of observations. First, there were measurements of the gas plume, which constrained its composition, and, in tandem with COSPEC data, an estimate of the total gas emission rate. Second, I collected recently erupted volcanic bombs to investigate the volatile contents of melt trapped as inclusions in phenocrysts. Thirdly, there were visual observations of degassing, and the size and structure of volcanic features such as the vent, pit crater and caldera. The results of these observations are summarised in figure 6-1.

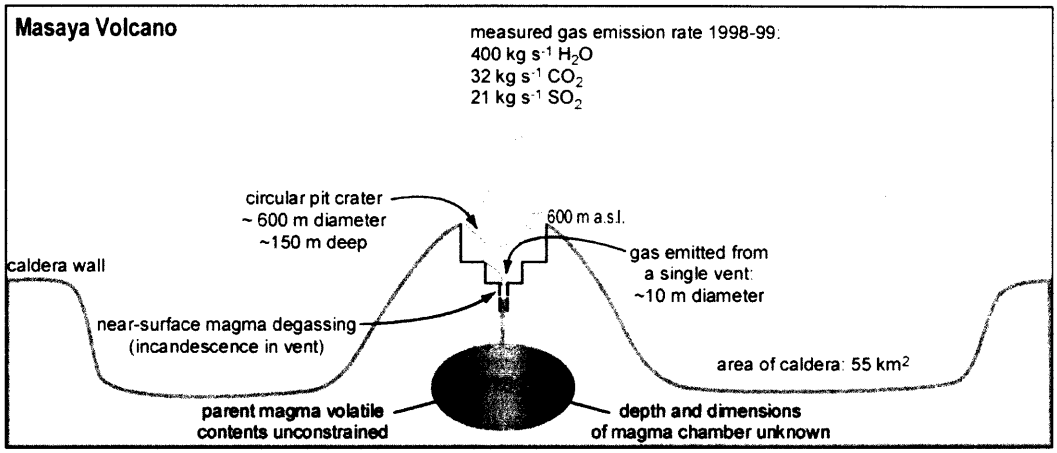

Figure 6-1: Cartoon summary of observations relevant to models for the degassing regime at Masaya Volcano in 1998–99. The measured gas plume also contained lesser amounts of HCl and HF. The existence of a magma chamber is unconfirmed, but is inferred from sustained summit activity: any such crustal chamber must, in turn, be fed by some deeper mantle magma supply.

6.1.1.1 Gas composition and emission rate

Measurements of the gas composition from Santiago Crater using OP-FTIR spectroscopy were discussed in detail in Chapter 5. Average compositions, and gas emission rates calculated using contemporaneous COSPEC data, are given in Table 6-1. For the purpose of considering physical models for degassing, H_2O, CO_2 and SO_2 are volumetrically the most important constituents of the gas phase. However, the presence of relatively large quantities of HF (and, to some extent, HCl) requires shallow level high temperature degassing of magma. The gas phase is unchanged in composition from 1998 to 1999, hinting that the source of volatiles remains undepleted over this timescale. This near-surface high rate gas emission unaccompanied by eruption of molten material requires an efficient replenishment of magma from depth to shallow levels in the system.

	1998			1999		
	Mol %	**Mass %**	**Emission Rate / kg s^{-1}**	**Mol %**	**Mass %**	**Emission Rate / kg s^{-1}**
H_2O	95	87	430	94	86	380
CO_2	2.9	6.5	32	3.3	7.3	33
SO_2	1.3	4.3	21	1.4	4.6	21
HCl	0.82	1.5	7.6	0.89	1.6	7.4
HF	0.17	0.17	0.9	0.17	0.18	0.8
Total	100	100	500	100	100	450

Table 6-1: Average gas composition and emission rates above Santiago Crater (from Table 5-3).

6.1.1.2 Magma composition and properties

Volcanic bombs erupted from Santiago Crater during minor explosions in October 1998 and September 1999 contained plagioclase as the predominant phenocryst in a vesiculated glassy matrix. In the absence of inclusion-containing olivines, I have analysed melt inclusions trapped in the plagioclases, along with matrix glasses, for their dissolved volatile contents using the Open University's Cameca SX100 electron microprobe (Table 6-2 and Appendix). Sulfur and chlorine concentrations in the melt inclusions were approximately 100 and 460 ppm, respectively, (see also Delmelle *et al.* 1999a), and measured totals were generally 99 % or higher, suggesting minimal amounts of e.g. dissolved water (volatiles by difference in Devine *et al.* 1995). Matrix glass volatile contents were negligible for S, and approximately 370 ppm for Cl. The volatile contents in the Masaya plagioclase melt inclusions are low, compared with parent magma volatile concentrations measured at other locations (e.g. Metrich *et al.* 1999, Roggensack *et al.* 1997), and suggest considerable degassing from the melt prior to entrapment. Further degassing occurred after growth of the plagioclase since matrix glasses are even more depleted.

Component	MI in plagioclase	Matrix Glass	Whole Rock	Plagioclase
SiO_2	50.81	51.12	51.31	49.47
TiO_2	1.45	1.40	1.11	0.03
Al_2O_3	13.06	13.67	17.61	30.74
MgO	5.15	4.92	4.25	0.14
CaO	8.66	8.79	10.08	15.10
FeO[a]	14.32	13.77	11.21	1.07
MnO	0.28	0.26	0.21	
P_2O_5	0.35	0.36	0.27	
Na_2O	2.93	3.04	2.79	2.86
K_2O	1.57	1.44	1.16	0.18
Total	98.64	98.81	100	99.61
S (ppm)[b]	100	30		
Cl (ppm)[c]	460	370		

Table 6-2: Average matrix glass and plagioclase melt inclusion compositions from recent volcanic bombs ejected from Santiago Crater. Melt inclusion, matrix glass and plagioclase compositions were analysed by electron microprobe, which was calibrated against three standard reference materials to confirm stable performance. Whole rock compositions were derived from XRF analysis of powdered samples. Full analyses and measurement conditions are listed in Appendix. Notes: [a] all iron calculated as Fe(II); [b] detection limit for S was approximately 50 ppm; [c] detection limit for Cl was approximately 100 ppm.

Processes of both phenocryst growth during ascent of magmas (Kuritani 1999), and shallow-level degassing-induced crystallisation (Cashman & Blundy 2000), are known, either of which could account for the trends in volatile contents of the Masaya bombs. Additionally, patterns of compositional zoning in the plagioclase phenocrysts may indicate circulation of growing crystals through changing depths in a magma column.

Better estimates of the *maximum* volatile contents in basaltic magma at depth were suggested in Chapter 5 from published data for other arc volcanoes (e.g. Holloway & Blank 1994, Metrich *et al.* 1999, Papale & Polacci 1999, Roggensack *et al.* 1997, Sisson & Layne 1993). These maximum volatile contents can be used to constrain a minimum estimate of the mass of magma that has been processed in order to support observed gas emission rates. Assuming typical melt concentrations of 1200 ppm (mass) S, 0.4 wt % CO_2 and 4–5 wt % H_2O for Masaya parent basalt, approximately 3×10^{11} kg of magma have been fully degassed to sustain emission rates of 21 kg s^{-1} SO_2, 32.5 kg s^{-1} CO_2 and 410 kg s^{-1} H_2O from February 1998 to March 1999.

Melt temperature and viscosity for the composition of Masaya basalt can be calculated using published algorithms. Liquidus temperatures calculated using the MELTS algorithm (Ghiorso & Sack 1995) were in the range of 1100 to 1150 °C for water contents between 0 and 4 wt %, and pressures equivalent to approximately 3 km depth. For pressures near to atmospheric, calculated temperatures were little different. Viscosities were calculated following the method of Shaw (1972), and were in the range 60 to 90 Pa s, depending on water content, for magma at 1100 °C

(figure 6-2). These values are similar to those calculated by Kazahaya *et al.* (1994) for Izu-Oshima tholeiitic basalt at 1150 °C, following the method of Persikov (1990).

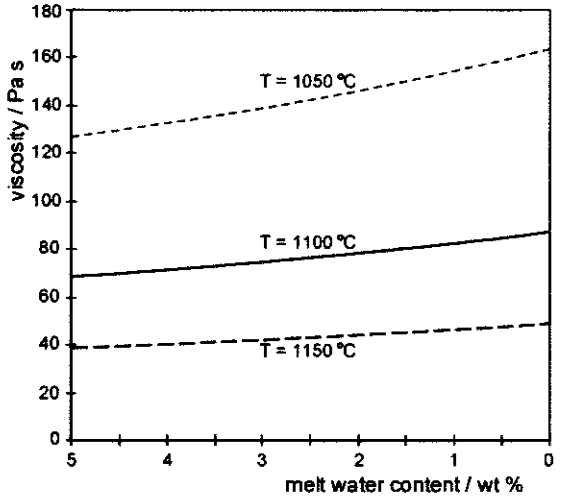

Figure 6-2: Dependence of magma viscosity on dissolved water content, for basaltic composition at Masaya, and at temperatures of 1050 °C, 1100 °C and 1150 °C. After Shaw (1972).

6.1.1.3 "Plumbing system"

The dimensions of volcanic features at the surface may reflect the dimensions of subsurface magma bodies. Masaya's summit craters are steep-sided cylinders, which formed by crater floor collapse into subsurface voids (Rymer *et al.* 1998). Thus the 600 m diameter (area approximately 0.3 km^2) of Santiago Crater may reflect the dimension of an underlying magma body less than a kilometre below the surface. Alternatively, the approximately 10 m diameter open vent at the bottom of the crater may be the surface expression of a narrow conduit which connects to a deeper (perhaps several kilometres) body of magma. The visibility of reflected incandescence within this vent implies that magma is present close to the surface. Finally, the 55 km^2 caldera, excavated via plinian eruptions, indicates that a much larger magma chamber existed at some level.

There is no unambiguous geophysical evidence for a magma chamber at Masaya, in part because of the similar densities of basaltic magma and the local country rocks. Connor and Williams (1989, cited by Metaxian *et al.* 1997) identified a shallow positive gravity anomaly, similar in shape to the present caldera, but displaced to its NE edge: this could, however, be related to an older caldera structure associated with prolonged volcanism in the region. From studies of seismic tremor in 1992 and 1993, Metaxian *et al.* (1997) confirmed the retention of shallow degassing magma in the upper parts of the volcano, even when lava was not visible at the bottom of Santiago Crater. The location of recent, historically inactive, cones in the NW half of the caldera may be explained by the existence of either a ring dyke (requiring a magma chamber more than 4.5 km in diameter) or a cone sheet (requiring a magma chamber with diameter less

than 2 km) (Maciejewski 1998). Thus, the exact size, shape and location of the magma body sustaining degassing at Masaya remains unconstrained.

6.1.2 Setting up the problem

A model to describe the vigorous degassing regime at Masaya can be broken down into a number of linked questions. These questions are also relevant to more general discussions of persistent volcanism.

(a) How does gas reach the surface?

(b) How is the gas composition buffered to remain constant over at least a 13 month timescale?

(c) How does a pathway to the surface (conduit) remain open (not solidified) without a steady flow of hot magma being expelled from it?

(d) What happens to the large volumes of magma which are processed at shallow levels during degassing, but are never erupted?

While similar questions have been asked, and partly addressed, by many authors working at persistently degassing volcanoes or lava lakes (e.g. Allard 1997, Allard *et al.* 1994, Delmelle *et al.* 1999a, Francis *et al.* 1993, Le Guern *et al.* 1979, Rymer *et al.* 1998), quantitative physical models are rarer.

Jaupart and Vergniolle (1989) and Vergniolle and Jaupart (1990) (hereafter referred to as JV) developed a model to describe Hawaiian and Strombolian eruption regimes of cyclic fire-fountaining and lava effusion for low viscosity static magmas. In doing so, they addressed problem (a) by considering how surface activity was controlled by the behaviour of a foam layer, which built up at the magma chamber roof and emptied through a narrow conduit. While problem (d) was largely irrelevant to the situation they envisaged, JV did not address problems (b) or (c) either.

Stevenson and Blake (1998) (hereafter referred to as SB) also considered volcanic activity at Stromboli, but particularly addressed problems of persistent volcanism, namely the maintenance of high thermal and volatile fluxes long-term. The model, similar to one proposed by Kazahaya *et al.* (1994) for Izu-Oshima Volcano, consisted of magma convection in a conduit connecting a deeper chamber with the surface. It quantitatively answered problems (a) and (c), by invoking transport of gas primarily dissolved within magma circulating in the conduit, which thereby remained hot and open. Problems (b) and (d) were answered implicitly on the understanding of a large chamber available for magma recycling and volatile buffering.

In another treatment of problem (a), Cardoso and Woods (1999) and Woods and Cardoso (1997) addressed the impact that gas bubbles might have on the mode of convection in a closed magma chamber as volatile-saturated basaltic magma cooled and crystallised. While their model primarily described modes of bubble-driven convection, it also put forward the time required for bubbly magma injected at the base of a chamber to separate to a foam layer at the roof. The timescales involved (10^7–10^9 s) mean that this model may be more appropriate to considerations of longer term behaviour at Masaya (e.g. Delmelle *et al.* 1999a), rather than the immediate problem of sustained high rate degassing.

For the situation at Masaya, measured gas emission rates and reasonable estimates for other volcanological parameters can be used to investigate which of the published models is more appropriate. In the rest of the chapter, the JV and SB models are discussed in turn, and results are used to constrain a final preferred model which can account for the observed intense degassing.

6.2 Degassing from a foam layer at the roof of a basaltic magma chamber

Jaupart and Vergniolle (1989) and Vergniolle and Jaupart (1990) developed a model for gas release from the top of a basaltic magma chamber. They envisaged gas supplied to the chamber roof by rising bubbles, which collected to form a foam layer. The model was tested by laboratory experiments in which nitrogen gas bubbles were generated at the base of a tank filled either with silicone oils or glycerol solutions. Depending on the balance between the rate of bubble addition to the base of the foam layer and the material properties controlling the strength of the foam, two regimes were possible. At relatively low gas fluxes, bubble input to the base of the foam layer was balanced by steady flow of bubbles into the conduit. At high gas fluxes, the pressure generated by rapid bubble influx caused coalescence and collapse across the foam layer, which then emptied as a large gas pocket into the conduit, and a new foam layer began to build at the roof.

6.2.1 Model Description

Readers are referred to the full derivation of the model theory presented in the original papers (Jaupart & Vergniolle 1989, Vergniolle & Jaupart 1990): only the essential equations are summarised here. Symbols used in the description are listed in Table 6-3.

Symbol	Quantity / unit	Value
ρ_l	Density of basaltic melt / kg m^{-3}	2600
ρ_g	Density of gas in foam layer / kg m^{-3}	~ 0
μ_l	Viscosity of basaltic melt / Pa s	80
μ_m	Viscosity of foam / Pa s	
σ	Surface tension / kg s^{-2}	0.36
W	Initial dissolved water in parent melt, by mass	4 %
r_t	Radius of cylindrical chamber roof / m	
S_t	Cross sectional area of chamber roof / m^2	
S_c	Cross sectional area of conduit / m^2	100
ε	Volume fraction of gas in foam layer / %	74
α	Vesicularity (volume fraction of gas in chamber)	
d	Bubble diameter / mm	
v_b	Bubble rise velocity / m s^{-1}	
Q_g	Volumetric gas flux provided by bubble rise / m^3 s^{-1}	≤ 2.5
h_m	Thickness of foam layer at steady state / m	
h_c	Critical foam thickness for collapse / m	
Q_c	Critical volumetric gas flux / m^3 s^{-1}	
t_c	Time for cyclic foam generation and collapse / s	
g	Gravitational acceleration / m s^{-2}	9.81
R	Gas constant / J mol^{-1} K^{-1}	8.315
M_r	Molecular mass of gas in foam layer / kg mol^{-1}	0.02
T	Temperature of melt and gas / K	1370
P	Pressure at level of foam layer / MPa	~ 90

Table 6-3: Material properties (ρ_l, μ_l, σ) were estimated for the composition of basalt at Masaya (Proussevitch & Sahagian 1998, Shaw 1972). An initial melt water content of 4 wt % is a reasonable value for arc basalts (e.g. Roggensack *et al.* 1997, Sisson & Layne 1993). Melt temperature was estimated for Masaya basalt using the computer algorithm MELTS (Ghiorso & Sack 1995). I consider a range of chamber roof areas corresponding to end-member sizes such as the observed areas of the crater and caldera. In the foam layer I assume a close packing bubble structure involving 74 vol % gas. The gas volume fraction in the chamber just below the foam layer (vesicularity) is modelled for different roof depths using a solubility law for water in basalt (Jaupart & Tait 1990). A range of reasonable bubble sizes, as suggested in published work (e.g. Vergniolle & Jaupart 1990) is allowed in the model. The current mass flux of gas vented from Masaya was measured (see Table 6-1). The volumetric equivalent is calculated from the Ideal Gas Law at lithostatic depths of 2–4 km, and is in the range 1.8–3.7 m^3 s^{-1}. The choice of 90 MPa (equivalent to approximately 3 km depth) for the pressure at the level of the foam layer is typical for the roofs of some basaltic magma chambers.

In the simplest case, a magma chamber is described as a flat-roofed cylinder. A gas flux is supplied to the roof by means of bubbles rising through volatile-saturated basaltic melt. The bubbles collect at the roof to form a layer of foam (figure 6-3).

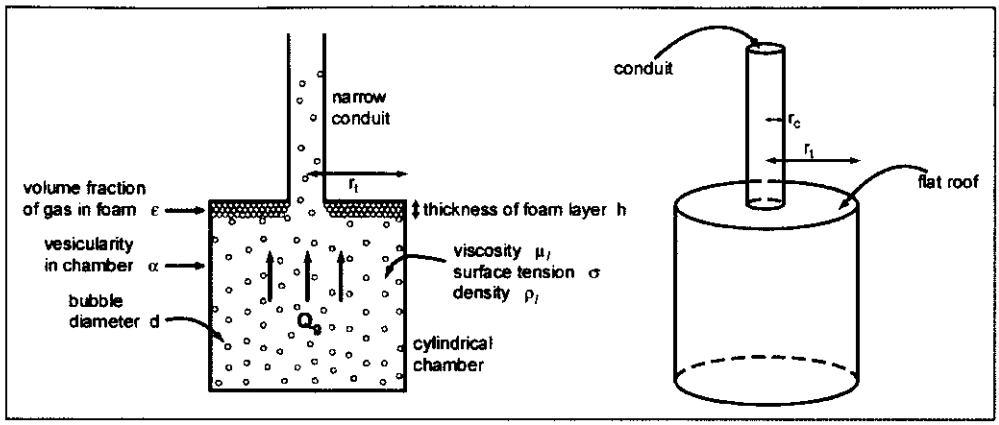

Figure 6-3: The main features of the JV model, as tested in their laboratory experiments.

Because the JV model is concerned with only the behaviour in and around the foam layer, it requires a volumetric gas flux. Measured gas mass emission rates from Masaya can be converted to volumetric rates via the ideal gas law, by assuming a reasonable pressure for the roof of the chamber. For Stromboli and Kilauea, chamber roofs have been modelled at depths of 2–4 km (e.g. Stevenson & Blake 1998, Vergniolle & Jaupart 1990): at pressures equivalent to 3 km, the observed gas emission from Masaya becomes a volumetric flux of 2.5 $m^3\ s^{-1}$. However, at these pressures, the full amount of H_2O and SO_2 would not yet be exsolved, so this is a maximum estimate for the gas flux supplied to the roof.

The supplied gas flux is a function of the size of the bubbles and the cross-sectional area over which they rise:

$$Q_g = \alpha v_b S_t \tag{6-1}$$

and:

$$v_b = (1-\alpha)\frac{1}{18\mu_l} d^2 (\rho_l - \rho_g) g \tag{6-2}$$

I include an expression to calculate the chamber vesicularity (α) as a function of initial melt water content (W) and the final depth at which the foam layer collects. I use the common solubility law for water in basalt from Jaupart and Tait (1990) with the constants a and n equal to 6.8×10^{-8} and 0.7, respectively:

$$\alpha = \left(1 + \frac{M_r P}{(W - aP^n)\rho_l RT}\right)^{-1} \tag{6-3}$$

Equation 6-1 is plotted in figure 6-4(a), showing the dependence of gas flux on bubble diameter, for an initial melt water content of 4 wt %. As the available roof area increases, the gas flux for a given bubble diameter also increases. Alternatively, given the observed gas flux of 2.5 $m^3\ s^{-1}$ a

suite of pairs of values of roof area and bubble size sufficient to supply this gas flux can be calculated (figure 6-4(b)). For bubble sizes in the range of 0.1–1 mm considered reasonable for the top of a basaltic magma chamber (Vergniolle & Jaupart 1990), the cross-sectional area must be at least equivalent to twice the size of the presently active crater area, and up to as large as twice the entire caldera. This upper limit seems too large, and the lower limit indicates that the zone beneath the active crater is not large enough to provide the currently observed gas flux. This discrepancy can be explained by inferring a broader chamber responsible for the majority of gas production at some greater depth than just below the floor of the pit crater.

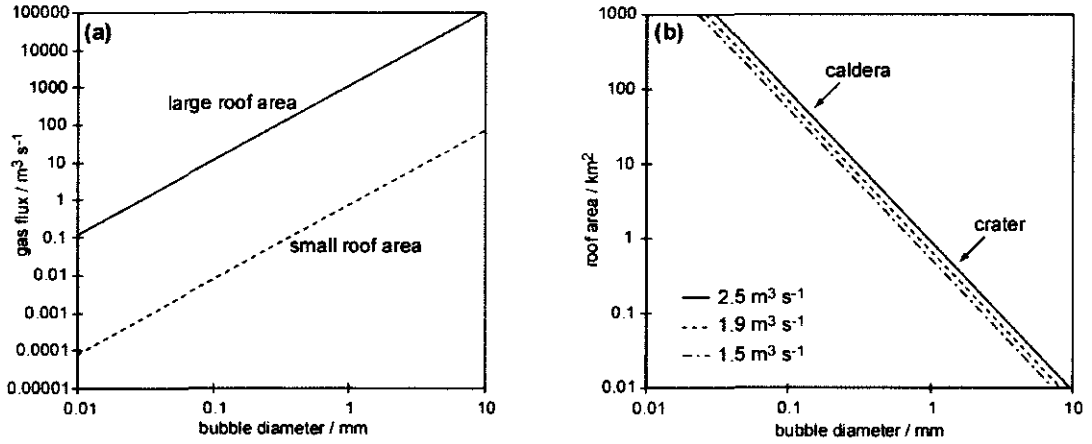

Figure 6-4: Graphical representation of equation 6-1. (a) Gas flux as a function of bubble diameter for two different roof areas. (b) Roof area and bubble size required to sustain a range of gas fluxes. For a roof at 3 km depth, the maximum volumetric gas flux for Masaya is 2.5 m^3 s^{-1}. For typical bubble sizes of between 0.1 and 1 mm, the chamber must have a cross-sectional area of 1 to 100 km^2, compared with areas of 0.3 km^2 and 55 km^2 for the Santiago Crater and the caldera, respectively (marked).

For any given gas flux supplied to the roof, there is a steady state foam thickness at which input of gas from below just balances gas output by foam flow into the conduit. In the flat roof scenario, the driving pressure for this foam flow is the continuous supply of bubbles from the tank interior. The exact form of the expression depends on the chamber and roof geometry. For the cylindrical chamber case, the thickness of the foam at steady-state (h_m) is given by:

$$h_m = \left\{\frac{\mu_m Q_g}{\varepsilon^2 \rho_l g}\right\}^{1/4} \left\{\frac{3}{\pi}\left[\ln\left(\frac{S_t}{S_c}\right) + \frac{S_c}{S_t} - 1\right]\right\}^{1/4} \qquad (6\text{-}4)$$

$$\text{where } \mu_m = \mu_l (1-\varepsilon)^{-5/2} \qquad (6\text{-}5)$$

As the foam thickens, it exerts an upward buoyant pressure tending to flatten the bubbles, and eventually the foam reaches a critical thickness above which bubbles cannot flatten further without coalescing: the foam becomes dynamically unstable. This critical thickness (h_c) depends on material properties such as viscosity, surface tension and melt density as well as bubble size:

$$h_c = \frac{4\sigma}{\varepsilon \rho_l g d} \tag{6-6}$$

If the steady-state foam thickness, h_m, is less than the critical coalescence thickness, h_c, then steady foam flow into the conduit continues under a stable regime. If the steady state thickness is greater than the critical coalescence thickness, then wholescale collapse of the foam layer to form a single large gas pocket will occur periodically: this is the collapse regime. For the case of Kilauea, Vergniolle and Jaupart (1990) found this regime to be characterised by cycles of fire-fountaining as the large gas pocket was erupted.

A critical gas flux (Q_c), where the two thicknesses are just equal, can be defined, such that any increase in gas flux will cause foam collapse to occur:

$$Q_c = \frac{4^4}{A^4} \frac{(1-\varepsilon)^{1/2}}{g^3 \varepsilon^2} \frac{\sigma^4}{\rho_l^3 \mu_l d^4} \tag{6-7}$$

(putting $h_m = h_c$ to define Q_c)

$$\text{where } A = \left\{ \frac{3}{\pi} \left[\ln\left(\frac{S_t}{S_c} \right) + \frac{S_c}{S_t} - 1 \right] \right\}^{1/4} \tag{6-8}$$

Equation 6-7 is shown in graphical form in figure 6-5.

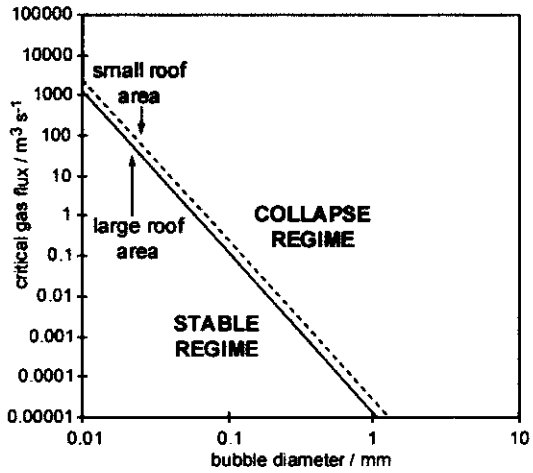

Figure 6-5: Critical gas flux as a function of bubble diameter (equation 6-7) for two different roof areas. The shaded region shows where cyclic foam generation and collapse will occur. If the gas flux supplied by bubble rise remains below the critical gas flux then steady state flow of foam into the conduit prevails.

If the gas flux supplied is greater than the critical gas flux then the collapse regime is in operation and a timescale (t_c) for the repeated generation, coalescence and collapse of the foam layer can be defined:

$$t_c = \pi r_t^2 \left(\frac{4\sigma}{\rho_l g d Q_g} \right) \qquad (6\text{-}9)$$

6.2.2 Trials with Masaya parameters

Results are shown in figure 6-6(a), which plots equations 6-1 and 6-7 for Masaya parameters. The conduit is assumed to be approximately 10 m in diameter (the dimension of the active vent), but a narrower width of 5 m makes very little difference to the model results. For a gas flux of 1.5–2.5 $m^3 s^{-1}$ (rate calculated at the pressure of the foam layer), the cyclic foam collapse regime is predicted for all chamber sizes except for unreasonably large roof areas of more than 400 km^2.

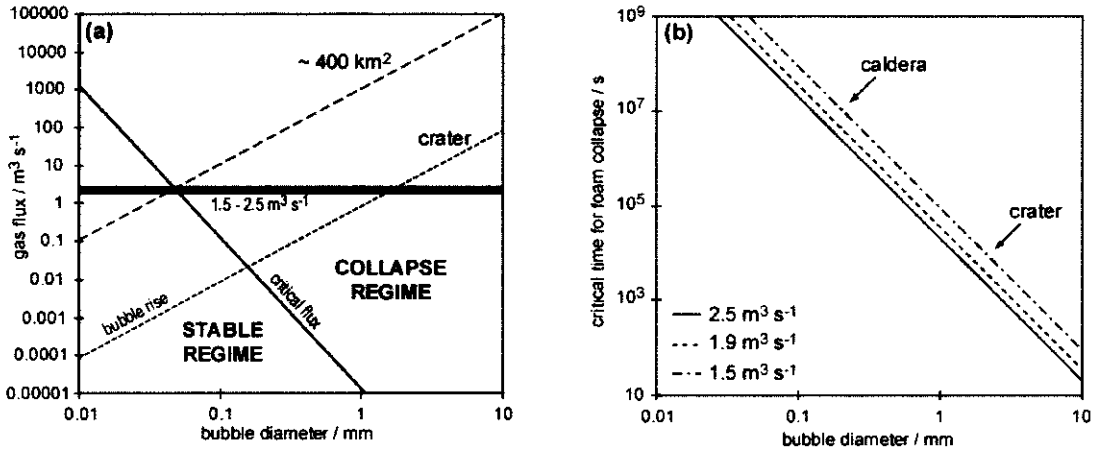

Figure 6-6: Results of the JV model for observed gas emission at Masaya. (a) Dependence of critical gas flux on bubble size (equation 6-7) is shown by solid black line, while the gas flux provided by bubble rise for two roof areas is shown by the dashed lines. The horizontal grey bar delimits gas fluxes of 1.5–2.5 $m^3 s^{-1}$, observed for Masaya. The observed gas flux indicates cyclic foam generation and collapse for roof areas less than an unreasonable 400 km^2. (b) Timescales (t_c) for foam build up and collapse (equation 6-9) for gas fluxes 1.5–2.5 $m^3 s^{-1}$, with roof areas equivalent to Masaya caldera and Santiago Crater marked (from equation 6-1).

If the system is operating in the cyclic foam collapse regime, then, from equation 6-9, the timescale for foam generation leading to rapid foam collapse can be calculated (figure 6-6(b)). The relevant timescales, constrained by the roof areas and bubble sizes previously considered, are in the range 10^4 to 10^7 s, (3 hrs to 4 months), and probably most likely at the lower end of this range. These timescales do not correlate well with observations of degassing at Masaya, which maintains a steady rate for periods of several years.

6.2.3 Discussion

Application of the JV model, as it stands, requires the assumption of a chamber roof located at some depth connected to the surface through a narrow conduit. Gas is supplied to the roof via bubble rise through a static chamber, and further exsolution in the conduit is assumed to be negligible (this assumption is discussed below). Conversion of the observed gas mass flux to a

volume flux to use in the model requires an estimate of pressure at the roof of the chamber. For lithostatic depths any shallower than about 3 km, the volume flux implied by a 400 kg s^{-1} mass emission rate becomes too large for reasonable treatment in this model. From equation 6-1 and figure 6-4, the roof area that was required to support the gas flux through rise of bubbles of typical sizes was at least twice the area of Santiago Crater, or up to 1 km^2. This value may be a realistic estimate for the roof area of a deep magma chamber.

If a smaller amount of dissolved volatiles were present in the initial melt than the 4 wt % used in the model, then the vesicularity at any given depth would be reduced (from equation 6-3). In order to maintain the same volumetric gas flux, either larger bubbles or a larger roof area are required (from equation 6-1). Alternatively, a roof at shallower depth would be needed to maintain the same vesicularity.

At Masaya, the volatile phase is predominantly H_2O, which is still relatively soluble in basaltic magma at pressures equivalent to 3 km. Assuming an initial melt water content of 4 wt %, the solubility law cited by Jaupart and Tait (1990) and used in equation 6-3, indicates that more than 60 % of the original dissolved water remains in the magma at 3 km. In order to support the high H_2O emissions along with proportions of relatively more soluble SO_2, HCl and HF in the gas phase, exsolution must continue to very shallow levels, an observation supported by the degassed nature of melt inclusions and matrix glass in erupted products. In this case, the assumption that negligible exsolution occurs in a conduit shallower than 3 km does not hold: a more satisfactory model should allow degassing from magma at shallower levels.

Pursuing the model, nonetheless, showed that, given the calculated volumetric gas flux for Masaya, for any reasonable roof area, the regime of cyclic foam generation, coalescence and collapse should be in operation (figure 6-6). However, none of the manifestations that Jaupart and Vergniolle (1989) associated with this regime were observed at Masaya, and the activity was more similar to their description of the stable regime, with gas leaking at steady rate into the conduit. The timescales predicted for the cyclic collapse regime were not matched by temporal observations at Masaya.

6.2.3.1 Extension of the model to allow fissure and sloping roof

JV developed an extension from the simplest form of their model to include the effect of alternative chamber and outlet geometries on the predicted degassing behaviour. Observations of dykes in the rock record indicate that fissures, rather than narrow cylindrical conduits, can often breach magma chambers. If the magma chamber is considered as rectangular, rather than cylindrical, and the outlet is a long fissure, instead of a narrow conduit, then a new set of expressions for the steady-state foam thickness and hence the critical gas flux are appropriate.

The gas flux supplied by rising bubbles is still given by equation 6-1, using appropriate values for the roof area.

The fissure extends over a length, Δ, and the chamber roof has half-width L in the direction perpendicular to the strike of the fissure (figure 6-7(a)). In the derivation of Vergniolle and Jaupart (1990), Δ is much larger than L. The maximum (steady-state) foam thickness (to compare with equation 6-4) is now given by:

$$h_m = \left\{\frac{\mu_m Q}{\varepsilon^2 \rho_l g}\right\}^{1/4} \left\{\frac{3}{2}\frac{S_t}{\Delta^2}\right\}^{1/4} \tag{6-10}$$

The expression for the critical collapse foam height is unchanged from equation 6-6, and so by equating these two heights, the critical gas flux for this situation is:

$$Q_c = \frac{2}{3}\left(\frac{4^4 \Delta^2}{S_t}\frac{(1-\varepsilon)^{5/2}}{g^3 \varepsilon^2}\frac{\sigma^4}{\rho_l^3 \mu_l d^4}\right) \tag{6-11}$$

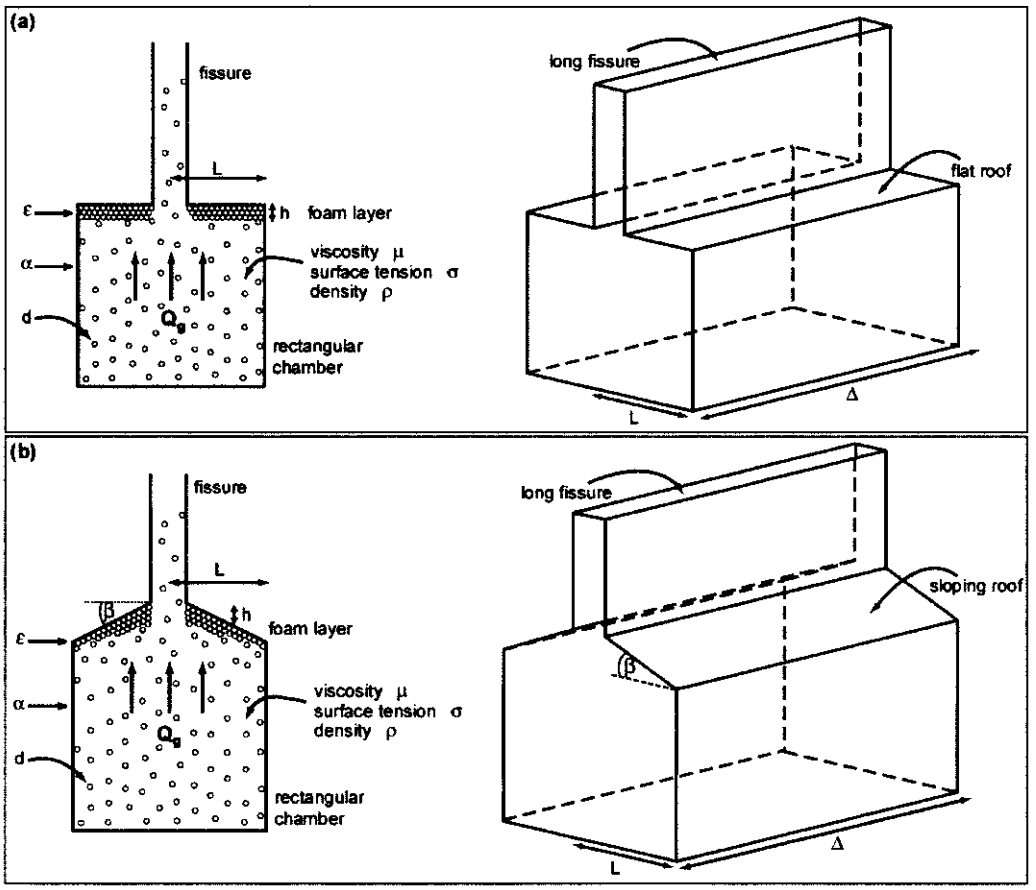

Figure 6-7: Illustration of the chamber parameters used in modifications of the original JV model. (a) A flat-roofed rectangular magma chamber feeds a fissure or dyke. (b) The roof of the chamber lies at some angle, β, from the horizontal.

If the chamber roof is allowed to lie at an angle, β, above horizontal (figure 6-7(b)), a further expression for the steady-state foam thickness can be derived. The difference, in this case, is that the driving pressure for foam flow out of the fissure includes an additional term due to the roof angle. For large angles of β this term dominates; the term due to the growth of the thin foam layer is neglected, and h_m, the steady-state foam thickness, is given by:

$$h_m = \left\{\frac{\mu_m Q}{\varepsilon^2 \rho_l g}\right\}^{1/3} \left\{\frac{3}{2\Delta \sin\beta}\right\}^{1/3} \qquad (6\text{-}12)$$

By equating the previous expression for h_c (equation 6-6) with this new h_m, the critical gas flux (Q_c) in the sloping roof case is defined:

$$Q_c = \frac{128\sigma^3(1-\varepsilon)^{3/2}}{3\mu_l \rho_l^2 g^2 \varepsilon} \frac{\Delta \sin\beta}{d^3} \qquad (6\text{-}13)$$

The major difference between this and the flat roof case is that although increasing gas flux still results in a transition from stable to collapse regimes, this no longer has a dependence on the roof area.

Results from equations 6-11 and 6-13 for Masaya are shown in figure 6-8. Three possible chamber roof areas of 55 km^2 (equivalent to the caldera), 1 km^2, and 0.3 km^2 (equivalent to the crater) have been used, with fissures of length 5 km, 1 km and 500 m, respectively. As with the cylindrical chamber geometry, for the flat-roofed rectangular chamber emptying into a long fissure, the cyclic regime is predicted for all but the largest roof areas. When the model is adapted to consider the effects of sloping roof geometry, the results are slightly different (figure 6-8(b)). For chamber cross sectional areas of 1 km^2, or greater, and a roof sloping at 45°, the stable foam flow regime is possible. However, only a slight increase in gas flux over this chamber area is enough to move the system into the cyclic collapse regime.

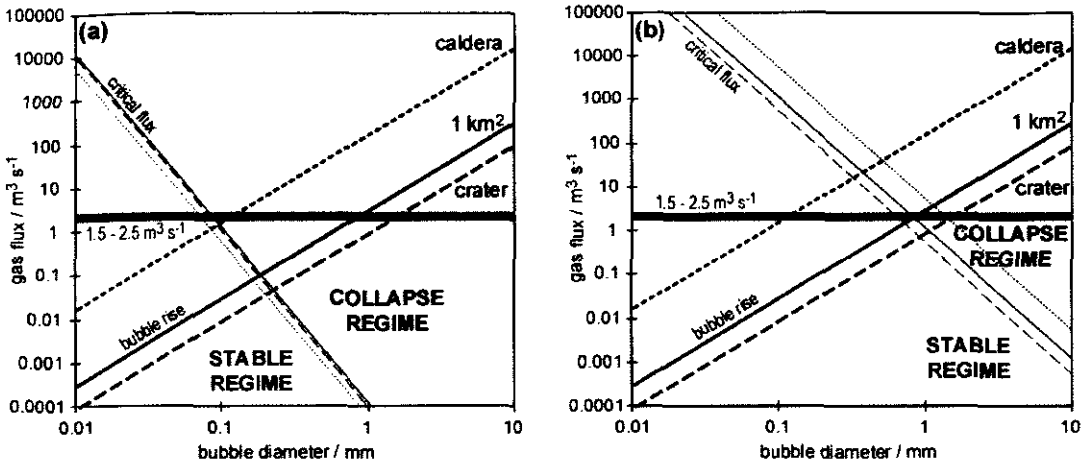

Figure 6-8: Results from the modification to the JV model, for a rectangular chamber and fissure exit. (a) The gas flux provided by bubble rise is calculated for three roof areas, equivalent to caldera, 1 km^2, and crater, shown by dotted, plain, and dashed bold lines, respectively. Critical gas flux was calculated for the same set of roof areas breached by fissures of suitable lengths of 5 km, 1 km, and 500 m, shown by dotted, plain, and dashed thin lines, respectively. Chamber roof was flat. The range of possible observed gas fluxes is indicated by horizontal grey bar. (b) Graph calculated with the same size constraints as in (a), but with chamber roof pitched at 45 °.

Magma chambers are perhaps more likely to have irregular boundaries than smooth flat roofs, and this extension to the model shows that irregularities tend to stabilise the foam and prevent cyclic eruptions compared to flat surfaces. For roof angles less than 45 °, the critical gas flux reduces and so the cyclic collapse regime is more likely. For larger roof angles (which may be physically unrealistic) steady state foam flow is favoured, but this situation is becoming very different from the original model.

6.2.3.2 Conclusion

In summary, the JV model has largely failed to describe the observed degassing at Masaya. The original model was developed with a particular focus on the more episodic volcanic activity at Kilauea, where CO_2 is more dominant in emitted gases: shallow exsolution is therefore relatively unimportant. However, the roof area which Vergniolle and Jaupart (1990) use for the shallow Kilauea magma storage zone (20 km^2) is arguably too large (L. Wilson, pers. com.), and the model may fail to predict behaviour at Kilauea accurately if a better estimate is used.

The strength of the model is its simple concept: if bubbles rise through a chamber then a foam layer will develop where gas is trapped against an impermeable roof, and the behaviour of the foam layer, rather than a deeper constant gas flux, will determine the activity seen at the surface. However, because it doesn't consider the role of convection in gas transport, or the possibility of continued degassing in the conduit, it has been unable to simulate the real behaviour at Masaya. For the relatively CO_2-poor and H_2O-rich gas composition at Masaya, deep exsolution of CO_2 may provide a gentle bubble flux to the roof of a magma chamber, but subsequent shallower

exsolution of H_2O and other volatiles is volumetrically more important, and responsible for the observed degassing behaviour. A deep CO_2-rich gas flux may be low enough that the stable foam flow regime is easily sustained. In this case, the scenario envisaged by Jaupart and Vergniolle (1989) may be in operation at depth, although it alone cannot account for the observations.

6.3 Degassing via convection in a conduit

Kazahaya *et al.* (1994) suggested the importance of magma convection in a conduit to account for excessive shallow-level degassing, unaccompanied by lava eruption, seen at Izu-Oshima Volcano in 1988–90. Independently, Stevenson and Blake (1998) developed a similar model for convection in a conduit driven by surface magma degassing. Model parameters for the convective flow were quantified using laboratory experiments with miscible fluids of various densities and viscosities in long narrow glass tubes. The theory relates gas emission rates and compositions with material properties of the magma, initial dissolved volatile contents, and the conduit dimensions.

6.3.1 Model description

The envisaged system is shown in figure 6-9, with a cylindrical conduit connecting a deep magma chamber to the surface. The conduit is kept open by a combination of rapid convection and magma fluid pressure. Magma in the chamber may already contain small bubbles of CO_2, but most of the volatiles remain in solution until shallow levels. Volatile rich magma has reduced density and rises towards the surface. Shallow level degassing and rapid escape of bubbles through an open conduit leave degassed magma with increased density, which then sinks back towards the chamber, driving convective overturn in the conduit. Thus the rate of gas emission is dependent upon the rate at which new volatile-rich magma is supplied to the shallow degassing zone by convection.

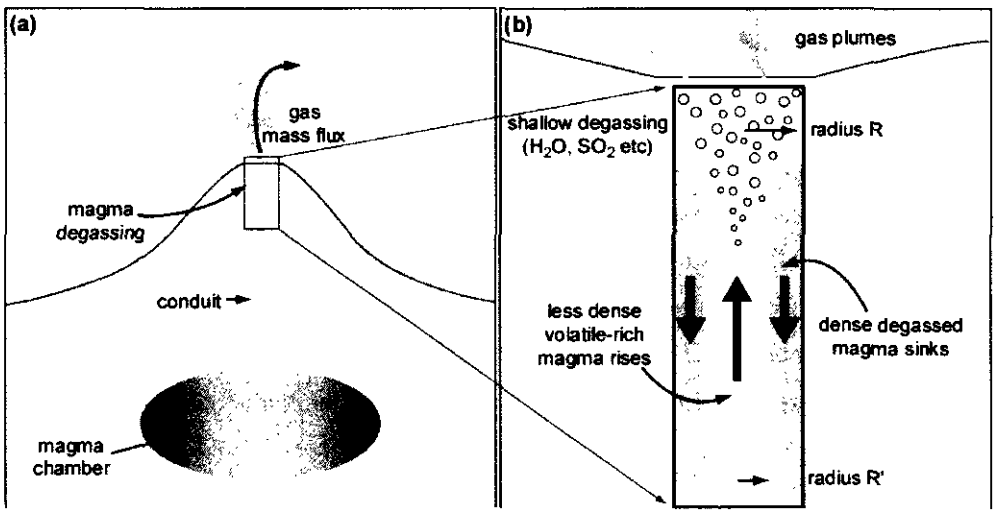

Figure 6-9: The volcanic system modelled by Stevenson and Blake (1998). (a) A magma-filled open conduit, of height H_c, links a deep chamber with the surface. (b) The conduit has radius, R, and the rising column of buoyant volatile-rich magma has radius R'. At shallow levels, soluble volatiles (mainly H_2O) exsolve from the volatile-saturated magma. Degassed magma is relatively dense and sinks, setting up convection in the conduit.

Readers are referred to the original paper (Stevenson & Blake 1998) for a fuller description of the theory and experimental parameterisation of the model: only the essential equations are summarised here. Symbols used in the description are listed in Table 6-4.

Symbol	Quantity / unit	Value
M	Gas mass emission rate / kg s^{-1}	
Ps	Poiseuille number	
V	Terminal rise velocity of upwelling magma / m s^{-1}	
Q	Volumetric magma upflow rate / m^3 s^{-1}	
R	Radius of conduit / m	
R'	Radius of upwelling magma / m	
R*	Dimensionless radius of upwelling magma (=R'/R)	0.6
μ_c	Viscosity of ascending chamber magma / Pa s	
μ_d	Viscosity of degassed magma / Pa s	
ρ_o	Density of anhydrous magma / kg m^3	2600
ρ_c	Density of ascending chamber magma / kg m^3	
ρ_d	Density of degassed magma / kg m^3	
$\Delta\rho$	Density difference driving convection (=ρ_d-ρ_c) / kg m^3	
C_c	Water mass fraction in chamber magma	
C_d	Water mass fraction in degassed magma	
ΔC	Difference in water content (=C_c-C_d)	
ϕ	Volume fraction of crystals in magma	
α	Volume fraction of exsolved gas in chamber magma	
β	Coefficient of compositional expansion for water in basaltic melt	1.55
g	Gravitational acceleration / m s^{-2}	9.81

Table 6-4: Symbols used in description of SB model. Estimates for R*, ρ_o and β are presented by Stevenson and Blake (1998).

The terminal velocity (V) of rising chamber magma is characterised by a Poiseuille number (Ps), at low Reynolds number:

$$\mathrm{Ps} = \frac{V\mu_d}{g\Delta\rho \mathrm{R}^2} = f\left(\mu_d/\mu_c, \mathrm{R}^*\right) \qquad 6\text{-}14$$

where R* is the dimensionless radius of the rising magma, equal to R'/R.

The gas emission rate depends upon the proportion of volatiles lost from the magma (ΔC) and the volumetric magma upflow rate (Q):

$$Q = \pi(R')^2 V = \pi(R^*)^2 \mathrm{Ps}\left(\frac{g\Delta\rho R^4}{\mu_d}\right) \qquad 6\text{-}15$$

$$\Delta C = C_c - C_d \qquad 6\text{-}16$$

where the dissolved water fraction in the ascending and degassed melts are C_c and C_d, respectively.

The density difference driving convection between the degassed and undegassed magmas, for the simple case of crystal-free liquids, is given by:

$$\Delta\rho = \rho_d - \rho_c \quad = \rho_o \beta \Delta C \qquad 6\text{-}17$$

where ρ_o is the density of anhydrous melt, and β is the coefficient of compositional expansion for water (equal to 1.55 for basalt).

Stevenson and Blake (1998) develop the model further by taking into account the presence of crystals and a small fraction of CO_2 bubbles in the magma rising from the chamber. For the present study, it is sufficient to take the simplest case, since no information on the crystallinity of Masaya chamber magmas is available, and the depth appropriate to estimate the CO_2 gas density is unknown.

Since the magma flow rate depends on melt viscosity (equations 6-14 and 6-15), I estimated viscosities of Masaya basalt as a function of dissolved water content, following the method of Shaw (1972) (see figure 6-2). Regardless of temperature, there is only a small change in viscosity related to water degassing, with μ_d/μ_c equal to 1.2 for a decrease from 4 to 0.5 wt % dissolved H_2O. I use a viscosity of 90 Pa s for the descending degassed magma (μ_d).

In their laboratory experiments, convective overturn in the conduit was confirmed, and Stevenson and Blake (1998) found that R* was approximately equal to 0.6, across a wide range of values of Ps and μ_d/μ_c. Ps is a function of μ_d/μ_c for constant R* (equation 6-14), and given the low viscosity ratio appropriate to Masaya magmas, a value of approximately 0.03 is derived (figure 3 in Stevenson & Blake 1998).

The proportion of volatiles lost from the magma and the rate of magma overturn in the conduit control the gas emission rate at the surface. With the simple assumptions that the ascending chamber magma is both crystal- and bubble-free, the gas mass flux, M, is:

$$M = Q \rho_c \Delta C \qquad 6\text{-}18$$

Q can be substituted using equation 6-15, to describe the dependence of gas mass flux on conduit radius:

$$M = \pi(R^*)^2 Ps \left(\frac{g \Delta\rho R^4}{\mu_d} \right) \rho_c \Delta C \qquad 6\text{-}19$$

$$\text{where } \rho_c = \rho_o (1 - \beta C_c) \qquad 6\text{-}20$$

With reasonable values for the density and viscosity of Masaya's basaltic magma, the gas emission rate can be calculated for pairs of values of ΔC and R.

6.3.2 Trials with Masaya parameters

Equation 6-19 is plotted in figure 6-10 to show the dependence of gas mass flux on conduit radius, for a range of initial dissolved water contents.

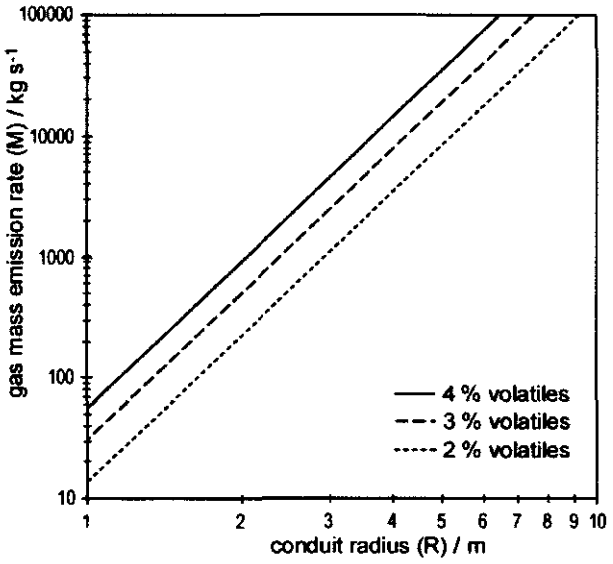

Figure 6-10: Dependence of gas mass flux on conduit radius, from equation 6-19. Grey bar indicates the observed gas flux at Masaya. The effect of different initial dissolved volatile contents is shown.

The results from a simple application of the SB model indicate that convection in a conduit of radius approximately 2 m supports a gas mass flux of approximately 450 kg s^{-1}, for the composition and conditions of Masaya magma. Changing the proportion of dissolved volatiles in the ascending magma changes both the density difference driving convection and the magma flux needed to provide a given gas emission rate. For the range of 2 to 4 wt % dissolved volatiles considered reasonable for the melt residing in some deeper chamber at Masaya, the range of conduit radii, given a gas emission rate of 450 kg s^{-1}, is only 1.7–2.4 m. The active vent at the base of Santiago Crater appears to be of the order of 10 m in diameter: this is larger than predicted by the model, although the conduit may be widened at the surface as a result of crater floor collapses.

6.3.3 Discussion

The model involves a number of assumptions which have direct bearing on the calculated relationship between magma volatile content, conduit radius and gas mass emission rate: these are discussed below. In addition I examine some of the implications of the model for observed degassing behaviour.

6.3.3.1 Model assumptions

Since the crystal content and bubble fraction of ascending chamber magma, as well as the height of the conduit, is unknown for Masaya, the model was applied assuming that no crystals or bubbles were present in the chamber. This assumption is unlikely to be true, since the CO_2 measured in Masaya's gases will have started to exsolve at the depth of the magma chamber, and olivine and clinopyroxene phenocrysts present in erupted products probably grew in a chamber rather than during magma ascent. In their original model, Stevenson and Blake (1998) allow for a crystallinity (ϕ_c) and gas fraction (α) in the chamber magma as they affect the density difference ($\Delta\rho$) driving convection and the magma flux (Q) required to sustain the gas emission rate (M):

$$\Delta\rho = \rho_o \beta \Delta C (1-\phi_d) + \alpha(\rho_c - \rho_{CO_2}) \qquad 6\text{-}21$$

where $\phi_d = \phi_c/(1-\alpha)$ 6-22

$$M_{H_2O} = Q(1-\phi_c-\alpha)\rho_c \Delta C \qquad 6\text{-}23$$

and $M_{CO_2} = Q\rho_{CO_2}\alpha$ 6-24

ρ_{CO2} is the density of exsolved CO_2 gas at the top of the chamber, and ϕ_d is the crystal fraction in degassed (descending) magma, corrected for the loss of the CO_2 gas fraction.

The effect of introducing a crystal and bubble fraction via equations 6-21 and 6-23 is in two opposing directions. Vesicularity of the chamber magma results in an increased density contrast (second term on the right hand side in equation 6-21) to drive convection and therefore an expected increase in magma upflow rate (and gas emission rate) for a fixed conduit radius. However, the presence of crystals (first term on the right hand side in equation 6-21) works to reduce the density contrast. Additionally, from equation 6-23, when upwelling magma is a mixture of volatile-rich liquid, bubbles, and crystals, the emitted gas flux is reduced from that sustained by uprise of a crystal- and bubble-free melt, for a fixed magma flux. The presence of crystals affects magma viscosity, which increases with increasing crystal fraction (cited in Stevenson & Blake 1998, e.g. Tait & Jaupart 1990), and bubbles similarly increase magma viscosity. With reference to equation 6-19, an increase in magma viscosity produces a small decrease in rate of convection and therefore gas emission rate, all other parameters remaining equal.

Given the relatively high H_2O/CO_2 mass ratio of 12–13 in Masaya gases, the CO_2 gas volume fraction in a magma chamber may be very small, so that the expected increase in density contrast due to ascending magma vesicularity is minimal. In contrast, the sum effect of the presence of bubbles and crystals in convecting magma is likely to be a decrease in gas emission rate compared to the simple liquid case, for a given conduit radius and initial volatile content. Alternatively, for a fixed initial volatile content, a larger conduit is required to sustain the

observed gas emission rate in the bubble- and crystal-containing magma scenario than in the modelled bubble- and crystal-free magma situation. The 2 m conduit radius suggested for Masaya from figure 6-10 is therefore a minimum value.

The model assumes that crystallisation in the conduit is negligible, such that crystal content in the magma remains constant throughout the convective cycle. Given the rapid overturn rates for this basaltic system, the assumption of minimal crystallisation for the majority of the cycle is reasonable, but degassing-induced crystallisation at the surface may be a significant factor. The effect of crystallisation is to induce an increase in the degassed magma viscosity, and a reduction in the gas emission rate (equation 6-19). Simultaneously, the density of the degassed magma will be higher, causing an increase in the driving force for convection and increased magma upflow rates: the overall effect of crystallisation in the conduit may therefore cancel out. Rapid formation of a large fraction of bubbles at shallow levels in the conduit may result in a viscosity increase that severely impedes the rate of convection of more fluid magma at deeper levels. In this case, a larger value for the viscosity term in equation 6-19 is required, and the gas emission rate is reduced.

The main assumption, inherent to the model, is that magma transport in the conduit is the rate-limiting process for degassing and that gas exsolution and escape from the magma at the surface is relatively instantaneous. The issue of gas transfer from a bubbly magma layer to the atmosphere, and especially the phenomenon of bubble bursting, is poorly understood. However, gas escape as bubbles reach the free surface of low viscosity basaltic melts is generally considered a rapid process for at least three reasons. First, observations of sustained high gas fluxes from lava-lakes and passively degassing basaltic volcanoes verify that exsolved gas can escape from magma relatively easily. Second, if a foamy layer were to develop at the magma surface because gas bubbles have some strength, then the timescale for collapse of that layer can be estimated from the theory developed by Jaupart and Vergniolle (1989). From equation 6-9, using values for the radius of the foam layer in the range 3–10 m appropriate to the conduit, bubble diameters of 1 mm, and volumetric gas fluxes in the range 2–10 $m^3\ s^{-1}$, the timescale for generation and collapse is of the order of 1–10 s.

Third, from a consideration of forces acting on soap film bubbles (J. Phillips, pers. com.), an analogous argument for gas bubbles in molten basalt shows that overpressure is sufficient to cause bubbles to burst on reaching the surface. Consider a bubble at the free surface of a basaltic lava lake. The surface of the bubble above the liquid surface is hemispherical, and to maintain this shape, the internal pressure and the surface tension force in the liquid film must be balanced:

$$\pi r^2 P = 2\pi r \sigma \qquad 6\text{-}25$$

where P is the maximum overpressure that can be sustained within the bubble, r is the bubble radius and σ is the surface tension.

For typical bubble radii of order 10^{-4} m within a magma chamber at depths of order 1 km, and assuming that diffusion maintains volatile equilibrium as the bubble rises, corresponding bubble radii at the surface are around 6×10^{-4} m (using the perfect gas law and a basalt density of 2600 kg m^{-3}). From the pressure and surface tension balance (equation 6-25), the maximum overpressure that the bubble can sustain is:

$$P = \frac{2\sigma}{r} \qquad 6\text{-}26$$

For basalt liquid, the surface tension, σ, is around 0.3 N m^{-1}, and so P is approximately 1000 Pa for a bubble of radius 6 x 10^{-4} m. This pressure corresponds to moving the bubble rapidly from only about 4 cm depth to the surface in order for it to burst. Any convective movement or bubble coalescence will increase the likelihood of overpressure at the surface, with the result that bubble bursting is almost always expected as soon as bubbles reach the melt-air surface.

Nonetheless, if a small fraction of bubbles are retained in the degassed magma, then a stable density stratification may be set up in the conduit, with a layer of frothy magma trapped at the top. If this arises, overturn would be inhibited until gas had escaped from the surface layer, resulting in density increase and sinking. So, a process of discontinuous magma convection occurs in the conduit with the gas emission rate diminished because gas is held within a surface layer.

6.3.3.2 Model implications

The SB model describes a steady-state situation in which magma convection and gas emission continue at constant rate until the whole magma reservoir is degassed or convection is blocked by the collapse of the conduit. Small changes in either magma volatile content or conduit radius will affect the rate of degassing, but not the process itself, which is driven by even a small density difference. Magma is continuously processed at shallow levels while the chamber becomes steadily depleted in volatiles. For the observed gas emission rate at Masaya, the volume of magma processed over the 13 month period from February 1998 to March 1999 can be calculated. Figure 6-11 shows the dependence of gas emission rate on magma flux from equation 6-19, for different initial magma volatile contents. For 4 wt % volatiles, a magma flux of about 5 kg s^{-1} is required, indicating that, over 13 months, a volume of almost 0.2 km^3 of chamber magma has been degassed. For smaller initial volatile contents, these figures are up to two times higher. Thus the minimum size of magma chamber required to support Masaya's emission rate is 0.2 km^3, but considering that similar activity was occurring both before and after my field measurements, a more realistic volume may be of the order of 1 km^3.

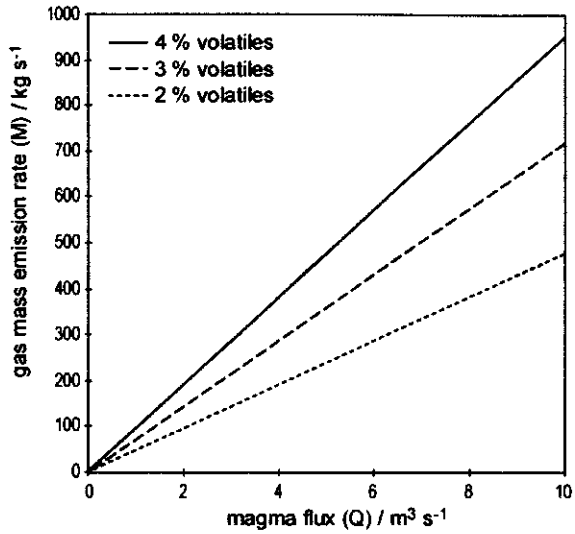

Figure 6-11: The dependence of gas mass emission rate on magma flux from equation 6-19, for different initial volatile contents. Magma flux was varied by changing the conduit radius used in the equation.

In the model, dense degassed magma is returned to the chamber, but its exact fate is unknown. If the degassed magma sinks to the bottom of the chamber with relatively little interaction with undegassed chamber magma, it may form cumulates or intrusions, or result in endogenous growth of the volcano (Francis *et al.* 1993). In this case, the volume of available chamber magma uniformly reduces, but remains with relatively constant composition. A constant gas emission rate and composition are expected at the surface, until the entire magma chamber has been used up, at which time a rapid truncation of degassing occurs. If, however, the descending degassed magma mixes with the original magma in the chamber, then the magma volume remains constant while its volatile content steadily decreases. In this situation, the gas emission rate at the surface is expected to decline steadily through time, providing that the conduit is stable. If the descending magma retains a proportion of dissolved volatiles (e.g. the more soluble components such as fluorine and chlorine), the composition of the dissolved volatiles in the chamber may change gradually and so a gradual change in emitted gas composition may be detected at the surface. The timescale over which changes in gas emission rate will occur depends upon the original magma chamber volume.

Since the emission rate and gas composition at Masaya remained essentially constant from 1998 to 1999, and if the SB model is appropriate here, the situation in which degassed magma sinks through the chamber to form cumulates at the base appears more likely. However, if the available volume of magma is very large then it may be that the timescale over which the gas flux would decline in the mixing scenario is very long.

The gas emission rate predicted by the model is very sensitive to the conduit radius (M proportional to R^4 in equation 6-19 and figure 6-10). If conduit collapse occurs, or crystals grow on the conduit walls, the gas flux will be dramatically affected.

6.3.3.3 Conclusion

A physical model which accounts for gas release as a result of rapid convection in a conduit (Stevenson & Blake 1998) has been adequate to explain observations of degassing at Masaya during 1998–99. The model has been able to account for sustained high gas emission rates without any eruption of magma, and fits the requirement for mainly shallow-level gas exsolution and constant gas compositions. Additionally, rapid convection provides a mechanism by which to keep the conduit (and vent) open and molten.

6.4 Synthesis

Two different quantitative models for degassing have been applied using gas data from Masaya. While a model of conduit convection can explain the gas data, a final model for Masaya's activity during the period of interest should also be able to account for any other geophysical data collected at the time.

6.4.1 Further constraints from published data

Colleagues from the Open University and Universite of Montreal have conducted microgravity surveys at Masaya since 1993 (Delmelle *et al.* 1999a, Rymer *et al.* 1998). The data covering the period of interest from 1998–1999 form part of another thesis (G. Williams-Jones, pers. com.), but were presented in raw form by Delmelle *et al.* (1999a). The earlier data have been more fully discussed and interpreted by Rymer *et al.* (1998).

Around the time of renewed intense degassing, between February 1993 and April 1994, Rymer *et al.* (1998) detected a localised gravity decrease in excess of 90 μGal, and up to 192 μGal, centred on Santiago Crater, signifying a mass decrease at some depth (figure 6-12). The wavelength of the gravity anomaly constrained the depth and dimensions of the causative body to be very shallow, perhaps just below the crater floor, and similar to the diameter of the crater in size. The magnitude of the gravity anomaly, which indicates the magnitude of the mass change at depth, was ill-constrained because the essential measurements directly over the crater could not be made. Since there was negligible vertical and horizontal ground deformation (i.e., no edifice volume change) detected at the same time, the decrease in gravity reflected a subsurface mass and density decrease. Rymer *et al.* (1998) interpreted the gravity decrease as relating to the replacement of dense degassed magma by low-density gas-rich partly-vesiculated magma in a broad shallow zone beneath the crater floor, possibly by means of a large-scale convective overturn. This shallow layer sourced the subsequent gas emission and resulted in a gradual gravity increase in the same region.

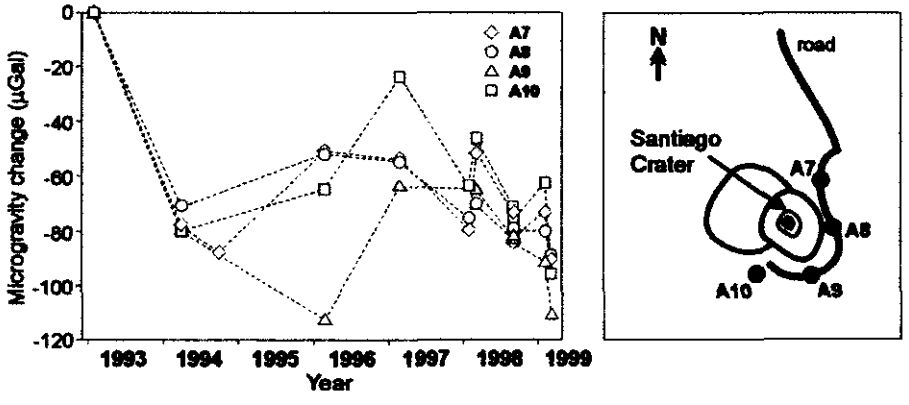

Figure 6-12: Microgravity changes at locations around Santiago Crater between February 1993 and March 1999 (figure published in Delmelle *et al.* 1999a).

This thesis is concerned with a later episode of activity, and between February 1998 and March 1999, the microgravity data are less dramatic (figure 6-12): with an average decrease of around 50 μGal. By analogy with the previous episode, this shift is likely related to changes across a broad shallow zone centred beneath Santiago Crater. However, over the course of a single day, Delmelle *et al.* (1999a) report that microgravity at Masaya can vary by as much as 45 μGal, tentatively correlated with the amplitude of the daily Earth tide. The annual gravity shift is only a little more than potential daily fluctuations and may require minimal magma movement at shallow depth for its explanation.

In summary, an integrated model accounting for the degassing behaviour monitored at Masaya in 1998–1999 must also offer a plausible explanation for small variations in gravity emanating from a broad shallow region below Santiago Crater. The scenario, considered previously, of a narrow conduit that links a magma chamber directly to the vent must be an oversimplification.

6.4.2 Integrated model

In February–March 1998 and March 1999 activity at Masaya Volcano was characterised by vigorous shallow open-conduit degassing which sustained a gas plume from a single vent on the floor of Santiago Crater with near constant composition. Gas emission rates were high (more than 400 kg s^{-1} of gaseous H_2O), but paradoxically there was negligible explosive activity and no eruption of lava. Intense degassing was accompanied by a minor decrease in gravity over the period linked to changes in a broad shallow zone beneath Santiago Crater. High rates of shallow degassing are best explained by a model of degassing-driven convection in the conduit at the expense of volatiles dissolved in magma in a deeper chamber. Figure 6-13 is a schematic cross-section through the system at Masaya indicating the degassing processes which may have been in operation during the period of observation in 1998–99.

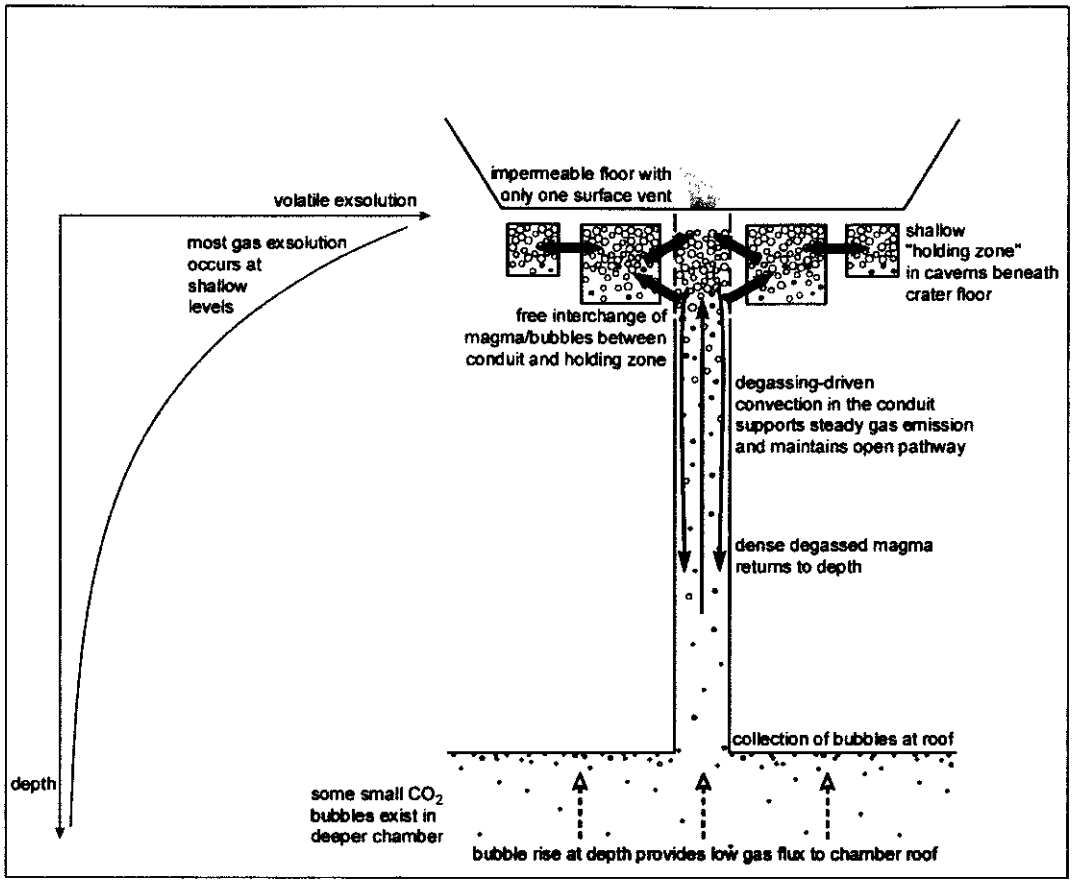

Figure 6-13: Schematic cross section illustrating the proposed model for Masaya's degassing behaviour during measurement periods in February–March 1998 and March 1999. At the depth of the magma chamber only CO_2 is exsolved, and may feed steady foam flow into the conduit. Exsolution of most of the dissolved H_2O and SO_2 at shallow levels results in degassing-driven convection in the narrow conduit. High gas emission rates at the surface are sustained at the expense of volatiles from the deep chamber. A "holding zone" may exist in caverns beneath the impermeable crater floor, with bubbly magma freely circulating while steady conduit convection is occurring.

A magma chamber is connected to the surface by a narrow conduit. Exsolution of CO_2 may begin at considerable depth so that small CO_2 bubbles exist within the chamber: these provide a flux to the chamber roof, where a bubbly layer collects in the manner described by Jaupart and Vergniolle (1989). This CO_2 flux is low enough that the system remains in the stable foam flow regime, and it has little control on the activity seen at the surface. Convection within the narrow conduit is driven by degassing at shallow levels, following the model proposed by Stevenson and Blake (1998), and discussed above. The measured gas emission rates sustained at Masaya for more than 13 months imply a magma chamber of at least 0.3 km^3, and probably of the order of 1 km^3. Rapid convection provides a means to maintain an open conduit for continued shallow degassing without the need for simultaneous eruption of magma, and controls the steady high emission rates measured at the surface. The conduit feeds into caverns at shallow levels beneath the crater floor, allowing free filling and draining of bubble-rich magma in a "holding zone". Such caverns were postulated by Rymer *et al.* (1998) on the basis of geological evidence. Since

the crater floor consists of frozen lava-lakes it is impermeable except where it is breached by the active vent.

Movement of bubbly magma in the holding zone beneath the crater floor can account for fluctuations in microgravity. If conduit convection is vigorous, then there is continual replenishment of the material in the subsurface caverns, and gravity variations will be minimal. If conduit convection is arrested, due to depletion of volatiles in the magma chamber or collapse of the conduit walls, then gas emission at the surface will be supplied only from the material remaining in the holding zone, with consequent subsurface mass changes related to reducing vesicularity. A reduction in gas emission rate will be delayed while gas continues to be released from this batch of bubbly magma. Once magma in the holding zone also becomes volatile-depleted, gas emission will decline. Injection of volatile-rich magma into the deep chamber, or re-opening of a pathway to the surface through tectonic events, could trigger a new episode of degassing and conduit convection. Replacement of degassed magma in the holding-zone with new bubbly magma may be associated with trends in gravity, in a similar way to that envisaged by Rymer *et al.* (1998).

During 1980–82, Masaya was reputedly undergoing a period of intense degassing similar to that monitored during the mid-late 1990s. Stoiber *et al.* (1986) reported average SO_2 emission rates of approximately 14 kg s^{-1}. Assuming that the H_2O/SO_2 and CO_2/SO_2 gas ratios were similar during that phase of activity, the total gas emission rate was around 300 kg s^{-1}. If the degassing at that time was facilitated by conduit convection following the model suggested here, then the lower gas flux can be explained either by a reduced conduit radius, or by degassing of a chamber magma less rich in volatiles (see figure 6-11).

The model can be tested by future monitoring of both gas emission rates and compositions, and microgravity at Masaya. The central requirement of the model is that open-vent degassing is maintained through a process of convection in a narrow conduit. The presence of bubbly magma in caverns beneath the crater floor may help to explain microgravity observations but is not necessary to explain the degassing. If high rates of gas emission were to continue at Masaya without accompanying changes in microgravity, then conduit convection is confirmed as the controlling regime. For uniform gas compositions to be sustained, both shallow-level exsolution of volatiles and a relatively undepleted volatile source are required. If gas emission is maintained simply by removal of gas from magma trapped and isolated in a broad shallow zone, then the system has no means to replenish lost volatiles, and both rates and gas compositions are expected to show correlated trends through time. Unless a shallow gas-rich layer were relatively vast, it is not expected to maintain a constant gas composition or emission rate, in contrast to the suggestion of Delmelle *et al.* (1999a).

6.5 Conclusions of Chapter 6

Observed gas emission rates and compositions at Masaya during 1998–99 were accurately described by straightforward application of a model involving magma convection in a conduit, following Stevenson and Blake (1998). When the full set of geophysical data for the period was considered, a slight modification to the conduit convection model was required allowing bubbly magma to occupy a broad zone beneath the crater floor.

The integrated model presented at the end of this chapter satisfactorily accounts for all the observations. Gas emission rates are controlled by degassing-driven convection in the conduit. Gas compositions remain relatively constant since degassing always occurs mainly at the surface. The sub-surface holding zone may occupy a region with horizontal dimensions similar to Santiago Crater, and may be exposed by periodic crater-floor collapses. The active vent may be the surface expression of a narrow conduit, which has radius less than 5 m at depth, broadened at the surface through collapses and weathering. Crystal growth as degassing continues in the shallowest parts of the conduit and in the holding zone can account for relatively degassed melt inclusions. In this model, variations in the intensity of degassing through history can be explained in a number of ways: as the result of depletion of volatiles in the deep chamber, or new magma with different volatile contents filling the deeper chamber, or through changes in the conduit radius. Because degassed magma sinks back to the chamber, the model also explains why there is negligible eruption of lava.

With reference to the more general problems relating to persistent volcanism that were mentioned at the beginning of the chapter, the final model addresses them all:

(a) Gas reaches the surface by convective transport of the magma in which it is dissolved.

(b) The gas composition can remain constant for as long as the chamber magma remains undepleted in volatiles as relatively complete degassing always occurs very near to the surface.

(c) The pathway to the surface remains molten as a result of vigorous convection in the conduit.

(d) Degassed magma sinks back down to the chamber once it has been processed at the surface. The ultimate fate of this magma is still unconstrained. It may solidify as cumulates at the edges of the chamber, or be intruded as dykes into the regionally faulted country rock.

CHAPTER 7
CONCLUSIONS AND FUTURE PROSPECTS

In this thesis, I began by noting that there are two facets to the study of volcanic gases: first, to make accurate and useful gas measurements, and second, to interpret measured compositions and emission rates correctly. I have tackled this dual challenge by confirming that open-path Fourier transform infrared spectroscopy is a valuable quantitative technique for the measurement of gas compositions at active volcanoes, and then by using OP-FTIR field data collected at Masaya Volcano to investigate its degassing processes. En route, I have made a formal analysis of the accuracy of the instrument, and investigated volcanic plume-troposphere interactions. Following a brief look back over the content of the chapters, I will here comment on avenues for future research, both toward greater understanding of volcanic processes at Masaya, and toward developing IR spectroscopy to its full potential for volcanological applications.

The introductory chapter set the context for this work by providing several motivations for the study of volcanic gases, highlighting OP-FTIR as a promising technique among the other available methods for volcanic gas measurement, and presenting Masaya as a prime natural laboratory at which to develop gas monitoring.

Chapter 2 was a technical introduction to OP-FTIR and its application at volcanoes. The MIDAC instrument used in this work was rugged, compact and portable, and suitable for measurements using an active lamp, a passive terrestrial source, or the sun as the IR source. Measured spectra contain information on the identity and concentrations of absorbing gas molecules within the optical path. This information was retrieved quantitatively by a line-by-line forward model and fitting routine carried out in discrete spectral microwindows. Retrieved gas amounts were displayed on scatter plots so that the gradient of a regression line provided a mean gas concentration ratio. Results from an empirical sensitivity analysis were encouraging, confirming that SO_2 can be retrieved from active OP-FTIR spectra with high accuracy.

Technical aspects of the gas measurements made at Masaya Volcano were reviewed in Chapter 3. Several sources of uncertainty associated with measurement and retrieval were identified. Contributions to error in the retrieval came from background noise, the instrument line shape used in the forward model, the choice of spectral microwindow, and signal to noise in the measurement itself. While these errors are captured within the total error calculated in the retrieval algorithm, further uncertainties are associated with the line parameter database and estimates of plume temperature and pressure. Retrievals of Masaya solar and active spectra should return SO_2/HCl ratios within an average error similar to 10 %.

In Chapter 4, I examined the impact of plume-tropospheric mixing on the gas compositions measured at Masaya Volcano, and three main points arose. The gas composition above Santiago Crater was essentially well-mixed and stable; the composition measured downwind was indistinguishable from that measured at the summit (at the resolution of this instrument); over short timescales, the local atmospheric water content affected only the proportion of HF in the plume. These observations implied that while rapid tropospheric chemistry likely occurred within the crater, there was little further compositional change beyond. Broader implications were that downwind measurements could reasonably be taken as representative of the at-crater gas composition, but that short-term (minutes to hours) compositional variability could not be confidently linked to volcanic causes.

I explored the volcanological implications of gas data collected at Masaya in 1998 and 1999 in Chapter 5. An overwhelmingly consistent gas composition was emitted from Masaya over all timescales, from minutes up to one month. This composition may have been unchanged since a previous study in 1980–82 (Stoiber *et al.* 1986). The in-plume concentrations of SO_2, HCl and HF above Santiago Crater were approximately 76 ppm, 46 ppm and 9 ppm, respectively, levels exceeding recommended health limits. Emission rates were high compared with other passively degassing volcanoes.

Finally, in Chapter 6, I used the constraints provided by the measured gas compositions and emission rates to assess possible models for the degassing behaviour occurring at Masaya during 1998–99. While the gas data were accurately described by straightforward application of a published model involving magma convection in a conduit (Stevenson & Blake 1998), some modification was required to satisfy the full set of geophysical data for the period. The integrated model that I presented in Chapter 6 satisfactorily accounted for all the observations and addressed some more general problems relating to persistent volcanism. However, the ultimate fate of unerupted dense degassed magma which sinks down after processing at the surface remains unconstrained.

7.1 Degassing at Masaya Volcano

A number of issues relating to volcanic activity at Masaya remain unresolved. While a general assumption of periods of strong degassing, interspersed by longer phases of quiescence, during the last 150 years exists, convincing scientific evidence for this is lacking. The size, shape and location of a magma chamber under Santiago crater are still open to question. The variation of gas composition and emission rate with evolving activity at Masaya has gone unobserved, apart from one study. Parent magma volatile contents are unconstrained, limiting the accuracy of gas budget calculations.

Continued plume gas measurements using OP-FTIR in active mode at Santiago Crater are essential in order to propagate the gas dataset throughout the current phase of activity. Degassing crises at Masaya are reported to last between 5 and 15 years (e.g. McBirney 1956, Stoiber *et al.* 1986): consistent observations over the next few years as activity declines will yield insight to the mechanisms in action. As set out with the model presented in Chapter 6, changes in gas compositions and/or emission rates can be interpreted in terms of sub-surface magmatic processes.

Volcano monitoring by other geophysical means is also necessary: integrated datasets provide extra constraints for models, as demonstrated in Chapter 6. In addition to the gas and microgravity data already available, further seismic studies (e.g. Metaxian *et al.* 1997) would also be strategic, in order to track the depth at which intense degassing is occurring. Tunable diode laser spectroscopy (TDLS) could provide an alternative dataset to confirm the plume compositions retrieved by OP-FTIR.

Existing analyses of the gas budget at Masaya rely heavily on estimates for parent magma volatile contents from literature on arc volcanoes in general (e.g. in Chapters 5 and 6). In order to constrain the precise situation, detailed petrological studies on Masaya products are required. Samples from the most recent lava flows, which date from 1680 and 1772, may be the most promising for melt inclusion investigations, although care must be taken to select the most glassy samples from the surfaces of blocks for inclusions which have quenched most rapidly and had less time to reequilibrate. Potentially, this work may yield melt inclusions trapped in phenocrysts which grew at greater depths than those common in the lava bombs erupted recently, and therefore which have volatile contents more closely representative of a deeper magma.

Proxy evidence for the so-called cyclic degassing activity over the last 150 years would be of value, and may be found in tree-rings. Dendrochronology has been used recently for dating larger volcanic eruptions having global climatological effects (Briffa *et al.* 1998). Tropospheric volcanic gases have a deleterious effect on the health of trees growing in the vicinity of Masaya, and especially on the Llano Pacaya. Episodic variation in the quantity of gas produced by the

volcano may be reflected in the annual growth rings of surviving trees. One limitation in this exercise may be that there are few trees appropriate for dendrochronological studies in the region of interest: at times in the past, gas emission rates may have been so strong as to have killed off much of the vegetation.

7.2 Remote sensing of volcanic gases using OP-FTIR

This thesis has demonstrated how the flexibility of OP-FTIR spectroscopy provides a unique advantage for remote gas monitoring on active volcanoes. Additional benefits of OP-FTIR for this application include fine temporal resolution, rapid analysis and quantifiable accuracy. Some limitations remain, including the fact that instrument operation and measurement quality may be severely impaired by factors such as inclement weather, high humidities, or a high ash content in the plume. Additionally, some locations may not offer favourable viewing geometries for absorption spectroscopy.

The value of remote sensing using OP-FTIR at present has been ably demonstrated in this work, and elsewhere (Burton *et al.* 2000, Burton *et al.* 2001, Edmonds *et al.* 2001, Francis *et al.* 1998, Francis *et al.* 1996a, Francis *et al.* 2000, Love *et al.* 1998, Love *et al.* 2000, Mori & Notsu 1997, Oppenheimer *et al.* 2001a, Oppenheimer *et al.* 2001b). However, there is scope for further exploitation of the technique in the future, in terms of instrument, retrieval and scientific development.

7.2.1 Instrument developments

The portability of the MIDAC instrument could be greatly enhanced if it were possible to collect spectra of adequate quality without the telescope attachment. Calibrated tests using primary gas standards are required to assess the degradation in measurement quality for data collected using the spectrometer alone. A further portability issue involves the detector cooling system. Current dependence upon liquid nitrogen limits the use of the spectrometer to roughly 8 hours before refilling is necessary. Stirling cycle cooled detectors, though costly, would allow for continuous operation of the spectrometer over longer periods (given adequate power supply), and easier transport to more remote locations. Currently, measurements are only possible at locations with vehicular access: these two developments would make it possible to take the instrument to less accessible vents.

Collection of spectra using the sun as a source currently relies upon manual alignment of the spectrometer and then manual solar tracking through the observation period. Connection of the instrument to an automatic solar tracker would allow for more consistent solar measurements, and could also be used to keep the instrument aligned while it is transported. Such a development makes transects under a volcanic plume possible, and data collected in this way may reveal new information on the spatial compositional structure of plumes. In-plume sampling using airborne closed-path FTIRs has opened up research in this direction already (e.g. Gerlach *et al.* 1998, McGee & Gerlach 1998).

7.2.2 Retrieval developments

Along with gas phase components, volcanic plumes also carry significant quantities of acid aerosol formed by oxidation of the hot gases as they enter the atmosphere. Theoretically, it should be possible to detect and quantify plume aerosol from infrared spectra, using the MCT detector. Indeed, Love *et al.* (2000) tentatively assign broad features in spectra collected during their field campaign at Popocatepetl to aerosol absorption. Further development of retrieval code should allow for routine quantification of such features, since the HITRAN database (Rothman *et al.* 1998) contains spectral parameters for a number of aerosol species.

A second avenue for retrieval development involves treatment of spectra collected using passive terrestrial infrared sources. The passive spectra discussed in Chapter 3 indicated that useful information on near-vent gas compositions and temperatures is obtainable. Retrieval of this information requires modelling radiative transfer through consecutive atmospheric parcels at different temperatures, rather than along a simple homogeneous path as currently used in the retrieval scheme for active spectra.

One further key computational step is the development of real-time spectral analysis. While the retrieval scheme is currently run off-line for an entire dataset, at the end of a day's observations or on return from fieldwork, it is a rapid procedure, and could be implemented after the collection of each individual spectrum (M. Burton, pers. com.). Highest quality data processing would still require time and effort spent at some later time to check the ILS and optimal retrieval parameters, but real-time analysis would offer a first-guess on the gas composition and would aid decisions made in the field about the ongoing measurement campaign.

7.2.3 Scientific developments

In Chapter 2, I showed that the retrieval of SO_2 from active OP-FTIR spectra collected at volcanoes could be achieved with high accuracy, by means of controlled experiments. Much work is needed to constrain the sensitivity with which other species (especially HCl, HF and CO_2) may be measured. Detailed calibrations with primary gas standards would be required, a task that is not trivial, due to the reactivity of the hydrogen halide gases. However, until such calibration has taken place, it will be difficult to confirm with a high degree of certainty how reliable and accurate are retrievals of these important plume components.

The deployment of two OP-FTIR spectrometers for fieldwork simultaneously could allow for further progress in instrument calibration, as well as in scientific research. A detailed intercomparison of the two instruments could be made. More interestingly, the variation inherent in measurements collected in different operating modes (e.g. active *vs* solar) could be quantified, and precise investigations of the plume composition monitored at different locations simultaneously could be undertaken. There are currently at least four groups worldwide involved

in the use of OP-FTIR for volcanic gas measurement: international collaborations are an obvious mechanism by which to carry out such "dual instrument" investigations.

As mentioned above, the use of a solar tracker in tandem with the spectrometer opens up a new mode of operation for the instrument. Compositional transects obtained by collecting solar spectra at regular intervals as the instrument is driven beneath a plume will reveal new insights to the structure of tropospheric volcanic plumes and the atmospheric processes occurring within them. The limited evidence from the few published studies of plume cross sections (e.g. Gerlach *et al.* 1997, Gerlach *et al.* 1998, McGee 1992, McGee & Gerlach 1998) points to a field worthy of further investigation, and linked with research into anthropogenic pollutant plumes.

Looking beyond the scope of this thesis, the use of infrared spectral techniques for volcanic plume measurements is increasing. Multispectral infrared imaging from airborne and spaceborne platforms is set to bridge the gap between ground-based methods, such as COSPEC, and satellite instruments, such as TOMS, at least for the quantification of SO_2 emissions in tropospheric plumes (Realmuto *et al.* 1994, Realmuto *et al.* 1997). Love *et al.* (2000) hinted that progress towards spectroscopic measurements of volcanic gas compositions from space was inevitable. In a recent article, Zolotov and Fegley (2000) showed how the chemistry of volcanic gases on other planets can even be detected, with measurements of the composition of the plume from Pele volcano on the Jovian satellite Io. These examples highlight the potential for future research using infrared spectral techniques: the application of OP-FTIR to ground-based volcanic gas monitoring is an important element within this expanding field.

Postscript

"Telegrams from within", or Chinese whispers?

This thesis has offered convincing evidence that volcanic gases are the former. With open-path Fourier transform infrared spectroscopy included within the full suite of tools available to the volcanologist, the gases emitted from Masaya, and elsewhere, provide vital information about active volcanic processes and the evolution of a volcano's behaviour.

Note added following viva

Gas emission rates at Masaya have remained at levels consistent with the data presented in this thesis. A small explosion occurred at Santiago Crater on 23 April 2001, ejecting bombs as far as 500 m from the crater, and resulting in the formation of a new 10-m vent on the crater floor. Preliminary analyses of new OP-FTIR data suggest an approximately twofold increase in the SO_2/HCl molar ratio between April 2000 and April 2001. Further analysis is needed to provide a full interpretation of this compositional change.

REFERENCES

Abrams, M. C., Goldman, A., Gunson, M. R., Rinsland, C. P. & Zander, R. 1996. Observations of the infrared solar spectrum from space by the ATMOS experiment. *Applied Optics* **35**(16), 2747–2751.

Abrams, M. C., Toon, G. C. & Schindler, R. A. 1994. Practical example of the correction of Fourier-transform spectra for detector nonlinearity. *Applied Optics* **33**(27), 6307–6314.

Allard, P. 1983. The origin of hydrogen, carbon, sulphur, nitrogen and rare gases in volcanic exhalations: evidence from isotope geochemistry. In: *Forecasting volcanic events* (edited by Tazieff, H. & Sabroux, J.-C.). Elsevier, Amsterdam, 337-386.

Allard, P. 1997. Endogenous magma degassing and storage at Mount Etna. *Geophysical Research Letters* **24**(17), 2219-2222.

Allard, P., Carbonelle, J., Metrich, N., Loyer, H. & Zettwoog, P. 1994. Sulphur output and magma degassing budget of Stromboli volcano. *Nature* **368**, 326-330.

Alt, J. C., Shanks III, W. C. & Jackson, M. C. 1993. Cycling of sulfur in subduction zones: The geochemistry of sulfur in the Mariana Island Arc and back-arc trough. *Earth and Planetary Science Letters* **119**, 477-494.

Anderson, A. T. 1975. Some basaltic and andesitic gases. *Reviews of Geophysics and Space Physics* **13**(1), 37–55.

Andres, R. J. & Kasgnoc, A. D. 1998. A time-averaged inventory of subaerial volcanic sulfur emissions. *Journal of Geophysical Research* **103**(D19), 25251-25261.

Banwell, C. N. 1972. *Fundamentals of molecular spectroscopy*. McGraw-Hill Book Company, Maidenhead, England.

Barclay, J., Carroll, M. R., Houghton, B. F. & Wilson, C. J. N. 1996. Pre-eruptive volatile content and degassing history of an evolving peralkaline volcano. *Journal of Volcanology and Geothermal Research* **74**, 75–87.

Baxter, P. J., Stoiber, R. E. & Williams, S. N. 1982. Volcanic gases and health: Masaya Volcano, Nicaragua. *The Lancet* **2**(8290), 150–151.

Baxter, P. J., Tedesco, D., Miele, G., Baubron, J. C. & Cliff, K. 1990. Health hazards of volcanic gases. *The Lancet* **336**(8708), 176.

Bekki, S. & Pyle, J. A. 1994. A 2-dimensional modeling study of the volcanic eruption of Mount Pinatubo. *Journal of Geophysical Research* **99**(D9), 18861-18869.

Bell, W. 2000. FTIR validation work at the NPL. In: *Industrial and environmental applications of open path FTIR spectroscopy* (edited by Bell, W.), National Physical Laboratory, Teddington, UK.

Bell, W., Paton Walsh, C., Woods, P. T., Gardiner, T. D., Chipperfield, M. P. & Lee, A. M. 1998. Ground-based FTIR measurements with high temporal resolution. *Journal of Atmospheric Chemistry* **30**, 131-140.

Bice, D. C. 1985. Quaternary volcanic stratigraphy of Managua, Nicaragua: Correlation and source assignment for multiple overlapping plinian deposits. *Geological Society of America Bulletin* **96**, 553-566.

Blank, J. G. & Brooker, R. A. 1994. Experimental studies of carbon dioxide in silicate melts: solubility, speciation, and stable carbon isotope behavior. *Reviews in Mineralogy* **30**, 157–186.

Bluth, G. J. S., Schnetzler, C. C., Krueger, A. J. & Walter, L. S. 1993. The contribution of explosive volcanism to global atmospheric sulphur dioxide concentrations. *Nature* **366**, 327-329.

Briffa, K. R., Jones, P. D., Schweingruber, F. H. & Osborn, T. J. 1998. Influence of volcanic eruptions on Northern Hemisphere summer temperature over the past 600 years. *Nature* **393**, 450-455.

Brown, L. R., Gunson, M. R., Toth, R. A., Irion, F. W., Rinsland, C. P. & Goldman, A. 1996. 1995 Atmospheric Trace Molecule Spectroscopy (ATMOS) linelist. *Applied Optics* **35**(16), 2828–2848.

Bruno, N., Caltabiano, T. & Romano, R. 1999. SO_2 emissions at Mt Etna with particular reference to the period 1993–1995. *Bulletin of Volcanology* **60**, 405-411.

Burnham, C. W. & Jahns, R. H. 1962. A method for determining the solubility of water in silicate melts. *American Journal of Science* **260**, 721-745.

Burton, M. R. 1998. Remote sensing of the atmosphere using Fourier transform spectroscopy. Unpublished Ph.D. thesis, University of Cambridge.

Burton, M. R., Oppenheimer, C., Horrocks, L. A. & Francis, P. W. 2000. Remote sensing of CO_2 and H_2O emission rates from Masaya Volcano, Nicaragua. *Geology* **28**(10), 915-918.

Burton, M. R., Oppenheimer, C., Horrocks, L. A. & Francis, P. W. 2001. Diurnal changes in volcanic plume chemistry observed by lunar and solar occultation spectroscopy. *Geophysical Research Letters* **28**(5), 843-846.

Caltabiano, T., Romano, R. & Budetta, G. 1994. SO_2 flux measurements at Mount Etna (Sicily). *Journal of Geophysical research* **99**(D6), 12809-12819.

Cardoso, S. S. S. & Woods, A. W. 1999. On convection in a volatile-saturated magma. *Earth and Planetary Science Letters* **168**, 301-310.

Carmichael, I. S. E. 1991. The redox states of basic and silicic magmas: a reflection of their source regions? *Contributions to Mineralogy and Petrology* **106**, 129-141.

Carr, M. J. 1984. Symmetrical and segmented variation of physical and geochemical characteristics of the Central American volcanic front. *Journal of Volcanology and Geothermal Research* **20**, 231-252.

Carr, M. J. 1999. Volcanic activity and tectonic earthquakes in Central America, 1961–1998. *Fall Meeting Abstracts, Eos, Transactions, AGU* **80**(46), F960.

Carr, M. J., Feigenson, M. D. & Bennett, E. A. 1990. Incompatible element and isotopic evidence for tectonic control of source mixing and melt extraction along the Central American arc. *Contributions to Mineralogy and Petrology* **105**, 369-380.

Carroll, M. R. & Webster, J. D. 1994. Solubilities of sulfur, noble gases, nitrogen, chlorine, and fluorine in magmas. *Reviews in Mineralogy* **30**, 231-279.

Casadevall, T., Rose, W., Gerlach, T., Greenland, L. P., Ewert, J., Wunderman, R. & Symonds, R. 1983. Gas emissions and the eruptions of Mount St Helens through 1982. *Science* **221**, 1383-1385.

Casadevall, T. J., Doukas, M. P., Neal, C. A., McGimsey, R. G. & Gardner, C. A. 1994. Emission rates of sulfur dioxide and carbon dioxide from Redoubt Volcano, Alaska during the1989–1990 eruptions. *Journal of Volcanology and Geothermal Research* **62**, 519-530.

Cashman, K. & Blundy, J. 2000. Degassing and crystallization of ascending andesite and dacite. *Philosophical Transactions of the Royal Society of London, series A* **358**(1770), 1487-1513.

Chan, L. H., Leeman, W. P. & You, C.-F. 1999. Lithium isotopic composition of Central American Volcanic Arc lavas: implications for modification of subarc mantle by slab-derived fluids. *Chemical Geology* **160**, 255-280.

Chandler, A. S., Choularton, T. W., Dollard, G. J., Eggleton, A. E. J., Gay, M. J., Hill, T. A., Jones, B. M. R., Tyler, B. J., Bandy, B. J. & Penkett, S. A. 1988. Measurements of H_2O_2 and SO_2 in clouds and estimates of their reaction rate. *Nature* **336**, 562-565.

Clough, S. A., Kneizys, F. X., Shettle, E. P. & Anderson, G. P. 1985. Atmospheric radiance and transmittance. In: *Sixth Conference on Atmospheric Radiation.* American Meteorological Society, Boston, MA, 141-144.

Connor, C. B., Stoiber, R. E. & Malinconico, L. L. 1988. Variation in sulfur dioxide emissions related to Earth tides, Halemaumau crater, Kilauea volcano, Hawaii. *Journal of Geophysical Research* **93**(B12), 14867-14871.

Connor, C. B. & Williams, S. N. 1989. Interpretation of gravity anomalies, Masaya caldera complex, Nicaragua. In: *12th Caribbean Conference*, St Croix, Virgin Islands.

Daag, A. S., Tubianosa, B. S., Newhall, C. G., Tungol, N. M., Javier, D., Dolan, M. T., Delos Reyes, P. J., Arboleda, R. A., Martinez, M. M. L. & Regalado, M. T. M. 1996. Monitoring sulfur dioxide emissions at Mt. Pinatubo. In: *Fire and Mud: The Eruptions and Lahars of Mount Pinatubo, Philippines* (edited by Newhall, C. G. & Punongbayan, R. S.). University of Washington Press, Seattle.

D'Alessandro, W., Giammanco, S., Parello, F. & Valenza, M. 1997. CO_2 output and $\delta^{13}C(CO_2)$ from Mount Etna as indicators of degassing of shallow asthenosphere. *Bulletin of Volcanology* **58**, 455–458.

Davies, N. M. 1999. The application of open-path Fourier transform infrared spectrometry using resolution enhancement to gaseous emissions monitoring. Unpublished Ph.D. thesis, University of Reading.

Delmelle, P., Stix, J., Bourque, C. P. A., Bazter, P. J., Garcia-Alvarez, J. & Barquero, J. 2001. Dry deposition and heavy acid loading in the vicinity of Masaya Volcano, a major sulfur and chlorine source in Nicaragua. *Environmental Science and Technology* **35**, 1289–1293.

Delmelle, P., Baxter, P., Beaulieu, A., Burton, M., Francis, P., Garcia-Alvarez, J., Horrocks, L. A., Navarro, M., Oppenheimer, C., Rothery, D. A., Rymer, H., St. Amand, K., Stix, J., Strauch, W. & Williams-Jones, G. 1999a. Origin, effects of Masaya's volcano continued unrest probed in Nicaragua. *EOS, Transactions, AGU* **80**(48), 575, 579, 581.

Delmelle, P., Stix, J., Williams-Jones, G., Rothery, D., Rymer, H., Horrocks, L., Burton, M., Baxter, P., Garcia-Alvarez, J., Navarro, M. & Strauch, W. 1999b. Global volcanism network report. *Bulletin of the Global Volcanism Network* **24**(4).

Devine, J. D., Gardner, J. E., Brack, H. P., Layne, G. D. & Rutherford, M. J. 1995. Comparison of microanalytical methods for estimating H_2O contents of silicic volcanic glasses. *American Mineralogist* **80**, 319-328.

Dixon, J. E., Clague, D. A. & Stolper, E. M. 1991. Degassing history of water, sulfur, and carbon in submarine lavas from Kilauea volcano, Hawaii. *Journal of Geology* **99**, 371-394.

Dixon, J. E. & Stolper, E. M. 1995. An experimental study of water and carbon dioxide solubilities in mid-ocean ridge basaltic liquids. Part II: Applications to degassing. *Journal of Petrology* **36**(6), 1633–1646.

Dixon, J. E., Stolper, E. M. & Holloway, J. R. 1995. An experimental study of water and carbon dioxide solubilities in mid-ocean ridge basaltic liquids. Part I: Calibration and solubility models. *Journal of Petrology* **36**(6), 1607–1631.

Doukas, M. P. & Gerlach, T. M. 1995. Sulfur dioxide scrubbing during the 1992 eruption of Crater Peak, Mount Spurr Volcano, Alaska. *U. S. Geological Survey Bulletin* **B-2139**, 47-57.

Dowrick, C. A. 1999. The GASPEC: Use and development of a prototype remote sensor at Mexican and Central American volcanoes. Unpublished M.Sc. thesis, Arizona State University.

Dudhia, A. 2000. Michelson interferometer for passive atmospheric sounding (MIPAS) Reference Forward Model: Software User's Manual: Issue 4.1. Department of Physics, Oxford University, Oxford, UK.

Eatough, D. J., Caka, F. M. & Farber, R. J. 1994. The conversion of SO_2 to sulfate in the atmosphere. *Israel Journal of Chemistry* **34**(3-4), 301-314.

Edmonds, M., Pyle, D., Oppenheimer, C. & Pearce, N. 2001. A model for degassing at Soufriere Hills Volcano. *Earth and Planetary Science Letters* **in review**.

Edner, H., Ragnarson, P., Svanberg, S., Wallinder, E., Ferrara, R., Cioni, R., Raco, B. & Taddeucci, G. 1994. Total fluxes of SO_2 from the Italian volcanoes Etna, Stromboli and Vulcano measured by differential absorption LIDAR and passive differential optical absorption spectroscopy. *Journal of Geophysical Research* **99**(D9), 18827-18838.

Edwards, D. P. 1992. GENLN2: A General Line-by-line atmospheric transmittance and radiance model. Version 3.0 Description and user's guide. NCAR, Boulder, CO, USA.

Feigenson, M., D. & Carr, M., J. 1993. The source of Central American lavas: inferences from geochemical inverse modeling. *Contributions to Mineralogy and Petrology* **113**, 226-235.

Finlayson-Pitts, B. J. & Pitts, J. N. 1986. *Atmospheric chemistry: Fundamentals and experimental techniques*. Wiley-Interscience, New York.

Fischer, T. P., Arehart, G. B., Sturchio, N. C. & Williams, S. N. 1996. The relationship between fumarole gas composition and eruptive activity at Galeras Volcano, Colombia. *Geology* **24**(6), 531-534.

Fischer, T. P., Giggenbach, W. F., Sano, Y. & Wiliams, S. N. 1998. Fluxes and sources of volatiles discharged from Kudryavy, a subduction zone volcano, Kurile Islands. *Earth and Planetary Letters* **160**, 81-96.

Fournelle, J., Carmody, R. & Daag, A. S. 1996. Anhydrite-bearing pumices from the June 15, 1991, eruption of Mount Pinatubo: geochemistry, mineralogy, and petrology. In: *Fire and Mud: The Eruptions and Lahars of Mount Pinatubo, Philippines* (edited by Newhall, C. G. & Punongbayan, R. S.). University of Washington Press, Seattle.

Francis, P., Burton, M. R. & Oppenheimer, C. 1998. Remote measurements of volcanic gas compositions by solar occultation spectroscopy. *Nature* **396**, 567-570.

Francis, P., Chaffin, C., Maciejewski, A. & Oppenheimer, C. 1996a. Remote determination of SiF_4 in volcanic plumes: A new tool for volcano monitoring. *Geophysical Research Letters* **23**(3), 249-252.

Francis, P., Maciejewski, A., Oppenheimer, C. & Chaffin, C. 1996b. New methods make volcanology research less hazardous. *EOS, American Geophysical Union*, 393-396.

Francis, P., Maciejewski, A., Oppenheimer, C., Chaffin, C. & Caltabiano, T. 1995. SO_2:HCl ratios in the plumes from Mt. Etna and Vulcano determined by Fourier transform spectroscopy. *Geophysical Research Letters* **22**(13), 1717-1720.

Francis, P., Oppenheimer, C. & Stevenson, D. 1993. Endogenous growth of persistently active volcanoes. *Nature* **366**, 554-557.

Francis, P. W., Horrocks, L. A. & Oppenheimer, C. 2000. Monitoring gases at andesite volcanoes. *Philosophical Transactions of the Royal Society of London - Series A: Mathematical, Physical and Engineering Sciences* **358**(1770), 1567-1584.

Gerlach, T. M. 1986. Exsolution of H_2O, CO_2, and S during eruptive episodes at Kilauea Volcano, Hawaii. *Journal of Geophysical Research* **91**(B12), 12177-12185.

Gerlach, T. M. 1991. Present-day CO_2 emissions from volcanoes. *EOS, Transactions, AGU* **72**, 249, 254–255.

Gerlach, T. M. 1993. Thermodynamic evaluation and restoration of volcanic gas analyses: An example based on modern collection and analytical methods. *Geochemical Journal* **27**, 305-322.

Gerlach, T. M., Delgado, H., McGee, K. A., Doukas, M. P., Venegas, J. J. & Cardenas, L. 1997. Application of the LI-COR CO_2 analyser to volcanic plumes: A case study, volcan Popocatepetl, Mexico, June 7 and 10, 1995. *Journal of Geophysical Research* **102**(B4), 8005-8019.

Gerlach, T. M. & Graeber, E. J. 1985. Volatile budget of Kilauea volcano. *Nature* **313**, 273-277.

Gerlach, T. M. & McGee, K. A. 1994. Total sulfur dioxide emissions and pre-eruption vapor-saturated magma at Mount St. Helens, 1980–88. *Geophysical Research Letters* **21**, 2833–2836.

Gerlach, T. M., McGee, K. A., Sutton, A. J. & Elias, T. 1998. Rates of volcanic CO_2 degassing from airborne determinations of SO_2 emission rates and plume CO_2/SO_2: Test study at Pu'u O'o cone, Kilauea volcano, Hawaii. *Geophysical Research Letters* **25**(14), 2675-2678.

Gerlach, T. M., Westrich, H. R., Casadevall, T. J. & Finnegan, D. L. 1994. Vapor saturation and accumulation in magmas of the 1989–1990 eruption of Redoubt Volcano, Alaska. *Journal of Volcanology and Geothermal Research* **62**, 317–337.

Ghiorso, M. S. & Sack, R. O. 1995. Chemical mass-transfer in magmatic processes 4. A revised and internally consistent thermodynamic model for the interpolation and extrapolation of liquid-solid equilibria in magmatic systems at elevated temperatures and pressures. *Contributions to Mineralogy and Petrology* **119**(2-3), 197-212.

Giggenbach, W. F. 1996. Chemical composition of volcanic gases. In: *Monitoring and mitigation of volcano hazards* (edited by Scarpa, R. & Tilling, R. I.). Springer-Verlag, Berlin Heidelberg, 221-256.

Goff, F., Janik, C. J., Delgado, H., Werner, C., Counce, D., Stimac, J. A., Siebe, C., Love, S. P., Williams, S. N., Fischer, T. & Johnson, L. 1998. Geochemical surveillance of magmatic volatiles at Popocatepetl volcano, Mexico. *Geologicl Society of America Bulletin* **110**(6), 695-710.

Gregg, T. K. P. & Williams, S. N. 1996. Explosive mafic volcanoes on Mars and Earth: Deep magma sources and rapid rise rate. *Icarus* **122**, 397-405.

Griffiths, P. R. 1975. *Chemical Infrared Fourier Transform Spectroscopy*. Wiley-Interscience, New York.

Hanst, P. L. 1979. Pollution: trace gas analysis. In: *Fourier transform infrared spectroscopy: applications to chemical systems* (edited by Ferraro, J. R. & Basile, L. J.). Academic Press, New York, 79-110.

Hanst, P. L. & Hanst, S. T. 1994. Gas measurement in the fundamental infrared region. In: *Air monitoring by spectroscopic techniques* (edited by Sigrist, M. W.). *Chemical Analysis Series*. John Wiley & Sons, 335–470.

Harris, A. J. L., Flynn, L. P., Rothery, D. A., Oppenheimer, C. & Sherman, S. B. 1999. Mass flux measurements at active lava lakes: Implications for magma recycling. *Journal of Geophysical Research* **104**(B4), 7117-7136.

Herget, W. F. & Brasher, J. D. 1979. Remote measurement of gaseous pollutant concentrations using a mobile Fourier transform interferometer system. *Applied Optics* **18**(20), 3404–3420.

Herrstrom, E. A., Reagan, M. K. & Morris, J. D. 1995. Variations in lava composition associated with flow of asthenosphere beneath southern Central America. *Geology* **23**(7), 617-620.

Hilton, M., Lettington, A. H. & Mills, I. M. 1995. Quantitative analysis of remote gas temperatures and concentrations from their infrared emission spectra. *Measurement Science and Technology* **6**(9), 1236–1241.

Hobbs, P. V., Radke, L. F., Lyons, J. H., Ferek, R. J. & Coffman, D. J. 1991. Airborne measurements of particle and gas emissions from the 1990 volcanic eruptions of Mount Redoubt. *Journal of Geophysical Research* **96**(D10), 18735–18752.

Holloway, J. R. 1981. Volatile interactions in magmas. In: *Thermodynamics of Minerals and Melts* (edited by Newton, R. C., Navrotsky, A. & Wood, B. J.). Springer-Verlag, New York, 273–294.

Holloway, J. R. & Blank, J. G. 1994. Application of experimental results to C-O-H species in natural melts. *Reviews in Mineralogy* **30**, 187–230.

Houghton, J. T. 1986. *The Physics of Atmospheres*. Cambridge University Press, Cambridge.

Ingamells, C. O. & Gittins, J. 1967. The stoichiometry of scapolite. *Canadian Mineralogist* **9**, 214-236.

Ito, E., Harris, D. M. & Anderson, A. T. 1983. Alteration of oceanic crust and geologic cycling of chlorine and water. *Geochimica et Cosmochimica Acta* **47**, 1613-1624.

Iwasaki, B. & Katsura, T. 1967. The solubility of hydrogen chloride in volcanic rock melts at a total pressure of one atmosphere and at temperatures of 1200 C and 1290 C under anhydrous conditions. *Bulletin of the Chemistry Society of Japan* **40**, 554-561.

Jaupart, C. & Allegre, C. J. 1991. Gas content, eruption rate and instabilities of eruption regime in silicic volcanoes. *Earth and Planetary Science Letters* **102**, 413–429.

Jaupart, C. & Tait, S. 1990. Dynamics of eruptive phenomena. *Reviews in Mineralogy* **24**, 213–238.

Jaupart, C. & Vergniolle, S. 1989. The generation and collapse of a foam layer at the roof of a basaltic magma chamber. *Journal of Fluid Mechanics* **203**, 347-380.

Johnson, N. & Parnell, R. A. 1986. Composition, distribution and neutralization of "acid rain" derived from Masaya volcano, Nicaragua. *Tellus* **38B**, 106-117.

Kazahaya, K., Shinohara, H. & Saito, G. 1994. Excessive degassing of Izu-Oshima volcano: magma convection in a conduit. *Bulletin of Volcanology* **56**, 207–216.

Keeling, C. D. & Whorf, T. P. 2000. Atmospheric CO_2 records from sites in the SIO air sampling network. In: *Trends Online: A compendium of data on global change (http://cdiac.esd.ornl.gov/trends/trends.htm)* (edited by Center, C. D. I. A.). Oak Ridge National Laboratory, U.S. Department of Energy.

Keys, J. G., Wood, S. W., Jones, N. B. & Murcray, F. J. 1998. Spectral measurements of HCl in the plume of the Antarctic volcano Mount Erebus. *Geophysical Research Letters* **25**(13), 2421-2424.

Kodosky, L. G., Motyka, R. J. & Symonds, R. B. 1991. Fumarolic emissions from Mount St. Augustine, Alaska: 1979–1984 degassing trends, volatile sources and their possible role in eruptive style. *Bulletin of Volcanology* **53**, 381-394.

Koepenick, K. W., Brantley, S. L., Thompson, J. M., Rowe, G. L., Nyblade, A. A. & Moshy, C. 1996. Volatile emissions from the crater and flank of Oldoinyo Lengai volcano, Tanzania. *Journal of Geophysical Research* **101**(B6), 13819-13830.

Kress, V. 1997. Thermochemistry of sulfide liquids. I. the system O-S-Fe at 1 bar. *Contributions to Mineralogy and Petrology* **127**, 176-186.

Kuritani, T. 1999. Phenocryst crystallization during ascent of alkali basalt magma at Rishiri Volcano, northern Japan. *Journal of Volcanology and Geothermal Research* **88**, 77-97.

Lambert, A., Grainger, R. G., Rodgers, C. D., Taylor, F. W., Mergenthaler, J. L., Kumer, J. B. & Massie, S. T. 1997. Global evolution of the Mt Pinatubo volcanic aerosols observed by the infrared limb-sounding instruments CLAES and ISAMS on the Upper Atmosphere Research Satellite. *Journal of Geophysical Research* **102**(D1), 1495-1512.

Le Guern, F. 1983. Magmatic gas monitoring. In: *Forecasting volcanic events* (edited by Tazieff, H. & Sabroux, J.-C.). Elsevier, Amsterdam, 293-310.

Le Guern, F., Carbonnelle, J. & Tazieff, H. 1979. Erta'Ale lava lake: heat and gas transfer to the atmosphere. *Journal of Volcanology and Geothermal Research* **6**, 27-48.

Leeman, W. P., Carr, M. J. & Morris, J. D. 1994. Boron geochemistry of the Central American volcanic arc: constraints on the genesis of subduction-related magmas. *Geochimica et Cosmochimica Acta* **58**(1), 149–168.

Love, S. P., Goff, F., Counce, D., Siebe, C. & Delgado, H. 1998. Passive infrared spectroscopy of the eruption plume at Popocatepetl volcano, Mexico. *Nature* **396**, 563-567.

Love, S. P., Goff, F., Schmidt, S. C., Counce, D., Pettit, D., Christenson, B. W. & Siebe, C. 2000. Passive infrared spectroscopic remote sensing of volcanic gases: Ground-based studies at White Island and Ruapehu, New Zealand, and Popcatepetl, Mexico. In: *Remote sensing of active volcanism* (edited by Mouginis-Mark, P., Crisp, J. A. & Fink, J. H.). *Geophysical Monograph Series*. American Geophysical Union, Washington, DC, 117-138.

Maciejewski, A. J. H. 1998. Remote measurements of volcanic gases: Applications of Open-path Fourier transform infra-red spectroscopy (OP-FTIR) and Correlation spectroscopy (COSPEC). Unpublished Ph.D. thesis, The Open University.

Malinconico, L. L. 1979. Fluctuations in SO_2 emission during recent eruptions of Etna. *Nature* **278**, 43–45.

Malinconico, L. L. 1987. On the variation of SO_2 emission from volcanoes. *Journal of Volcanology and Geothermal Research* **33**, 231-237.

Mankin, W. G. & Coffey, M. T. 1984. Increased stratospheric hydrogen chloride in the El Chichon cloud. *Science* **226**, 170–172.

Mankin, W. G., Coffey, M. T. & Goldman, A. 1992. Airborne observations of SO_2, HCl, and O_3 in the stratospheric plume of the Pinatubo volcano in July 1991. *Geophysical Research Letters* **19**(2), 179-182.

Marquardt, D. W. 1963. An algorithm for least squares estimation of nonlinear parameters. *Journal of the Society of Industrial and Applied Mathematics (SIAM)* **11**, 431–441.

Marshall, T. L., Chaffin, C., T., Hammaker, R. M. & Fateley, W. G. 1994. An introduction to open-path FT-IR atmospheric monitoring. *Environmental Science and Technology* **28**(5), A224-A232.

Martin, D., Ardouin, B., Bergametti, G., Carbonelle, J., Faivre-Pierret, R., Lambert, G., Le Cloarec, M. F. & Sennequier, G. 1986. Geochemistry of sulfur in Mount Etna plume. *Journal of Geophysical Research* **91**(B12), 12249-12254.

Martini, M. 1996. Chemical characters of the gaseous phase at different stages of volcanism: precursors and volcanic activity. In: *Monitoring and mitigation of volcano hazards* (edited by Scarpa, R. & Tilling, R. I.). Springer-Verlag, Berlin Heidelberg, 199-220.

Matsuo, S. 1975. Chemistry of volcanic gases. *Bulletin of the Volcanological Society of Japan* **20**, 319-329.

McBirney, A. R. 1956. The Nicaraguan volcano Masaya and its caldera. *Transactions of the American Geophysical Union* **37**(1), 83-96.

McCormick, M. P., Thomason, L. W. & Trepte, C. R. 1995. Atmospheric effects of the Mt Pinatubo eruption. *Nature* **373**, 399–404.

McGee, K. A. 1992. The structure, dynamics, and chemical composition of noneruptive plumes from Mount St. Helens, 1980–88. *Journal of Volcanology and Geothermal Research* **51**, 269-282.

McGee, K. A. & Gerlach, T. M. 1998. Airborne volcanic plume measurements using a FTIR spectrometer, Kilauea volcano, Hawaii. *Geophysical Research Letters* **25**(5), 615-618.

McGee, K. A. & Jefferson Sutton, A. 1994. Eruptive activity at Mount St Helens, Washington, USA, 1984-1988: a gas geochemistry perspective. *Bulletin of Volcanology* **56**, 435-446.

Metaxian, J.-P., Lesage, P. & Dorel, J. 1997. Permanent tremor of Masaya Volcano, Nicaragua: Wave field analysis and source location. *Journal of Geophysical Research* **102**(B10), 22529–22545.

Metrich, N. & Clocchiatti, R. 1996. Sulfur abundance and its speciation in oxidized alkaline melts. *Geochimica et Cosmochimica Acta* **60**(21), 4151-4160.

Metrich, N. & Rutherford, M. J. 1992. Experimental study of chlorine behaviour in hydrous silicic melts. *Geochimica et Cosmochimica Acta* **56**, 607-616.

Metrich, N., Schiano, P., Clocchiatti, R. & Maury, R., C. 1999. Transfer of sulfur in subduction settings: an example from Batan Island (Luzon volcanic arc, Philippines). *Earth and Planetary Science Letters* **167**, 1–14.

Michael, P. J. & Schilling, J.-G. 1989. Chlorine in mid-ocean ridge magmas: Evidence for assimilation of seawater-influenced components. *Geochimica et Cosmochimica Acta* **53**, 3131-3143.

Mori, T. & Notsu, K. 1997. Remote CO, COS, CO_2, SO_2, HCl detection and temperature estimation of volcanic gas. *Geophysical Research Letters* **24**(16), 2047-2050.

Mori, T., Notsu, K., Tohjima, Y. & Wakita, H. 1993. Remote detection of HCl and SO_2 in volcanic gas from Unzen volcano, Japan. *Geophysical Research Letters* **20**(13), 1355-1358.

Mori, T., Notsu, K., Tohjima, Y., Wakita, H., Nuccio, P. M. & Italiano, F. 1995. Remote detection of fumarolic gas chemistry at Vulcano, Italy, using an FT-IR spectral radiometer. *Earth and Planetary Science Letters* **134**, 219-224.

Morris, J. D., Leeman, W. P. & Tera, F. 1990. The subducted component in island-arc lavas: constraints from Be isotopes and B-Be systematics. *Nature* **344**, 31-36.

Mosbah, M., Clocchiati, R., Metrich, N., Piccot, D., Rio, S. & Tirira, J. 1995. The characterisation of glass inclusions through nuclear microprobe. *Nuclear instruments & methods in physics research Section B - Beam interactions with materials and atoms* **104**(1–4), 271–275.

Mueller, R. F. 1970. Energetics of HCl and HF in volcanic emanations. *Geochimica et Cosmochimica Acta* **34**, 737–744.

Naughton, J. J., Derby, J. V. & Glover, R. B. 1969. Infrared measurements on volcanic gas and fume: Kilauea eruption, 1968. *Journal of Geophysical Research* **74**(12), 3273-3277.

Norton, G. & Young, S. R. 2000. Activity during October–November 1999 at Soufriere Hills. *Montserrat Volcano Observatory Scientific Report* **105**.

Notholt, J. 1994. The Moon as a light source for FTIR measurements of stratspheric trace gases during the polar night: Application for HNO_3 in the Arctic. *Journal of Geophysical Research* **99**(D2), 3607-3614.

Notsu, K., Mori, T., Igarashi, G., Tohjima, Y. & Wakita, H. 1993. Infrared spectral radiometer: A new tool for remote measurement of SO_2 of volcanic gas. *Geochemical Journal* **27**, 361–366.

Oppenheimer, C. 1996. On the role of hydrothermal systems in the transfer of volcanic sulfur to the atmosphere. *Geophysical Research Letters* **23**(16), 2057-2060.

Oppenheimer, C., Burton, M. R., Durieux, J. & Pyle, D. M. 2001a. Water, carbon and sulfur degassing from Oldoinyo Lengai volcano. *Earth and Planetary Science Letters* **submitted**.

Oppenheimer, C., Edmonds, M., Francis, P. & Burton, M. 2001b. Variation in $HCl:SO_2$ gas ratios at Soufriere Hills volcano observed by Fourier transform spectroscopy, 1996-1999. *Geological Society of London Memoir* **in review**.

Oppenheimer, C., Francis, P., Burton, M., Maciejewski, A. J. H. & Boardman, L. 1998a. Remote measurement of volcanic gases by Fourier transform infrared spectroscopy. *Applied Physics B* **67**, 505-515.

Oppenheimer, C., Francis, P. & Maciejewski, A. 1998b. Volcanic gas measurements by helicopter-borne Fourier transform spectroscopy. *International Journal of Remote Sensing* **19**(2), 373-379.

Oppenheimer, C., Francis, P. & Stix, J. 1998c. Depletion rates of sulfur dioxide in tropospheric volcanic plumes. *Geophysical Research Letters* **25**(14), 2671-2674.

Papale, P. & Polacci, M. 1999. Role of carbon dioxide in the dynamics of magma ascent in explosive eruptions. *Bulletin of Volcanology* **60**, 583-594.

Parfitt, E. A. & Wilson, L. 1995. Explosive volcanic eruptions—IX. The transition between Hawaiian-style lava fountaining and Strombolian explosive activity. *Geophysical Journal International* **121**, 226–232.

Paton Walsh, C., Bell, W., Gardiner, T., Swann, N., Woods, P., Notholt, J., Schutt, H., Galle, B., Arlander, W. & Mellqvist, J. 1997. An uncertainty budget for ground-based Fourier transform infrared column measurements of HCl, HF, N_2O, and HNO_3 deduced from results of side-by-side instrument intercomparisons. *Journal of Geophysical Research* **102**(D7), 8867–8873.

Pennisi, M. & Le Cloarec, M.-F. 1998. Variations of Cl, F, and S in Mount Etna's plume, Italy, between 1992 and 1995. *Journal of Geophysical Research* **103**(B3), 5061-5066.

Perrin, A., Flaud, J.-M., Goldman, A., Camy-Peyret, C., Lafferty, W. J., Arcas, P. & Rinsland, C. P. 1998. NO_2 and SO_2 line parameters: 1996 HITRAN update and new results. *Journal of Quantitative Spectroscopy and Radiative Transfer* **60**(5), 839–850.

Persikov, E. S. 1990. The viscosity of magmatic liquids: experiment, generalized patterns, a model for calculation and prediction, applications. In: *Physics and Chemistry of magmas* (edited by Perchuk, L. L. & Kushiro, I.). Springer-Verlag, 1-40.

Phillips, J. C. & Woods, A. W. 2000. Bubble plumes generated during recharge of basaltic magma reservoirs. *Earth and Planetary Science Letters* **in review**.

Pinto, J. P., Turco, R. P. & Toon, O. B. 1989. Self-limiting physical and chemical effects in volcanic eruption clouds. *Journal of Geophysical Research* **94**(D8), 11165-11174.

Poorter, R. P. E., Varekamp, J. C., Poreda, R. J., van Bergen, M. J. & Kreulen, R. 1991. Chemical and isotopic compositions of volcanic gases from the east Sunda and Banda arcs, Indonesia. *Geochimica et Cosmochimica Acta* **55**, 3795-3807.

Proussevitch & Sahagian. 1998. Bubble growth in magmas. *Journal of Geophysical Research* **103**(B8), 18223.

Proussevitch, A. A., Sahagian, D. L. & Kutolin, V. A. 1993. Stability of foams in silicate melts. *Journal of Volcanology and Geothermal Research* **59**, 161–178.

Punongbayan, R. S., Newhall, C. G., Bautista, M. L. P., Garcia, D., Harlow, D. H., Hoblitt, R. P., Sabit, J. P. & Solidum, R. U. 1996. Eruption hazard assessment and warnings. In: *Fire and Mud: The Eruptions and Lahars of Mount Pinatubo, Philippines* (edited by Newhall, C. G. & Punongbayan, R. S.). University of Washington Press, Seattle.

Pyle, D. M. 1989. The thickness, volume and grainsize of tephra fall deposits. *Bulletin of Volcanology* **51**, 1-15.

Raffle, P. A. B. 1994. *Hunter's Diseases of Occupations*. E. Arnold, London.

Ravishankara, A. R. 1997. Heterogeneous and multiphase chemistry in the troposphere. *Science* **276**, 1058–1065.

Read, W. G., Froidevaux, L. & W., W. J. 1993. Microwave Limb Sounder measurement of stratospheric SO_2 from the Mt Pinatubo Volcano. *Geophysical Research Letters* **20**(12), 1299-1302.

Reagan, M. K., Morris, J. D., Herrstrom, E. A. & Murrell, M. T. 1994. Uranium series and beryllium isotope evidence for an extended history of subduction modification of the mantle below Nicaragua. *Geochimica et Cosmochimica Acta* **58**(19), 4199–4212.

Realmuto, V. J., Abrams, M. J., Buongiorno, M. F. & Pieri, D. C. 1994. The use of multispectral thermal infrared image data to estimate the sulfur dioxide flux from volcanos - A case study from Mount Etna, Sicily, July 29, 1986. *Journal of Geophysical Research* **99**(B1), 481-488.

Realmuto, V. J., Sutton, A. J. & Elias, T. 1997. Multispectral thermal infrared mapping of sulfur dioxide plumes: A case study from the East Rift Zone of Kilauea Volcano, Hawaii. *Journal of Geophysical Research* **102**(B7), 15057-15072.

Rodgers, C. D. 1976. Retrieval of atmospheric temperature and composition from remote measurements of thermal radiation. *Reviews of Geophysics and Space Physics* **14**(4), 609-624.

Roggensack, K., Hervig, R. L., McKnight, S. B. & Williams, S. N. 1997. Explosive basaltic volcanism from Cerro Negro Volcano: Influence of volatiles on eruptive style. *Science* **277**, 1639-1642.

Roscoe, H. K. & Clemitshaw, K. C. 1997. Measurement techniques in gas-phase tropospheric chemistry: a selective view of the past, present, and future. *Science* **276**, 1065-1072.

Rose, W. I., Heiken, G., Wohletz, K., Keppler, D., Barr, S., Miller, T., Chuan, R. L. & Symonds, R. B. 1988. Direct rate measurements of eruption plumes at Augustine volcano—a problem of scaling and uncontrolled variables. *Journal of Geophysical Research* **93**(B5), 4485–4499.

Rosenberg, P. E. 1973. HF/SiF_4 ratios in volcanic and magmatic gases. *Geochimica et Cosmochimica Acta* **37**, 109–112.

Rothman, L. S., Rinsland, C. P., Goldman, A., Massie, S. T., Edwards, D. P., Flaud, J.-M., Perrin, A., Camy-Peyret, C., Dana, V., Mandin, J.-Y., Schroeder, J., McCann, A., Gamache, R. R., Wattson, R. B., Yoshino, K., Chance, K. V., Jucks, K. W., Brown, L. R.,

Nemtchinov, V. & Varanasi, P. 1998. The HITRAN molecular spectroscopic database and HAWKS (HITRAN Atmospheric WorKStation): 1996 edition. *Journal of Quantitative Spectroscopy and Radiative Transfer* **60**(5), 665–710.

Rymer, H., van Wyk de Vries, B., Stix, J. & Williams-Jones, G. 1998. Pit crater structure and processes governing persistent activity at Masaya Volcano, Nicaragua. *Bulletin of Volcanology* **59**, 345-355.

Sabroux, J.-C. 1983. Volcano energetics: volcanic gases and vapours as geothermometers and geobarometers. In: *Forecasting Volcanic Events* (edited by Tazieff, H. & Sabroux, J.-C.). Elsevier, Amsterdam, 17–25.

Sander, R. 2000. Henry's Law Constants. In: *NIST Chemistry WebBook, NIST Standard Reference Database 69* (edited by Mallard, W. G. & Linstrom, P. J.). National Institute of Standards and Technology, http://webbook.nist.gov.

Sano, Y. & Williams, S. N. 1996. Fluxes of mantle and subducted carbon along convergent plate boundaries. *Geophysical Research Letters* **23**(20), 2749–2752.

Scaillet, B., Clemente, B., Evans, B. W. & Pichavant, M. 1998. Redox control of sulfur degassing in silicic magmas. *Journal of Geophysical Research* **103**(B10), 23937-23949.

Schneider, D. J., Rose, W. I., Coke, L. R., Bluth, G. J. S., Sprod, I. E. & Krueger, A. J. 1999. Early evolution of a stratospheric volcanic eruption cloud as observed with TOMS and AVHRR. *Journal of Geophysical Research* **104**(D4), 4037-4050.

Seinfeld, J. H. 1986. *Atmospheric chemistry and physics of air pollution*. John Wiley and Sons, New York.

Self, S., Zhao, J.-X., Holasek, R. E., Torres, R. C. & King, A. J. 1996. The atmospheric impact of the 1991 Mount Pinatubo eruption. In: *Fire and Mud: The Eruptions and Lahars of Mount Pinatubo, Philippines* (edited by Newhall, C. G. & Punongbayan, R. S.). University of Washington Press, Seattle, 1089-1115.

Shaw, H. R. 1972. Viscosities of magmatic silicate liquids: an empirical method of prediction. *American Journal of Science* **272**, 870–893.

Signorelli, S. & Capaccioni, B. 1999. Behaviour of chlorine prior and during the 79 A.D. Plinian eruption of Vesuvius (southern Italy) as inferred from the present distribution in glassy mesostases and whole-pumices. *Lithos* **46**, 715-730.

Sisson, T. W. & Layne, G. D. 1993. H_2O in basalt and basaltic andesite glass inclusions from four subduction-related volcanoes. *Earth and Planetary Science Letters* **117**, 619-635.

Stenchikov, G. L., Kirchner, I., Robock, A., Graf, H. F., Antuna, J. C., Grainger, R. G., Lambert, A. & Thomason, L. 1998. Radiative forcing from the 1991 Mount Pinatubo volcanic eruption. *Journal of Geophysical Research* **103**(D12), 13837-13857.

Stevenson, D. S. & Blake, S. 1998. Modelling the dynamics and thermodynamics of volcanic degassing. *Bulletin of Volcanology* **60**, 307-317.

Stix, J., Zapata G., J. A., Calvache V., M., Cortes J., G. P., Fischer, T. P., Gomez M., D., Narvaez M., L., Ordonez V., M., Ortega E., A., Torres C., R. & Williams, S. N. 1993. A model of degassing at Galeras Volcano, Colombia, 1988–1993. *Geology* **21**, 963-967.

Stoiber, R. E. & Carr, M. J. 1973. Quaternary volcanic and tectonic segmentation of Central America. *Bulletin of Volcanology* **37**, 304–325.

Stoiber, R. E., Malinconico, L. L. & Williams, S. N. 1983. Use of the correlation spectrometer at volcanoes. In: *Forecasting volcanic events* (edited by Tazieff, H. & Sabroux, J.-C.). Elsevier, Amsterdam, 425-444.

Stoiber, R. E., Williams, S., N. & Huebert, B., J. 1986. Sulfur and halogen gases at Masaya Caldera Complex, Nicaragua: total flux and variations with time. *Journal of Geophysical Research* **91**(B12), 12215-12231.

Stolper, E. 1982. Water in silicate glasses: an infrared spectroscopic study. *Contributions to Mineralogy and Petrology* **81**, 1-17.

Stolper, E. & Holloway, J. R. 1988. Experimental determination of the solubility of carbon dioxide in molten basalt at low pressure. *Earth and Planetary Science Letters* **87**, 397–408.

Symonds, R. B., Mizutani, Y. & Briggs, P. H. 1996. Long-term geochemical surveillance of fumaroles at Showa-Shinzan dome, Usu volcano, Japan. *Journal of Volcanology and Geothermal Research* **73**, 177-211.

Symonds, R. B., Reed, M. H. & Rose, W. I. 1992. Origin, speciation and fluxes of trace-element gases at Augustine volcano, Alaska: Insights into magma degassing and fumarolic processes. *Geochimica et Cosmochimica Acta* **56**, 633–637.

Symonds, R. B., Rose, W. I., Bluth, G. J. S. & Gerlach, T. M. 1994. Volcanic-gas studies: methods, results and applications. *Reviews in Mineralogy* **30**, 1-66.

Symonds, R. B., Rose, W. I., Gerlach, T. M., Briggs, P. H. & Harmon, R. S. 1990. Evaluation of gases, condensates, and SO_2 emissions from Augustine volcano, Alaska: the degassing of a Cl-rich volcanic system. *Bulletin of Volcanology* **52**, 355-374.

Symonds, R. B., Rose, W. I. & Reed, M. H. 1988. Contribution of Cl- and F-bearing gases to the atmosphere by volcanoes. *Nature* **334**, 415-418.

Tabazadeh, A. & Turco, R. P. 1993. Stratospheric chlorine injection by volcanic eruptions: HCl scavenging and implications for ozone. *Science* **260**, 1082-1086.

Tait, S. & Jaupart, C. 1990. Physical processes in the evolution of magmas. *Reviews in Mineralogy* **24**, 125-152.

Tazieff, H. 1983. Gas release, observed facts. In: *Forecasting volcanic events* (edited by Tazieff, H. & Sabroux, J.-C.). Elxevier, Amsterdam, 275-291.

Tazieff, H. 1994. Permanent lava lakes: observed facts and induced mechanisms. *Journal of Volcanology and Geothermal Research* **63**, 3-11.

Teggi, S., Bogliolo, M. P., Buongiorno, M. F., Pugnaghi, S. & Sterni, A. 1999. Evaluation of SO_2 emission from Mount Etna using diurnal and nocturnal multispectral IR and visible imaging spectrometer thermal IR remote sensing images and radiative transfer models. *Journal of Geophysical Research* **104**(B9), 20,069–20,079.

Thordarson, T., Self, S., Oskarsson, N. & Hulsebosch, T. 1996. Sulfur, chlorine and fluorine degassing and atmospheric loading by the 1783-1784 AD Laki (Skaftar Fires) eruption in Iceland. *Bulletin of Volcanology* **58**, 205-225.

Tittel, F. K., Lancaster, D. G. & Richter, D. 2000. Novel diode laser-based sensors for gas sensing applications. *Laser Physics* **10**(1), 348-354.

Valenza, M. 1998. Gas Hazard Field Data Collection. In: *"Mitigation of Volcanic Risk by Remote Sensing" Second term scientific progress report of EC contract ENV4 CT96 0288* (edited by Francis, P. W.).

van Wyk de Vries, B. 1993. Tectonics and Magma Evolution of Nicaraguan Volcanic Systems. Unpublished Ph.D. thesis, The Open University.

Vergniolle, S. & Jaupart, C. 1990. Dynamics of degassing at Kilauea Volcano, Hawaii. *Journal of Geophysical Research* **95**(B3), 2793–2809.

Villemant, B. & Boudon, G. 1998. Transition from dome-forming to plinian eruptive styles controlled by H_2O and Cl degassing. *Nature* **392**, 65-69.

Villemant, B. & Boudon, G. 1999. H_2O and halogen (F, Cl, Br) behaviour during shallow magma degassing processes. *Earth and Planetary Science Letters* **168**, 271-286.

Voight, B., Sparks, R. S. J., Miller, A. D., Stewart, R. C., Hoblitt, R. P., Clarke, A., Ewart, J., Aspinall, W. P., Baptie, B., Calder, E. S., Cole, P., Druitt, T. H., Hartford, C., Herd, R. A., Jackson, P., Lejeune, A. M., Lockhart, A. B., Loughlin, S. C., Luckett, R., Lynch, L., Norton, G. E., Robertson, R., Watson, I. M., Watts, R. & Young, S. R. 1999. Magma flow instability and cyclic activity at Soufriere Hills volcano, Montserrat, British West Indies. *Science* **283**, 1138-1142.

Wadge, G. 1984. Comparison of volcanic production rates and subduction rates in the Lesser Antilles and Central America. *Geology* **12**, 555–558.

Walker, G. P. L., Self, S. & Wilson, L. 1984. Tarawera 1886, New Zealand – a basaltic plinian fissure eruption. *Journal of Volcanology and Geothermal Research* **21**, 61–78.

Walker, J., A., Williams, S., N., Kalamarides, R., I. & Feigenson, M., D. 1993. Shallow open-system evolution of the basaltic magma beneath a subduction zone volcano: the Masaya Caldera Complex, Nicaragua. *Journal of Volcanology and Geothermal Research* **56**, 379-400.

Wallace, P. & Carmichael, I., S.E. 1992. Sulfur in basaltic magmas. *Geochimica et Cosmochimica Acta* **56**, 1863-1874.

Wallace, P. J. & Gerlach, T. M. 1994. Magmatic vapor source for sulfur dioxide released during volcanic eruptions: Evidence from Mount Pinatubo. *Science* **265**, 497-499.

Webster, J. D. 1990. Partitioning of F between H_2O and CO_2 fluids and topaz rhyolite melt: Implications for mineralizing magmatic-hydrothermal fluids in F-rich granitic systems. *Contributions to Mineralogy and Petrology* **104**, 424–438.

Webster, J. D., Kinzler, R. J. & Mathez, E. A. 1999. Chloride and water solubility in basalt and andesite melts and implications for magmatic degassing. *Geochimica et Cosmochimica Acta* **63**(5), 729–738.

Weibring, P., Edner, H., Svanberg, S., Cecchi, G., Pantani, L., Ferrara, R. & Caltabiano, T. 1998. Monitoring of volcanic sulphur dioxide emissions using differential absorption lidar (DIAL), differential optical absorption spectroscopy (DOAS), and correlation spectroscopy (COSPEC). *Applied Physics B* **67**(4), 419-426.

White, A. F. & Hochella, M. F. 1992. Surface chemistry associated with the cooling and subaerial weathering of recent basalt flows. *Geochimica et Cosmochimica Acta* **56**, 3711-3721.

Williams, S. N. 1983a. Geology and eruptive mechanisms of Masaya Caldera Complex, Nicaragua. Unpublished Ph.D. thesis, Dartmouth College.

Williams, S. N. 1983b. Plinian airfall deposits of basaltic composition. *Geology* **11**, 211-214.

Williams, S. N. & Dick, R. 1995. Remote measurement of CO_2 in volcanic plumes: First tests on plumes from fossil-fired power plants. *Fall Meeting Supplement, Eos, Transactions, AGU* **76**(46), F670.

Williams, S. N., Schaefer, S. J., Calvache V., M. L. & Lopez, D. 1992. Global carbon dioxide emission to the atmosphere by volcanoes. *Geochimica et Cosmochimica Acta* **56**, 1765-1770.

Wilson, L. 1980. Relationships between pressure, volatile content and ejecta velocity in three types of volcanic explosion. *Journal of Volcanology and Geothermal Research* **8**, 297–313.

Woods, A. W. 1995. The dynamics of explosive volcanic eruptions. *Reviews of Geophysics* **33**(4), 495–530.

Woods, A. W. & Cardoso, S. S. S. 1997. Triggering basaltic volcanic eruptions by bubble-melt separation. *Nature* **385**, 518–520.

Zolotov, M. Y. & Fegley, B. 2000. Eruption conditions of Pele volcano on Io inferred from chemistry of its volcanic plume. *Geophysical Research Letters* **27**(17), 2789-2792.

Zreda-Gostynska, G. & Kyle, P. R. 1997. Volcanic gas emissions from Mount Erebus and their impact on the Antarctic environment. *Journal of Geophysical Research* **102**(B7), 15039-15055.

APPENDIX A
MEASUREMENTS OF GAS CONCENTRATIONS IN THE ATMOSPHERE

Relationship between molecules per cm^2 and ppm

While a common unit for gas concentration used by workers in the atmospheric sciences is molecules cm^{-3}, in gas geochemistry or volcanology literature, units are most commonly ppm by volume. Gas concentrations integrated across a pathlength are therefore given in molecules cm^{-2} or in ppm m, in the two different fields. Units involving ppm do not relate to a single absolute concentration of molecules because they are dependent on temperature and pressure. The relationship between the two forms of unit is derived starting with the Ideal Gas Law.

The ideal gas equation relates pressure to the number of moles, n, of a gas mixture present:

$$p_t = \frac{nRT}{V} \qquad \text{(A-1)}$$

(where R is the ideal gas constant)

The partial pressure, P_i, of one component consisting of x_i ppm of a mixture is:

$$P_i = x_i p_t \qquad \text{(A-2)}$$

So for one component of the mixture equation (A-1) is rewritten:

$$P_i = \frac{x_i nRT}{10^{-6}V} \qquad \text{(A-3)}$$

Rearranging equation (A-3), and substituting for P_i with equation (A-2) gives:

$$x_i n = \frac{x_i p_t V}{RT} \times 10^{-6} \qquad \text{(A-4)}$$

Now let $V = L \times A$, where L is pathlength in m and A is the cross-sectional area in m^2. Then:

$$\frac{x_i n}{A} = \frac{x_i p_t L}{RT} \times 10^{-6} \qquad \text{(A-5)}$$

But we want the concentration of the gas component, X_i in molecules per cm^2, where:

$$X_i = \frac{x_i n}{A \times 10^4} \times N_A \qquad \text{(A-6)}$$

(where N_A is Avogadro's number)

So:

$$X_i = \frac{x_i p_t L N_A}{R T} \times 10^{-6} \times 10^{-4} \qquad \text{(A-7)}$$

Now expressing pressure in millibars, this becomes:

$$X_i = \frac{x_i \, p_t(mb) \, L N_A}{R T} \times 10^{-6} \times 10^{-4} \times 10^{2} \qquad \text{(A-8)}$$

Finally, collecting all the constants together, the relationship between concentration in ppm and molecules/cm^2 is written:

$$X_i \, (molec / cm^2) = \frac{x_i \, (ppm) \, L(m) \, p_t(mb)}{T(K)} \times 7.243 \times 10^{14} \qquad \text{(A-9)}$$

APPENDIX B
ROCK ANALYSES

Whole rock analyses using X-ray fluorescence

Analysis of major element concentrations in glass pellets created from powdered whole rock samples was carried out under the supervision of John Watson on the Open University's XRF machine. A check on accuracy was made by simultaneous analyses of two well-characterised samples.

Table D-1: Powdered samples of lava bombs ejected from Santiago Crater in 1997 and 1998 were analysed for their major element composition using X-ray fluorescence.

Sample	BV97A	BV97B	BV97-1	BV97-2	MNIN-1	MNIN-4	Mean [III]	Mean [II]
SiO2	50.89	50.77	50.54	50.28	50.72	50.87	50.68	51.31
TiO2	1.093	1.112	1.107	1.084	1.063	1.124	1.10	1.11
Al2O3	17.39	17.15	17.41	17.42	17.89	17.12	17.40	17.61
Fe2O3	12.33	12.54	12.32	12.16	12.10	12.58	12.34	
FeO								11.21
MnO	0.205	0.205	0.202	0.199	0.201	0.208	0.20	0.21
MgO	4.20	4.35	4.12	4.07	4.15	4.28	4.20	4.25
CaO	9.93	9.84	9.87	9.86	10.27	9.97	9.96	10.08
Na2O	2.74	2.71	2.68	2.66	2.88	2.85	2.75	2.79
K2O	1.14	1.15	1.12	1.12	1.16	1.20	1.15	1.16
P2O5	0.269	0.272	0.265	0.259	0.265	0.269	0.27	0.27
Total	100.3	100.2	99.7	99.3	100.7	100.5	100.1	100

Notes: [III] initial analysis calculated all iron as Fe_2O_3. [II] mean composition converted to count all iron as FeO, comparable with the electron microprobe point analyses on polished specimens (below).

Electron microprobe analyses of melt inclusions, matrix glasses and plagioclase phenocrysts

Major elements, sulfur and chlorine were analysed in melt inclusions, matrix glasses and plagioclase phenocrysts using the Open University's 4-spectrometer Cameca SX100 electron microprobe. Analytical conditions were 20 keV accelerating voltage, 20 nA beam current and a defocused 10 μm beam. Sulfur and chlorine were measured first (in the glasses) for 100 s peak count times (maximised for highest accuracy), followed by Na and K, due to their higher potential for volatilisation during the analysis, and then the other major elements, each for between 15 and 25 s peak count times. Similar sulfur concentrations were obtained regardless of whether the primary S standard used in the spectrometer was pyrite or barite, indicating that S was probably present in the melt in similar quantities in both its reduced and oxidised forms. The primary Cl standard was sylvite.

The microprobe was calibrated both before and after a set of analyses against three standard reference materials, to check for reliability of performance. A standard calibration against a sample of kaersutite was used to check the general performance regarding major elements. Calibrations to check the analysis of volatile elements were run on a scapolite standard (Gib Lake sample PSU4-294 (Ingamells & Gittins 1967), containing 2.3 wt % Cl and 0.18 wt % SO_3) and a well-characterised mid-ocean ridge basaltic glass standard (USNM-113716, 0.11 wt % S).

Melt inclusions in plagioclase phenocrysts

Table D-2: Electron microprobe point analyses of melt inclusions.

Sample	SiO2	TiO2	Al2O3	MgO	CaO	MnO	FeO	P2O5	Na2O	K2O	SO2	Cl	Total	S	Cl
	wt %	wt %	wt %	wt %	wt %	wt %	wt %	wt %	wt %	wt %	wt %	wt %	wt %	ppm	
M98.1A	51.79	1.36	13.68	4.85	8.62	0.26	13.43	0.34	3.20	1.61	0.015	0.042	99.19	75	420
M98.1B	52.54	1.20	13.84	4.68	8.59	0.26	12.84	0.30	3.24	1.62	0.016	0.041	99.16	80	410
M98.1C	52.31	1.20	13.85	4.73	8.47	0.25	12.85	0.28	3.19	1.64	0.013	0.049	98.84	65	490
M98.1E	50.97	1.45	13.55	4.95	8.84	0.26	13.77	0.31	3.07	1.47	0.010	0.044	98.68	50	440
M98.1F	51.36	1.42	13.66	4.86	8.60	0.26	13.64	0.34	3.21	1.57	0.006	0.046	98.96	30	460
M98.1G	51.01	1.39	13.50	5.09	8.50	0.26	13.77	0.30	2.96	1.70	0.031	0.049	98.56	155	490
M98.1H	50.03	1.54	12.83	5.10	8.49	0.28	14.22	0.37	2.63	1.59	0.029	0.072	97.18	145	720
M98.1I	51.40	1.45	13.57	4.99	8.95	0.28	13.92	0.35	2.95	1.37	0.019	0.044	99.29	95	440
M98.1J	50.94	1.24	13.81	4.98	9.06	0.27	13.97	0.30	2.89	1.45	0.042	0.050	99.03	210	500
M98.1K	50.86	1.32	13.51	5.12	8.76	0.28	13.96	0.29	3.00	1.56	0.034	0.046	98.73	170	460
M98.1L	51.24	1.31	12.85	5.25	8.51	0.29	14.32	0.30	2.98	1.68	0.035	0.046	98.80	175	460
M98.1M	51.17	1.40	13.62	4.94	8.70	0.25	13.62	0.37	3.09	1.57	0.019	0.042	98.79	95	420
M98.1N	51.26	1.46	13.43	4.96	8.73	0.27	13.81	0.40	3.06	1.52	0.023	0.040	98.95	115	400
M98.2A	50.81	1.55	13.59	5.10	8.79	0.25	13.74	0.42	3.11	1.54	0.003	0.042	98.94	15	420
M98.2B	51.54	1.31	13.25	5.18	8.49	0.27	13.84	0.32	2.96	1.58	0.018	0.061	98.80	90	610
M98.4A	51.39	1.37	13.72	4.96	8.97	0.26	13.68	0.33	3.19	1.41	0.003	0.039	99.33	15	390
M98.4B	51.31	1.36	13.63	4.94	8.92	0.26	13.60	0.33	3.19	1.45	0.020	0.039	99.06	100	390
M98.4D	50.96	1.30	13.60	5.33	8.60	0.30	14.61	0.29	2.84	1.66	0.029	0.041	99.56	145	410
M98.4E	51.01	1.39	13.72	4.84	8.82	0.28	13.63	0.34	3.17	1.42	0.005	0.041	98.65	25	410

Sample	SiO2	TiO2	Al2O3	MgO	CaO	MnO	FeO	P2O5	Na2O	K2O	SO2	Cl	Total	S	Cl
	wt %	wt %	wt %	wt %	wt %	wt %	wt %	wt %	wt %	wt %	wt %	wt %	wt %	ppm	
M98.4F	50.86	1.42	13.57	5.05	8.99	0.27	14.12	0.37	2.97	1.51	0.037	0.037	99.20	185	370
M98.7A	51.06	1.40	13.62	4.92	8.81	0.27	13.84	0.38	3.10	1.55	0.013	0.049	99.01	65	490
M98.7B	51.19	1.37	13.62	4.88	8.82	0.27	13.82	0.34	3.20	1.53	0.013	0.042	99.08	65	420
M98.7C	51.15	1.49	12.95	5.16	8.30	0.31	14.52	0.37	2.74	1.83	0.016	0.049	98.87	80	490
M98.12a	50.97	1.46	13.57	4.95	8.86	0.28	13.97	0.36	3.01	1.42	0.011	0.047	98.91	55	470
M98.12B	49.95	1.43	13.50	5.10	9.09	0.29	14.74	0.38	2.87	1.35	0.037	0.046	98.77	185	460
M98.12C	49.70	1.43	13.47	5.12	9.10	0.28	14.38	0.38	2.82	1.42	0.031	0.048	98.18	155	480
M98.6A	50.26	1.61	13.54	5.14	8.97	0.25	14.20	0.38	2.81	1.52	0.016	0.042	98.73	80	420
M98.6B	50.60	1.44	13.58	5.06	8.60	0.27	14.04	0.34	2.94	1.66	0.027	0.058	98.61	135	580
M98.6C	49.92	1.66	13.51	5.11	9.00	0.28	14.09	0.40	2.85	1.47	0.006	0.042	98.33	30	420
M98.6D	51.02	1.45	13.83	4.90	8.82	0.26	13.59	0.35	3.06	1.47	0.013	0.039	98.78	65	390
M98.6E	50.62	1.45	13.67	5.03	8.80	0.28	13.99	0.40	3.00	1.46	0.007	0.048	98.74	35	480
M98.6F	51.00	1.45	13.60	5.00	8.77	0.27	13.65	0.39	2.91	1.51	0.020	0.045	98.61	100	450
M98.6G	50.41	1.63	13.60	5.11	9.00	0.27	14.15	0.40	2.99	1.36	0.015	0.040	98.98	75	400
M98.6H	50.84	1.49	13.58	5.15	8.65	0.28	13.86	0.37	2.88	1.66	0.014	0.047	98.84	70	470
M98.6I	51.01	1.38	13.66	5.05	8.62	0.27	14.06	0.34	2.78	1.69	0.013	0.050	98.92	65	500
M98.6K	49.65	1.65	13.42	5.08	8.89	0.27	14.31	0.40	2.85	1.47	0.010	0.041	98.04	50	410
M98.6L	49.71	1.61	13.47	4.95	8.97	0.27	14.12	0.37	2.91	1.43	0.013	0.041	97.87	65	410
M98.6N	50.73	1.38	13.84	4.84	8.80	0.25	13.75	0.30	3.07	1.43	0.018	0.043	98.45	90	430
M98.6N	51.07	1.40	13.75	4.90	8.84	0.26	13.70	0.39	3.09	1.41	0.021	0.041	98.88	105	410
M98.6N	50.91	1.42	13.78	4.82	8.92	0.27	13.67	0.31	3.02	1.45	0.005	0.039	98.60	25	390
M98.6P	50.88	1.38	13.75	4.83	8.93	0.26	13.74	0.33	3.10	1.43	0.014	0.045	98.67	70	450
M98.1a	51.62	1.22	13.71	4.75	8.39	0.26	13.27	0.24	3.04	1.59	0.044	0.044	98.17	220	440
M98.1c	51.44	1.31	13.68	4.91	8.57	0.25	13.38	0.33	3.12	1.55	0.018	0.041	98.60	90	410
M98.1f	50.26	1.54	12.43	5.37	8.37	0.27	14.59	0.35	2.74	1.53	0.032	0.058	97.53	160	580
M98.4a	50.32	1.32	13.60	4.91	8.70	0.25	13.47	0.32	3.11	1.47	0.020	0.044	97.52	100	440
M98.4c	50.07	1.41	13.34	4.99	8.87	0.27	13.90	0.36	3.05	1.47	0.026	0.044	97.81	130	440
M98.7a	50.29	1.37	13.58	4.98	8.62	0.28	13.78	0.36	3.10	1.55	0.026	0.043	97.97	130	430
M98.7b	50.57	1.41	13.42	4.93	8.39	0.28	13.94	0.31	3.05	1.64	0.021	0.041	98.00	105	410
M97.1A	50.09	1.97	9.03	6.55	7.95	0.37	18.24	0.53	2.27	1.85	0.004	0.062	98.90	20	620
M97.5A	50.27	1.65	9.33	6.31	7.93	0.35	17.82	0.36	2.30	1.93	0.024	0.057	98.33	120	570
M97.5B	50.21	1.66	9.24	6.26	7.71	0.36	17.72	0.36	2.32	1.85	0.016	0.056	97.76	80	560
M97.5C	50.80	1.64	9.33	6.28	7.88	0.36	17.64	0.37	2.44	1.95	0.023	0.049	98.76	115	490
M97.5D	50.82	1.57	9.70	6.08	7.92	0.35	17.57	0.33	2.72	1.88	0.015	0.057	99.02	75	570
M97.5E	49.59	1.91	8.89	6.58	8.14	0.37	18.46	0.44	2.30	1.88	0.027	0.058	98.64	135	580
mean MI	50.81	1.45	13.06	5.15	8.66	0.28	14.32	0.35	2.93	1.57	0.019	0.046	98.64	96	464

Matrix glasses

Table D-3: Electron microprobe point analyses of glassy matrix in Masaya lava bombs.

Sample	SiO2	TiO2	Al2O3	MgO	CaO	MnO	FeO	P2O5	Na2O	K2O	SO2	Cl	Total	S	Cl
	wt %	wt %	wt %	wt %	wt %	wt %	wt %	wt %	wt %	wt %	wt %	wt %	wt %	ppm	
M98mgA	51.06	1.37	13.70	4.89	8.87	0.27	13.89	0.34	3.01	1.42	0.007	0.037	98.86	35	370
M98mgA	51.37	1.41	13.65	4.88	8.97	0.26	13.75	0.41	3.13	1.44	0.000	0.037	99.28	0	370
M98mgB	50.97	1.38	13.66	4.84	8.85	0.29	13.86	0.36	2.99	1.44	0.007	0.044	98.66	35	440
M98mgB	51.25	1.42	13.72	4.86	8.88	0.26	13.80	0.37	3.01	1.43	0.007	0.032	99.04	35	320

Sample	SiO2	TiO2	Al2O3	MgO	CaO	MnO	FeO	P2O5	Na2O	K2O	SO2	Cl	Total	S	Cl
	wt %	wt %	wt %	wt %	wt %	wt %	wt %	wt %	wt %	wt %	wt %	wt %	wt %	ppm	
M98mgB	50.80	1.41	13.62	4.94	8.99	0.27	14.11	0.36	2.96	1.40	0.005	0.043	98.90	25	430
M98mgC	51.89	1.38	13.70	4.93	8.92	0.27	13.73	0.36	3.13	1.48	0.000	0.033	99.81	0	330
M98mgC	51.43	1.39	13.65	4.90	8.80	0.27	13.79	0.40	3.03	1.46	0.008	0.038	99.15	40	380
M98mgC	51.38	1.40	13.72	4.92	8.79	0.25	13.75	0.37	3.11	1.47	0.002	0.036	99.18	10	360
M98mgC	51.34	1.43	13.62	4.92	8.79	0.27	13.87	0.35	3.06	1.49	0.006	0.037	99.17	30	370
M98mgD	51.59	1.40	13.67	4.83	8.84	0.25	13.76	0.33	3.08	1.47	0.003	0.036	99.25	15	360
M98mgD	51.61	1.40	13.81	4.90	8.87	0.28	13.75	0.34	3.07	1.45	0.012	0.040	99.54	60	400
M98mgD	51.40	1.42	13.64	4.87	8.85	0.25	13.91	0.34	3.03	1.46	0.008	0.039	99.21	40	390
M98mgD	51.41	1.42	13.72	4.86	8.86	0.27	13.70	0.38	3.03	1.48	0.002	0.034	99.15	10	340
M98mgE	51.20	1.41	13.66	4.90	8.94	0.26	13.79	0.29	3.06	1.49	0.001	0.040	99.03	5	400
M98mgE	51.35	1.43	13.69	4.92	8.85	0.25	13.80	0.35	3.06	1.44	0.003	0.030	99.17	15	300
M98mgE	51.58	1.43	13.77	4.97	8.78	0.27	13.79	0.36	3.02	1.48	0.002	0.035	99.48	10	350
M98mgE	51.40	1.43	13.75	4.88	8.81	0.28	13.79	0.34	3.01	1.39	0.004	0.037	99.10	20	370
M98mgE	51.29	1.44	13.81	4.91	8.90	0.27	13.77	0.39	3.07	1.42	0.006	0.045	99.32	30	450
M98mgE	51.25	1.44	13.71	4.93	8.97	0.28	13.69	0.34	3.00	1.46	0.005	0.036	99.09	25	360
M98mgF	50.53	1.41	13.76	4.88	8.83	0.27	13.82	0.37	3.13	1.40	0.008	0.029	98.42	40	290
M98mgF	50.71	1.40	13.72	4.91	8.88	0.28	13.76	0.40	3.05	1.46	0.000	0.034	98.60	0	340
M98mgF	51.02	1.39	13.78	4.94	8.87	0.28	13.85	0.35	3.10	1.41	0.004	0.033	99.03	20	330
M98mgF	50.62	1.43	13.75	4.90	8.84	0.25	13.90	0.39	3.08	1.44	0.013	0.033	98.66	65	330
M98mgF	50.58	1.44	13.72	4.96	8.90	0.25	13.86	0.34	2.99	1.41	0.010	0.037	98.48	50	370
MmgG	51.13	1.42	13.63	4.89	8.71	0.26	13.75	0.34	3.00	1.44	0.008	0.035	98.60	40	350
MmgG	50.96	1.41	13.71	5.00	8.81	0.25	13.76	0.39	3.01	1.48	0.000	0.040	98.82	0	400
MmgG	51.19	1.40	13.65	4.94	8.75	0.26	13.80	0.34	3.02	1.44	0.000	0.032	98.81	0	320
MmgG	51.38	1.41	13.68	4.96	8.73	0.27	13.79	0.36	3.06	1.43	0.001	0.032	99.09	5	320
MmgG	51.34	1.35	13.70	5.02	8.68	0.25	13.74	0.37	3.08	1.46	0.004	0.037	99.03	20	370
MmgH	51.43	1.39	13.76	4.92	8.81	0.27	13.55	0.35	3.04	1.47	0.012	0.039	99.05	60	390
MmgH	51.11	1.39	13.68	4.98	8.75	0.24	13.66	0.33	2.98	1.41	0.006	0.036	98.56	30	360
MmgH	51.08	1.36	13.65	4.99	8.73	0.23	13.66	0.35	3.01	1.43	0.010	0.041	98.54	50	410
MmgH	50.74	1.39	13.60	4.91	8.67	0.26	13.81	0.38	2.96	1.43	0.000	0.037	98.19	0	370
MmgH	50.97	1.40	13.57	4.93	8.83	0.25	13.72	0.32	3.00	1.40	0.010	0.037	98.43	50	370
MmgI	50.72	1.39	13.53	4.89	8.60	0.25	13.74	0.40	2.97	1.47	0.002	0.039	97.99	10	390
MmgI	50.94	1.42	13.55	4.90	8.68	0.27	13.78	0.35	3.00	1.39	0.001	0.037	98.31	5	370
MmgI	51.13	1.40	13.52	4.82	8.53	0.24	13.41	0.37	3.12	1.48	0.000	0.040	98.07	0	400
MmgI	50.71	1.40	13.60	4.94	8.64	0.27	13.69	0.36	3.04	1.43	0.023	0.038	98.15	115	380
MmgI	50.60	1.40	13.46	4.92	8.55	0.26	13.83	0.35	3.04	1.43	0.011	0.035	97.88	55	350
MmgJ	51.05	1.40	13.68	4.97	8.61	0.23	13.75	0.36	3.06	1.47	0.008	0.034	98.62	40	340
MmgJ	51.18	1.35	13.65	4.91	8.68	0.26	13.77	0.34	3.05	1.47	0.000	0.044	98.70	0	440
MmgJ	50.93	1.34	13.61	4.91	8.65	0.26	13.67	0.35	3.05	1.47	0.008	0.042	98.30	40	420
MmgJ	50.58	1.38	13.51	4.98	8.61	0.27	13.71	0.35	3.04	1.46	0.005	0.038	97.93	25	380
mean	51.12	1.40	13.67	4.92	8.79	0.26	13.77	0.36	3.04	1.44	0.005	0.037	98.81	27	369

Inclusion-holding plagioclase phenocrysts

Table D-4: Electron microprobe point analyses of the plagioclase phenocrysts from which melt inclusions were sampled.

Sample	SiO2	TiO2	Al2O3	MgO	CaO	FeO	Na2O	K2O	Total
	wt %	wt %	wt %	wt %	wt %	wt %	wt %	wt %	wt %
M98.1XA	48.93	0.030	31.09	0.148	15.38	1.10	2.67	0.145	99.49
M98.1XB	50.41	0.019	30.34	0.151	14.61	1.06	3.02	0.194	99.81
M98.1XC	48.32	0.030	31.49	0.125	16.09	1.10	2.38	0.122	99.66
M98.1XD	48.11	0.050	31.87	0.126	16.30	1.04	2.23	0.130	99.87
M98.1XE	48.59	0.022	31.27	0.129	15.68	1.10	2.60	0.134	99.52
M98.1XF	49.16	0.033	30.96	0.125	15.31	1.07	2.70	0.149	99.51
M98.1XF	49.53	0.033	30.74	0.139	15.11	1.07	2.86	0.186	99.70
M98.1XF	49.80	0.034	30.43	0.149	14.77	1.03	2.98	0.204	99.40
M98.1XG	49.63	0.030	30.50	0.140	14.98	1.08	3.14	0.202	99.73
M98.1XG	51.23	0.038	29.83	0.154	13.98	1.08	3.44	0.244	100.01
M98.1XG	51.43	0.051	29.47	0.160	13.73	1.09	3.60	0.247	99.82
M98.2XA	48.59	0.038	31.53	0.131	15.92	1.04	2.48	0.153	99.92
M98.2XA	49.37	0.017	30.86	0.142	15.20	1.07	2.83	0.172	99.66
M98.2XA	48.87	0.011	31.50	0.132	15.89	1.05	2.47	0.143	100.09
M98.2XA	48.32	0.020	31.48	0.131	15.87	1.05	2.46	0.140	99.51
M98.2XA	49.16	0.021	31.18	0.122	15.48	1.05	2.69	0.147	99.86
M98.2XB	48.54	0.030	31.50	0.139	15.81	1.09	2.58	0.153	99.85
M98.2XC	50.28	0.010	30.30	0.153	14.54	1.05	3.12	0.206	99.70
M98.2XD	48.28	0.026	31.51	0.135	15.91	1.10	2.48	0.147	99.64
M98.2XE	48.03	0.032	31.53	0.118	16.15	1.09	2.31	0.127	99.38
M98.2XE	48.81	0.040	30.94	0.163	15.38	1.12	2.75	0.165	99.40
M98.2XE	47.61	0.031	31.65	0.126	16.37	1.07	2.17	0.111	99.15
M98.2XG	51.04	0.026	29.64	0.155	13.95	1.14	3.46	0.232	99.66
M98.2XG	51.18	0.042	29.42	0.152	13.67	1.08	3.64	0.248	99.46
M98.4XA	48.98	0.034	31.29	0.140	15.66	1.12	2.57	0.141	99.97
M98.4XB	47.95	0.017	31.93	0.136	16.38	1.11	2.20	0.124	99.85
M98.4XC	48.01	0.018	31.89	0.128	16.29	1.07	2.22	0.112	99.80
M98.4XD	48.78	0.027	31.49	0.135	15.76	1.10	2.47	0.146	99.90
M98.4XE	47.80	0.026	31.95	0.110	16.47	1.07	2.24	0.115	99.80
M98.4XF	50.73	0.034	29.59	0.148	14.03	1.08	3.44	0.245	99.33
M98.4XF	49.91	0.014	30.44	0.151	14.65	1.08	3.04	0.184	99.47
M98.4XF	50.10	0.035	30.11	0.164	14.50	1.06	3.17	0.202	99.38
M98.4XF	50.02	0.018	30.37	0.163	14.87	1.08	3.03	0.206	99.77
M98.7XA	50.51	0.043	30.01	0.147	14.08	1.08	3.34	0.244	99.48
M98.7XA	48.84	0.041	31.00	0.138	15.41	1.05	2.61	0.149	99.24
M98.6XA	47.64	0.036	32.01	0.120	16.39	1.05	2.15	0.126	99.52
M97.1XA	50.20	0.051	30.32	0.160	14.48	1.03	3.19	0.196	99.66
M97.5XB	51.30	0.031	29.50	0.160	13.56	1.10	3.65	0.258	99.58
M97.5XB	51.51	0.057	29.23	0.169	13.47	1.08	3.71	0.283	99.53
M97.5XB	52.02	0.071	28.82	0.154	13.18	1.02	3.83	0.309	99.47
M97.4XA	50.93	0.041	29.47	0.152	13.87	1.07	3.55	0.243	99.34
mean	49.47	0.032	30.74	0.142	15.10	1.07	2.86	0.180	99.61